



## Micromachined Integrated 2D Transducers for Ultrasound Imaging

Havreland, Andreas S.

*Publication date:*  
2019

*Document Version*  
Publisher's PDF, also known as Version of record

[Link back to DTU Orbit](#)

*Citation (APA):*  
Havreland, A. S. (2019). *Micromachined Integrated 2D Transducers for Ultrasound Imaging*. DTU Health Technology.

---

### General rights

Copyright and moral rights for the publications made accessible in the public portal are retained by the authors and/or other copyright owners and it is a condition of accessing publications that users recognise and abide by the legal requirements associated with these rights.

- Users may download and print one copy of any publication from the public portal for the purpose of private study or research.
- You may not further distribute the material or use it for any profit-making activity or commercial gain
- You may freely distribute the URL identifying the publication in the public portal

If you believe that this document breaches copyright please contact us providing details, and we will remove access to the work immediately and investigate your claim.

TECHNICAL UNIVERSITY OF DENMARK

PH.D. THESIS

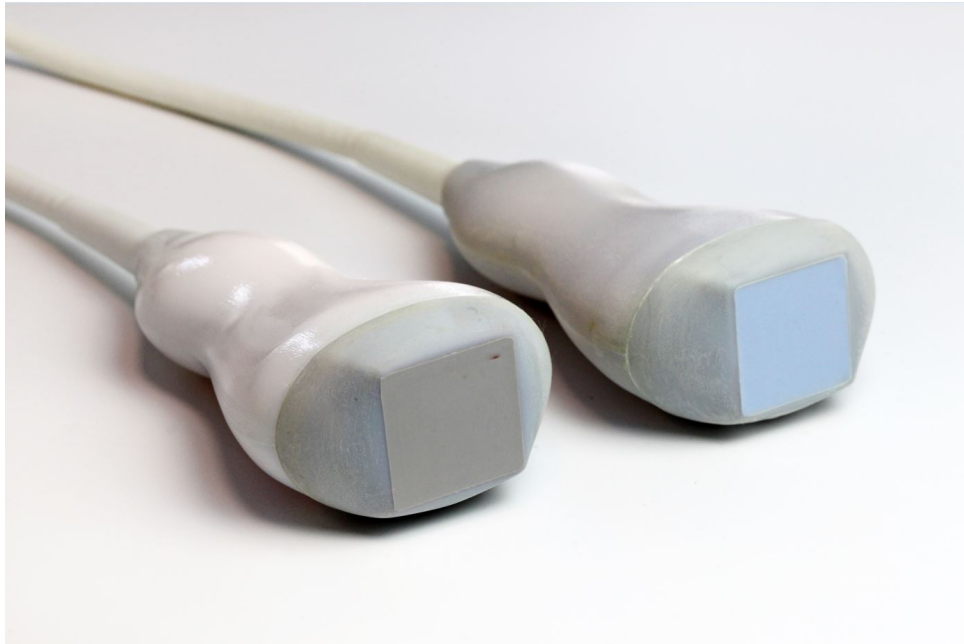
---

# MICROMACHINED INTEGRATED 2D TRANSDUCERS FOR ULTRASOUND IMAGING

---

*Author:*  
Andreas S. Havreland

*Supervisors:*  
Prof. Erik V. Thomsen  
Prof. Jørgen A. Jensen



14<sup>st</sup> September 2019

Kgs. Lyngby, Denmark

**Cover image:** Two row-column addressed ultrasound probes developed in this work. Photo by Jesper Scheel.

**Technical University of Denmark**  
**Department of Health Technology**  
Ørsteds Plads 345C  
2800 Kgs. Lyngby  
DENMARK  
Tel: (+45) 4525 5700  
Fax: (+45) 4588 7762  
Web: [www.healthtech.dtu.dk](http://www.healthtech.dtu.dk)  
Author e-mail: [ahav@dtu.dk](mailto:ahav@dtu.dk)

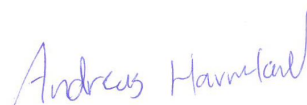
---

## Preface

---

This PhD thesis has been submitted to the Technical University of Denmark, in partial fulfillment of the requirements for the degree of Doctor of Philosophy. The work has been supervised by Professor Erik Vilain Thomsen and Professor Jørgen Arendt Jensen. This thesis consists of a recapitulation of the research work carried out from September 2016 to September 2019 at DTU Health Tech, Technical University of Denmark.

The MEMS group has conducted research within the field of Capacitive Micromachined Ultrasonic Transducer (CMUT) for several years, and profound knowledge of the CMUT technology was therefore already established before my project.



Andreas Havreland  
Kgs. Lyngby, September 2019



---

## Summary

---

Conventional ultrasound imaging produces 2D images of the human body, and these images are today routinely used for diagnostics purposes. The two-dimensional images can efficiently be displayed on a computer screen and are easy to interpret, whereas 3D images are more difficult to interpret but provide additional information about the imaged objects. The added dimension in a 3D image can provide vital information and can be used for new innovative imaging techniques. However, the complexity of the underlying transducer technology increases enormously when the imaging capabilities go from 2D to 3D. New advances in the transducer technology, such as row-column addressed arrays, drastically reduce the complexity of ultrasound systems capable of 3D imaging. The row-column technology reduces the required number of electrical interconnections from  $N^2$  to  $2N$ , where  $N$  is the number of channels in the ultrasound system. The main goal of this thesis is to develop the row-column addressed transducer array. The technology of capacitive Micromachined Ultrasound Transducers (CMUT) is used for the development platform for the row-column arrays due to the high flexibility and desired imaging properties offered by this technology.

Theoretical analysis of a CMUT is presented in the first part of thesis, including investigation of the static and dynamic properties. Multiple CMUT fabrication methods are developed, demonstrated, and used to fabricate various row-column arrays of different sizes. The area of row-column addressed arrays can be larger than conventional ultrasound transducers which introduces new challenges that has to be addressed. These challenges included increased resistance in the electrodes, and a design criterion for sufficient resistance of long row-column elements is derived and experimentally documented.

Two  $92 \times 92$  4.5 MHz row-column addressed CMUT arrays are assembled into ultrasound probes. The CMUT probes are electrically characterized,

long term stability test during 16 h showed no sign of dielectric charging and the electromechanical coupling coefficient is estimated to be 18.3%. The acoustical performance of the probes are characterized and 3D imaging capabilities are demonstrated at a depth of 7 cm in a cyst phantom.

---

## Resumé

---

Ultralydsbilleddannelse bliver rutinemæssigt brugt til diagnosticering i medicinsk sammenhæng. Konventionelt er ultralydsbilleder i 2D, hvilket både gør det nemt at fortolke og afbillede på en computerskærm, hvorimod 3D-billeder er sværere at fortolke men indeholder mere information om det afbillede objekt. Den ekstra dimension i 3D- billede kan give livsvigtig information og bane vejen for nye billedeteknikker. Men kompleksiteten af den bagvedliggende transducertechnologi stiger voldsomt når man går fra 2D til 3D. Den nyeste udvikling af transducerkoncepter, såsom række-søjle adressering, reducerer denne kompleksitet drastisk. Række-søjle-adressering reducerer antallet individuelle elektriske forbindelse fra  $N^2$  til  $2N$ , hvor  $N$  er antallet af kanaler i ultralydssystemet. Hovedfokuset i denne afhandling er at udvikle transducere baseret på teknologien bag rækkesøjle-adressering. Til at facilitere denne udvikling er teknologien baseret på kapacitive mikrofremstillet ultralydstransducer (CMUT) valgt som platform. Dette valg er grundet fleksibilitet og den øget billedkvalitet som CMUT teknologien tilbyder.

Den første del af afhandlingen indeholder en teoretisk analyse af en CMUT, som inkluderer en gennemgang af de statiske og dynamiske egenskaber. Derudover bliver flere forskellige CMUT fabrikationsmetoder gennemgået, demonstreret, og brugt til at fabricere række-søjle adresseret CMUT transducere i forskellige størrelser. Arealet af en række-søjle adresseret CMUT kan blive betydelig større end konventionelle ultralyds transducere hvilket medfører nogle problemstillinger, der skal håndteres i CMUT design processen. Et af disse problemer er øget elektrisk modstand, og et kriterium for den højeste tilladte modstand i elektroderne er udledt og eksperimentelt demonstreret i denne afhandling. To 92+92 4.5 MHz række-søjle adresseret CMUT transducere er blevet samlet til en ultralydsprobe, og disse prober er akustisk karakteriseret og har demonstreret 3D ultralydsbilleddannelse ned til 7 cm dybde på et cystefantom.





---

## Acknowledgements

---

First of all I would like to thank my supervisor Prof. Erik V. Thomsen and my co-supervisor Prof. Jøregn Arendt Jensen. I have learned many things from both of you during the past three years on a personal and professional level. It has been a great experience for me to participate in the important research you are conducting.

Then I would like thank my colleagues at DTU Health Tech. Thank you for making my time as a PhD student very joyful. A special thank you goes to my office mate Martin Lind Ommen for always providing a friendly atmosphere at our office and equally important thank you for all the constructive professional debates we have had on various subjects. Thanks to all the students that I have supervised, you have been an important part of the CMUT development in the MEMS group.

I would also like to thank our partners at BK Medical and DTU Nanolab for facilitating the research conducted in this thesis. A proper thank you should also be given to Jan Bagge for his lessons regarding CMUT electronics.

Last, but not least, a huge thanks goes to my family for the continuous support. First and foremost to you Mathilde. Thank you for the endless support and love you have provided.



---

## Acronyms

---

<b>AFM</b>	Atomic Force Microscope
<b>ASIC</b>	Application Specific Integrated Circuit
<b>BCB</b>	BenzoCycloButene
<b>BHF</b>	Buffed HydroFluoric acid
<b>BOX</b>	Burried OXide
<b>CMP</b>	Chemical Mechanical Polishing
<b>CMUT</b>	Capacitive Micromachined Ultrasonic Transducer
<b>CT</b>	Computed Tomography
<b>CV</b>	Capacitance-Voltage
<b>DREM</b>	Deposit, Remove, Etch, Mask
<b>DTU</b>	The Technical University of Denmark
<b>EFE</b>	EigenFunction Expansion
<b>FBW</b>	Fractional BandWidth
<b>FORCES</b>	Fast Orthogonal Row–Column Electronic Scanning
<b>FPM</b>	Fully Populated Matrix

<b>FWHM</b>	Full Width Half Max
<b>IUS</b>	International Ultrasound Symposium
<b>IV</b>	Current-Voltage
<b>KOH</b>	potassium hydroxide
<b>LOCOS</b>	Local oxidation of silicon
<b>LPCVD</b>	Low Pressure Chemical Vapour Deposition
<b>MMS</b>	Method of Multiple Scales
<b>MR</b>	Magnetic Resonance
<b>PCB</b>	Printed Circuit Board
<b>PDMS</b>	polydimethylsiloxane
<b>PECVD</b>	Plasma Enhanced Chemical Vapour Deposition
<b>PMUT</b>	Piezoelectric Micromachined Ultrasonic Transducers
<b>PSOI</b>	Poly-Silicon-On-Insulator
<b>PZT</b>	ceramic material with piezoelectric properties
<b>RCA</b>	Row-Column-Addressed
<b>RMS</b>	Root mean square
<b>SEM</b>	Scanning Electron Microscope
<b>SNR</b>	Signal to Noise Ratio
<b>SOI</b>	Silicon-On-Insulator
<b>SPM</b>	Sparsely Populated Matrix
<b>TOBE</b>	Top-Orthogonal-to-Bottom-Electrode

---

## Nomenclature

---

### CMUT array

$A_{\text{trans}}$	Area of transducer surface	[m <sup>2</sup> ]
$f_0$	Center frequency	[Hz]
$L$	Length of an element	[m]
$N$	Number of channels	[#]
$W$	Width of an element	[m]

### Single CMUT cell

$A$	Area of a single CMUT cell	[m <sup>2</sup> ]
$a$	Radius of a single CMUT cell	[m]
$F$	Force (frequency domain)	[N·s]
$f_{RI}$	Force from the radiation impedance (time domain)	[N]
$g$	Gap height in CMUT cavity	[m]
$h$	Thickness of the CMUT plate	[m]
$k_s$	Linear spring constant of CMUT	[N/m]
$m$	Mass of a single CMUT cell	[kg]
$U$	Applied DC bias	[V]

$U_{pi}$	Pull-in voltage	[V]
$V$	Velocity of the CMUT plate (frequency domain)	[m]
$v$	Velocity of the CMUT plate (time domain)	[m/s]
$x$	Displacement of the CMUT plate	[m]
$Z$	Radiation impedance (frequency domain)	[kg/s]
$z$	Radiation impedance (time domain)	[kg/s <sup>2</sup> ]

### Material properties

$\rho_m$	Density of medium	[kg/m <sup>3</sup> ]
$\rho_p$	Density of plate	[kg/m <sup>3</sup> ]
$\varrho$	Resistivity	[ $\Omega \cdot \text{cm}$ ]
$c_m$	Speed of sound	[m/s]

### Other

$\lambda$	Wavelength	[m]
$\omega$	Angular frequency	[rad]
$\varepsilon$	Permittivity	[F/m]
$A_c$	Cross-sectional area	[m <sup>2</sup> ]
$C$	Capacitance	[F]
$F_e$	Electrostatic force	[N]
$F_s$	Spring force	[N]
$k$	Wave number	[m <sup>-1</sup> ]
$R$	Resistance	[ $\Omega$ ]
$t$	Time	[s]

---

# Contents

---

<b>Preface</b>	<b>iii</b>
<b>Summary</b>	<b>v</b>
<b>Resumé</b>	<b>vii</b>
<b>Acknowledgements</b>	<b>ix</b>
<b>Acronyms</b>	<b>xii</b>
<b>Nomenclature</b>	<b>xii</b>
<b>1 Introduction</b>	<b>1</b>
1.1 CMUT . . . . .	2
1.1.1 CMUT outlook . . . . .	5
1.2 2D ultrasound imaging . . . . .	5
1.3 3D ultrasound imaging . . . . .	7
1.4 Thesis outline . . . . .	8
1.5 Publications . . . . .	9
<b>2 Theory</b>	<b>11</b>
2.1 Static model . . . . .	12
2.1.1 Lumped model . . . . .	12
2.1.2 Clamped plate . . . . .	13
2.1.3 Approximate solutions . . . . .	14
2.2 Dynamic model . . . . .	16



2.2.1	Small $ka$ limit . . . . .	18
2.2.2	Large $ka$ limit . . . . .	23
2.2.3	Full description . . . . .	26
2.3	Chapter summery . . . . .	27
<b>3</b>	<b>Row-Column-Addressed Arrays</b>	<b>29</b>
3.1	Scaling laws . . . . .	30
3.2	Geometry . . . . .	35
3.3	Edge waves . . . . .	37
3.4	Silicon substrates for row-column CMUT fabrication . . . . .	39
3.5	Chapter summery . . . . .	41
<b>4</b>	<b>CMUT fabrication</b>	<b>43</b>
4.1	Fusion bonding . . . . .	44
4.1.1	Characterization . . . . .	47
4.2	Polymer bonding . . . . .	52
4.2.1	Characterization . . . . .	54
4.3	Anodic bonding . . . . .	57
4.3.1	Characteriaztion . . . . .	58
4.4	Combined anodic and fusion bonding . . . . .	62
4.4.1	Rodent one . . . . .	63
4.4.2	Mask layout . . . . .	67
4.4.3	Characterization . . . . .	67
4.5	Poly-Silicon-On-Insulator wafer . . . . .	70
4.6	Chapter summery . . . . .	76
<b>5</b>	<b>CMUT characterization</b>	<b>79</b>
5.1	Acoustic characterization . . . . .	79
5.2	Electrode resistance . . . . .	87
5.3	Ultrasound imaging results . . . . .	101
5.4	Chapter summery . . . . .	102
<b>6</b>	<b>Conclusion</b>	<b>105</b>
	<b>Bibliography</b>	<b>118</b>
	<b>A Paper A - BCB polymer based row-column addressed CMUT119</b>	
	<b>B Paper B - Design of a novel zig-zag 192+192 Row Column Addressed Array Transducer: A simulation study.</b>	<b>125</b>

<b>C</b>	<b>Paper C - CMUT Electrode Resistance Design: Modeling and Experimental Verification by a Row-Column Array</b>	<b>131</b>
<b>D</b>	<b>Paper D - Wafer bonded CMUT technology utilizing Poly-Silicon-on-Insulator wafers</b>	<b>141</b>
<b>E</b>	<b>Paper E - A Row-Column-Addressed 2D Probe with and Integrated Compound Diverging Lens</b>	<b>147</b>
<b>F</b>	<b>Fabrication processes</b>	<b>153</b>
	F.1 LOCOS . . . . .	153
	F.2 BCB . . . . .	160
	F.3 Anodic bond . . . . .	165
	F.4 LOCOS + Anodic bond . . . . .	171



# CHAPTER 1

---

## Introduction

---

Medical applications of ultrasound dates back to 1950 [1], and have since grown to be a conventional tool for diagnostic purposes. Ultrasound is additionally routinely used in multiple other applications ranging from park assist, non destructive testing, fingerprint sensing, gas sensing among other. Ultrasound imaging is like X-ray, Computed Tomography (CT), and Magnetic Resonance (MR) used to examine the internal part of the human body, and ultrasound imaging has the advantages of offering real time imaging opposite to the other modalities and additionally at a low cost. However, the resolution of ultrasound imaging is in general inferior compared to the three other imaging modalities, and ultrasound is limited to predominantly visualization of tissue. Imaging of bone structures is challenging for ultrasound, the reason being bone structures reflect the majority of generated pressure from an ultrasound transducer while tissue allows penetration of the ultrasound waves. This is in technical terms explained by acoustic impedance mismatch between two mediums. The interface between two adjacent mediums acts as a reflector if the acoustic impedance mismatch is large, which prohibits imaging beyond the interface. Medical imaging of bone structures is therefore commonly acquired using imaging modalities such as X-ray, CT, and MR.

Today, nearly all commercial ultrasound transducers for medical imaging are made by a ceramic material with piezoelectric properties (PZT).  $\text{Pb}[\text{Zr}_x\text{Ti}_{1-x}]\text{O}_3$  is the chemical composition of these types of ceramics, and the abbreviation PZT is used as a generic term for the entire class of piezoelectric ceramics. Other chemical compositions can also be used, but the

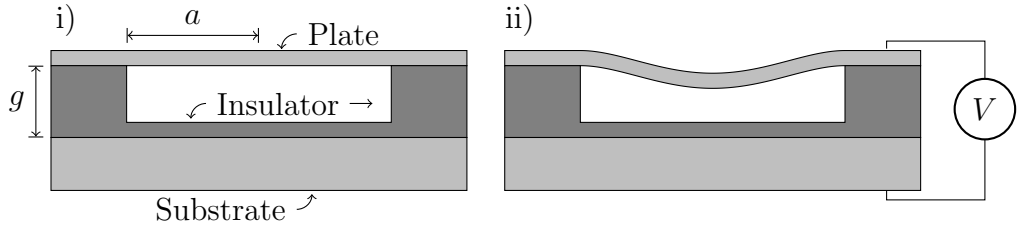


**Figure 1.1:** Cross-section sketch of a single CMUT. i) Geometrical CMUT parameters are indicated as well as definitions of the different layers.  $a$  is the CMUT radius and  $g$  is the gap height. ii) The working principle of a CMUT. An electrical field is created by applying a voltage between the plate and the substrate that forces the plate towards substrate. The deflection of the CMUT plate can thereby be controlled by applying a voltage, and ultrasonic pressure waves can be generated by applying a time varying pulse.

terminology PZT will be used throughout this thesis for all piezoelectric ceramics. Modern ultrasound transducers are fabricated by dicing pieces of PZT into small adjacent elements next to each other. The geometry of the diced PZT elements as well as the quality of the PZT crystallinity determine the performance of the transducer, and notably advances in the PZT crystallinity have significantly increased the performance of the transducers used for medical imaging over the years [2]. But, new semiconductor based technologies have begun to compete with the conventional PZT technology. These new promising technologies are the Piezoelectric Micromachined Ultrasonic Transducers (PMUT) and Capacitive Micromachined Ultrasonic Transducer (CMUT) technology that both have been used to demonstrate medical ultrasound images, and the CMUT technology is already being sold commercially for medical imaging applications.

The PZT and PMUT are both interesting technologies, however, the focus of this thesis is exclusively development of the CMUT technology, and in particular for 3D ultrasound imaging.

## 1.1 CMUT

A CMUT is a micro sized device that consists of a substrate and a vibrating plate (or membrane) separated by an electrically insulating material. A cross sectional sketch of a single CMUT is shown on Fig 1.1 i). The horizontal dimension of a typical CMUT ranges between 5 and 100  $\mu\text{m}$  whereas the common vertical dimension is in the sub micron regime. The high aspect ratio geometry of a single CMUT makes it impractical to draw sketches to

scale, and all sketches of CMUTs are therefore not drawn to scale for visual purposes. The semiconductor technology is the obvious choice for fabricating devices on this length scale. Conventional semiconductor fabrication techniques provide a large degree of freedom in design process of CMUTs, which is one of the main selling points for the CMUT technology.

The geometry of a CMUT is defined by conventional UV lithography and the most common shapes for the individual CMUTs are either circles or squares in which case the parameter  $a$  becomes either the radius or half side length and  $g$  is in both cases the gap height. CMUTs are operated by applying a voltage between a top and a bottom electrode that are designed into the CMUT structure, see Fig. 1.1 ii). The applied voltage creates an electric field that forces the plate towards to substrate due to the electrostatic force. The CMUT is a high field device, meaning the applied voltage does not necessarily has to be high, but the electric field between top and bottom electrode is in many applications required to be on the order of  $0.5 \text{ V/nm}$ , which is high compared to other MEMS devices. The electromechanical coupling between the electrostatic and mechanical domain makes a CMUT inherently non-linear. It should, however, be emphasized that the structural deformation of the plate caused by an applied bias can in most cases be described by a linear deformation theory. The DC bias is required for CMUT applications within the field of medical imaging, since the generated pressure and the receive sensitivity both increases as function of the applied bias. Acoustic signals are generated by imposing a voltage pulse on top of the DC bias which effectively forces the plate to oscillate. In transmit situation, the kinetic energy of the plate couples into the medium as propagating pressure waves. The mechanism is opposite in receive, where an external pressure wave couples into kinetic energy of the plate, that can be measured and converted into an ultrasound image.

The non-linearity of the CMUT is in many cases used advantageously, since, the Signal to Noise Ratio (SNR) has a non-linear increase with the applied bias. The plate is forced towards the substrate due to the electrostatic force as the DC bias is increased. The mechanical stiffness of plate gets reduced as the applied DC-bias increases, a phenomenon called the spring softening effect. The non-linear effects become more and more dominant as the bias voltage is increased until a point where the spring force from the plate no longer can counter the electrostatic force. It results in an unstable state where the plate is forced to the bottom of the cavity. This is a non-linear phenomenon that occurs at a specific voltage known as pull-in voltage or collapse voltage. The gap height, the plate thickness, and the radius or side length of a CMUT determine the pull-in voltage, and other parameters such as resonance frequency, bandwidth, and output pressure.

The top plate and the substrate of a CMUT are separated by an electrical insulator in the CMUT literature commonly denoted the post region, or in short just post. Excellent insulating properties are essential for functional CMUTs, since the insulator has to be able to withstand the high electrical field. The purity of the insulator also of crucial importance, even a tiny amount of mobile impurities in the insulator can give rise to dielectric charging during operation, which greatly reduces the functionality of the CMUT.

To achieve high quality insulation properties layers of silicon oxide or silicon nitride are commonly used for CMUT fabrication. An insulating layer in the bottom of the cavity is often used to prevent the CMUT from short circuiting if the pull-in voltage is applied. The same effect can be obtained by having an insulating layer on the plate (on the side towards the cavity), both cases require high quality dielectric properties for a satisfying CMUT performance.

The CMUT technology was first proposed in the early 1990's by Khuri-Yakub from Stanford University. Two papers from 1994 and 1996 by the same name *A Surface Micromachined Electrostatic Ultrasonic Air Transducer* and both by Haller and Khuri-Yakub are the first and most influential CMUT papers [3,4]. The interest for the CMUT technology has after these papers grown steadily ever since and is still an expanding technological field, which can be seen in Fig. 1.2 where the number of publications is shown as function of time. The publication count from 2019 is prior the to large International Ultrasound Symposium (IUS) where a substantial amount of CMUT papers are published. Two of the many reasons behind the success of the CMUT technology are the design flexibility and the possibility of parallelism. The sketched CMUT in Fig. 1.1 ii) constitutes a single CMUT, which henceforth is called a CMUT cell, that by itself produces a small signal regardless of it being acoustically or electrically. But, by grouping hundreds or even thousands of individual CMUT cell together and operating all of them in parallel enhance the SNR to a level capable of competing at a commercially level within various applications.

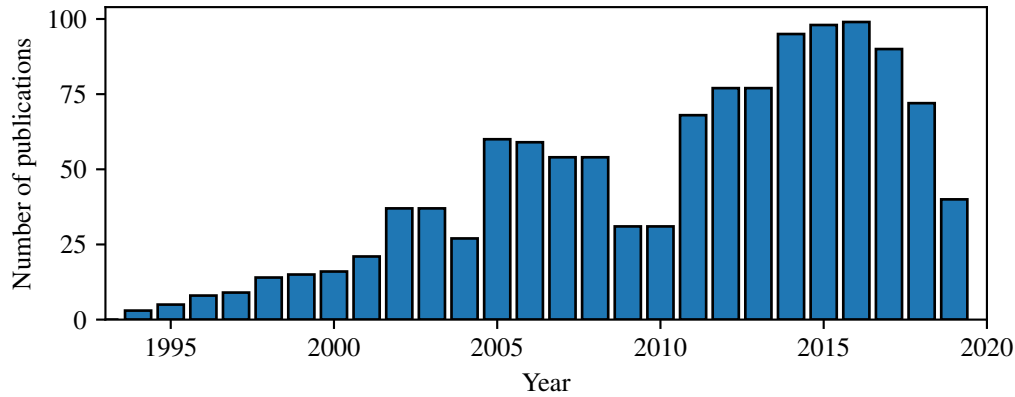


**Figure 1.2:** Number of CMUT publications versus time. The data has been acquired from the Web of Science database using the keywords: CMUT or Capacitive Micromachined Ultrasound Transducer or Surface micromachined transducer.

### 1.1.1 CMUT outlook

The first commercialization of a CMUT probe for medical imaging was back in 2009 where Hitachi released the *Mappie* probe. In the following years KOLO and Butterfly Network have released their respective CMUT probes, where especially the latter has gotten a lot of positive attention. The CMUT probe from Butterfly Network is portable and uses a smartphone or a tablet to display the acquired ultrasound image. Furthermore, the Butterfly iQ – Ultrasound app, used for visualization on the smart devices, was announced as one of the winners of the Apple design Awards in 2019.

The publicity, especially associated with the Butterfly Network, has boosted the confidence in the CMUT technology, that is predicted to have a significant increase during the next couple of years. The market share of CMUT transducers within the field of medical imaging was less than 1% back in 2017, but is according to a report from Yole Développement [5] predicted to occupy 30 % of the market in 2023 as illustrated in Fig. 1.3.

## 1.2 2D ultrasound imaging

Conventional ultrasound transducers produce two-dimensional images of the internal body and such transducers will henceforth be referred to as a linear arrays or 1D arrays. A Linear array can be further decomposed into  $N$  elements. Each of the  $N$  individual elements has to be electrically connected



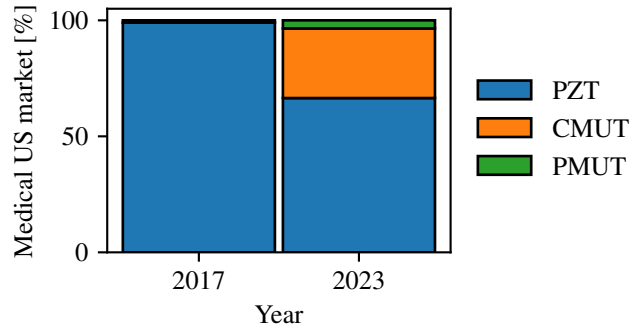


**Figure 1.3:** Prediction of the medical ultrasound market distribution in 2023 compared with the numbers from 2017 [5].

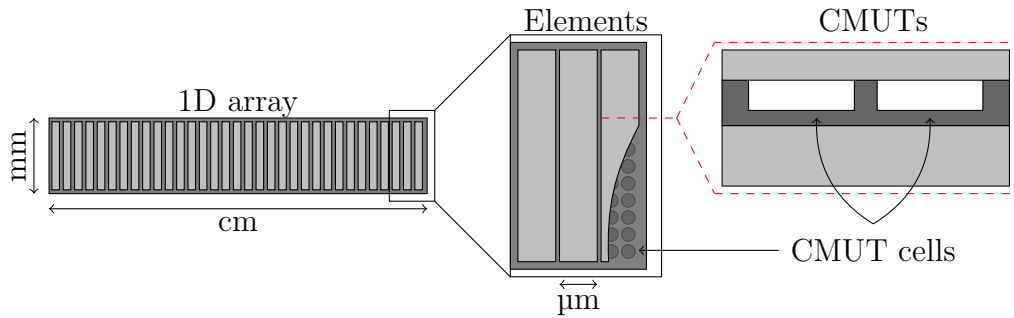


**Figure 1.4:** Sketch of all the components in a 1D CMUT array. The 1D array consists of  $N$  individual elements. The end of the 1D array is magnified and the zoom-in shows the three last elements. The plate is partially removed from the last element to illustrate the positions of the CMUT cells. The red dashed line indicates the in-plane cross section in which CMUTs commonly are drawn.

while being insulated from all the other elements. Each element in a linear CMUT array consists of numerous CMUT cells, typically several hundreds of CMUT cells per element. All the components that make up a linear CMUT array are sketched together in Fig. 1.4. The number of elements should preferably be as high as possible, since the image quality improves with the number of elements. The surface area and the complexity of the probe assembly do also increase with number of element, hence, application specific trade-offs have to be considered for all ultrasound transducers. To put things in perspective, modern ultrasound images are typically acquired by transducers with more than 100 individual elements.

Multiple ultrasound images have been documented by CMUTs probes

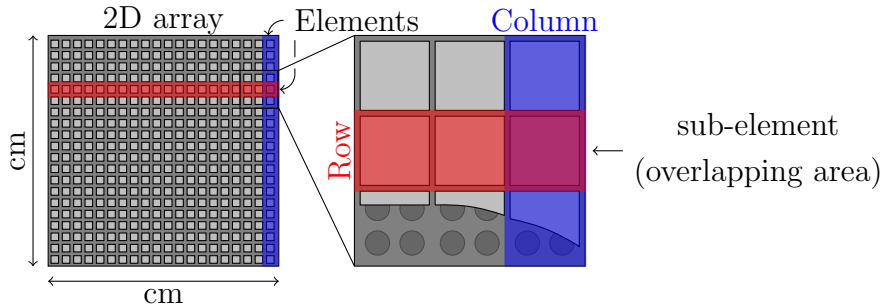


**Figure 1.5:** Sketch of all the components in a 2D CMUT array. The 2D array consists of  $N$  individual rows and  $N$  individual columns, highlighted in red and blue, respectively. The area where rows and columns overlap defines a sub-element. The zoom-in shows nine sub-elements where the plate is partially removed from three of them to illustrate the positions of the CMUT cells.

since the discovery back in the 1990s [6–8]. Notably, the presented probe in [8] was fully capable of producing commercially comparable B-modes images and doppler blood flow estimation of the carotid artery.

### 1.3 3D ultrasound imaging

All objects inside the human body are three dimensional and information is inevitably lost by evaluating 2D images of the body. It is therefore naturally to think in terms of three dimensional imaging. The terminology for 2D transducers is not as well defined as the 1D counterpart, but the terminology used throughout this thesis is the following. 2D arrays can, equivalent to the 1D arrays, be divided into elements. A 2D transducer consists of  $2N$  elements,  $N$  rows and  $N$  columns as sketched in Fig. 1.5. The overlapping region of a row and a column is called a sub-element.

Fully Populated Matrix (FPM) arrays are the direct extension from 1D arrays to 2D arrays. These arrays require electrical interconnections to all the individual sub-elements and therefore defined by  $N \times N$  channels. This configuration is problematic due to a quadratic scaling law of electrical interconnections. Thus, more than 10000 electrical interconnections are required for a FPM transducer to obtain the same 3D image quality as a linear transducer with plus 100 elements. Multiple transducer architectures have been proposed in the literature to overcome the challenge with the enormous amount of electrical interconnections [9] associated with 3D imaging. One way of achieving 3D images is to use a conventional 1D transducer with an integrated accelerometer, capable of monitoring the relative position of the

transducer. Three dimensional ultrasound images are reconstructed by combining the knowledge of the transducer position with multiple 2D images. This 3D transducer architecture does not provide real time 3D images and is also sensitive to movement of the imaged object between the first and last acquired image. A rather similar architecture, that also stitch multiple images together, is a motorized 1D transducer, where the transducer surface is steered periodically back and forth by a motor inside the probe handle. It has the advantage of being less operator dependent, and also provide a higher frame rate for the reconstructed 3D images. These two technologies can provide 3D images, but will inherently have difficulties with estimating blood flow in 3D, due to the time shift between images used for the reconstruction. The transducer design should be structured as a 2D array to efficiently perform 3D blood flow estimations. Either by the FPM configuration, at the expense of a high amount of interconnections, or by a sparse array configuration where a smaller percentage of the sub-elements are electrically connected. A third option is a Row-Column-Addressed (RCA) array, this configuration utilizes the fact that the rows and columns make up two orthogonal linear arrays on top of each other. The channel count is significantly reduced to  $2N$  compared to the  $N^2$  dependency for the FPM array, and the RCA array configuration provides the opportunity of real time 3D images and flow estimation [10].

Development of RCA CMUT arrays with large surface area and a high channel count is the focus of this thesis. The different 2D transducer technologies are discussed in more detail in chapter 3, where a more technical and in depth analysis between the different 2D transducer technologies are given.

## 1.4 Thesis outline

The thesis is divided into six chapters. Theoretical modelling of a CMUT is discussed in chapter 2 where design parameters and scaling laws are derived and discussed. The chapter is divided into two parts. The first part addresses the static behaviour of a single CMUT cell, and the dynamics of a single CMUT cell is examined in the second part.

The row-column technology is discussed in chapter 3. After a brief literature review are relevant scaling laws for 2D arrays considered. The geometrical structure of a RCA CMUT array will be provided followed by an analysis of challenging phenomenons associated with the row-column geometry. It includes the issue of edge waves and problems with capacitive substrate coupling, the later is CMUT specific.

CMUT fabrication and process development are examined in chapter 4.

Three different fabrications methods are discussed with a special focus on RCA arrays. The first method utilizes fusion bonding, the second method is a polymer based CMUT fabrication, and an anodic bonded CMUT is the third and last process. An additional fourth fabrication process is also presented, it combines the beneficial properties of the fusion bonding method and the anodic bonding method. Finally, a novel fabrication technique of Poly-Silicon-On-Insulator (PSOI) wafer is presented. PSOI wafers can be used for CMUT fabrication as a substitution of conventional Silicon-On-Insulator (SOI) wafers. A characterization of PSOI wafer are given and the PSOI technology is demonstrated for both fusion bonded and anodic bonded CMUTs.

An acoustic characterization of the developed CMUTs are presented in chapter 5. This chapter is divided in two parts. A developed single channel acoustic set-up is considered in the first part. The frequency response from the instruments and electronics are optimized to provide optimal conditions for acoustic CMUT characterization. Acoustic measurements of a fabricated linear CMUT array is demonstrated with two different configurations in the electronics.

In the second part of the chapter is a fabricated 92+92 RCA CMUT probe acoustically characterized, where an attenuated pressure field was observed for the columns. A delay line model is derived and used to describe the observed attenuation for the columns. At the end of the chapter is 3D ultrasound row-column images presented.

The thesis is concluded in chapter 6.

## 1.5 Publications

The results from this thesis has been published in six IUS conference proceedings and one journal article.

### Articles included in the thesis:

**Paper A** A. S. Havreland, M. L. Ommen, C. Silvestre, M. Engholm, J. A. Jensen, and E. V. Thomsen, “BCB polymer based row-column-addressed CMUT,” in *Proc. IEEE Ultrason. Symp.*, 2017, pp. 1–4.

**Paper B** M. Schou, A. S. Havreland, M. Engholm, M. B. Stuart, E. V. Thomsen and J. A. Jensen, “Design of a novel zig-zag 192+192 Row Column Addressed Array Transducer: A simulation study,” in *Proc. IEEE Ultrason. Symp.*, 2018, pp. 1–4.

**Paper C** A. S. Havreland, M. Engholm, B. G. Tomov, J. A. Jensen, O. Hansen, and E. V. Thomsen, “CMUT Electrode resistance design:

Modeling and experimental verification by a row-column array” in *IEEE Transactions on Ultrasonics, Ferroelectrics, and Frequency Control*, vol.66, no. 6, pp.1110-118, 2019.

**Paper D** A. S. Havreland, M. Engholm, R. S. Grass, J. A. Jensen and E. V. Thomsen, “Wafer bonded CMUT technology utilizing a Poly-Silicon-on-Insulator wafer,” in *Proc. IEEE Ultrason. Symp.*, 2019, pp. 1–4.

**Paper E** M. Engholm, C. Beers, A. S. Havreland, B. G. Tomovz, J. A. Jensen, and E. V. Thomsen, “A Row-Column-Addressed 2D Probe with an Integrated Compound Diverging Lens,” in *Proc. IEEE Ultrason. Symp.*, 2018, pp. 1–4.

**Articles not included in the thesis:**

**Paper F** R. S. Grass, A. S. Havreland, M. Engholm, , J. A. Jensen and E. V. Thomsen, “188+188 Row-Column Addressed CMUT Transducer for Super Resolution Imaging,” in *Proc. IEEE Ultrason. Symp.*, 2019, pp. 1–4.

**Paper H** E. V. Thomsen, M. Petersen, K. Steenberg, A. S. Havreland, R. S. Grass, M. L. Ommen and M. Engholm, “Wafer Level Characterization of Row-Column Addressed CMUT Arrays,” in *Proc. IEEE Ultrason. Symp.*, 2019, pp. 1–4.

## CHAPTER 2

---

### Theory

---

In this chapter both the static and dynamic behavior of a CMUT is described through mathematical models. The CMUT is an inherently non-linear device and is therefore complicated to model, however, dimensionless parameters will be derived as they provide valuable insight in the scaling of different relevant CMUT parameters.

Multiple mathematical models for the static and dynamic behaviour of CMUTs can be found in the literature. The models include finite difference models [11], time domain FEM analysis [12], large lumped element models [13], simulink/BEM models [14] and harmonic oscillator models [15] among others. The dynamics of a single CMUT cell will in this chapter be modeled as a harmonic oscillator with a non-linear electrostatic force term. All the developed models in this theory chapter evaluates the behaviour of a single isolated CMUT cell, thus, effects from electronics, backing, array couplings are not included.

A hat notation will be used throughout the chapter and will be assigned to all non-dimensional variables. The same letter will be used for both physical and non-dimensional variables. For instance, the plate displacement is denoted  $x$  and has a length unit, whereas the  $\hat{x}$  is the normalized distance with respect to the gap height and is dimensionless.

The assumptions in for the modeling is as follows: A circular cell geometry is assumed for all models in this chapter, and a vertical electric field is assumed between the top and bottom electrode, hence, effects from fringing fields are not included. The dynamic CMUT models are applicable for both a transmit and a receive situation. However, displacement of the plate is

small enough to justify linearization of the electrostatic force in a receive analysis. But, a transmit analysis has to include the non-linearity due to a large displacement of the plate. Finally, the models used for dynamical modeling do not include a time dependent driving term, but, focus solely on the dynamical properties of the CMUT itself.

## 2.1 Static model

Two static models are presented in this section. The first model is a lumped element model that is used to find a characteristic voltage for a CMUT system. The second model is perturbative solution used to estimate the deflection profile of a clamped CMUT plate applied to an electrostatic pressure.

### 2.1.1 Lumped model

The most simple approach to model the static behavior of a CMUT is to consider a parallel plate capacitor, where one plate is fixed and the other plate is attached to a linear spring. When a DC bias is applied the system consists of two opposite forces i.e. a spring force  $F_s$  and an electrostatic force  $F_e$

$$\underbrace{k_s x}_{F_s} = \frac{\varepsilon A U^2}{\underbrace{2(g-x)^2}_{F_e}}, \quad (2.1)$$

where  $x$  is the displacement of the plate,  $k_s$  is the spring constant,  $\varepsilon$  is the permittivity,  $U$  is the applied DC bias,  $g$  is the gap height, and  $A$  is the surface area of the CMUT cell. The solution to Eqn. 2.1 yields the stationary point of the displacement for a given applied voltage. The electrostatic force is non-linear and introduces an unstable regime where the spring force no longer can balance the electrostatic force. It leads to an unstable state where the plate gets pulled into the bottom of the cavity. The critical voltage at which this phenomenon occurs for a CMUT is denoted the pull-in voltage or the collapse voltage, which the parallel plate capacitor CMUT model is given by [16]

$$U_{pi} = \sqrt{\frac{8}{27} \frac{k_s g^3}{\varepsilon A}}. \quad (2.2)$$

This closed form solution can be difficult to directly apply to a real system, since precise estimates of the spring constant can be difficult to obtain. However, the scaling laws of the different parameters are very valuable in a design and fabrication process of CMUTs.

A pull-in condition is a sign of non-linearity in any given system, since such instabilities never occurs in linear systems. Analysis of non-linear instabilities are widely documented in the literature of non-linear dynamics where the terminology for this kind of pull-in condition is called a saddle node bifurcation [17].

### 2.1.2 Clamped plate

The lumped model assumes a uniform displacement of the plate, and this assumption will in many CMUT designs not be a realistic scenario. A more accurate description of a CMUT plate under an applied DC potential is mathematically formulated by the plate equation, given here in a coordinate free form

$$\nabla^2 \nabla^2 w = \frac{p}{D}, \quad (2.3)$$

where  $w$  is the deflection profile of the plate,  $p$  is the electrostatic pressure and  $D$  is the flexural rigidity given by

$$p = \frac{\varepsilon U^2}{2(1-w)^2} \quad (2.4)$$

$$D = \frac{Yh^3}{12(1-\nu)}, \quad (2.5)$$

where  $Y$  is Young's modulus,  $h$  is the plate thickness, and  $\nu$  is the Poisson's ratio. A polar coordinate system is introduced due to the assumed circular geometry. An axis symmetric argument can be used to conclude that the deflection profile,  $w$ , must to rotational symmetric and therefore depend entirely on the radial component,  $r$ . The radius of the CMUT cell will be denoted,  $a$ , and is used to define the horizontal non-dimensional parameter  $\hat{r} = r/a$ . The vertical displacement is normalized to the gab height,  $\hat{w} = w/g$ , and the non-dimensional version of Eqn. 2.3 can then be expressed as

$$\underbrace{\left[ \frac{1}{\hat{r}} \frac{d}{d\hat{r}} \hat{r} \frac{d}{d\hat{r}} \right]}_{\nabla^2} \underbrace{\left[ \frac{1}{\hat{r}} \frac{d}{d\hat{r}} \hat{r} \frac{d\hat{w}}{d\hat{r}} \right]}_{\nabla^2 \hat{w}} = \frac{\varepsilon U^2 a^4}{2Dg^3(1-\hat{w})^2} = \frac{\hat{U}_r^2}{(1-\hat{w})^2}, \quad (2.6)$$

where  $\hat{U}_r$  is a voltage ratio between between the applied voltage and a characteristic voltage,  $U_c$ , defined as

$$\hat{U}_r = \frac{U}{U_c} \quad \text{where} \quad U_c = \sqrt{\frac{2Dg^3}{\varepsilon a^4}}. \quad (2.7)$$



To find a unique solution to Eqn. 2.6 four imposed boundary conditions are required, and the used boundary conditions in this analysis are

$$\hat{w}(0) = \text{finite} \quad \hat{w}'(0) = 0 \quad \hat{w}(1) = 0 \quad \hat{w}'(1) = 0. \quad (2.8)$$

Equation 2.6 is a non-linear boundary value problem without any known closed form solution for the four imposed boundary conditions. However, the dimensionless form allows extraction of valuable information. The derived parameter,  $U_c$ , contains the scaling properties of the pull-in voltage and differs only by a numerical constant. The numerical constant has been determined by a FEM analysis in [18], and the relationship between  $U_c$  and  $U_{pi}$  is calculated to be

$$U_{pi} = 14.23U_c. \quad (2.9)$$

### 2.1.3 Approximate solutions

Equation 2.6 cannot be solved analytically, but, approximate solution can be found for small deflections. To do so the differential equation is linearized by Taylor expanding the electrostatic pressure to first order

$$\nabla^2 \nabla^2 \hat{w} = \frac{\hat{U}_r^2}{(1 - \hat{w})^2} \approx \hat{U}_r^2 (1 + 2\hat{w}). \quad (2.10)$$

Under the assumption of an infinite sum representation a perturbative solution can be defined as

$$\hat{w} = \sum_{n=0}^{\infty} \hat{U}_r^{2n} \hat{w}_n \approx \hat{w}_0 + \hat{U}_r^2 \hat{w}_1 + \hat{U}_r^4 \hat{w}_2 \quad \text{for} \quad \hat{U}_r^2 \ll 1. \quad (2.11)$$

Here  $\hat{U}_r^2$  is used as the perturbation parameter, and the infinite sum is truncated and substituted into equation 2.10 to obtain a sequence of linear differential equations

$$\text{order } \hat{U}_r^0 \quad \nabla^2 \nabla^2 \hat{w}_0 = 0 \quad (2.12)$$

$$\text{order } \hat{U}_r^2 \quad \nabla^2 \nabla^2 \hat{w}_1 = 1 + 2\hat{w}_0 \quad (2.13)$$

$$\text{order } \hat{U}_r^4 \quad \nabla^2 \nabla^2 \hat{w}_2 = 2\hat{w}_1 \quad (2.14)$$

$\hat{w}_0$  is the solution to the plate equation when electrostatic pressure is zero and deflection is therefore completely flat or expressed mathematically  $w_0 = 0$ .

$w_1$  corresponds to a plate with a uniform applied pressure and has the fourth order polynomial solution

$$\hat{w}_1 = \frac{(1 - \hat{r}^2)^2}{64}. \quad (2.15)$$

When the plate is forced downwards due to the electrostatic force the center of the plate will experience a larger force than the circumference of the CMUT.  $\hat{w}_2$  is the first correction term that incorporates the distance dependency in the applied electrostatic pressure and has the solution

$$\hat{w}_2 = \hat{w}_1 \frac{23 - 6\hat{r}^2 + \hat{r}^4}{1152} \quad (2.16)$$

The largest deflection and numerical difference between  $w_1$  and  $w_2$  occur at the center, where  $\hat{r} = 0$ . The presented perturbative analysis predicts a slight overall increase of the deflection, with a maximum displacement at the center. The approximate solution to the problem is given by

$$\hat{w}(\hat{r}) \approx \hat{w}_1(\hat{r}) \hat{U}_r^2 \left( 1 + \frac{23 - 6\hat{r}^2 + \hat{r}^4}{1152} \hat{U}_r^2 \right). \quad (2.17)$$

The correction term is positive for all values of  $\hat{r}$  and depends on the magnitude of the bias ratio. The derived approximate solution to Eqn. 2.10 is shown in Fig. 2.1 plotted together with the constant pressure solution  $\hat{U}_r^2 \hat{w}_1$ . Additional displacement is observed for the higher order model, although the overall shape of the deflection is preserved. The model predicts a maximum discrepancy of approximately 0.15% when the CMUT is biased with 10% of the pull-in voltage.

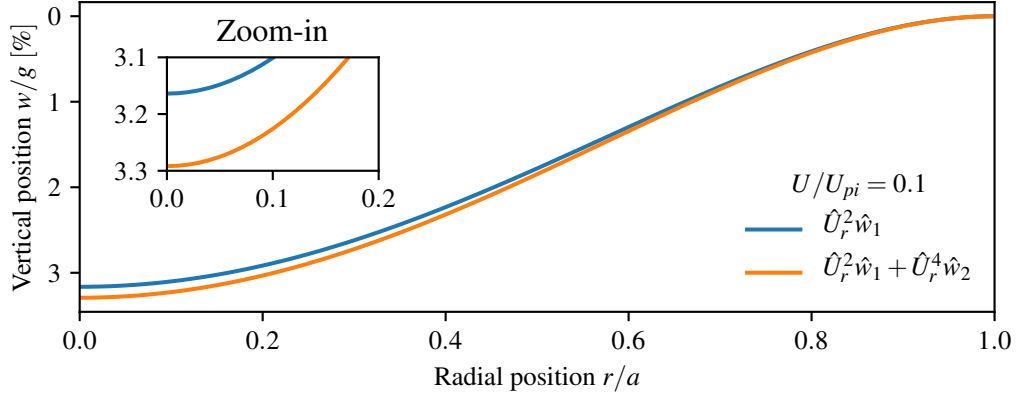


**Figure 2.1:** The deflection of a clamped plate with an electrostatic applied pressure.  $\hat{w}_1 \hat{U}_r^2$  corresponds to the deflection under a constant pressure assumption. The solution  $\hat{w}_1 \hat{U}_r^2 + \hat{w}_2 \hat{U}_r^4$  accounts for the distance dependency of the electrostatic pressure, and the larger displacement is therefore expected and observed.

## 2.2 Dynamic model

Dynamic modeling of CMUTs in immersed applications becomes rapidly complicated due to the intrinsic non-linear behavior of the CMUT itself and the fluid structure interaction between the vibrating plate and the surrounding medium. The equations of the CMUT dynamics will be governed by four force contributions in the following section. The contributions include an inertia term, a linear spring term, an electrostatic term, and a force term that describes the interacting between the plate and the surrounding medium. The four forces are assumed to be the dominant forces in this system, and are used to define the non-linear harmonic oscillator given by

$$\underbrace{m \frac{d^2 x}{dt^2}}_{\text{Inertia}} + f_{RI} + \underbrace{kx}_{\text{Spring}} = \underbrace{\frac{\varepsilon AU^2}{2(g-x)^2}}_{\text{Electrostatic}}, \quad (2.18)$$

where the assumed initial conditions are

$$x(0) = 0 \quad \text{and} \quad x'(0) = 0. \quad (2.19)$$

Two additional terms have been added when compared to the static model in section 2.1, the force from the radiation impedance,  $f_{RI}$ , and the inertia term. The radiation impedance is used to model an interaction between the plate and the surrounding medium. The interacting mechanism of  $f_{RI}$  depends

on frequency and the size of the CMUT geometry, it will be introduced in different configurations depending regime of operation.

Radiation impedance is conventionally defined in the frequency domain, however, medical ultrasound is a time domain system. Thus, an inverse Fourier transform is required to proceed with a time domain analysis. The equations used to model the radiation impedance assumes a harmonically driven system, and is naturally still assumed in the time domain. But, this assumption will not be met in medical imaging applications, since pulses are used instead of continuous signals, though the scaling laws are assumed to be similar. Radiation impedance is defined as complex quantity in the frequency domain, where the real part is called radiation resistance and is measure of how much acoustic energy that radiates from the transducer surface. The imaginary part is called radiation reactance and can be interpreted as a mass loading of the medium in front of the transducer. The force acting on a transducer surface can, in the frequency domain, be expressed as

$$F(\omega) = Z(\omega)V(\omega) \quad (2.20)$$

where  $Z$  is the radiation impedance,  $V$  is the velocity of the transducer surface, and  $\omega$  is the angular frequency. The radiation impedance for a circular piston in rigid baffle is given by [19]

$$Z(2ka) = \rho_m c_m A \left[ 1 - 2 \frac{J_1(2ka)}{2ka} + i2 \frac{H_1(2ka)}{2ka} \right] \quad (2.21)$$

where  $\rho_m$  is the density of the medium,  $c_m$  is the speed of sound in the medium,  $A$  is the transducer area,  $k$  is the wave number, and  $J_1$  is the Bessel function of first kind and order one,  $H_1$  is the Struve function of order one. The two special functions,  $J_1$  and  $H_1$ , complicate analytical modeling, but simple approximations can be used in the two limiting cases where  $ka \ll 1$  or  $ka \gg 1$ . The real and the imaginary part of radiation impedance are plotted in Fig. 2.2 in both the low and high  $ka$  limits. The solid lines represent the exact expressions and dashed lines represent approximations.

In the following two sections 2.2.1 and 2.2.2 CMUT dynamics will be studied for small and large  $ka$  values, respectively. No damping mechanisms are initial included in Eqn. 2.18, thus, the radiation impedance is the only term that can introduce damping properties. However, CMUTs will experience multiple other damping mechanisms during operation. These damping mechanisms counts clamping losses, material damping, squeeze film damping, thermoelastic damping among other. The damping is heavily dependent on the medium in which the CMUT is operated. For instance is squeeze film damping more dominant for CMUT in airborne applications, whereas the

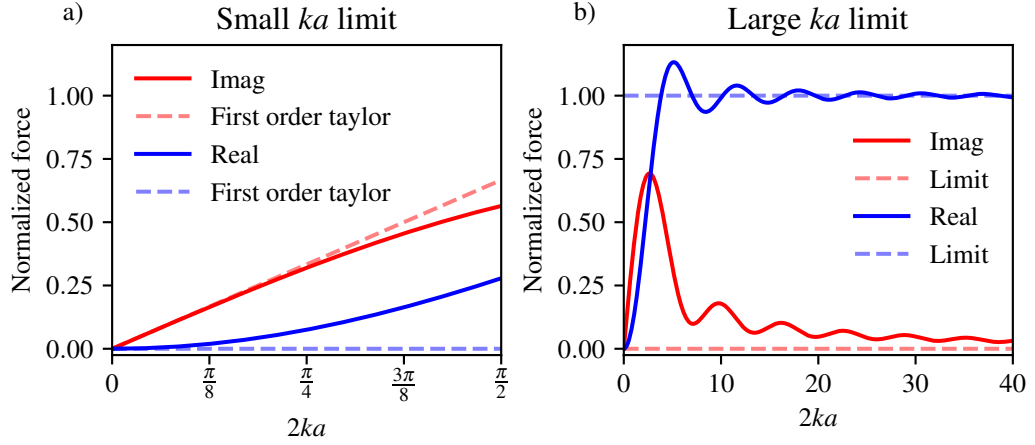


**Figure 2.2:** The radiation impedance normalized to  $\rho_m c_m A$  for both low and high  $ka$  values. First order Taylor expansions of the radiation impedance are plotted as dashed lines in the small  $ka$  limit a). The limiting value of the radiation impedance is plotted as dashed lines in the large  $ka$  limit b).

damping from the medium becomes more dominant for immersed applications, such as medical imaging.

### 2.2.1 Small $ka$ limit

A pitch of  $\lambda/2$  between two neighbouring elements is beneficial in medical imaging applications, since it minimizes the effect from grating lobes [20].  $\lambda$  is here the wavelength of the transmitted ultrasound. This design criterion constrains the possible values of  $2ka$  between 0 and  $\pi/2$ , where the latter case corresponds to CMUT cell diameter equal to the width of the element. The small  $ka$  regime is modelled by a Taylor expansion of Eqn. 2.21 and yields

$$Z \approx \rho_m c_m A \frac{8ika}{3\pi} \quad \text{for } ka \ll 1. \quad (2.22)$$

This approximation will be used throughout the entire analysis for small  $ka$  values. Notice, the approximation is purely imaginary, and both real part (zero) and the imaginary part of the approximation are indicated in Fig. 2.2 a). The transformation of Eqn. 2.22 back to the time domain is done by first employing the substitution  $ka = \omega a/c_m$  followed by an inverse Fourier

transform

$$f_{RI} = \frac{8\rho_m A a}{6\pi^2} \int_{-\infty}^{\infty} i\omega V(\omega) e^{i\omega t} d\omega \quad (2.23)$$

$$= \frac{8\rho_m a^3}{3} \frac{d^2 x}{dt^2}, \quad (2.24)$$

where the following Fourier transform rule has been used

$$\frac{d^n g}{dt^n} = \frac{1}{2\pi} \int_{-\infty}^{\infty} (i\omega)^n G(\omega) e^{i\omega t} d\omega. \quad (2.25)$$

This results implies that the system will experience an additional mass, and the equation of motion becomes

$$\left( m + \frac{8\rho_m a^3}{3} \right) \frac{d^2 x}{dt^2} + kx = \frac{\varepsilon A U^2}{2(g-x)^2}. \quad (2.26)$$

The non-dimensional version of this equation is obtained by defining the displacement relative to the gap height  $\hat{x} = x/g$ . The time is scaled with the unperturbed natural frequency  $\hat{t} = \omega_0 t$  where  $\omega_0^2 = k/m$  and the final non-dimensional equation can then be expressed as

$$\frac{d^2 \hat{x}}{d\hat{t}^2} + \hat{\omega}_m^2 \hat{x} = \hat{\omega}_m^2 \frac{\hat{U}_r^2}{(1-\hat{x})^2}. \quad (2.27)$$

This equation shows the dynamics of a single CMUT cell, in the small  $ka$  regime, is fully described by two parameters,  $\hat{U}_r$  and  $\hat{\omega}_m$ . The bias ratio,  $\hat{U}_r$ , and a reduced resonance frequency parameter,  $\hat{\omega}_m$ , defined as

$$\hat{U}_r^2 = \frac{4}{27} \frac{U^2}{U_{pi}^2} \quad (2.28)$$

$$\hat{\omega}_m^2 = \left( 1 + \frac{8\rho_m a^3}{3m} \right)^{-1} = \left( 1 + \frac{8}{3\pi} \frac{\rho_m a}{\rho_p h} \right)^{-1}, \quad (2.29)$$

where  $\rho_p$  is the density of the plate, and  $h$  is the thickness of the plate. The constant  $4/27$  is merged into the bias voltage ratio,  $U_r$ , to reduced numerical constants in the following expressions and  $U_{pi}$  is defined in Eqn. 2.2. The reduced resonance frequency parameter predicts a significant frequency change between applications in air and water, simply caused by the ratio of the densities. This effect is validated experimentally where the center frequency of the same CMUT typically differs a factor of  $\approx 2$  between air and immersed applications. For a silicon plate the density ratio is on the

order of  $5 \times 10^{-4}$  when operated in air, whereas the ratio is 0.43 between when operated in water. Additionally, the reduced frequency also depends on the plate aspect ratio,  $a/h$ , according to the model.

Eqn. 2.27 is a non-linear differential equation where the energy is conserved for all applied voltages smaller than the pull-in voltage. Physically it implies the CMUT does not radiate sound into the medium, which is a completely non-satisfying performance from a transducers point of view. However, to avoid or reduce low acoustic radiation, the CMUT plate should have a large radius, which is obtained by packing an the elements with few but large CMUT cells instead of many smaller CMUT cells.

A close form solution to Eqn. 2.27 is not known, but approximate solutions can be found by expanding the non-linear electrostatic term. The linear response is modeled by a first order expansion and non-linear corrections can be captured in higher order expansions. Equation 2.27 simplifies to

$$\frac{d^2 \hat{x}}{d\hat{t}^2} + \hat{\omega}_m^2 \hat{x} = \hat{\omega}_m^2 \hat{U}_r^2 \left[ \underbrace{1 + 2\hat{x}}_{\text{linear}} + \underbrace{3\hat{x}^2}_{\text{Non-linear}} \right], \quad (2.30)$$

after a Taylor expanding. The linear and non-linear system are indicated in the equation. The exact solution to the linear problem is given by

$$\hat{x}_{lin} = \frac{\hat{U}_r^2}{1 - 2\hat{U}_r^2} \left[ 1 - \cos \left( \hat{\omega}_m \hat{t} \sqrt{1 - 2\hat{U}_r^2} \right) \right]. \quad (2.31)$$

The linear solution predicts an increased amplitude and further reduction of the resonance frequency as the bias ratio increases. This additional reduction of the resonance frequency is the well known spring softening effect. A closed form solution does not exist for the non-linear approximation. Hence, at this point the original hard non-linear differential equation is converted into another hard non-linear differential equation. Fortunately, an approximate solution can be found to the non-linear problem on the form in Eqn. 2.30. The Method of Multiple Scales (MMS) is an efficient perturbative method suited for approximate solutions to non-linear problems such as this one. MMS has the advantage over regular perturbation methods that it is capable of canceling out secular terms in the expansion, that otherwise leads to unbounded solutions. The idea of MMS is to find an approximate solutions on the form

$$x = x_0(T_0, T_1, \dots) + \epsilon x_1(T_0, T_1, \dots) + \dots \quad \text{where} \quad T_n = \epsilon^n t, \quad (2.32)$$

where  $\epsilon$  is the perturbation parameter,  $T_n$  represents different time scales,  $T_0$  is the fastest time scales and the time scales become progressively slower

as  $n$  increases. The solution of interest is an extended version of the general linear solution,  $x_{lin}$ , where the amplitude and frequency varies on higher order time scales

$$x_0 = A(T_1)e^{-i\omega(T_1)T_0} + A^*(T_1)e^{i\omega(T_1)T_0}\hat{U}_r^2. \quad (2.33)$$

The solution provided by the MMS analysis yields

$$\hat{x}_{MMS} = \underbrace{\frac{\hat{U}_r^2}{1 - 2\hat{U}_r^2}}_{\text{amplitude}} \left[ 1 - \cos \left( \underbrace{\hat{\omega}_m t \sqrt{1 - \hat{U}_r^2}}_{\text{Linear}} \left[ 1 - \underbrace{\frac{3\hat{U}_r^4}{(1 - 2\hat{U}_r^2)^2}}_{\text{Non-linear}} \right] \right) \right]. \quad (2.34)$$

The same amplitude as the linear approximation is found by the MMS analysis, but the resonance frequency has a correction term.

$U_r$  is a positive parameter ranging from zero to  $4/27$ , consequently a subtraction of the positive non-linear correction term will always lead to a further reduction in frequency or from a physical point of view a larger degree of spring softening. Notice, the higher order frequency correction term equals to three times the amplitude squared. It indicates a direct coupling between the amplitude and the frequency, which is not predicted by the linear model. Equation 2.30 is a variation of the well known duffing equation, and MMS step by step derivations of similar problems can be found in [21]. The linear model and the MMS model have both been used to approximate the dynamics of Eqn. 2.27, and the two models are compared to numerical results in Fig. 2.3. The solution to Eqn. 2.27 is shown in a) for  $\hat{\omega}_m$  and  $U/U_{pi}$  equal to 0.9 and 0.6, respectively. The higher precision of the phase is clearly visible for the MMS model. It is the general case for all bias values as seen in b), where the resonance frequency is plotted as function of bias ratio. The displacement amplitude is plotted in c) where a good agreement between the models and the numerical solution is observed up to approximately 70 % of the pull-in voltage, above this point even higher order corrections will be required. Finally, the errors of the modelled parameters are compared to the numerical solution in d). The same color coding has been used, blue and red are used for the resonance frequency and green is used for the amplitude. The numerical resonance frequency is determined by Fourier transforming the displacement solution and then locating the position of the main peak. The plateau observed for the frequency estimates (blue and red) is due the precision of the numerical determination of the frequency.

The energy is conserved for the small  $ka$  models due to the absence of damping. Higher order expansions of the radiation impedance would be very interesting, since such models include a non-zero real part and allow the system



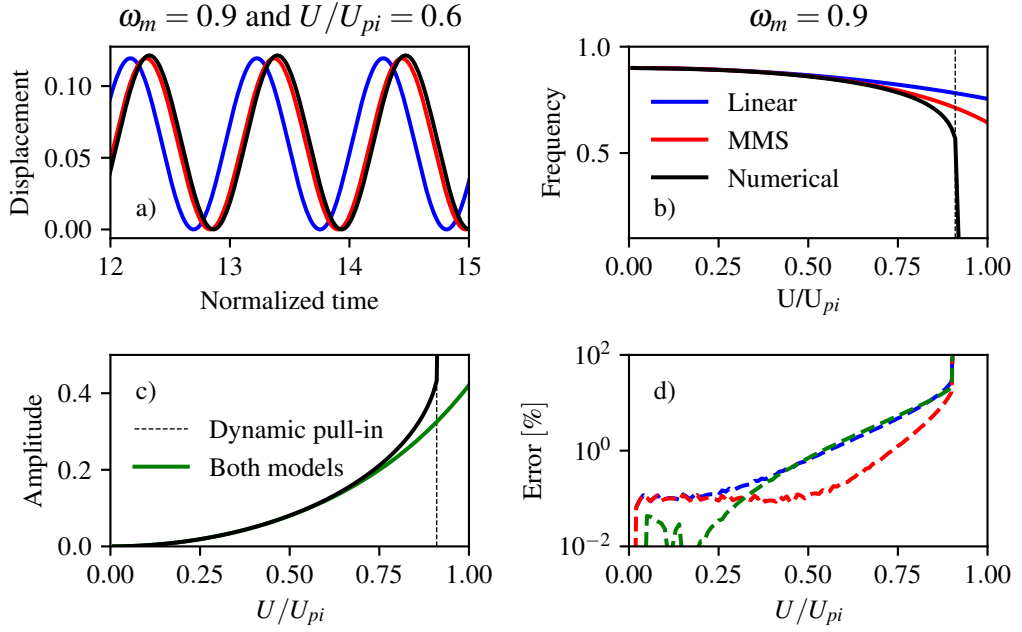


**Figure 2.3:** The linear and non-linear models are compared to a numerical solution to Eqn. 2.27 for various parameters. The solution to Eqn. 2.27 is plotted in figure a) for  $\omega_m$  and  $U/U_{pi}$  equal to 0.9 and 0.6, respectively. The resonance frequency versus applied DC bias is plotted in b), with  $\omega_m = 0.9$ . Figure c) shows amplitude versus applied DC bias. The amplitude is identical for both models and independent of  $\omega_m$ . Figure d) shows the error between the models and the numerical solution. The green dashed line is the amplitude error, and the error of the resonance frequency is shown by the blue and red dashed lines for the linear and the MMS model, respectively.

to radiate energy into the medium. A higher order expansion of the radiation impedance is an effortless procedure which gives

$$Z \approx \rho_m c_m A \left[ \frac{(ka)^2}{2} + \frac{8ika}{3\pi} \right], \quad (2.35)$$

but problems occur when this expression is transformed back to the time domain. By using Eqn. 2.25 to transform the second order approximation back to the time domain one gets

$$f_{RI} = - \underbrace{\frac{\pi \rho_m a^4}{2 c_m} \frac{d^3 x}{dt^3}}_{\text{Jerk}} + \underbrace{\frac{8 \rho_m a^3}{3} \frac{d^2 x}{dt^2}}_{\text{Inertia}}. \quad (2.36)$$

Multiple challenges arise from this expression. First and most important is the minus in front of the jerk term. A non-positive constant in front of a derivative in a linear  $n^{\text{th}}$ -order differential equation will have a positive eigenvalue that guarantees an unstable system. Though the CMUT equation is non-linear this unstably criterion still applies. A second challenge is the additional initial conditions. The order of the differential equation increases with the expansion order of the radiation impedance. The original equation is a second order differential equation, but, by introducing Eqn. 2.36 the approximate differential equation becomes of third order. The problem here is how to address the additional initial condition in a physical meaningful way. These challenges are not easy to overcome and illustrate the complexity of modelling the CMUT dynamics, which suggests advanced numerical methods to model the interaction with the CMUT and the medium.

### 2.2.2 Large $ka$ limit

All CMUT design in this thesis are designed by the  $\lambda/2$  pitch constraint, which only allows  $2ka$  values between 0 and  $\pi/2$ . Nevertheless, the large  $ka$  regime is still interesting as damping appears in this limit. An asymptotic expansion efficiently approximates the radiation impedance in the limit where  $ka \rightarrow \infty$

$$Z \sim \rho_m c_m A \quad \text{as} \quad ka \rightarrow \infty. \quad (2.37)$$

A constant radiation impedance transforms into a damping term, and now all the stored energy in the system will be converted into acoustic radiation. The rate at which the energy is converted is determined by a damping term, which is given by

$$f_{RI} = \rho_m c_m A \frac{dx}{dt} = \rho_m c_m \pi a^2 \frac{dx}{dt} \quad (2.38)$$

and the equation of motion in the large  $ka$  regimes can then be expressed as

$$m \frac{d^2x}{dt^2} + \rho_m c_m A \frac{dx}{dt} + kx = \frac{\varepsilon AU^2}{2(g-x)^2}. \quad (2.39)$$

After nondimensionalization using the same dimensionless parameters as in section 2.2.1 the equation simplifies to

$$\frac{d^2\hat{x}}{d\hat{t}^2} + \frac{1}{\hat{\tau}} \frac{d\hat{x}}{d\hat{t}} + \hat{x} = \frac{\hat{U}_r^2}{(1-\hat{x})^2} \quad \text{where} \quad \hat{\tau} = \frac{m\omega_0}{\rho_m c_m \pi a^2}. \quad (2.40)$$

The dynamics in both the small  $ka$  regime and the large  $ka$  regime is fully determined by two parameters, and both regimes share the electrostatic voltage ratio  $\hat{U}_r$ . The small  $ka$  regime has an added mass, whereas the large  $ka$  regime has a damping term with a characteristic decay time  $\hat{\tau}$ . The characteristic decay time determines the bandwidth of the CMUT, large bandwidth corresponds to a small  $\hat{\tau}$  and narrow bandwidth corresponds to a large  $\hat{\tau}$ . Hence, from a medical imaging perspective a small  $\hat{\tau}$  is desired, since it improves the axial resolution in an ultrasound image. Equation 2.40 does, equivalent to the small  $ka$  model, not have any exact analytical solution due to the non-linear electrostatic term, and the options are therefore once again either approximate or numerical solutions. One approach is to use a phase-space analysis, it allows multiple solutions to be visualized at the same time and provides a quick overview of the dynamics. The phase space is easily obtained by expressing Eqn. 2.40 as two coupled first order differential equations given by

$$\frac{d\hat{x}}{d\hat{t}} = \hat{v} \quad (2.41)$$

$$\frac{d\hat{v}}{d\hat{t}} = -\frac{1}{\hat{\tau}}\hat{v} - \hat{x} + \frac{\hat{U}_r^2}{(1-\hat{x})^2}. \quad (2.42)$$

The phase-space analysis describes the dynamics of a CMUT with a fixed DC bias subject to multiple initial conditions. For each set of initial conditions an ODE solver has been used to determine whether the CMUT spirals into a stable stationary point or if it collapses into the pull-in configuration. The stationary point (also called the operation point) can be found analytically for the non-linear CMUT parallel plate model as a solution to Eqn. 2.1. The phase-portrait analysis can be used to examine the concept of a dynamic pull-in voltage. When inertia and damping are included in CMUT modeling the pull-in condition becomes more involved than the static case and cannot no longer be expressed in simple terms. If the kinetic energy stored in the CMUT

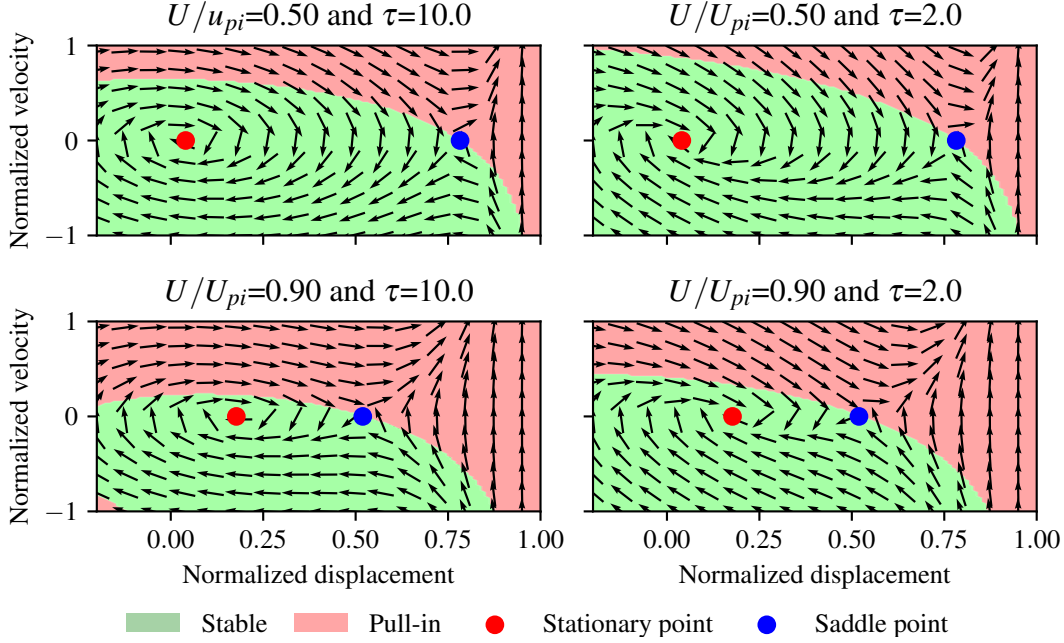


**Figure 2.4:** The phase portrait of a CMUT modeled as a nonlinear harmonic oscillator. The stationary point is marked with a red dot and the saddle point is marked with the blue dot. The green region indicates a stable state and the red region indicates an unstable state (dynamic pull-in).

plate is high enough, then ending up in the pull-in condition is inevitable even though the applied bias is below the static pull-in voltage. The dynamic pull-in condition depends on both the damping and the applied bias, and is not a one dimensional parameter as the static case, but should in the simplest possible way, be perceived as a two dimensional parameter space. A single point on the rim of the dynamic pull-in region can be found analytically by examining the additional two solutions of Eqn. 2.1, here denoted  $x_2$  and  $x_3$ . The second solution  $x_2$  is physical in the sense that  $x_2 < 1$ , meaning that it represents a point inside the CMUT cavity. One can show this solution is semi stable and therefore defines a saddle point in the phase portrait. This saddle point must lie on the rim of the dynamic pull-in region. The last solution  $x_3$  possesses no physical meaning since the  $x_1 > 1$  for all applied biases, and corresponds to a displacement below the CMUT. Four different CMUT phase portraits are shown in Fig. 2.4 for multiple values of  $U/U_{pi}$  and  $\hat{\tau}$ .

The direction of each arrow in the phase portrait is evaluated by inserting values of  $x$  and  $v$  into Eqn. 2.41 and 2.42. On top of the phase portraits are

a green and red color coding added to indicate stable and unstable states, respectively. The code used to determine the final state of the CMUT is verified by the analytic saddle point that lies on the rim of the stable region in all cases, as predicted. The stable dynamic region is reduced as the applied bias approaches the static pull-in condition. Likewise a reduction of the dynamic region is observed when the characteristic decay time is increased.

The large  $ka$  model radiates 100% of the stored energy into the medium, which is highly desired from a transducer point of view. Unfortunately,  $2ka$  has an upper bound of  $\pi/2$  due to the  $\lambda/2$  pitch constraint used in medical imaging applications. The small  $ka$  models radiation 0% and the large  $ka$  model radiates 100% and the true radiation is somewhere in between.

### 2.2.3 Full description

In the previous sections the case of small and large  $ka$  values were examined. In this section the radiation impedance is transformed back to the time domain without any approximations. It leads to a complicated differential equation, and the aim is not to solve this equation but to determine dimensionless parameters. When the radiation impedance is known in the time domain, the force acting on the transducer surface can be found by applying a convolution integral

$$f(t) = \int_0^t z(t - \beta)v(\beta) d\beta. \quad (2.43)$$

The exact radiation impedance in the time domain of a piston in a rigid baffle is derived in [19] and is given by

$$z(t) = \rho_m c_m \pi a^2 \left[ \delta\left(\frac{c_m t}{2a}\right) - \frac{4}{\pi} \left[ 1 - \left(\frac{c_m t}{2a}\right)^2 \right]^{1/2} \right] \quad (2.44)$$

with  $\delta$  being a delta function. The convolution of a delta yields a damping term, whereas the convolution of square root has to be expressed in terms of an integral. The physical interpretation of this integral is a memory term that depends on the dynamics from the past. The equation of motion after non-dimensionalization can be expressed as

$$\frac{d^2 \hat{x}}{d\hat{t}^2} + \frac{1}{\hat{\tau}} \frac{d\hat{x}}{d\hat{t}} - \underbrace{2\hat{\eta} \int_0^{\hat{t}} \frac{d\hat{x}}{d\hat{\beta}} \sqrt{1 - \frac{4\hat{\eta}^2 \hat{\tau}^2}{\pi} (\hat{t} - \hat{\beta})^2} d\hat{\beta}}_{\text{Memory}} + \hat{x} = \frac{\hat{U}_r^2}{(1 - \hat{x})^2}, \quad (2.45)$$

where

$$\hat{\tau} = \frac{m\omega_0}{\rho_m c_m \pi a^2} \quad \hat{\eta} = \frac{\rho_m c_m^2 a}{m\omega_0^2} \quad (2.46)$$

An analysis of the non-dimensional parameters can provide some quantitative information and scaling laws. The product of  $\hat{\tau}\hat{\eta}$  is a measure of the ratio between the damping and memory force. The square product is present inside the convolution integral, and will therefore directly influence the dynamics of the system.

$$\hat{\tau}\hat{\eta} = \frac{1}{\pi} \frac{c_m}{a\omega_0} \quad (2.47)$$

The product between the damping and the memory term contains three parameters,  $c_m$ ,  $a$ , and  $\omega_0$ . From a medical imaging perspective the sound of speed is fixed and approximately 1540 m/s. The frequency and the radius are two coupled parameters, which can be chosen independently of each other by adjusting the plate thickness accordingly. As an example a 10 MHz CMUT transducer with a 25  $\mu\text{m}$  cell radius would have a  $\hat{\tau}\hat{\eta}$ -product of 0.31 in immersion, whereas the ratio would be 0.07 for applications in air, assuming a sound of speed of 340 m/s. These simple calculations predict an increased influence of the memory term for immersed applications, which is one of the reasons why modeling of CMUTs in immersion rapidly becomes complicated and not suited for analytic modeling. From this point advanced numerical methods such as FEM will be necessary in order to move forward, and these methods can include effects that has been neglected in this theory chapter, such as substrate/backing effects, array configuration, lens materials, electronics among other.

## 2.3 Chapter summery

A theoretical analysis of the a single CMUT cell was given in this chapter. A perturbative solution to the deflection of the clamped plate subject to an electrostatic pressure was derived. The dynamics of a single CMUT cell was analyzed using a non-linear model in the regime of small and large  $ka$  values. The small  $ka$  analysis demonstrated a reduction of the resonance frequency due to an additional mass loading and a damping mechanism was introduced in the large  $ka$  regime. A phase portrait analysis was used to visualize the dynamics of the large  $ka$  regime. The dynamical parameter space was observed to depend on the applied bias and the damping of the CMUT plate.



## CHAPTER 3

---

### Row-Column-Addressed Arrays

---

A generic examination of a Row-Column-Addressed (RCA) array will be presented in this chapter, the geometry, the advantageous properties, and challenges associated with such arrays are the main focus. A short literature review of the row-column technology will initially be given. Relevant scaling laws of RCA arrays are presented after the literature review, and then theoretical considerations regarding edge waves, and finally, a discussion of a substrate coupling phenomenon that can occur for specific CMUT row-column fabrication techniques.

The row-column addressing scheme was first theoretically proposed in 2003 by Morton and Lockwood [22] and the development of the row-column technology has since then been carried out by multiple groups. The first experimentally row-column results were demonstrated in 2006 by Seo [23] based on a PZT transducer with a channel count of 64+64. Rasmussen presented in 2013 a combined simulation and measurement study of the row-column imaging performance, where the row-column performance was compared the results of a Fully Populated Matrix (FPM) array with an identical channel count [24, 25]. The Canadian group from the University of Alberta demonstrated in 2014 a CMUT RCA array [26] and did at the same time introduce a different name for the row-column technology. The Canadian group uses the name Top-Orthogonal-to-Bottom-Electrode (TOBE) instead of the row-column terminology. The acronym TOBE is still being used by the Alberta group, but all other groups seem to have adapted the row-column terminology. A line element beamformer and concept of integrated apodization were introduced in 2015 [27, 28] Rasmussen and Christiansen, both con-



cepts provide improved image quality for row-column imaging. The Alberta group published in 2017 a paper regarding a novel imaging sequence abbreviated Fast Orthogonal Row–Column Electronic Scanning (FORCES) [29], an imaging sequence capable of employing two way focusing for row-column addressed arrays. The architecture of the row-column design prohibits conventional two-way focusing, which is the most common criticism of the row-column technology. The FORCES scheme solves this problem, at the cost of a more complex electronics and a reduced frame rate. Other row-column imaging sequences are limited to one way focusing, which significantly degrade the quality of B-mode images. Additionally, the FORCES scheme is interesting from a CMUT perspective since it depends on the biasing properties of a CMUT, thus, not directly applicable for conventional PZT RCA arrays. However, the FORCES scheme has a reduced frame rate compared to other image sequences and requires substantial changes in the CMUT electronics. In general CMUT row-column probes are therefore not applicable unless the electronics is specifically designed for this scheme. The focusing issue has been addressed differently by the Italian group from the Roma Tre University, where a static fresnel lens biasing scheme has been suggested [30]. The focusing properties of such fresnel lens are not as good as the FORCES scheme, but, the required electronics is much closer to conventional CMUT electronics. Finally, a detailed analysis of row-column probe development has been published in 2018, where a thorough comparison between a RCA PZT probe and a RCA CMUT probe [31] is given.

The interest for the row-column technology has significantly increased during the last couple of years, which is illustrated in Fig. 3.1 where the number of row-column publications and citations are plotted versus time. A clear increase is observed for both the publications and citations during the past five years. The data is collected prior to the IUS, where several conference proceedings regarding row-column technology are published. This is presumably the explanation to the drop in 2019, and with that in mind the activity seems to continue. Though, the publication counts fall into category of low number statistic and the trend is therefore associated with high uncertainty.

### 3.1 Scaling laws

The channel count scales linearly with number electrical interconnections for conventional 1D arrays and a linear scaling law is preserved for RCA arrays, which is the main selling point for the row-column technology. The required interconnections for the RCA scheme scales as  $2N$ , where  $N$  is the number

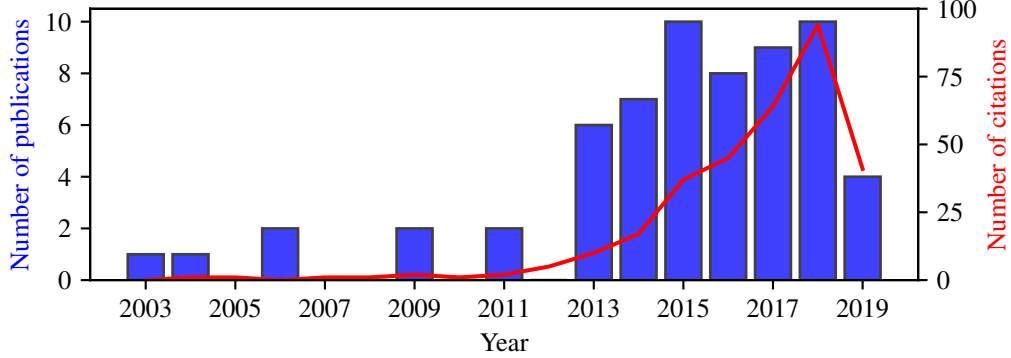


**Figure 3.1:** The number of row-column publications and citations plotted with a double y-axis versus time. The data has been acquired from the Web of Science database using the keywords: Ultrasound or CMUT and Row-Column or Top orthogonal to bottom electrode.

of channels. Another 2D transducer architecture is the FPM array, which is direct 2D to 3D extension with individual electrical connection to each sub-element. This technology has the advantage of being able to focus in both transmit and receive, which is possible due to the individual control of each sub-element. However, the required interconnections scale as  $N^2$  for FPM arrays, which is highly impractical for the packaging process of an ultrasound transducer.

The image quality of volumetric imaging (3D) has to compete with the modern standard of 2D ultrasound images where more than 100 channels are used. Hence, to achieve the same image quality in both elevation and azimuth as conventional 2D ultrasound images, 2D arrays should have a channel count of more than 100 in both directions. For a FPM array it leads to more than 10000 interconnections, where only plus 200 is required for a RCA array. A high amount of interconnections make the transducer cable rigid, costly, difficult to maneuver, and will for all practical purposes be the limiting factor in the transducer design. The row-column technology is one way to overcome the issue related to a massive amount of interconnects required for volumetric imaging. Another approach is Application Specific Integrated Circuit (ASIC) based solutions, and the commercially available CMUT probes from Butterfly Network utilize an ASIC platform. Though, ASIC solutions enable the possibility of dealing with high channel count at the expense of highly specialized/customized electronics, reduced design flexibility, and high economical costs, but it is definitely possible for both CMUT [32] and PZT [33]. A third way of achieving 3D images is by utilizing

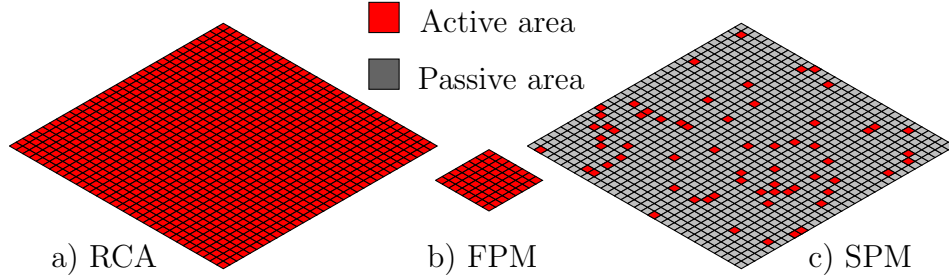


**Figure 3.2:** An illustration of the transmitting area for three different 64 channel 2D transducers. Red indicates pressure generation areas and gray indicates passive areas. a) A 32+32 RCA array. b) A  $8 \times 8$  FPM array. c) A 64 channel SPM array, where a stochastic pattern strategy has been used.

Sparsely Populated Matrix (SPM) arrays. SPM arrays are basically a  $N \times N$  FPM array, where  $N$  selectively chosen sub-elements are connected. Different patterns in which the sub-element are chosen have been proposed in the literature ranging from stochastic patterns [34], to periodic pattern [35], to a Fermat's spiral [36] among other. Equivalent to the row-column technology does the number of interconnections scale linearly for a SPM array. However, the pressure generating area will be significantly lower which translates into a lowered output pressure. This effect is visually illustrated in Fig. 3.2 where the three 2D transducer technologies are sketched. Notice all three technologies have exactly 64 channels, but the pressure generating areas (active area) are vastly different.

A larger transducer surface produces pressure which translates into larger penetration depth and a higher SNR in receive. The active area of the RCA array is much larger than two other technologies, which enables ultrasound imaging deeper into the body. Quantitative scaling laws for 2D transducers can be derived by simple calculations, and when the  $\lambda/2$  pitch constraint is applied, it becomes possible to express the scaling laws solely in terms of the wavelength. Hence, these normalized scaling laws become applicable to all transducer designs. A square footprint will be assumed in the following section, but, the scaling properties are equivalent for a rectangular geometry as well. The size of a row-column array can be expressed in terms of channel count and wave length, since the area of a sub-element is  $(\lambda/2)^2$  and the length of an element is  $N\lambda/2$ . The surface area,  $A_{\text{trans}}$ , of a RCA array can then be expressed as

$$A_{\text{trans}} = \underbrace{(N \cdot \lambda/2)}_L \times \underbrace{(N \cdot \lambda/2)}_L = N^2 \lambda^2 / 4. \quad (3.1)$$

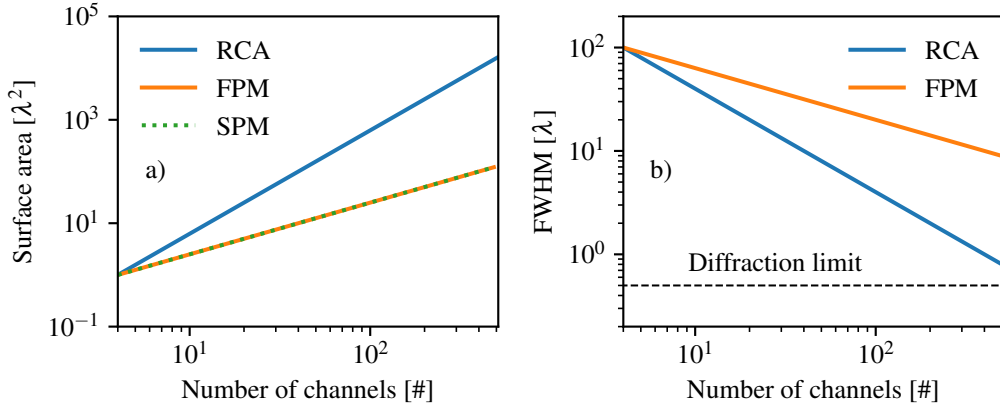


**Figure 3.3:** A comparison of scaling properties between RCA, FPM, and SPM arrays, notice the plots are on a double log scale. The plotted scaling laws are subject to a  $\lambda/2$  pitch constrain and is therefore expressed in terms of wavelength. The surface area scaling is plotted in a) expressed in units of  $\lambda^2$ . A rough estimation of the FWHM for the main lobe expressed in units of  $\lambda$  is plotted in b). The calculation is for a focal point  $100\lambda$  below the transducer surface. The black dashed line indicates the diffraction limit.

This expression allows a comparison between the transmitting area. The area scaling for all three transducer technologies are shown in Fig. 3.3 a). The incitement of increasing the channel count is explicit, since the RCA area progressively exceeds the other technologies as the channel count increases. Other parameters are also advantageous for the RCA array, such as the Full Width Half Max (FWHM) of the point spread function, which can estimated roughly by

$$\text{FWHM} = \frac{\lambda d}{L} \quad (3.2)$$

where  $d$  is the distance to the focal point, and  $L$  is the element length or the width of the 2D transducer. The FWHM calculations performed by Eqn. 3.2 do only consider the width of the main lobe, and cannot be used as a measure for the side lobe level. Furthermore, Eqn. 3.2 assumes focusing properties in both transmit and receive and is therefore not directly applicable for RCA arrays, but the FWHM has been estimated 35 % wider than prediction of Eqn. 3.2 [24]. The FWHM has been plotted against number of channels in Fig. 3.3 b) at a distance of  $100\lambda$  from the transducer surface, corresponding to a depth of 3 cm for a 5 MHz transducer. This plot illustrates the 35% bias become insignificant as the channel count goes up. The diffraction limit of

**Table 3.1:** Summary of relevant parameters for 2D array.

Type	Connections	Focusing	$A_{\text{trans}}$	FWHM
RCA	$2N$	One way	$\propto N^2$	$\propto N^{-1}$
FPM	$N^2$	Two way	$\propto N$	$\propto N^{-1/2}$
SPM	$N$	Two way	$\propto N$	-

the systems is indicated with the black dashed line, and any resolution model should approach the diffraction limit asymptotically. However, Eqn. 3.2 is an idealized model and not applicable in regime below the diffraction limit. The FWHM can also be expressed in terms of wavelength when the  $\lambda/2$  pitch constraint is applied, which reduces Eqn. 3.2 to

$$\text{FWHM} = \frac{\lambda d}{L} = \frac{2d_0\lambda}{N} \quad \text{where} \quad d_0 = \frac{d}{\lambda} \quad (3.3)$$

where is  $d_0$  the numerical factor used to express the distance to the focal in terms of wavelength ( $d_0 = 100$  in Fig. 3.3 b)).

The difference between the technologies become once again larger as function of channel count which translates into an increased image quality for the row-column technology. This simple equation for cannot be used to calculate the FWHM for SPM array, since, the length of an element cannot be lumped into a single parameter. Hence, FWHM calculations for SPM arrays require more advanced simulation tools such as FIELD II [37, 38].

In short, row-column arrays have a large transmitting surface and the resolution scales favourably compared to conventional FPM arrays, and these properties make the row-column technology particularly interesting volumetric ultrasound imaging. The discussed parameters are summarized in Table. 3.1 and images of RCA and FPM probes are shown in Fig. 3.4. The presented scaling laws are clearly demonstrated in these images. The two RCA probes have been developed in this work and both probes have a channel count of 92+92, corresponding to a FPM probe with 8464 active channels. The FPM probe imaged in Fig. 3.4 is a probe from Vermon with a total channel count of 1024 ( $32 \times 32$ ).

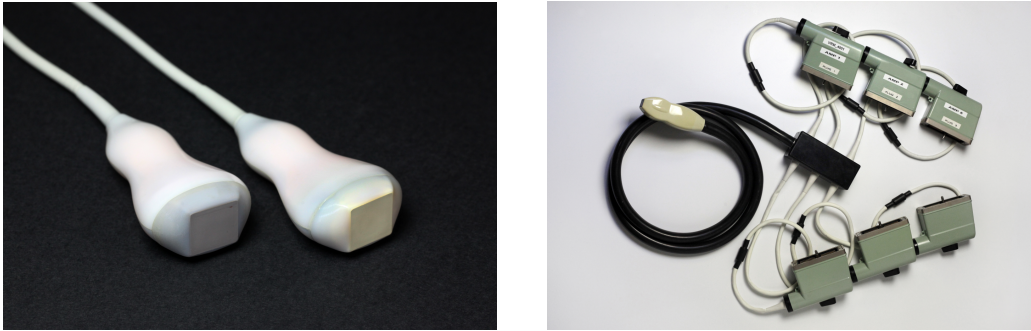


**Figure 3.4:** Realization of 2D ultrasound transducers. Two 92+92 RCA transducers (left) and a single  $32 \times 32$  FPM transducer (right).

## 3.2 Geometry

The natural way of comprehending the row-column geometry is to think of two orthogonal linear arrays that share sub-elements between them. One of the linear arrays consists of the rows and the other consists of the columns. A 3D sketch of the row-column geometry can be found in Fig. 3.5. The three-dimensional structure shows the corner of a generic silicon-based row-column array, where the indexing of the individual rows and columns are included. The row and column configurations have to be considered by two different cross-sectional planes. The two planes are indicated by the red and blue dashed lines that run along rows and columns, respectively. Cross-sectional views of these planes are shown in Fig. 3.6.

The insulating layers are used to electrically decouple all rows and columns from each other, whereas the semiconductor and metalization have conductive properties, and are used to electrically control the CMUTs. Notice the top electrodes are electrically separated in Fig. 3.6 a) and electrically connected through a wire bond in Fig. 3.6 b) and vice versa for the bottom electrodes.

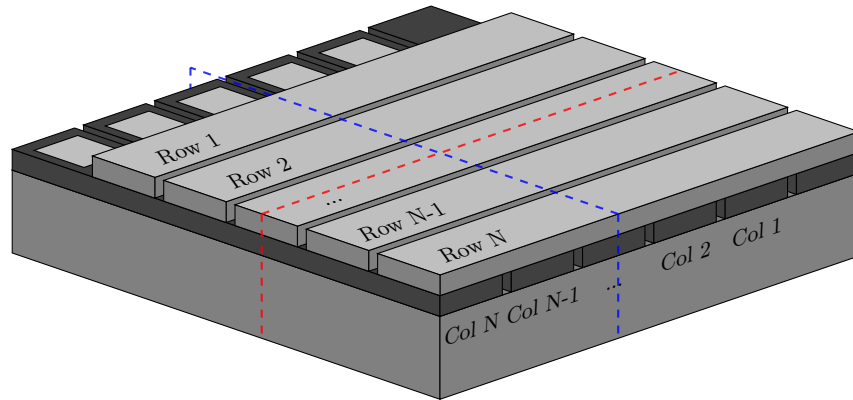


**Figure 3.5:** A sketch of geometry of a RCA array. The rows and columns form two orthogonal linear arrays on top of each other. The numbering scheme of the row and columns are illustrated in the figure. A blue and red dashed line are plotted along a row and a column, respectively. The cross section of these planes can be viewed in Fig. 3.6.

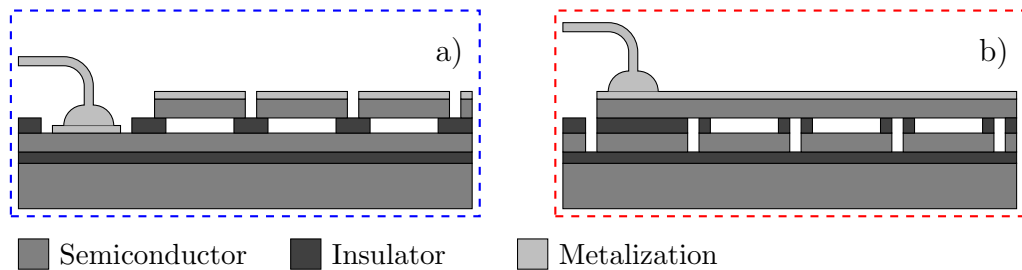


**Figure 3.6:** Sketch of the geometry of a row-column array seen from the row a) and columns b). Notice, the shown cross sections are for a CMUT row-column and not PZT or PMUT. The contact pads are indicated with wirebonds (not depicted in Fig. 3.5).

### 3.3 Edge waves

High aspect ratio row-column elements are inevitable for row-column arrays if the channel count is similar to conventional linear arrays. An elongated geometry of the elements amplifies the impact from edge waves. These edge waves occur for all transducers, but are especially pronounced for RCA arrays. The reason being the length of the elements, which is significantly larger than a conventional elements in a linear array and much larger than the individual sub-elements in a FPM array. The length of the elements increases with the number of channels as well as many of the desired imaging properties as explained in section 3.1.

The edge wave phenomenon can be described by a piston in a rigid baffle, such model can be interpreted as a single CMUT cell or a single sub-element. A sketch of a circular piston in a rigid baffle is shown in Fig. 3.7. Under the assumption of harmonic motion, can the on-axis ( $z$ -axis) pressure,  $p$ , be expressed analytically for this system, and is given by [39]

$$p = p_0 \left( \underbrace{e^{i(\omega t - kr)}}_{\text{Center}} - \underbrace{e^{i(\omega t - kr_1)}}_{\text{Edge}} \right) \quad (3.4)$$

where  $p_0$  is the surface pressure amplitude,  $k$  is the wave number,  $\omega$  the angular frequency.  $r$  and  $r_1$  are the distance from the observable point,  $P$ , to the center and a the edge of the piston, respectively, as depicted in Fig. 3.7. Equation 3.4 is derived under a harmonic assumption. The on axis pressure field from Eqn. 3.7 is fully described by two plane waves, one originating from the center of the circular CMUT cell (or rigid baffle) and one from the edge. The same behaviour is observed in transient systems, such as an ultrasound transducer, where short pulses are used instead of a harmonic signal. The edge wave travels a longer distance than the wave from the center, and will therefore be observed later in the RF data. The delay between the center wave and the edge wave introduces a ghost echo of the imaged object that creates unwanted artifacts in the ultrasound image. The distance to the point,  $P$ , in Fig. 3.7 is on the order of cm for imaging applications, whereas the CMUT diameter is in on the order of  $\mu\text{m}$ . Hence,  $r$  and  $r_1$  are for all practical purposes identical and cancel out in the far field when a single cells or a sub-elements are considered. Edges waves are therefore not an issue for FPM arrays. But, the edge wave problem occurs also when numerous CMUTs are combined into a long element that radiates as one large rectangular radiator, and row-column elements can be on the order of cm. Thus, the added distance becomes substantial when an



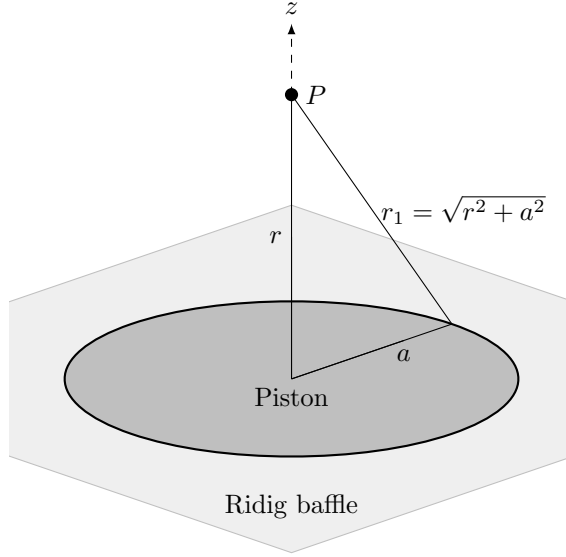


**Figure 3.7:** A sketch of the system used to calculate the on axis pressure for a circular piston in a rigid baffle.

entire row-column element is considered and the impact becomes progressively pronounced as the channel count increases. Suppression of the edge waves can be achieved in several ways. One option is to introduce a roll-off apodization region where the transmitted pressure gradually reduces near the edges of an element [27, 28]. This solution is schematically shown for an element in Fig. 3.8. The roll-off apodization has the main advantage of being entirely hardware based, and this solution will therefore not require any specialized imaging sequences. The ability to suppress the edge waves becomes progressively better as the length of the apodization region increases [27], however, the receive sensitivity gets reduced as the apodization region increases due to an added parasitic capacitance. Finally, the footprint of the RCA becomes larger when integrated roll-off apodization is included, and larger footprints increase the requirements for cleanliness during the fabrication of the CMUTs. Hence, the size of the apodization region is a trade of between image artifacts, sensitivity, and fabrication complexity.

Other alternatives for suppression of the edge waves have also been published. The group from the University of Waterloo has published several papers with an algorithmic approach to suppression of edge waves and general image improvement of RCA arrays [40–43].

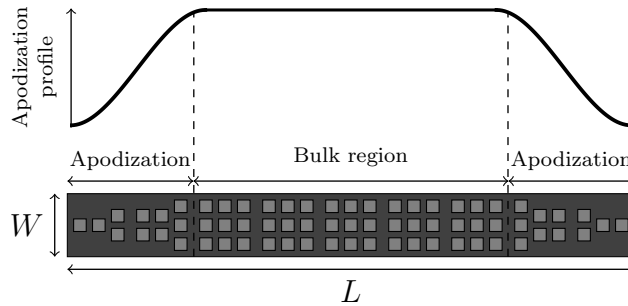


**Figure 3.8:** Sketch of the implementation of roll-off apodization for CMUT RCA element as suggested in [27, 28]. The light gray squares are CMUT cells and the dark gray represents the insulating bonding area. The gradual suppression of the edge wave are obtained by reducing the density of CMUT cells towards to edges.

### 3.4 Silicon substrates for row-column CMUT fabrication

Several papers regarding RCA arrays and probes have been published using multiple row-column platforms, that includes RCA PMUT [44], PZT [23], and CMUT [31, 45, 46]. Although many techniques are available and interesting for row-column development the CMUT technology will be the focus in this section. The various well documented semiconductor fabrication techniques have facilitated the birth of the CMUT technology where silicon is the cornerstone. There are multiple reasons why for silicon is specifically interesting, and three of the many reasons are given here.

**High control of contamination:** It is possible to achieve crystal lattices of a extremely high quality, thus, almost all of the atoms in the silicon crystal is determined by the purchase specification. It ensures large reproducibility for many semiconductor processes.

**Doping:** The electrical properties of silicon can be controlled by doping of foreign atoms (commonly phosphorous or boron atoms). The resistivity of silicon can vary eight orders of magnitude depending on the doping concentration.

**Clean room compatibility:** Silicon has the advantage of having a negligible effect on the condition and the performance of used equipment, and is therefore allowed in more equipment than other materials.

These are some of the reasons why the majority of the published CMUT papers use silicon technology. However, a challenge occurs for RCA arrays when

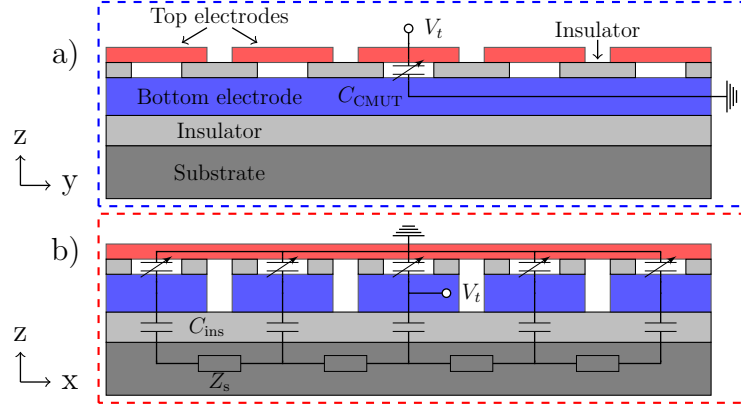


**Figure 3.9:** Sketch of the different circuit configurations for rows and columns imposed on top of cross sectional views of the geometry. The different circuit configurations of the top and bottom electrodes are probed differently. All bottom electrodes shorted when the top electrodes are probed in  $V_t$  in a) and visa versa in b). Blue and red dashed lines have been added to help the understanding of the three dimensional structure, and these lines are in accordance with the color coding from Fig. 3.5.

silicon is used as a substrate. An insulating layer has to be introduced, as seen in Fig. 3.9 a) and b), to obtain individually insulated bottom electrodes.

An electrical circuit is imposed on top of the two cross sectional planes. and the circuit for the rows (top electrodes, Fig. 3.9 a)) consists only of the variable CMUT capacitance  $C_{CMUT}$ . This configuration is the desirable since contributions from parasitic capacitance are minimized, which ensures the best possible receive sensitivity. Unfortunately, this circuit configuration does not apply to the columns (bottom electrodes, Fig. 3.9 b)) where an additional parasitic capacitance is introduced due to the insulating layer in the substrate, which thereby reduces the receive sensitivity. The different receive sensitivities between rows and columns cause a non symmetric point spread function, that degrades the quality of an ultrasound image.

The capacitance of the insulating layer,  $C_{ins}$ , couples through the substrate and make up a large distributed network that contributes to an additional parasitic capacitance. This effect has been experimentally demonstrated for a 62+62 CMUT RCA probe [31], and the capacitance of this probes is plotted as function of element number in Fig. 3.10. The measured capacitance is observed to differ with a factor 2.5 between rows and columns, which henceforth will be defined as the substrate coupling factor. Different solutions and an extended description regarding the subject of substrate coupling can be found in [47], but only one of the solutions will be considered

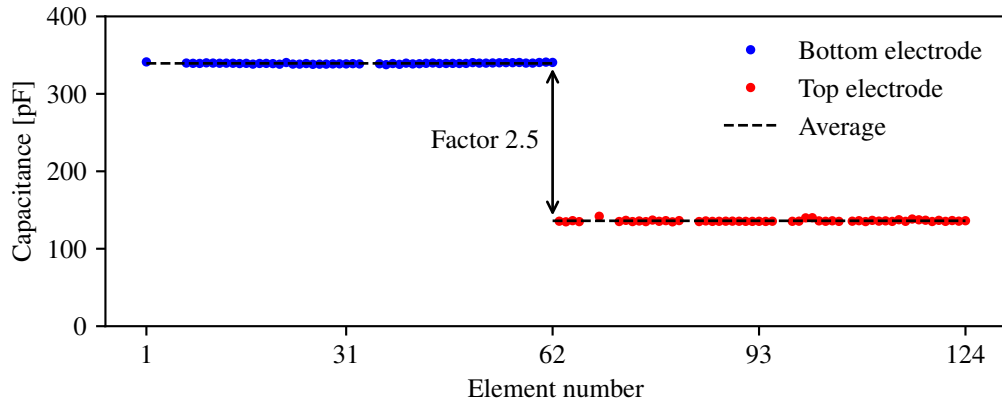


**Figure 3.10:** Element capacitance of all rows and columns for the 62+62 CMUT RCA probe presented in [31]. The capacitance differs with a factor of 2.5 between rows and columns due to substrate coupling.

in this work. The particular solution where the silicon substrate is substituted with an insulating substrate, such as glass. Two different glass based fabrication methods will be examined in the next chapter, and capacitance measurements of rows and columns will be used as a reference measurement for the receive sensitivity. Measurements throughout the thesis will furthermore be compared to the result capacitance shown in Fig. 3.10, where the aim will be to achieve a the substrate coupling factor of 1.0.

### 3.5 Chapter summery

Different concepts of the row-column addressing scheme were described in this chapter. A brief literature review was given and relevant scaling laws were provided. Edges waves and capacitive substrate coupling effects of row-column arrays were explained and solutions to over these challenges were given. The capacitive substrate introduce an increased parasitic capacitance for the columns and measurements from a 62+62 CMUT row-column probe will be used as a reference in this thesis. The capacitance of the columns was observed to be 2.5 times higher than the rows for this probe, and this substrate coupling factor of 2.5 will be used as a benchmark throughout the thesis.



## CHAPTER 4

---

### CMUT fabrication

---

Fabrication of RCA CMUT arrays is the main focus of this chapter, and three different CMUT fabrication techniques will be presented. The used techniques are distinguished by the applied bonding method and comprise of adhesive, anodic, and fusion bonding. Conventional semiconductor fabrication techniques are used to fabricate CMUTs, and CMUT fabrication can be divided into two categories: Sacrificial release processes and wafer bonding techniques. The fundamental difference between the two categories is how the CMUT cavity is defined. Multiple papers have demonstrated CMUTs based on the sacrificial release process [16, 48–52] and linear CMUT probes [6, 8] have as well as RCA arrays [26] been demonstrated. All these papers demonstrate the feasibility of the sacrificial release processes, but, the conducted work of this thesis has been focused solely on wafer bonding techniques.

This chapter is divided into six sections. Different fabrication methods are examined in the first four sections, and these sections are structured such that a brief introduction of the bonding mechanism is given initially, followed by a detailed examination of a CMUT fabrication process. A characterization of relevant CMUT and row-column parameters will be given at the end of each section.

The first section examines a fabrication method based on the semiconductor technique known as Local oxidation of silicon (LOCOS). This method has been used for fabrication of two 4.5 MHz 92+92 RCA CMUT probes with integrated apodization. A polymer based fabrication process is investigated in the subsequent section, where a fabricated 62+62 RCA CMUT array is

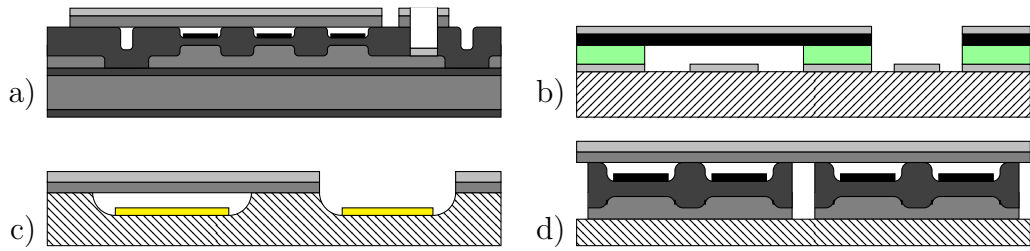


**Figure 4.1:** The four developed fabrication processes for RCA arrays. a) LOCOS process. b) Polymer bonding process. c) Anodic bonding process. d) Combined LOCOS and anodic bonding process.

demonstrated and characterized. An anodic bonded CMUT fabrication is demonstrated in the third section, and multiple row-columns of different sizes have been fabricated using this method. The fabrication of two large 190+190 RCA arrays have been successfully demonstrated together with multiple smaller 16+16 row-column arrays. A preliminary electrical characterization of the 16+16 row-columns arrays will be presented.

The best properties of the LOCOS and the anodic bonding process are combined into a new fabrication method explained in section four. Design considerations of a new 8MHz 188+188 RCA CMUT probe with integrated apodization will be given. A novel CMUT cell layout will be elaborated followed by a discussion of the fabrication issues associated with this fabrication process. Cross sectional sketches of all four CMUT designs are shown in Fig. 4.1. The different developed processes are discussed and compared in the fifth section. Finally, a novel fabrication method of a Poly-Silicon-On-Insulator (PSOI) wafer is demonstrated in the final section, which is an alternative to SOI wafers.

## 4.1 Fusion bonding

A fusion bonding process (also called direct bonding) consists of three steps: surface preparation, contacting, and annealing. The wafer surface is initially prepared by a chemical cleaning process to remove particles from the surface. The surfaces of two cleaned wafers are subsequently brought together in a clean environment, and by doing so the atomically flat surfaces of modern silicon wafers will start to pre-bond. This process can be enhanced by applying pressure on the wafer stack. The pre-bond process is commonly performed by commercial machines to ensure an evenly distributed pressure across the wafer stack. An annealing step at an elevated temperature, on the order of 1000 °C, finishes the bonding process. The two first steps are

required to facilitate a good bonding conditions, but, the bonding itself occurs during the last annealing step, where strong irreversible covalent bonds are established between the two surfaces. The bonding strength is strongly correlated to the annealing temperature [53], and successful fusion bonds require two extremely flat surfaces and a wafer bow less than 5  $\mu\text{m}$ . The surface roughness should be lower than 1 nm and preferably even lower [54]. The bulk parts of the fusion bonded wafers should preferably be the same material, since the high annealing temperature introduces thermal strain in the bonded structure. Finally, thin film stresses are also influential of the success rate for fusion bonded structures, and will inevitably be introduced in a fusion bonded CMUT fabrication. A successful fusion bond is an irreversible process and well suited for CMUT fabrication due to the strong bonding strength. The fusion bonding technique was first demonstrated for CMUT fabrication back in 2003 [55]. The fusion bond is used to seal the cavity in CMUT applications which is demonstrated in multiple papers [56–59]. Fusion bonded linear [7] and RCA [31] CMUT probes have also been demonstrated.

The fusion bonded CMUTs in this work are all fabricated using the semiconductor technique called Local oxidation of silicon (LOCOS). Topological patterns on the surface of a silicon wafer, such as a CMUT cavity, can be fabricated precisely using the LOCOS process. The principle of LOCOS is simply to pattern a silicon nitride film (other material can also be used) on top of a silicon (or silicon dioxide) surface and afterwards carry out a thermal oxidation process. The silicon nitride acts as a diffusion barrier during the thermal oxidation, and spatially different oxidation rates create in the topology changes that is used to construct CMUT cavities. The LOCOS process has been thoroughly demonstrated for CMUT applications in [60]. This LOCOS design has the advantage of reducing the parasitic capacitance from the post region, while the CMUT capacitance is preserved. The cavity height is furthermore controlled with nanometer precision, which translates into high control of the pull-in voltage. Additional details about the design space of CMUTs fabricated using a LOCOS process is comprehensively discussed in [61].

Prior work in our group at DTU has shown reliable results for wafer bonded CMUTs and the LOCOS process has in particular showed promising results. Multiple linear CMUT arrays and a single LOCOS based 62+62 RCA array have been successfully developed [31]. However, the array yield of the row-column process has been observed much lower than the linear counterpart, presumably due to the SOI substrate wafer used in the row-column process. An additional undesired consequence of using a SOI wafer as substrate is the added parasitic capacitance from the substrate coupling.



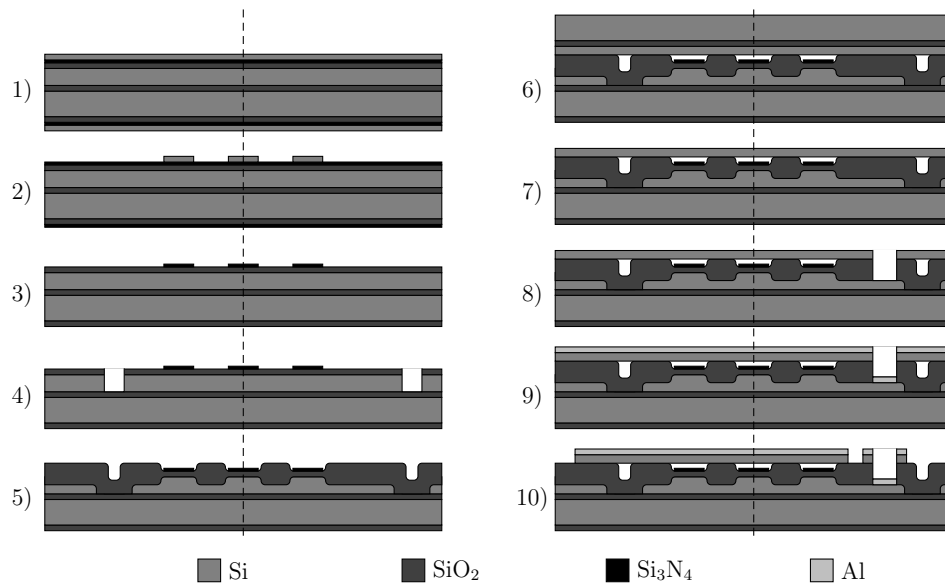


**Figure 4.2:** Process flow of LOCOS process. Step 1: Thermal oxidation and LPCVD deposition of nitride and poly-silicon. Step 2: Lithography process followed by a dry etch process to remove poly-silicon. Step 3: Wet etching of nitride using poly-silicon as mask, which afterwards is removed in a dry etch process. Step 4: Lithography process followed by a dry etch process to electrically insulate the bottom electrodes. Step 5: Thermal oxidation process used to create the cavities utilizing the LOCOS principle. Step 6: Fusion bonding between the processed wafer and a SOI wafer. Step 7: Removal the handle in a dry etch process followed by a wet Buffered HydroFluoric acid (BHF) etch to remove the Burried OXide (BOX) layer. Step 8: Aluminum deposition process. Step 9: Lithography process followed by dry etching of aluminum and silicon, which end up defining the top electrodes. Figure is adapted from [62] and is not to scale.

Despite these associated challenges have two additional LOCOS based 92+92 RCA CMUT probes been successfully fabricated during this work.

The process flow for the fabricated fusion bonded RCA CMUT arrays is shown in Fig. 4.2, notice a SOI wafer is used as the starting point. The vertical dashed lines are included to illustrate both cross sections of the rows and the columns. The rows are sketched in the left region and the columns are sketched in the right region.

Multiple thin-films are grown and deposited in step 1. An insulation oxide is thermally grown initially, and silicon nitride and poly-silicon thin films are subsequently deposited on top of the oxide in a Low Pressure Chemical Vapour Deposition (LPCVD) process. In step 2, a resist is patterned in a lithography process and the pattern is transferred into the poly-silicon using

a dry etch process. A 160 °C  $\text{H}_3\text{PO}_4$  solution is afterwards employed to etch the unmasked silicon nitride in step 3. High selectivity towards the insulation oxide is crucial in this step to preserve a low surface roughness. A 160 °C  $\text{H}_3\text{PO}_4$  solution has been used in this work due to a reported selectivity of 40 between  $\text{SiN}:\text{SiO}_2$  [63]. After the wet etch is the masking poly-silicon removed in a dry etch process. The bottom electrodes are defined in step 4 by lithography and a dry etch process. The BOX ensures electrical insulation between the bottom electrodes and are in this step also used as an etch stop layer. The second thermal oxidation is conducted in step 5, where the cavities are created by the LOCOS principle. Atomic Force Microscope (AFM) measurements of the cavity profile and the surface roughness should be conducted to confirm acceptable bonding conditions and to ensure the correct gap height. If the surface roughness is lower than 1 nm the wafer can proceed to the fusion bonding process in step 6. Process reliability and reproducibility are up until this point close to 100%, however, the array yield of the row-column arrays drops drastically after the handle removal, in step 7. The handle layer is removed in a dry etch process, and rupture of the plate has often been observed during this part of the process. The damages caused by plate rupture is documented in Fig. 4.3, where significant stress effects are tearing the plate apart. Fortunately, if the handle has been successfully removed, the remaining part of the fabrication process is less critical. The BOX of the top SOI wafer acts as an etch stop layer for the handle removal and is subsequently etched away selectively in BHF. A combined lithography and dry etch process is, in step 8, used to access the bottom electrodes. In step 9, 400 nm aluminum is deposited on top of the entire wafer to enable the possibility of wire bonding for both rows and columns. Finally, the top electrodes are patterned in a lithography process, and electrically separated by etching through the aluminum and silicon in a dry etch process.

The specifications of the fabricated LOCOS based CMUTs in this project can be found in Tab. 4.1.

#### 4.1.1 Characterization

The LOCOS CMUTs were electrically characterized prior to the probe assembly. Impedance measurements have been performed using an Agilent 4294A Precision Impedance Analyzer with multiple DC biases and an AC voltage of 50 mV. The measurements were conducted in air and used to confirm long term stability and CMUT characteristics such as resonance frequency, the spring softening effect, and capacitive properties. The magnitude and phase of the impedance measurements are shown in Fig. 4.4. The characterized array is a linear LOCOS CMUT array from the same fabrication batch as

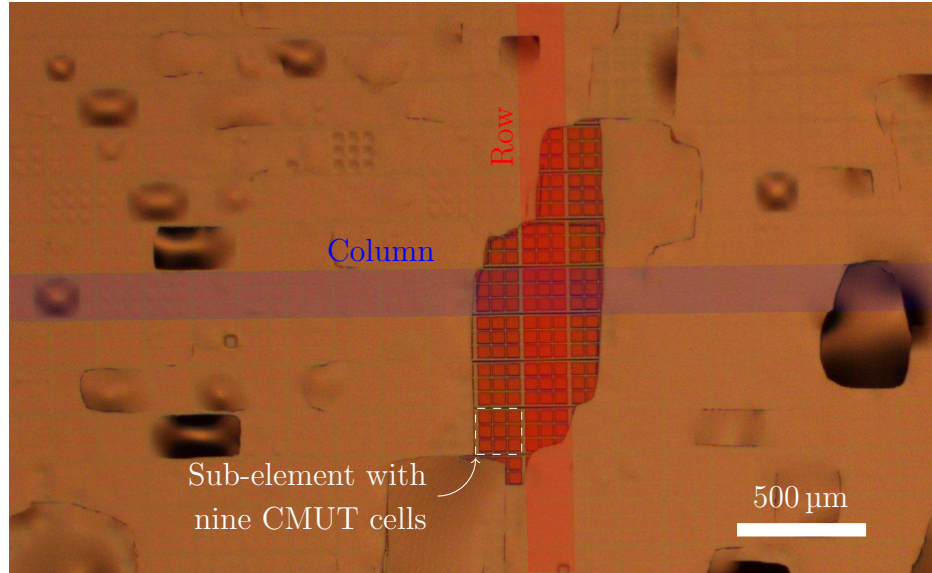


**Figure 4.3:** Microscope image of the processed LOCOS wafer after the handle removal etch. The plate rupture is so severe that the row-column array cannot be used. Notice, the sample is rotated 90° and rows and columns are therefore swapped.

**Table 4.1:** 92+92 CMUT row-column specifications

<i>CMUT parameter</i>	
Plate thickness	3 $\mu\text{m}$
Side length of cell	50 $\mu\text{m}$
Cavity height	180 nm
Pull-in voltage	220 V
<i>Array parameters</i>	
Elements	92+92
Integrated apodization (apo)	yes
Transducer surface area w/o apo	1.66 $\times$ 1.66 $\text{cm}^2$
Transducer surface area w/ apo	2.24 $\times$ 2.24 $\text{cm}^2$
Pitch	180 $\mu\text{m}$
Center frequency	4.5 MHz

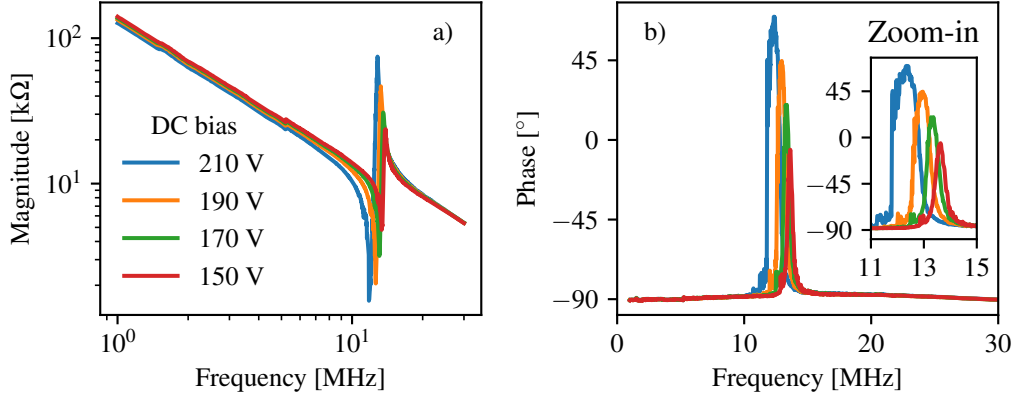


**Figure 4.4:** Impedance measurements of the LOCOS CMUTs for four different bias voltages. The measurements are conducted on a linear test element in air. a) The absolute magnitude of the impedance plotted in a double log plot, where a clear and distinct resonance and anti resonance are observed between 11 MHz and 15 MHz. The capacitive properties of the CMUT arrays are confirmed by the power law dependency for off-resonance frequencies. b) The phase of the impedance measurements. The bias dependency of the resonance frequency is explicitly shown in the zoom-in figure, where the spring softening effect is detected.

the row-column arrays used in two developed probes.

The expected CMUT behaviour is observed in both plots, a distinct resonance frequency is observed and the spring softening effect is confirmed by the frequency shift towards lower frequencies for increasing DC biases. The capacitive properties of the CMUT are confirmed in both plots, since a power law dependency is observed for the magnitude and the phase is  $-90^\circ$  for all off-resonance frequencies. The impedance measurements show capacitive properties for all off-resonance frequencies up to 30 MHz, which can be used as an indication for high quality as it demonstrates the absence of parasitic inductance in the system. The pull-in voltage of this particular CMUT has been measured to be approximately 230 V, hence, the applied DC bias ramp used for the impedance measurements corresponds to 65%, 74%, 83%, and 92% of the pull-in voltage. The electromechanical coupling coefficient,  $\kappa^2$ , is estimated by the formula [64]

$$\kappa^2 = \left[ 1 - \left( \frac{f_r}{f_{ar}} \right)^2 \right] \times 100\%, \quad (4.1)$$

where  $f_r$  is the resonance frequency and  $f_{ar}$  is the anti-resonance frequency. The resonance and anti-resonance frequencies have been read off from Fig. 4.4 a)

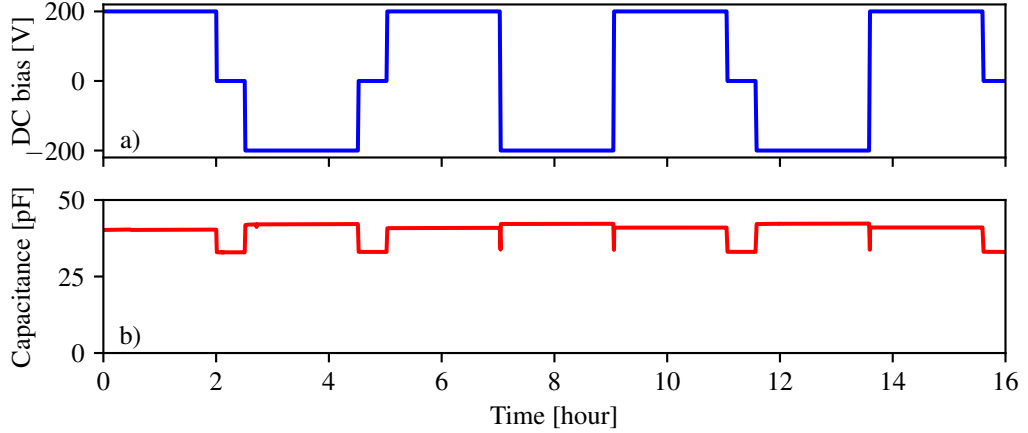


**Figure 4.5:** Capacitance measurements of the LOCOS CMUTs during 16 h of operation. a) the applied DC voltage ramp as function of time. The ramp changes between 200 V, 0 V, and  $-200$  V corresponding to 87% of the pull-in voltage. b) Capacitance versus time. The capacitance is stable for both positive and negative bias voltages, hence, no indications of time dependent charging effects.

and 7.10%, 7.78%, 9.57%, and 15.8% were the corresponding electromechanical coupling coefficients for the different biases (monotonically increasing). Continuous impedance measurements during 16 h of operation have been executed to demonstrate long term performance of the CMUTs. Three different voltage levels of 200 V, 0 V, and  $-200$  V constituted the DC bias ramp during the stability measurements. The 0 V step was held for 30 min to ensure completion of any discharging effects, and the two other steps  $\pm 200$  V were each held for 2 h. The capacitance has then been estimated from the impedance by fitting a straight line (double log transformed) to the low frequency data points. The used bias ramp versus time and the corresponding capacitance are all shown in Fig. 4.5. The capacitance is observed to be stable for both the positive and the negative bias. Thus, significant charging effects are not present in this LOCOS CMUT array.

Linear CMUT arrays have up until this point been used for the electrical characterization. Electrical characterization of a row-column array is inherently difficult due to the array configuration. Characterization of the rows requires electrical contact to all of the columns and visa versa. Full characterization of row-column arrays become much simpler after the arrays are assembled into probes where all rows and columns can be controlled individually. Capacitance measurements for the assembled 92+92 row-column array are plotted in Fig. 4.6. The substrate coupling factor is 1.6 for this

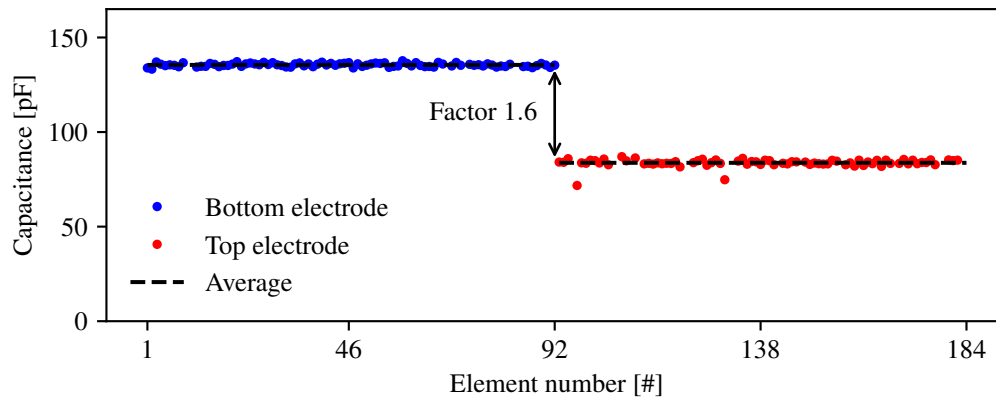


**Figure 4.6:** Element capacitance of all rows and columns for the 92+92 CMUT RCA probe. The substrate coupling factor is 1.6 for this row-column array.

row-column array and thereby reduced compared to the reference of 2.5. However, the substrate coupling factor is still too high for acceptable row-column ultrasound imaging. Additional characterization of the developed row-column probes will be given in chapter 5.

## 4.2 Polymer bonding

The first polymer bonded CMUT was demonstrated back in 2006 by [65] and multiple new papers have been published since then [66–69]. The most common approach for adhesive/polymer bonded CMUT is to spin coat a polymer and afterwards bond the surface to a new wafer. A sacrificial release polymer fabrication is also possible and has been demonstrated in [70].

Polymer bonded CMUTs are fabricated by spin coating a polymer on a wafer, define the cavities directly into polymer using a lithography process, then bring the patterned surface in contact with another wafer. The polymer is used as the post region in this kind of CMUT design. After the two wafers are brought in contact a thermal curing step is required where the temperature increased to approximately 250 °C. The polymer liquefies as the temperature increases and solidifies upon cooling in a state that bonds the two wafers together. The curing temperature is the highest temperature during the fabrication and thereby significantly lower compared to fusion bonding. The low process temperature is one of the more attractive properties of polymer bonded CMUTs, since it allows easy implementation with integrated circuits. Highly advanced electronics could therefore be implemented on the same chip as the CMUT itself. Another attractive property of the polymer bonding technique is the material flexibility, since polymer bonding is applicable between the most common semiconductor materials. The material flexibility allows processes where the CMUT is polymer bonded directly on top of an ASIC as demonstrated in [71]. Polymer bonding techniques have also proven to be an attractive techniques for flexible CMUT applications. Functional flexible polymer bonded CMUTs have already been demonstrated [68], and even flexible RCA arrays have been demonstrated [72]. Finally, the majority of demonstrated polymer based CMUTs have a polymer based post region and a silicon plate, however, a CMUT with a polymer based plate has also been demonstrated in [67].

BenzoCycloButene (BCB) and SU-8 are the two commonly used polymers in the CMUT literature. BCB and SU-8 share many of the desired parameters for CMUT fabrication, both polymers are thermosetting materials, have excellent bonding strengths, and high chemical stability among other [73]. An important difference, between the two polymers, is the dielectric strength or the break down voltage, which is 0.53 V/nm for BCB and 0.11 V/nm for SU-8 according to their respective data sheets. Hence, as a post material the BCB should be the better choice, and this has been the reason for choosing BCB in this work. The developed BCB process flow can be found in Fig. 4.7. The bottom electrodes are structured in a lithography process and electrically connected to the contact pads (indicated in the

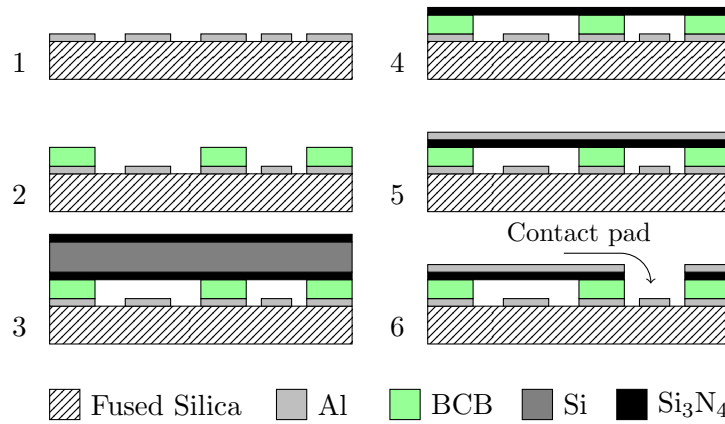


**Figure 4.7:** Process flow of BCB process. Step 1: Lithography, metalization and lift-off. Step 2: BCB lithography on top of patterned metal. Step 3: A wafer with a deposited silicon nitride is bonded to the BCB. Step 4: The top nitride layer and the silicon are etched away using a dry etch and at wet KOH etch, respectively. Step 5: Metal deposition. Step 6: Lithography followed by an etch through metal and silicon. Figure is not to scale.

figure). Three dimensional sketches are necessary to illustrate such structured electrodes, however, cross sectional sketches are easier to interpret and therefore used for all the designs with structured electrodes.

The developed BCB fabrication is a three mask process and uses a fused silica wafer as substrate to reduce the substrate coupling for RCA CMUT arrays. Step 1 is a lithography step where a negative tone resist (AZ nLOF 2020) is spun on the glass wafer followed by 400 nm aluminum deposition and a lift-off process using Microposit<sup>TM</sup> remover 1165. CYCLOTENE resin 4022-25 BCB from Dow Chemical Company is, in step 2, spin coated on top of the structured bottom electrode followed by a 60 °C bake for 90 s. The BCB is afterwards exposed (@ 365 nm) for 3.2 s with an intensity of 13 mW/cm resulting in a final dose of 41.6 mJ/cm<sup>2</sup>. A post exposure bake at 60 °C for 90 s is done subsequently. Development of the BCB is carried out in two beakers using the developer DS3000 from Dow Chemical Company. The development time and temperature in the first beaker are approximately 1 min at 30 °C, next in the second beaker for 2 min at room temperature DS3000 which stops the development. A final 90 °C bake for 1 min is performed after development resulting in an approximate BCB thickness of 450 nm. Notice the BCB is spun on top of aluminum pads. The purpose of these pads are to planarize the surface, and thereby achieve the flat condition for the spin coating process. The planarization pads are not electrically connected in the final device. The plate of the CMUT is made of silicon nitride, and has been



fabricated using stoichiometric nitride from a LPCVD nitride furnace. The top wafer consists of a 350  $\mu\text{m}$  double side polished wafer, where 350 nm low stress LPCVD silicon nitride has been deposited. The nitride is kept on both sides during bonding, in step 3, to lower the stress induced curvature across the wafer. The wafer are bonded in a CNI v2.0 desktop nanoimprint tool from NIL Technology. The temperature is first ramped to 125  $^{\circ}\text{C}$  and kept constant for 15 min and subsequently raised to 240  $^{\circ}\text{C}$  and kept constant for 1 h. This step is a combined bonding and curing step.

Using a nitride plate instead of a conventional SOI wafer serves two purposes. First, it lower the fabrication costs compared to a SOI based method, and secondly, the dielectric properties of the nitride increase the overall breakdown voltage and allows the plate to go into pull-in without short circuiting. The top nitride layer and the silicon are etched away in step 4. The nitride is removed in a fluorine plasma and the silicon is etched in potassium hydroxide (KOH). The silicon has an initial thickness of 350  $\mu\text{m}$  and requires approximately 4.5 h of etching in 28wt.% KOH at 80  $^{\circ}\text{C}$ . The bonded wafers are etched without any backside or edge protection, which leaves the BCB directly exposed to KOH at the edges. The transparent glass substrate enables visual inspection of potential damages of the CMUT structures, and it has visually been observed that KOH etches BCB at the edges with a rate of approximately 1 mm/h. Hence, a safety margin of 1 cm should be sufficient for this process. 400 nm aluminum is, in step 5, deposited on top of the nitride layer and patterned in a lithography step. In step 6, the aluminum is etched in a wet solution of  $\text{H}_2\text{O}:\text{H}_3\text{PO}_4$  in the volume ratio 1:2, followed by a dry etch process where the nitride is removed to enable access the bottom electrode.

### 4.2.1 Characterization

Multiple BCB arrays have been fabricated during this work and an image of a 62+62 RCA BCB array and two linear BCB arrays can be found in Fig 4.8. The dimensions of the design mimic the 62+62 RCA LOCOS CMUT reference probe [31]. The capacitance of the rows and the columns have been measured and plotted in Fig. 4.9, where a substrate coupling factor of 1.1 is observed. Thus, the difference in capacitance between rows and columns are strongly reduced. The array yield of the developed BCB process has been observed to be high (close to 100%).

However, the missing data in Fig. 4.9 corresponds to electrically dead elements. Thus, this developed fabrication technique has shown high structural array yield, but the element yield is low from an electrical point of view. Additionally, the dielectric properties of the present design are not sufficient for

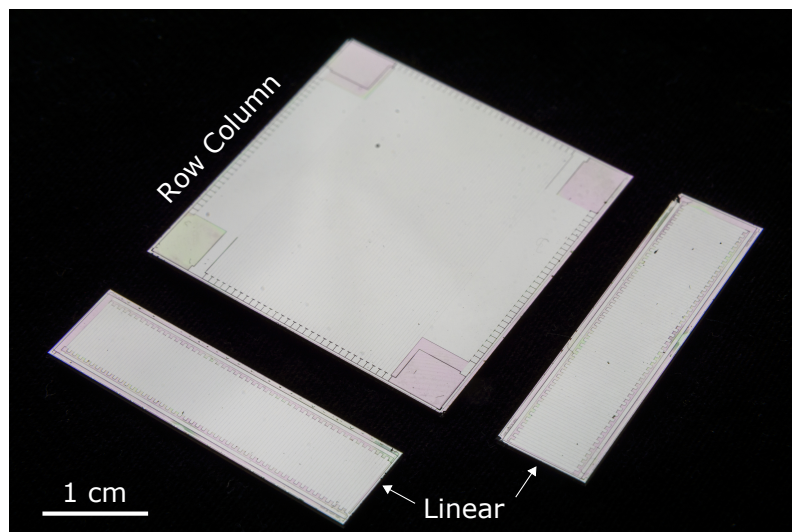


**Figure 4.8:** Image of three BCB CMUT arrays. 62+62 BCB Row-Column addressed CMUT array with integrated apodization and two 92-element linear BCB CMUT arrays.

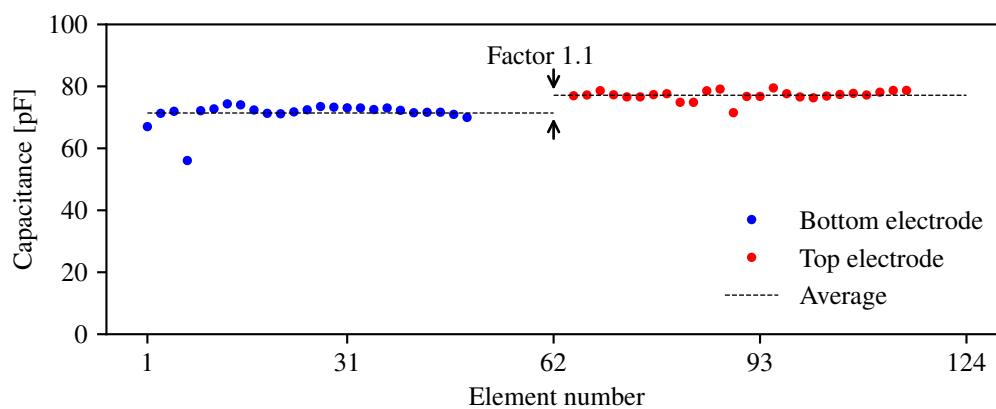


**Figure 4.9:** Capacitance measurement of rows and columns for the fabricated BCB based 62+62 RCA CMUT array. The difference between rows and columns are significantly reduced compared to the LOCOS RCA array.

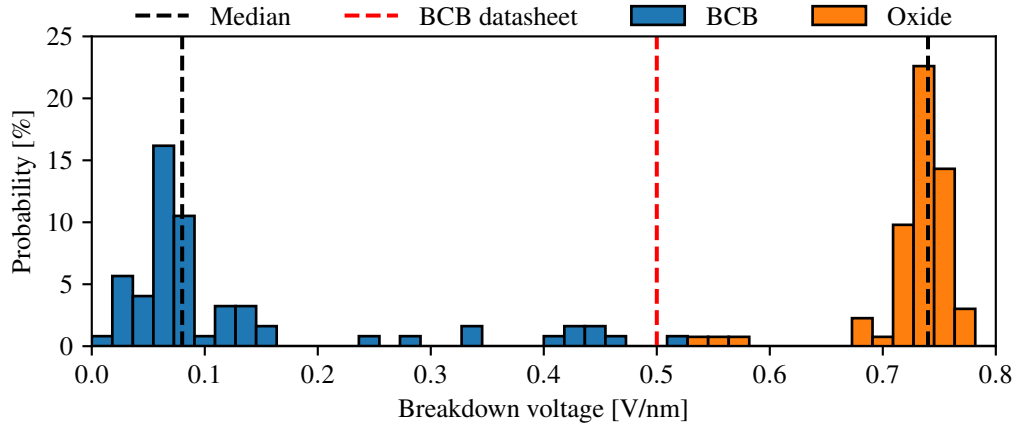


**Figure 4.10:** Measured breakdown voltage of BCB and a thermally grown oxide. Measurements are from six different wafers. Three wafers with BCB and three wafers with a thermal oxide. The histogram is generated from 68 BCB data points and 73 oxide data points.

a reliable CMUT fabrication. A median breakdown voltage of  $0.08 \text{ V/nm}$  has been observed by measuring multiple positions across a BCB coated wafer. For comparison, the median breakdown voltage of a thermally grown oxide has been measured to  $0.74 \text{ V/nm}$ . These data of the breakdown voltage are plotted together in the histogram shown in Fig. 4.10.

The distribution of the BCB data is observed to have a substantial positive skew, which is the reason why the median is used as the quantitative measure in this analysis. The mean is biased towards higher values due to the skewness of the distribution. The oxide measurements show a more symmetric distribution and the median and mean are approximately identical, but the median is for consistency used in both cases. Only 16% of the data sheet value has been obtained experimentally, even though recommendations from the BCB data sheet has been followed. The discrepancy between the measured breakdown voltage and the data sheet value is not fully understood. One explanation could be data sheet value is measured on micron thick BCB films, where a thickness of approximately  $500 \text{ nm}$  has been used in this analysis. Bulk properties might not be the right measure on this length scale.

Additional acoustic characterization of the two linear BCB arrays and long term electrical performance of a row-column element can be found in paper A.

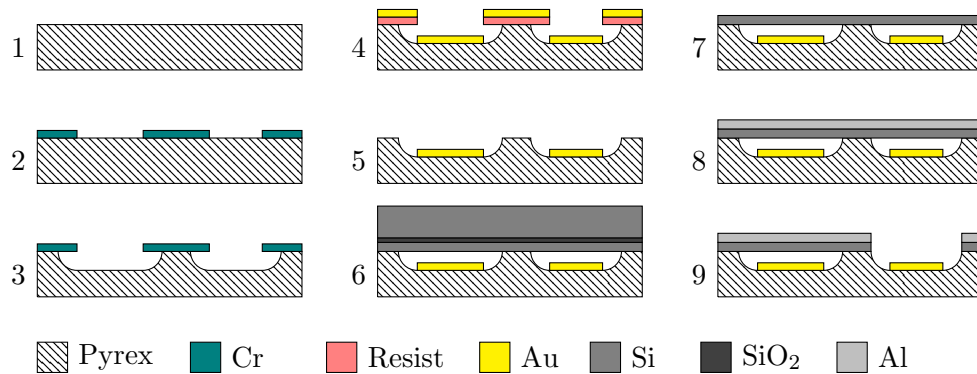


**Figure 4.11:** Process flow of the developed anodic bonding process. Step 1: Heat treatment of a Pyrex glass wafer in a 250°C furnace to remove moisture from the surface. Step 2: Chromium deposition and lithography followed by a wet chromium etch. Step 3: The CMUT cavities are defined in a BHF etch with the patterned chromium as the masking material. Step 4: Lithography step and gold deposition and a lift-off process. Step 5: The chromium mask is removed in a wet chromium etch. Step 6: A SOI-wafer is anodically bonded to the glass surface. Step 7: The handle and BOX layer are etched in a KOH and BHF etch, respectively. Step 8: Aluminum is deposited on top of the device layer. Step 9: A lithography step combined with a dry etch process used to define top electrodes and open up to the bottom electrodes. Figure is not to scale.

### 4.3 Anodic bonding

The first anodically bonded CMUT was demonstrated in 2009 [74], and functional anodically bonded CMUTs have since then been published in multiple papers [75–77]. A RCA array has also recently been demonstrated [46], and the anodic bonding technique has several intrinsic advantageous features for CMUT fabrication and especially for row-column fabrication. The anodic bonding shares many of the same desired features from polymer bonding, such as the possibility of structured metal electrodes, low process temperature, and reasonable requirement for the surface roughness. A surface roughness of 50 nm has been reported as the upper bound for anodic bonding [78].

An array yield on the order of 95% has been observed for the fabricated anodic bonded CMUTs. The process flow for the developed anodically bonded CMUTs is sketched in Fig. 4.11.

The developed fabrication process is a three mask process, that uses a Pyrex wafer as substrate. The Pyrex wafer is, in step 1, heated in a furnace at 250° for more than 1 h. The Pyrex is afterwards, in step 2, moved directly from the furnace into a metal deposition system, where 100 nm chromium is deposited. The initial furnace step removes moisture from the surface

and provides optimal conditions for metal deposition. A resist (AZ 5214E) mask is defined in a lithography process on top of the chromium layer, and the exposed chromium is then etched by Chrome Etch 18 from Micro Resist Technology. The CMUT cavities are, in step 3, defined in a 40% BHF solution. The masking material has to withstand more than 10 min of etching to reach a cavity depth of some hundreds of nanometers, with an etch rate of approximately 25 nm/min. A resilient masking material is therefore a requirement, and both resist masks and chromium masks have been investigated. The best results in terms of underetch were observed for the chromium masks. The chromium mask is removed after the cavities are defined into the Pyrex wafer and, in step 4, is a new resist mask (AZ nLOF 2020) patterned and aligned to the cavities followed by a metal deposition step. A 20 nm chromium layer is first deposited as an adhesive layer (not shown on figure) followed by a gold deposition. The height of the gap is adjusted in this step to match the desired specification on the pull-in voltage. The wafer is, in step 5, submerged into a bath of remover 1165 from Microposit™. Usually 45 min and applied ultrasound are required to lift-off the entire resist mask. The processed Pyrex wafer and a SOI wafer are cleaned in Piranha solution and anodically bonded immediately after, in step 6. Good and reliable bonding results have been observed for a three step voltage ramp (300V/600V/800V) at 350 °C. The handle and BOX are, in step 7, etched away using KOH and BHF, respectively. Five hours are approximately required to remove the 350 μm silicon handle. The long etching process demands a high bonding quality, otherwise does the etch simply peel of the entire device layer. An image of a processed wafer at step 7 is shown in Fig. 4.12, where only minor defects/holes are observed in the device layer. The remaining part of the wafer is structural intact at this point, which clearly demonstrates an acceptable array yield. Step 8 is a metal deposition step, where 20 nm titanium is deposited as an adhesive (not shown) followed by 400 nm aluminum deposition. The final step 9 provides access to the bottom electrode and separates of the top electrode, and is initiated by a lithography process using a AZ 5214E resist followed by two etch processes. The aluminum is etched in solution of H<sub>2</sub>O:H<sub>3</sub>PO<sub>4</sub> and the silicon is subsequently etched in a dry etch process.

### 4.3.1 Characterization

The anodic bonding process has from a fabrication point of view proven to be utterly suitable for row-column CMUT fabrication. The array yield for row-columns have been observed on the order of 95 % by visually inspection of the wafer in Fig. 4.12. However, the electrical properties CMUTs fabri-

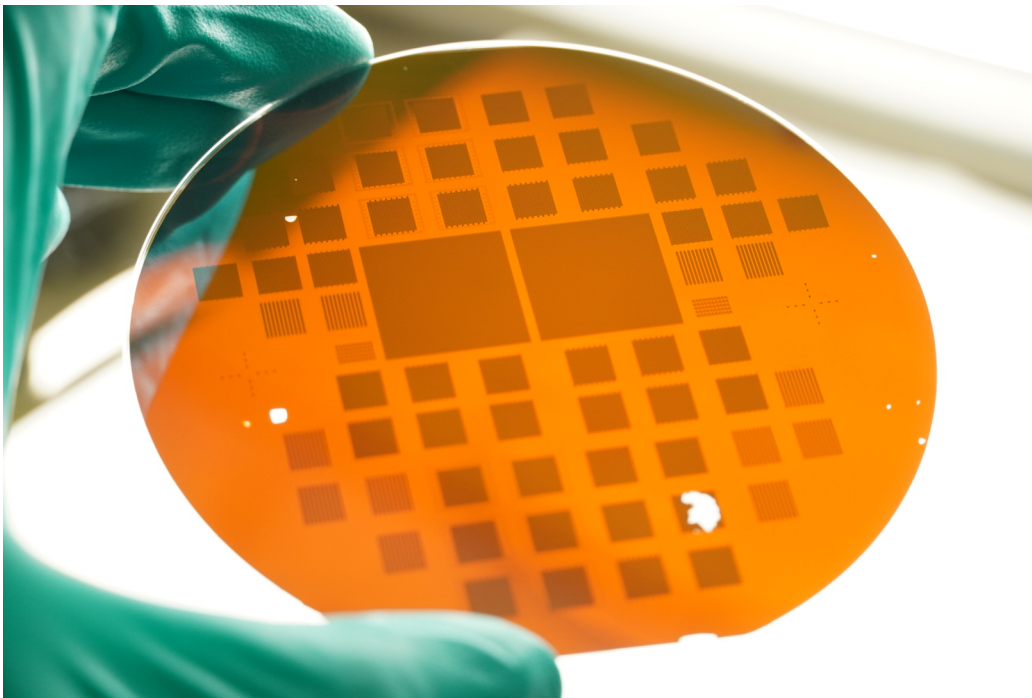


**Figure 4.12:** Image of anodically bonded RCA CMUT arrays. The image is captured right after removal of the handle and BOX layer, corresponding to step 7 in Fig. 4.11. The used mask set consists of two large  $190 \times 190$  RCA array with a  $\lambda/2$  pitch constrain, 48 smaller RCA arrays with channel a count of  $16 \times 16$ , and finally some linear test structures.

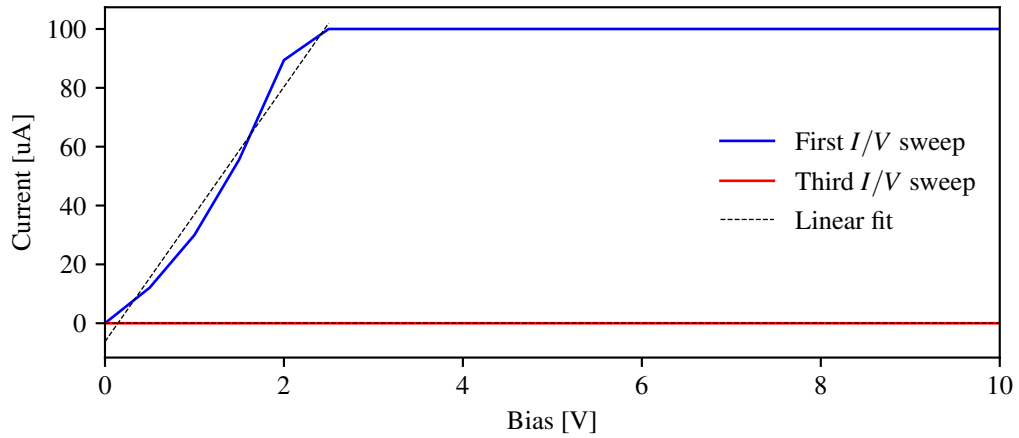


**Figure 4.13:** IV measurements of the anodically bonded CMUTs. The first IV measurement reaches the compliance value of  $100\ \mu\text{A}$  after an applied bias of approximately  $2.5\ \text{V}$ , whereas, the third IV measurement shows excellent electrical insulation.

cated have not been sufficient for an acceptable CMUT performance. Short circuiting has been observed for a large number of elements between the top and bottom electrode. The causality of this short circuit phenomenon is not fully understood. Redeposited pieces of metal that electrically connects the top and bottom electrode is the current hypothesis. Small pieces of gold could be redeposited during the lift-off process where the bottom electrodes are defined. Neither images from an optical microscope or Scanning Electron Microscope (SEM) have been able to confirm this hypothesis. However, Current-Voltage (IV) measurements performed by a B1500A semiconductor device analyzer support the hypothesis. The observed short circuit can be repealed by repeating measurements with an increased bias voltage. The material that causes the short circuit is believed to evaporate due to a high amount of deposited power during IV measurements. This phenomenon can be seen in Fig. 4.13 where the first and the third IV measurement are shown. The first sweep reaches the compliance value of  $100\ \mu\text{A}$  after an applied bias of approximately  $2.5\ \text{V}$ , whereas electrical insulation is observed at the third IV sweep. The corresponding resistance is estimated by a linear fit and increases from  $2.3\ \text{k}\Omega$  to  $2.4\ \text{T}\Omega$  between the first and third bias sweep. The resistance changes nine orders of magnitude during the first and third bias sweep, which is believed to be caused by evaporation of the short circuiting material.

A new batch of anodically bonded CMUTs was fabricated to solve the

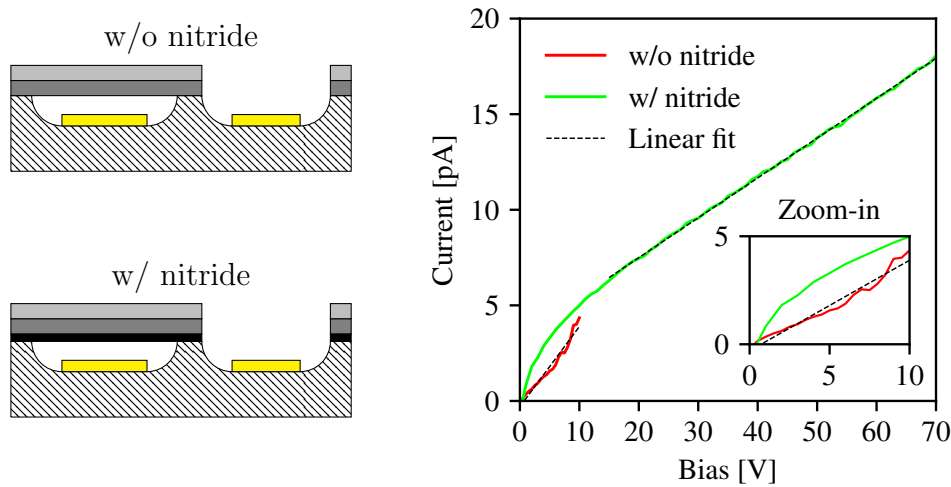


**Figure 4.14:** IV measurements of fabricated CMUTs with and without a nitride film at the bonding interface. Both designs have insulating properties with a resistance in the  $T\Omega$  regime.

short circuit issue. The only adjustment in the new design is an additional nitride film at the bonding interface. The nitride serves two purposes, it provides additional insulation and allows the CMUT to go into the pull-in state without a destructive short circuit. The IV measurements of an equivalent CMUT is shown in Fig. 4.14 together with the previous IV measurement (third sweep in Fig. 4.13). The resistance is estimated to be  $4.8 T\Omega$  for new batch of CMUTs with nitride, and the insulating properties are comparable to the third IV sweep for the CMUTs without nitride. The implementation of the nitride layer has proven to significantly reduce the short circuiting issue, but more process development is still required. The CMUT parameters such as pull-in voltage, resonance frequency, and bandwidth among other are yet to be measured for these CMUTs. However, a linear anodic bonded CMUT array, without the nitride layer, has been acoustically characterized for different applied DC biases. The acoustic measurements were conducted in a water tank. The pressure was measured by an ONDA HGL-0400 hydrophone positioned 1 cm from the CMUT surface. Polydimethylsiloxane (PDMS) has, prior to the acoustic measurements, been coated on top of the arrays to ensure electrical isolation of the elements during immersed operation. The frequency response has been determined by sinusoidal pulse train with a varying excitation frequency to map out the transfer function. Multiple measurements have been acquired for each frequency, and the the average value of the transfer function with one standard deviation is plotted in Fig. 4.15. The pressure increases with the magnitude of DC bias as ex-



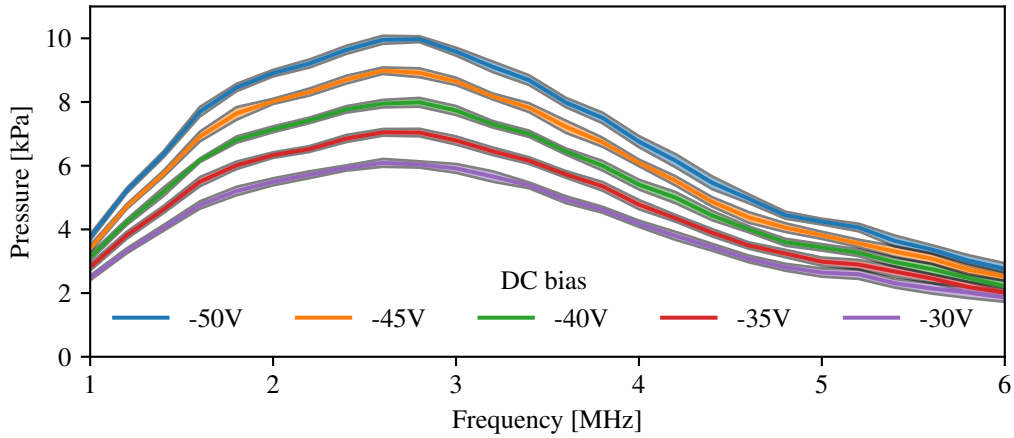


**Figure 4.15:** The transfer function of an anodically bonded CMUT w/o nitride at five different DC biases. The pressure increases as the magnitude of the bias increases, as expected. Multiple measurements have been conducted and the shown data is the mean with one standard deviation.

pected. The center frequency is unaffected by increased bias, which indicates CMUT is operated at very low voltages with respect to the pull-in voltage. The spring softening effect is simply too small to be detected with the frequency resolution used for these measurements. An increased bias would be required to resolve the spring softening effect and determine the pull-in voltage, unfortunately, the CMUT malfunctioned when the bias was changed to  $-55$  V.

The anodic bonding process has many desired features for row-column arrays. The fabrication process has proven to be structural stable across an entire 4" wafer, more process development is still required to solve the short circuit issue. However, the implementation of the additional nitride film seems very promising.

## 4.4 Combined anodic and fusion bonding

Fabrication of large RCA arrays has proven to be difficult when SOI wafers are used as the substrate wafer. Rupture of the plate/device layer has been observed for RCA arrays especially during removal of the handle layer. These effects are not observed to same degree for linear arrays, where a standard silicon wafer can be used as the substrate. In addition, the area of RCA arrays are larger than the linear arrays, which complicates the fabrication process due to a higher particle sensitivity. The BCB and anodic bonding

methods are both attractive solutions as a row-column fabrication platform, both facilitate the possibility of fabricating on insulating substrates, both are rapid fabrication processes, both processes have showed high structural yield, even close to 100%. But, both processes have electrical weaknesses that are not observed for the LOCOS process. On the other hand, the row-column array yield for the LOCOS process is critically low. One possible way of increasing the array yield for the LOCOS process would be to decrease the area, but, the beneficial properties of row-column arrays become progressively better as the size and the channel count increase as explained in chapter 3.

A new fabrication process has been developed to over these challenges. This process combines the best properties from LOCOS and the anodic bonding and do not require a SOI wafer as substrate.

#### 4.4.1 Rodent one

Development of a 8 MHz RCA CMUT transducer with 188+188 channels and  $\lambda/2$  pitch constrain has begun during this thesis. This transducer is called rodent one and abbreviated TR1 henceforth. TR1 will be approved for rat studies and is designed for 3D super resolution applications, an imaging concept that originates from fluorescence microscopy. Noticeably, the development of the super resolution principle was awarded the Nobel prize in chemistry back in 2014 [79]. The super resolution principle relies on imaging strongly illuminating objects smaller than the diffraction limit. Such objects cannot per definition be resolved by conventional methods due to its small size. Sub-wavelength objects will be blurred and highly distorted by the point spread function of the imaging system. The spatial position of the sub-wavelength objects can be estimated by center of mass calculations. Changes in center of mass can accurately be measured at length scales much smaller than the diffraction limit, which is the underlying principle of super resolution imaging. The principle of super resolution can be adapted to ultrasound imaging by injecting micro bubbles into the blood flow. The size of the bubbles are on the order of a few microns, thus, typically two orders of magnitude smaller than the diffraction limit of a common medical ultrasound transducer. High amplitude signals are generated from the bubbles due to the vastly different acoustic impedance compared to the surrounding blood and tissue. Super resolved ultrasound images have already been extensively demonstrated using 1D transducers [80]. However, micro bubbles will not in vivo be confined in a two dimensional plane, but follow the directions of the blood flow inside vessels. The idea behind TR1 is to overcome the issue of 2D confinement and do ultrasound super resolution imaging in 3D. The design specifications of TR1 are listed in Tab. 4.2, and are inspired by the

**Table 4.2:** TR1 specifications

<i>CMUT parameter</i>	
Plate thickness	3 $\mu\text{m}$
Side length of cell	50 $\mu\text{m}$
Cavity height	180 nm
Pull-in voltage	220 V
<i>Array parameters</i>	
Elements	188+188
Integrated apodization (apo)	yes
Transducer surface area w/o apo	17.9 $\times$ 17.9 $\text{cm}^2$
Transducer surface area w/ apo	2.1 $\times$ 2.1 $\text{cm}^2$
Pitch	95 $\mu\text{m}$
Center frequency	8 MHz

lessons learned from the two 92+92 RCA probes from section 4.1. The developed fabrication process for TR1 combines the best properties from the LOCOS process and the anodic bonding process. The electrical properties of the LOCOS process has been thoroughly tested within our group, whereas further development is still necessary for the anodic bonding process. The array yield has been observed low for the LOCOS based RCA CMUT arrays, and very high for the anodic bonding process. The combination of the two processes could be a promising way of fabrication RCA CMUT arrays.

The developed fabrication process is very similar to the LOCOS process. The process is a four mask process, and the masks are identical to those used in the LOCOS process. A schematic process flow is shown in Fig. 4.16. A thermally insulation oxide is grown in step 1 and a LPCVD nitride film is deposited and patterned on top of the oxide. The substrate material is a standard highly doped silicon wafer and not a SOI wafer. The bottom electrodes are electrically isolated in the LOCOS process by etching trenches into the device layer of the SOI substrate until the BOX insulates the bottom electrodes. In this process a (3  $\mu\text{m}\times$ 100  $\mu\text{m}$ ) trench is etched into the silicon and trenches are etched using a specialized high aspect ratio dry etch, abbreviated DREM (Deposit, Remove, Etch, Mask). The DREM etch is designed to have an extreme selectivity towards photo resist [81] and at the same time preserve the geometry throughout trenches. Cross sectional SEM images of the DREM trench is shown in Fig. 4.17.

These SEM images confirm the actual geometry is in agreement with intended design. A uniform width is observed throughout trenches, and only

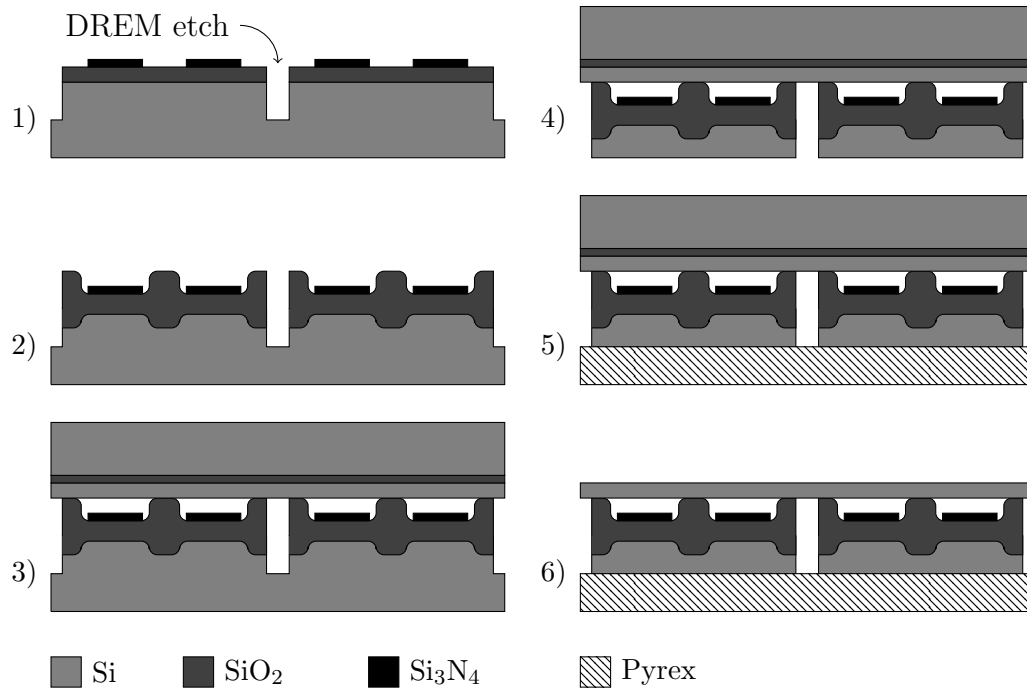


**Figure 4.16:** Process flow of the TR1 transducer. The first part of the process is similar to the LOCOS process presented in section 4.1. Step 1: An isolation oxide and a LPCVD nitride are grown and deposited, respectively. A DREM etch is afterwards used to define 100  $\mu\text{m}$  deep trenches into the silicon, that later will be used to separate the bottom electrodes. Step 2: A thermal oxidation step that defines the cavities utilizing the LOCOS process. Step 3: Fusion bond between the processed substrate and a SOI wafer. Step 4: The substrate wafer is dry etched until 100  $\mu\text{m}$  is left and the separation pattern appears. Step 5: The backside of the wafer is polished in a CMP process and afterwards anodically bonded to a borosilicate wafer. Step 6: The handle and BOX layer are etched away and the remaining steps are identical to step 7 to 10 in Fig. 4.2. Figure not to scale.

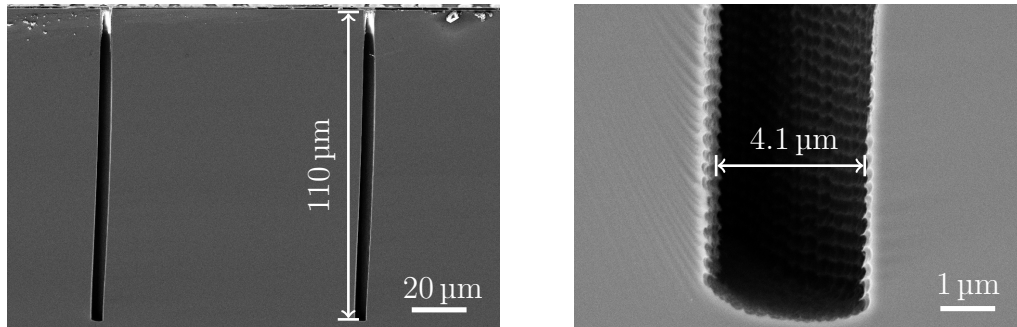


**Figure 4.17:** Cross sectional SEM images showing the DREM trench etch. The SEM image to the left shows the cross section of an entire element and the right image shows a zoom-in at the bottom of the DREM trench.

a slight broadening effect is observed. The mask opening at the surface is designed is  $3\ \mu\text{m}$  wide and the width at bottom of a  $110\ \mu\text{m}$  deep trench is measured to  $4.1\ \mu\text{m}$ . The CMUT cavities are defined after the DREM etch, in step 2, using a thermal oxidation process, where the principle of LOCOS are utilized. The CMUT cavities are subsequently sealed, in step 3, by fusion bonding a SOI wafer to the processed substrate. In step 4, the bottom electrodes are separated by removing the substrate silicon in a dry etch until the point where the pattern of the DREM etched bottom electrodes becomes exposed. The top SOI wafer is used to structurally stabilize the wafer stack during the removal of the original silicon substrate. The bottom electrodes are electrically insulated from one another at this stage, and are accessible from the backside of the wafer, which is an attractive property since it enables connection to the element using a flip chip bonding technology. This process is designed for wire bonding, hence, all channels are still connected from the front side. The back side is anodically bonded to a Pyrex wafer in step 5. The Pyrex keeps the bottom electrodes electrically isolated and provides mechanical stability during removal of the handle and BOX. A Chemical Mechanical Polishing (CMP) process is used to lower the surface roughness of the backside prior to the anodic bond. The handle is subsequently, in step 6, etched away using dry etch process. Clamping issues in the chamber of the dry etch equipment have been experienced due to the insulating Pyrex substrate. Depositing  $100\ \text{nm}$  poly-silicon on the back side of Pyrex, using a Plasma Enhanced Chemical Vapour Deposition (PECVD) process, solves this problem. The remaining BOX oxide is then removed in BHF. The remaining steps of this process is identical to the last four steps of LOCOS process flow (step 7-10 in Fig. 4.2).

The combined LOCOS and anodic bond process is still being developed. Two wafers have at this point been fabricated using the developed process. Both linear and row-column arrays were included in the mask layout, and the linear arrays were successfully fabricated, while plate rupture caused fully destroyed the row-column arrays. These observations are similar to the yield problems in the LOCOS process, and the structural stability might be completely unchanged for this purposed process. However, a larger sample size will be required for a conclusively determination. In addition, removal of the silicon substrate wafer between step 3 and 4 in Fig. 4.16 has shown to be challenging due to a non-uniform etch rate across the wafer. The non-uniformity creates a convex profile that complicates the following anodic bonding process.

#### 4.4.2 Mask layout

The center frequency of a CMUT is dominantly determined by the plate thickness, plate material, size of the CMUT cell, and the built-in stress. The plate thickness for TR1 was determined to be  $3\ \mu\text{m}$ , since, the previously fabricated CMUTs using a  $3\ \mu\text{m}$  plate, have shown a satisfying performance. The built-in stress is assumed small in this design, and the plate material is silicon. The size of the CMUT cell is therefore only degree of freedom. The size of the CMUT cell combined with the  $\lambda/2$  pitch constraint introduce a challenge, since the CMUT cells cannot be closely packed in a grid. The side length of a square CMUT cell has to be  $50\ \mu\text{m}$  to match the specified center frequency while the pitch is  $95\ \mu\text{m}$ , which only allows a single CMUT cell per sub-element as seen in Fig 4.18 a). However, the number of CMUT cells can be doubled by rotating the cells  $45^\circ$  and introducing an interwoven element structure as shown in Fig. 4.18 b).

The interwoven design increases the transmit pressure by a factor of 2 and reduces the parasitic capacitance. Additional details about how the interwoven element structure impacts on the ultrasound image can be found in paper B.

#### 4.4.3 Characterization

The fabricated linear arrays have been electrically characterized using both Capacitance-Voltage (CV) and impedance measurements. The electrostatic force has a square dependency on the applied bias which translates into a square dependency of the displacement. The capacitance versus voltage characteristics of a CMUT must therefore follow a parabola for small voltages relative to the pull-in voltage. A Taylor expansion of the capacitance,  $C$ ,

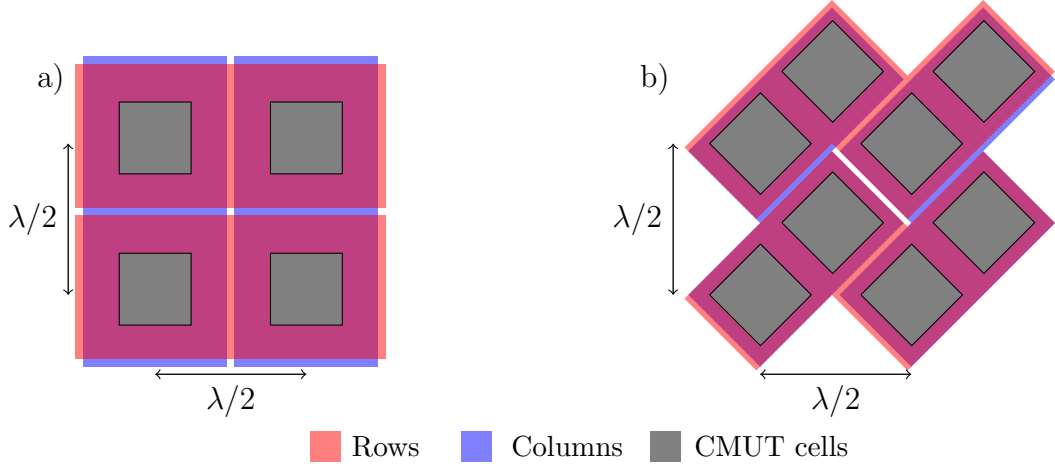


**Figure 4.18:** Sketch of two different CMUT cell configurations for CMUT cell with a side length of the side length  $50 \mu\text{m}$  and a element pitch of  $95 \mu\text{m}$ . a) straight rows and columns where a single CMUT cell can fit into each sub element. b) Zig-Zag pattern that allows two CMUT cell into each sub element, and thereby increases the active area with a factor of 2.

yields

$$C(x(U^2)) \approx C(0) + \underbrace{C'(0) \frac{dx}{dU^2}}_{\text{Constant}} \Big|_{U=0} U^2 \quad \text{for } U \ll U_{pi}. \quad (4.2)$$

where  $x$  is the displacement of the plate and  $U$  is the applied bias. A parabolic CV relationship is predicted for small voltages and the theory agrees with measurements shown in Fig. 4.19. The capacitance has been measured using a B1500A semiconductor device analyzer at 100 kHz. An additional off-set parameter that shifts the vertex of the parabola is added to the fitting function given by

$$C(V) = C_0 [1 + \alpha (U - U_{\text{offset}})^2]. \quad (4.3)$$

The vertex shift can be physically explained by the Schottky barrier between the metal contact pad and the doped silicon electrode, an extensive analysis of this phenomenon can be found [82]. Work function differences between metal and silicon introduce a built-in electric field, that enhances the electric field in one polarity and retards in the opposite polarity. The applied bias voltage is swept from  $-100 \text{ V}$  to  $100 \text{ V}$  and back again to  $-100 \text{ V}$  to verify the absence of any hysteretic Behavior. The voltage sweep back and forth

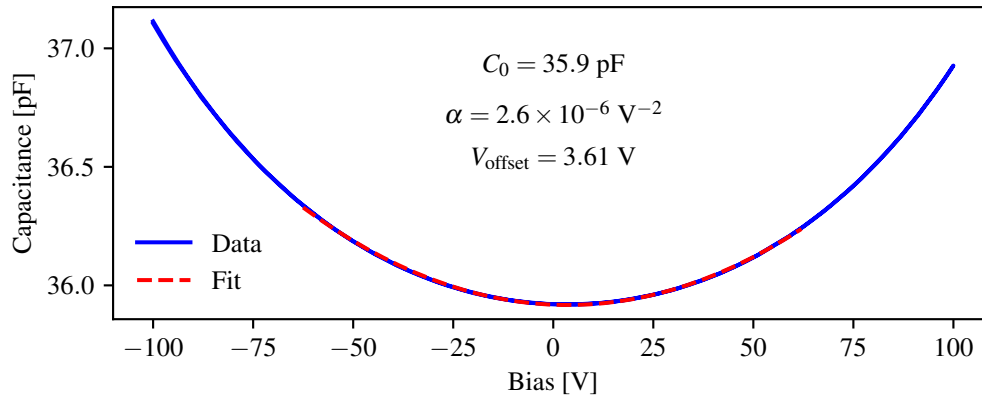


**Figure 4.19:** Capacitance versus voltage measurement of CMUT fabricated with a PSOI wafer. A parabolic function has been fitted for small bias voltages to verify the expected square dependence of the voltage. The pull-in voltage of this array is 160 V.

are indistinguishable from each other and implies the absence of undesired charging effects.

The resonance frequency in air has been determined by the impedance measurements shown in Fig. 4.20. The expected bias dependency of the resonance frequency is observed and shifted from 6.5 MHz to 5.0 MHz as the magnitude of the bias is increased from  $-65$  V to  $-85$  V. Notice the pull-in voltage of this element is approximately  $-90$  V. The impedance spectra are otherwise comparable with the results from the LOCOS process from section 4.1, however, the electromechanical coupling coefficient is lower and has been estimated to 3.74%, 3.83%, 3.92%, 4.41%, and 7.83%. The reason why the coupling is reduced relative to the LOCOS process is not fully understood and should be studied further in future work.

The electrical characterization of the combined LOCOS and anodic bonding process substantiates the potential of this fabrication method. The expected CV characteristics is observed and the absence of hysteresis during voltage sweeps implies electrical stability. The ability to operate the CMUT around the pull-in voltage has also been demonstrated for this new process, though, only for linear arrays.



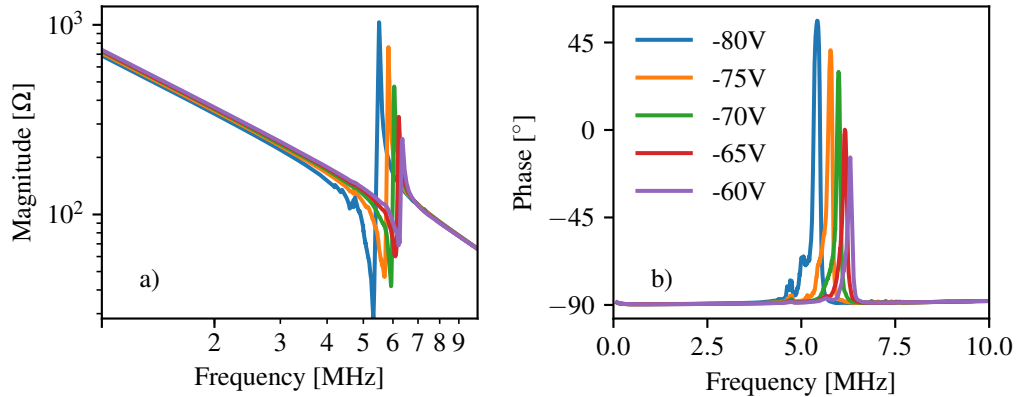


**Figure 4.20:** Impedance measurements of the CMUTs fabricated using the combined LOCOS and anodic bonding process. The measurements are conducted by a linear element operated in air. The absolute magnitude of the impedance is plotted in a double log plot in a), where a distinct resonance and anti resonance are observed between 5.0 MHz and 6.5 MHz. The capacitive properties are confirmed the power law dependency for off-resonance frequencies. The phase of the impedance measurements is plotted in b). The CMUT used for impedance has a pull-in voltage of  $-90$  V.

## 4.5 Poly-Silicon-On-Insulator wafer

The device layer of a SOI wafer constitutes the plate in all the investigated CMUT designs. However, purchasing 4" SOI wafers for CMUT research and development has in the past couple of years been difficult, in the sense that suppliers demand large minimum wafer quantities and have long a delivery time on the order of months. Both parameters are not suited university level research and development. The reason for this is twofold, the first reason is 4" SOI wafers are being phased out by some of the large SOI wafer manufacturers. Secondly, the wafer fabrication industry is currently in a high conjecture, hence, the demand is larger than the supply, which increases the delivery time.

Multiple options are available to overcome the problem with SOI wafers. One option is to simply prolong the development process and wait months for the customized SOI wafers. Another approach is to purchase SOI wafers from a stock list which typically can be delivered within a week. It has the disadvantage of excluding the possibility of determining all the relevant SOI parameters, and such wafers can often be sub optimal for a given CMUT fabrication.

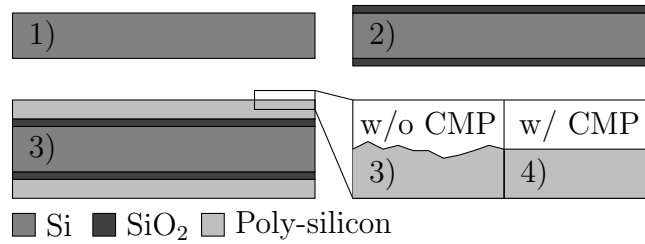


**Figure 4.21:** Fabrication process of PSOI wafers. 1) A standard silicon wafer is chemically cleaned prior to the furnace processes. 2) A thermal oxide is grown. 3) A boron rich poly-silicon is deposited in a LPCVD process. 4) The poly-silicon layer is polished (CMP) to reduce surface roughness. Figure is not to scale.

A third way, to overcome the issues associated with getting SOI wafers, is to use a PSOI wafer that has been developed in this work. The structure of a PSOI wafer is essentially identical to a conventional SOI wafer, with the only exception being the device layer material. A LPCVD deposited poly-silicon constitutes the device layer of a PSOI wafer instead of single crystalline silicon used for conventional SOI wafers. PSOI wafers can be fabricated in three days and can therefore significantly reduce the development time of CMUT fabrication and development. The fabrication of PSOI wafers consists of four steps as shown in Fig. 4.21. The first step is to choose a silicon wafer with the desired specifications for the handle layer. Next, grown an oxide, in step 2, and on top of oxide is, in step 3, a boron doped poly-silicon film deposited using a LPCVD process. The poly-silicon could also be doped with phosphor, but the deposition rate is substantially lower compared to boron. In step 4, the surface of the poly-silicon is polished in a CMP process to lower the surface roughness. The developed PSOI wafers are designed to have a 400 nm BOX layer and a device layer thickness of approximately 3.0  $\mu\text{m}$ . The final poly-silicon thickness of a fabricated PSOI has been measured across two wafers using multi-angle reflectometry. The resulting thickness maps are shown in Fig. 4.22. The measured thickness is approximately 400 nm lower than expected. The LPCVD system at our clean room facility is only allowed to deposit poly-silicon during working hours due to the extremely poisonous gases involved in the LPCVD process. The thickness of the fabricated poly-silicon layer is the result of an entire day of deposition, two or more days are needed if thicker layers are required.

The surface roughness of the deposited LPCVD poly-silicon has been measured using confocal microscopy before and after the CMP process. The Root mean square (RMS) of the measured surface topology is 6.98 nm prior to the CMP process and 0.47 nm after the CMP process. The acquired images from

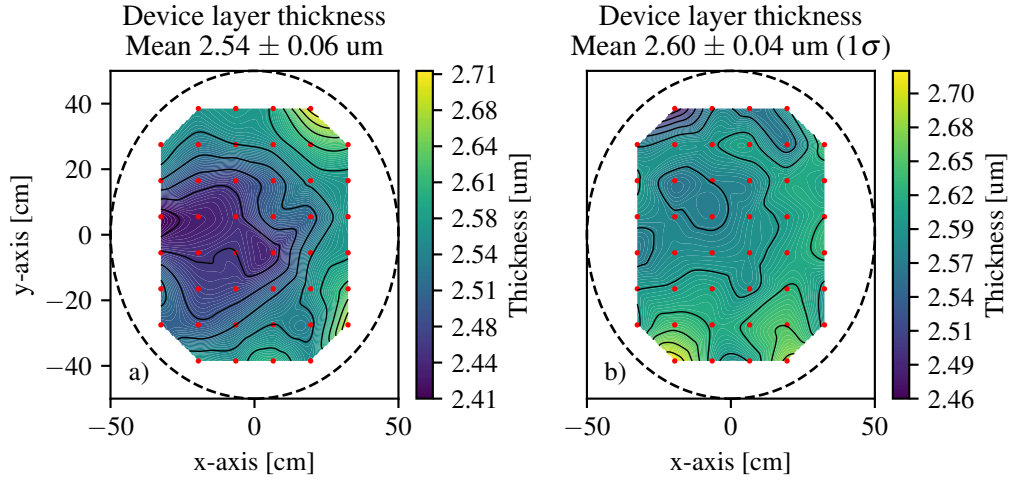


**Figure 4.22:** Multiple thickness measurements of the device layer thickness across two PSOI wafers. The measurements have been carried out by multi-angle reflectometry. a) The PSOI closest to the furnace opening. b) The PSOI furthest away from the furnace opening. The 44 red dots in each plot are the measured data point, the black dashed lines indicates the circumference of the wafers.

the confocal microscopy can be found in Fig. 4.23.

The surface roughness measurements are calculated based on data from an area of approximately  $100 \times 100 \mu\text{m}^2$ . The surface topology prior to the CMP process ranges between  $-30 \text{ nm}$  and  $30 \text{ nm}$  without any clear tendency or pattern, see Fig. 4.23 a). The range of the polished wafer is reduced by more than factor of 10, and structures or patterns seem to appear. It is believed to be the surface of the microscope objective and not necessarily the surface of the PSOI wafer, AFM measurements will be necessary if higher precision is needed. The CMP process is an absolute requirement when PSOI wafers are used for fusion bonded CMUTs, but is not a strict requirement for anodic bonded CMUTs. Though, the bonding quality has been observed greatly improved when the surface has been polished.

The mechanical and electrical properties of LPCVD poly-silicon are influenced by multiple parameters, including deposition temperature, deposition time, gas composition, tube pressure, flow conditions among other. The deposition rate of the LPCVD poly-silicon should be high enough to produce a  $5 \mu\text{m}$  poly-silicon film within a reasonable time, while the resistivity and built-in stress are low. The stress should preferably be tensile since it will prohibit buckling effects in the final CMUT structure. A criterion for an acceptable resistivity can be found in paper C.

Four point probe measurements of the device layers have been performed

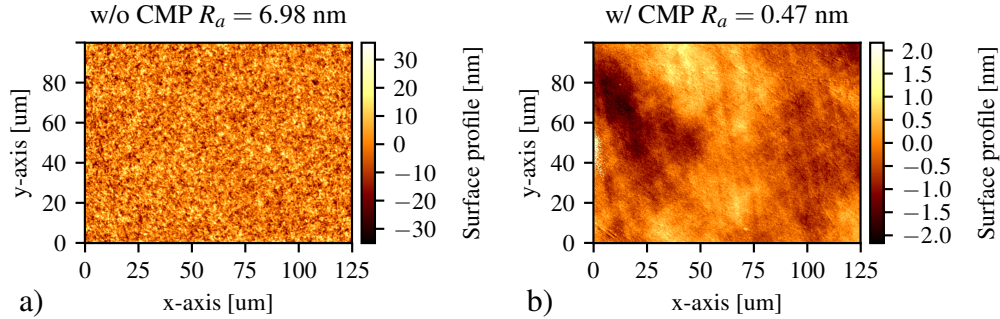


**Figure 4.23:** Surface topology maps of the surface of a PSOI wafer before and after CMP. The topology before and after CMP is shown in a) and b), respectively. Notice the range of the scale bar differs with more than a factor of 10.

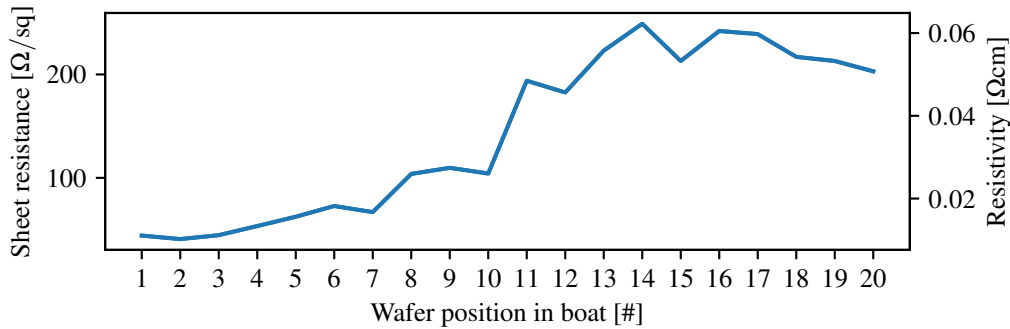


**Figure 4.24:** Sheet resistance and resistivity of the PSOI device layer as function position in the boat. Wafer position 1 is closest to the opening of the furnace tube.

to characterize the resistivity. The measurements were conducted on 19 fabricated PSOI wafers and the result is shown in Fig. 4.24. The largest measured resistivity is  $0.062 \Omega \text{ cm}$ , and the mean and standard deviation are  $0.036 \Omega \text{ cm} \pm 0.019 \Omega \text{ cm}$ , which is sufficient for the CMUT plate in many applications.

The material properties of the poly-silicon are determined by a large parameter space that varies between different LPCVD furnaces. For a reliable and reproducible production of PSOI wafers optimization of the LPCVD process is required. A starting point for this optimization is given in Fig. 4.25 where published deposition rates, resistivities, and stresses from multiple papers are plotted as function of deposition temperature [83–88]. The depo-

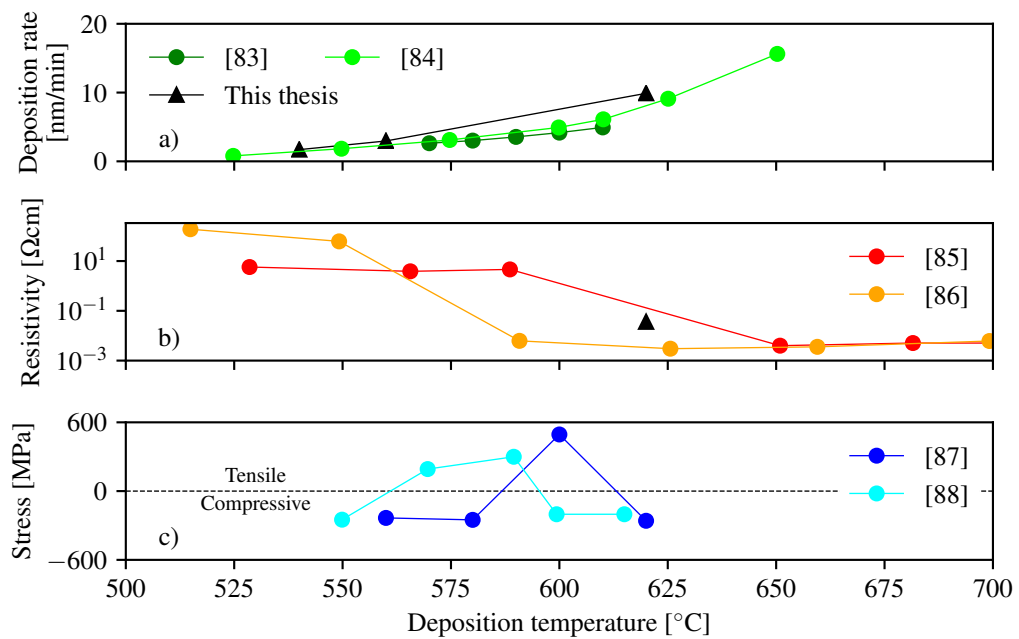


**Figure 4.25:** The deposition rate, resistivity, and stress as function of deposition temperature. The circular markers are data from the literature and represents either boron doped or undoped LPCVD poly-silicon and triangular markers indicate measurements of LPCVD boron doped poly-silicon from this thesis.

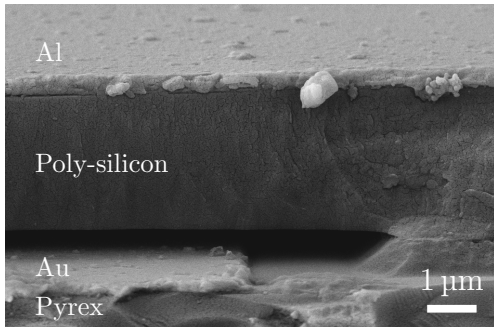


**Figure 4.26:** Cross sectional SEM image of an anodic bonded CMUT fabricated using a PSOI wafer.

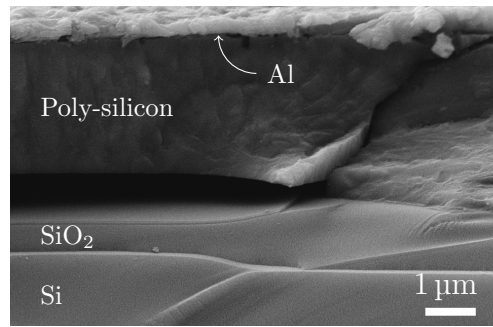


**Figure 4.27:** Cross sectional SEM image of a fusion bonded CMUT fabricated using a PSOI wafer.

sition rates are seen, in Fig. 4.25 a), to increase as function of the deposition temperature, whereas a reduction in the resistivity is observed in Fig. 3 b) (notice the log y-scale). Hence, rapid fabrication time and low resistivity are gained by increasing deposition temperature. However, the temperature dependency of the stress is not as unambiguous as the deposition rate and resistivity, and extrapolation is therefore difficult.

The fabricated PSOI wafers have been used for all the fabricated anodic bonded CMUTs and all the CMUTs from the TR1 process described in section 4.3 and 4.4, respectively. Cross sectional SEM images of both anodically and fusion bonded CMUTs can be found in Fig. 4.26 and 4.27, respectively. The CMUTs are tilted  $10^\circ$  in both images to improve the visualization of the CMUT structures, and a thin layer of gold is sputtered to prevent dielectric charging of the insulating layer. Both CMUTs are diced using an automatic dicing saw, and the fact that the poly-silicon plate is intact after dicing indicates a strong bond. The poly-silicon plates are in both images bonded to the post region (right side of the images). Notice, the structure of silicon substrate in the TR1 process (right image) is substantially different from the poly-crystalline structure of the plate. Hence, CMUT fabrication using PSOI wafers are applicable for both fusion bonded and anodic bonded devices, and PSOI wafers might even provide improved bonding conditions for anodic bonded devices. The front and the back side of a SOI wafer will be electrically insulated from one another. This is a direct consequence of the fabrication method of SOI wafers [89] and this is also a desired feature in many applications. However, the insulation is a disadvantage during an anodic bonding process, since the current has to run through the BOX layer with poor conducting properties. The anodic bonding temperature, of

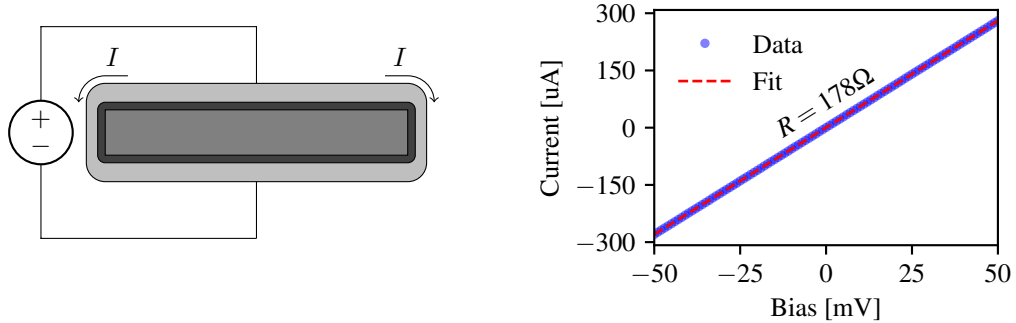


**Figure 4.28:** IV characterization between the front and back of a PSOI wafer, where a resistance of  $178\ \Omega$  is estimated by a linear fit. The sketch to the left illustrates how the current flows around the edges of a PSOI due to a conformal deposited layer of poly-silicon. The results from the IV measurement are shown to the right, where a linear relationship is observed.

approximately  $350\ ^\circ\text{C}$ , increases the conductivity of  $\text{SiO}_2$  multiple orders of magnitude [90], and is essential for the success of the anodic bonding processes. However, the introduction of an additional insulator impedes the bonding current during anodic bonding, which is inevitable when SOI wafers are involved due to the BOX layer. The BOX layer of an SOI wafer increases the electrical resistance during an anodic bonding process, and prohibits the accumulation of charges in the generated depletion region.

The device layer of a PSOI encapsulates the entire wafer due to a conformal deposition process, and thereby facilitates a short circuit between the front and back side. This is confirmed by IV measurements between the front and the back side of a PSOI wafer, and the result is shown in Fig. 4.28 together with an illustrative sketch of how the measurement was conducted. An ohmic relationship is observed in the IV measurement and a resistance of  $178\ \Omega$  is estimated by a linear fit. Hence, the front and back side of PSOI wafers are, opposite to SOI wafers, not electrically insulated from each other, and larger bonding currents are therefore expected.

The results of the PSOI wafer are summarized in paper D.

## 4.6 Chapter summary

Four different row-column fabrication methods were investigated in this chapter, and all of the demonstrated methods possessed desirable properties for CMUT based row-column fabrication. The most relevant row-column prop-

**Table 4.3:** Row-column CMUT fabrication summery.

	LOCOS	BCB	Anodic	LOCOS + Anodic
Masks	4	3	3	4
Breakdown voltage in post region	0.74 V/nm	0.08 V/nm	0.92 V/nm <sup>a</sup>	0.74 V/nm
Array yield	Low	High	High	Insufficient statistics
Required surface roughness	< 1 nm	High	< 50 nm	< 1 nm
Substrate coupling factor	1.6 - 2.5	1.1	1.0 <sup>b</sup>	Not known
Fabrication time	Weeks	Days	Days	Weeks
Highest process temp.	≈ 1000 °C	≈ 250 °C	≈ 350 °C	≈ 1000 °C
Clean room limitations <sup>c</sup>	None	BCB	Pyrex	Pyrex
Other	-	-	Short circuit <sup>d</sup>	-

erties are summarized in Table 4.3, where a green and red color coding have been used to emphasize the desired and undesired properties, respectively. Notice, the individual parameters are not equally important.

A low array yield of row-column arrays was observed for the LOCOS based CMUTs, but excellent CMUT performance was observed for the few successfully fabricated row-column arrays. Many desirable row-column properties were observed for the BCB fabrication process, but the dielectric strength of the BCB was simply not suited for CMUTs operated close to the pull-in condition. The Anodic bonded and BCB processes share many of desired row-

<sup>a</sup>Dielectric strength found in the literature [91].

<sup>b</sup>Substrate coupling factor calculated from [46].

<sup>c</sup>Contamination rules at the DTU-nanolab clean room facilities.

<sup>d</sup>Described in details in section 4.3.



column properties including structured bottom electrodes, excellent bonding properties, low process temperatures among other. But, the dielectric strength of Pyrex, used in the anodic bonding process, was in the literature found to be  $0.92 \text{ V/nm}$  [91] and therefore more suited for high field applications. A problem with short circuiting between the top and the bottom electrode was observed for the anodic bonded CMUTs. This problem was addressed by introducing an insulating nitride film at the bonding interface. A second generation of anodic bonded CMUTs were designed and fabricated including the additional nitride layer. Preliminary IV measurements suggested the new design to be a feasible solution to the problem. The final presented CMUT fabrication combined the best properties from the LOCOS process and the anodic bonding process. This process was been developed to increase the array yield and reduce the substrate coupling factor relative to the LOCOS process. Linear arrays of this new process was electrically characterized and showed an expected CMUT performance without any indications of unwanted charging effects. The row-column performance of this new process is still unknown and additional process development is therefore necessary.

The concept of a PSOI wafer was introduced in the last part of the chapter as an alternative to conventional SOI wafers. The fabrication of multiple PSOI wafers were described and characterized, and the fabrication of two different CMUTs using PSOI wafers were demonstrated.

## CHAPTER 5

---

### CMUT characterization

---

This chapter investigates the acoustical properties of the CMUTs fabricated during this thesis. The chapter consists of two parts. The first part considers acoustic characterization of a single linear CMUT element. The analysis includes characterization of both the acoustic response from the CMUT and the overall experimental set-up. The transmit impulse response is calculated and bias dependency of the transmit pressure, center frequency, and bandwidth has been measured.

The second part of the chapter considers acoustic characterization of the fabricated 92+92 row-column probe. The pressure fields of rows and columns are measured, and the pressure field is observed to be attenuated long the columns. A detailed analysis of electrode resistance is developed and used to describe the attenuated pressure field for the columns. Volumetric row-column images of wire and cyst phantoms acquired by the developed 92+92 RCA CMUT probe are presented in the last part of the chapter.

### 5.1 Acoustic characterization

A characterization set-up for a single channel system has been developed during this work. The system is designed to perform an isolated acoustic analysis of CMUT, where the influence from the instruments and the electronics are minimized. This task can be approached either by calibration curves or by changing the hardware. The frequency response of the overall system distorts the applied AC signals, however, the distortion can be accounted for by

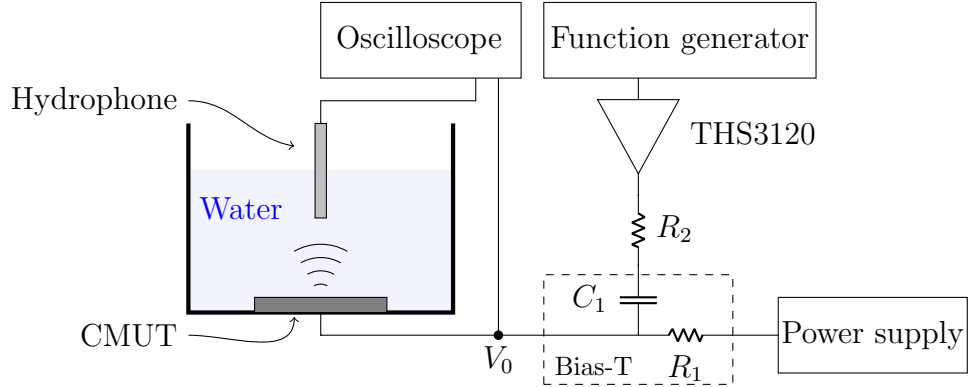


**Figure 5.1:** Sketch of the acoustic set-up. The bias-T consists of a capacitor,  $C_1$ , and a resistor,  $R_1$ , with the discrete values of 100 nF and 1 M $\Omega$ , respectively.  $V_0$  is the nodal point of interest in this analysis and represents the AC signal at CMUT electrode. THS3120 is an operational amplifier used to buffer the output of the function generator, and the resistor,  $R_2$ , is required to stabilize the buffered signal.

calibration curves. This approach assumes linearity and errors will therefore be introduced when non-linear CMUTs are investigated. The other approach is to design the electronics such that the frequency response is approximately constant in the frequency range of interest. This approach allows characterization of non-linear systems and will therefore be used in this analysis. The experimental set-up is sketched in Fig. 5.1, where the nodal point,  $V_0$ , will be the reference point during the analysis. This nodal point represents the actual AC signal at the CMUT electrode, and a completely flat frequency response would be expected for an ideal system without any distortions.

The pressure waves generated by the CMUT are measured by a HGL-0400 hydrophone from Onda. The hydrophone is positioned and aligned 4 cm above the transmitting CMUT element, and the measured signal is picked up by a 5442D oscilloscope from PicoScope using 12 bit resolution and a sampling frequency of 62.5 MHz. The CMUT has prior to the acoustic measurements been wire-bonded to a Printed Circuit Board (PCB) and afterwards covered with PDMS to ensure electrical isolation between elements during immersed operation. The signal at the nodal point  $V_0$  is also monitored by the PicoScope using 10X probes to reduce effects from of capacitive loading. The applied AC signals are generated by a TexTronix AFG31102 arbitrary function generator and the applied DC bias is provided by a Keithley 2490 1100V sourcemeter. To reduce the source/generator impedance of the measuring system, a wide-band, low noise, high-output drive THS3120 operational amplifier is used to buffer the output. The operational amplifier

is coupled as a non-inverting amplifier with a gain of 5 V/V. The magnitude of  $R_2$  is comparable to commercially available ultrasonic transmitters/drivers which typically have an output impedance of 7-15  $\Omega$ . The resistor,  $R_2$ , isolates the phase shift at high frequency caused by the capacitive load from the amplifier feedback path. Resistance values of 5  $\Omega$  and 10  $\Omega$  have been used for  $R_2$  in this analysis, all other parameters have been kept unchanged. Resistance lower than 5  $\Omega$  lead to instabilities in the feedback loop of the buffer amplifier.

A linear CMUT array from the combined LOCOS and anodic bonding fabrication process is used in this analysis. The side length of the CMUT cell in this array is 70  $\mu\text{m}$  and not 50  $\mu\text{m}$  as specified for the TR1 row-column arrays, hence, the center frequency and pull-in voltage are lower than the designed specifications.

Pulses of uniform white noise have been used to characterize the frequency response of both the system and the CMUT. The noise is generated synthetically in MatLab and the frequency response is therefore known to be flat for all frequency components (on average). However, the frequency dependency of the CMUT, the instruments, and electronics cause a distorted frequency spectrum. Measurements of a noise pulse and the average frequency content are shown in Fig. 5.2. The length of noise pulse is approximately 15  $\mu\text{s}$  and long noise pulses are desirable since the information stored in the noise signal scales with the length. The size of the water tank is the limiting factor for the length of the noise pulse. The water tank has to be large enough to ensure no reflections from boundaries. The colored part of the excitation signal showed in Fig. 5.2 a) indicates the part of the signal that is used to generate the frequency spectrum, notice the first and the last part of the pulse are omitted to reduce transient effects. The average Fourier spectrum of 100 generated noise pulses is shown in Fig. 5.2 b) for two different  $R_2$  values. The measured frequency response can be divided into three parts indicated by  $\alpha$ ,  $\beta$ , and  $\gamma$ . The  $\alpha$  part is a constant plateau for frequencies lower than 15 MHz. The  $\beta$  part is a region between 15 MHz and 25 MHz where a reduction in the Fourier amplitude is observed. Finally, the  $\gamma$  part is another constant plateau for high frequencies above 25 MHz. The observed response is modelled by an empirical model,  $U_f$ , given by

$$|U_f(f)| = \frac{a}{2} \cdot \operatorname{erfc}(b \cdot (f - f_0)) + c \quad (5.1)$$

where  $a$  and  $c$  are amplitude parameters,  $f_0$  defines the frequency at which the amplitude difference between  $a$  and  $c$  has dropped 50%, and  $b$  determines the width of the  $\beta$  part. The expression  $f_0 - 1/b$  is used as a measure for a cut-off frequency, and corresponds to the frequency at which the amplitude has

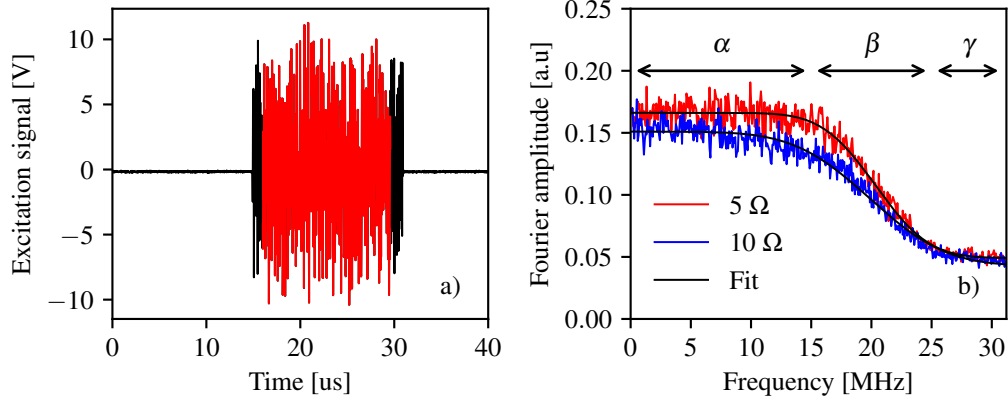


**Figure 5.2:** Analysis of the excitation signal measured at the nodal point,  $V_0$ . The noise excitation pulse is plotted in a). The data used to generate the Fourier spectrum is colored (red), and the corresponding Fourier spectrum is plotted in b) for two different values of  $R_2$ . The frequency data is an average of 100 Fourier spectra.

**Table 5.1:** Fitted parameters for two values of  $R_2$

<i>Fitted parameters</i>	$R_2 = 5\Omega$	$R_2 = 10\Omega$	$R_{2,5\Omega}/R_{2,10\Omega}$
$a$	0.12 a.u	0.11 a.u	9.1 %
$b$	0.20 $\text{MHz}^{-1}$	0.14 $\text{MHz}^{-1}$	42.8 %
$c$	0.049 a.u	0.043 a.u	14.0 %
$f_0$	20.3 MHz	19.9 MHz	6.3 %
$a + c$	0.17 a.u	0.15 a.u	13.3 %
$f_0 - 1/b$	15.3 MHz	12.6 MHz	21.4 %

dropped approximately 16%. The interpretation of  $c$  is the amplitude of the last plateau (part  $\gamma$ ), and the sum of  $a$  and  $c$  is the amplitude of first plateau (part  $\alpha$ ). An overview of the fitted parameter can be found in Table 5.1. All the fitted parameters are observed to increased for  $R_2 = 5\Omega$  when compared to  $R_2 = 10\Omega$ . An increase of 13.3% is observed for the amplitude of the  $\alpha$  plateau ( $a + c$ ), hence, the AC signal at the CMUT electrode has become larger. Additionally, an increase of 21.4% is observed for the cut-off frequency which implies a reduced suppression of high frequency components.

The stabilization resistor,  $R_2$ , perturbs the frequency response of the system and thereby also the acoustic performance of the CMUT, which can be observed in the transmit impulse response. The acoustic response and the

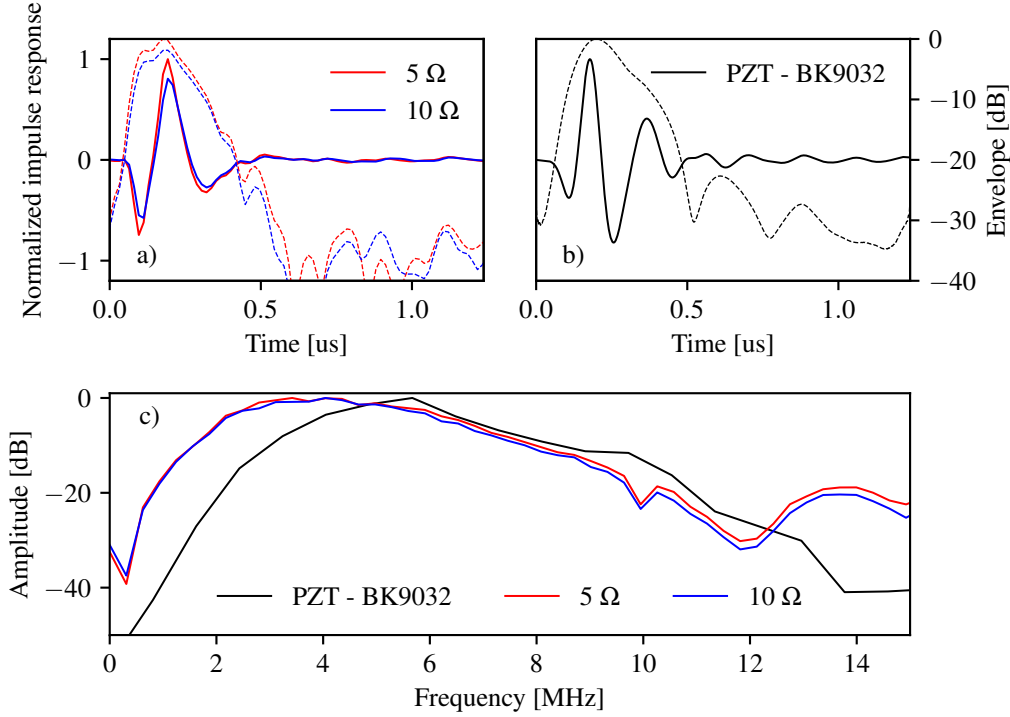


**Figure 5.3:** Normalized transmit impulse response of the developed CMUT and a commercial PZT. The results from the CMUT is shown in a) for two values of  $R_2$ . The transmit impulse response of a commercial BK9032 probe is shown in b). The solid lines are the impulse responses and is read on the left y-axis, and the dashed lines are the envelopes and is read on the right y-axis. The corresponding transfer functions are plotted in c). A DC bias of 90 V was used for the CMUT measurements corresponding to approximately  $U/U_{pi} = 85\%$ .

excitation signal have been deconvolved in order to calculate the transmit impulse response shown in Fig. 5.3 a).

The overall shape of the impulse response is similar in both cases, but, a 26.3% peak-to-peak amplitude increase is observed for  $R_2 = 5\Omega$ . The amplitude increase corresponds approximately to  $2(a + c)$ , and thus in excellent agreement with the previous analysis. The envelope of the impulse responses show the subsequent ring down process is suppressed more than  $-30$  dB for all times after the main peak. However, the some of ring down dynamics could be numerical noise from the deconvolution operation. The transmit impulse response of a BK9032 transducer (5 MHz linear PZT transducer) from BK medical is shown in Fig. 5.3 b), where a substantial ringing is observed compared to the developed CMUT transducer. Notice, the impulse response for the BK9032 transducer is calculated using a different method described in

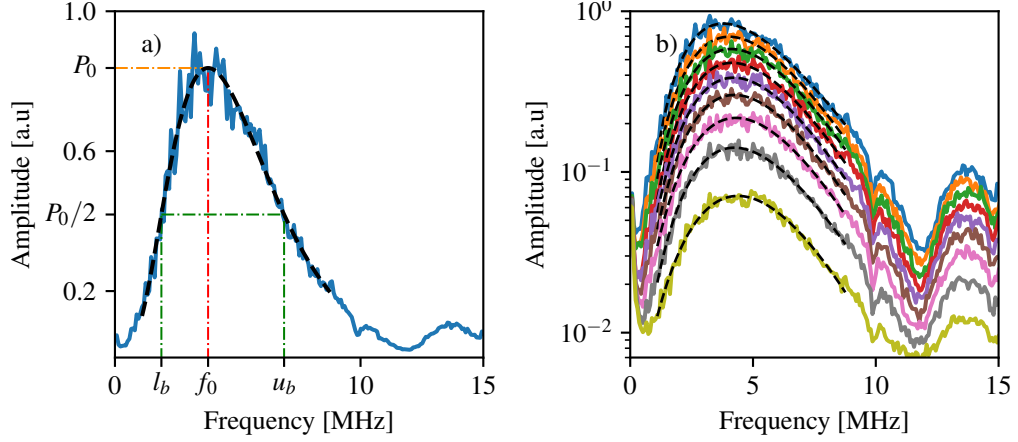


**Figure 5.4:** The transfer function of the fabricated CMUT. A single spectrum is plotted in a). The pressure parameter, the center frequency, and bandwidth are indicated on the axes. Multiple transfer functions where the DC bias has been varied from 10 V to 90 V. The measured data is for  $R_2 = 5\Omega$  configuration.

[92]. The corresponding transfer functions are all shown in Fig. 5.3 c), where a higher bandwidth is observed for the CMUT. All features in the CMUT transfer function is known to be acoustical effects, since a flat frequency spectrum has been measured up to 12.6 MHz and 15.3 MHz for  $R_2 = 10\Omega$  and  $R_2 = 5\Omega$ , respectively.

The final analysis in this section investigates how  $R_2$  influences the output pressure, center frequency, and bandwidth of the CMUT as function of applied DC bias. The three parameters are estimated by fitting an empirical model to the transfer function. The model is empirical and given by

$$P(f) = P_0 \exp\left(-\frac{(f - f_0)^2}{2\sigma_0^2 + f\sigma_1^2}\right) \quad (5.2)$$

where  $P_0$  is a pressure parameter,  $\sigma_0$  and  $\sigma_1$  are parameters used to calculate the bandwidth, and  $f_0$  is center frequency. The  $\sigma_1$  parameter allows the impulse response to be asymmetric around the center frequency, which is seen to be the case in for the CMUT transfer function. Notice, the model becomes a symmetric Gaussian function in the limit where  $\sigma_1 \rightarrow 0$ , and  $\sigma_1$  is therefore a measure of asymmetry in the transfer function. The model has been used to determine parameters for different DC biases. The model is fitted to a single spectrum in Fig. 5.4 a) and the fitting parameters are indicated on the axes. The same measurement is plotted in Fig. 5.4 b) for nine different DC biases ranging from 10 V to 90 V.

The fitted parameters are plotted in Fig. 5.5 as function of applied DC bias. The pressure parameter,  $P_0$ , is observed to monotonically increase with the applied bias and the  $5\ \Omega$  configuration emits more pressure as expected. The center frequency is observed to decrease with the applied bias. Both observations are in perfect agreement with the CMUT theory from chapter 2. The decrease of the bandwidth is not fully understood, and this phenomenon has not to the author best knowledge, not been described in the CMUT literature. The observation could be explained by an increased imaginary part of the radiation impedance. The decrease in the center frequency lowers the  $ka$  value and therefore introduces a higher mass loading of the water in front of the CMUT, the additional mass increases the characteristic decay time and thereby reduces the bandwidth. However, the effect of the bandwidth is small relative to the effect on the center frequency, it is seen from the Fractional BandWidth (FBW). The fraction bandwidth increases from 117% to approximately 130% between the smallest and largest applied voltage. Finally, the output pressure is clearly perturbed by the  $R_2$  stabilization resistor, but, the center frequency and the bandwidth are similar for both values of  $R_2$ .



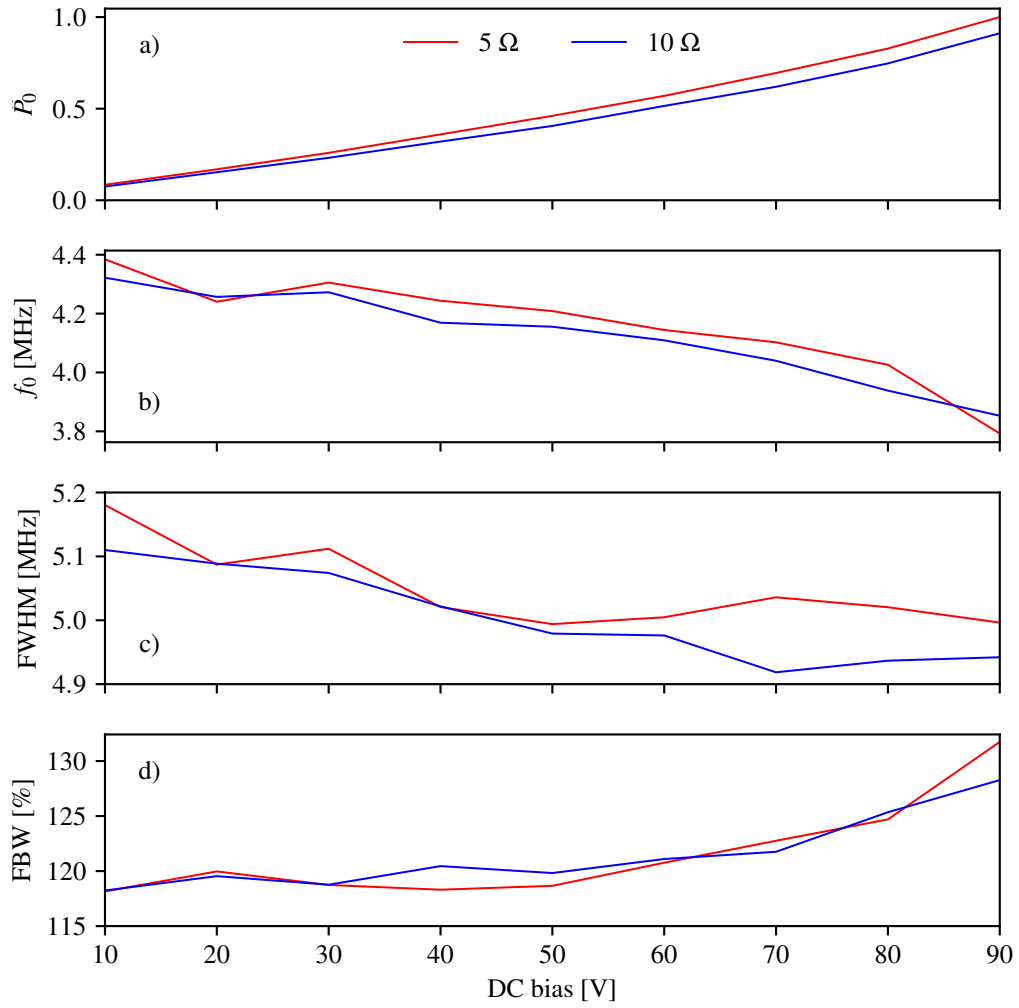


**Figure 5.5:** The fitted parameters as function of applied DC bias for two values of  $R_2$ . a) Normalized pressure. b) Center frequency. c) Bandwidth (FWHM). d) Fractional bandwidth.

## 5.2 Electrode resistance

The 92+92 LOCOS RCA CMUT array is characterized in this section, and the electrode resistance is an essential part of this analysis. A change in terminology will be introduced to uniquely define the electrodes. The top and bottom electrodes will be used instead of rows and columns, respectively. The reason being that rows and columns are not uniquely defined, since rows become columns after a  $90^\circ$  rotation of a RCA array. Using the top and bottom terminology allows a unique description that is invariant to rotation. A characterization of the transmit pressure showed a significant pressure difference between the rows and columns. The peak-to-peak amplitude of the impulse responses differs a factor of 3.5 between rows and columns as seen in Fig. 5.6 a). The difference is caused by high resistance in the bottom electrode, which will be shown in this section. The frequency components of the impulse response are shown in Fig. 5.6 b), where a magnitude difference between top and bottom electrodes is observed to be frequency dependent. The difference between the bottom and top is plotted in Fig. 5.6 c). An exponential tendency is observed (semilog plot) between 2.5 MHz and 15 MHz, and the attenuation is estimated to  $-1.0$  dB/MHz in this region.

The top electrode is made by aluminum and the bottom electrode is made by doped silicon. The electrical resistivity differs substantially between the two materials. The resistivity of metal electrodes is on the order of  $10^{-6}$   $\Omega\text{cm}$  [93], while the resistivity of a silicon electrode varies from  $10^4$  to  $10^{-4}$   $\Omega\text{cm}$  depending on the doping level [94]. The resistance in the electrode has to be sufficiently low to achieve acceptable performance of the CMUTs, which in most cases never become an issue for metal electrodes due to their low resistivity. However, in special cases it becomes challenging to use even highly doped silicon, particularly for long elements such as row-column elements. If the resistivity in an electrode is too high, the overall system will behave as a low-pass filter, which will attenuate applied AC signals along the electrodes. A non-uniform transmitting element will skew the transmitted field and seriously degrade the receive focusing.

A delay line model is used to mathematically describe the attenuation of the AC signal along a CMUT element. The element is lumped into a distributed network of resistors and capacitors as shown in Fig. 5.7, where a) shows a common CMUT design with an equivalent circuit on top. The resistivity of the electrode determines the magnitude of the resistors. The variable capacitors represent CMUT cells and the constant capacitors represent the parasitic capacitance. The electronic circuit can be described by Resistor Capacitor delay line model if the electrical components are lumped together as shown in Fig. 5.7 b). In this model the resistors and capac-

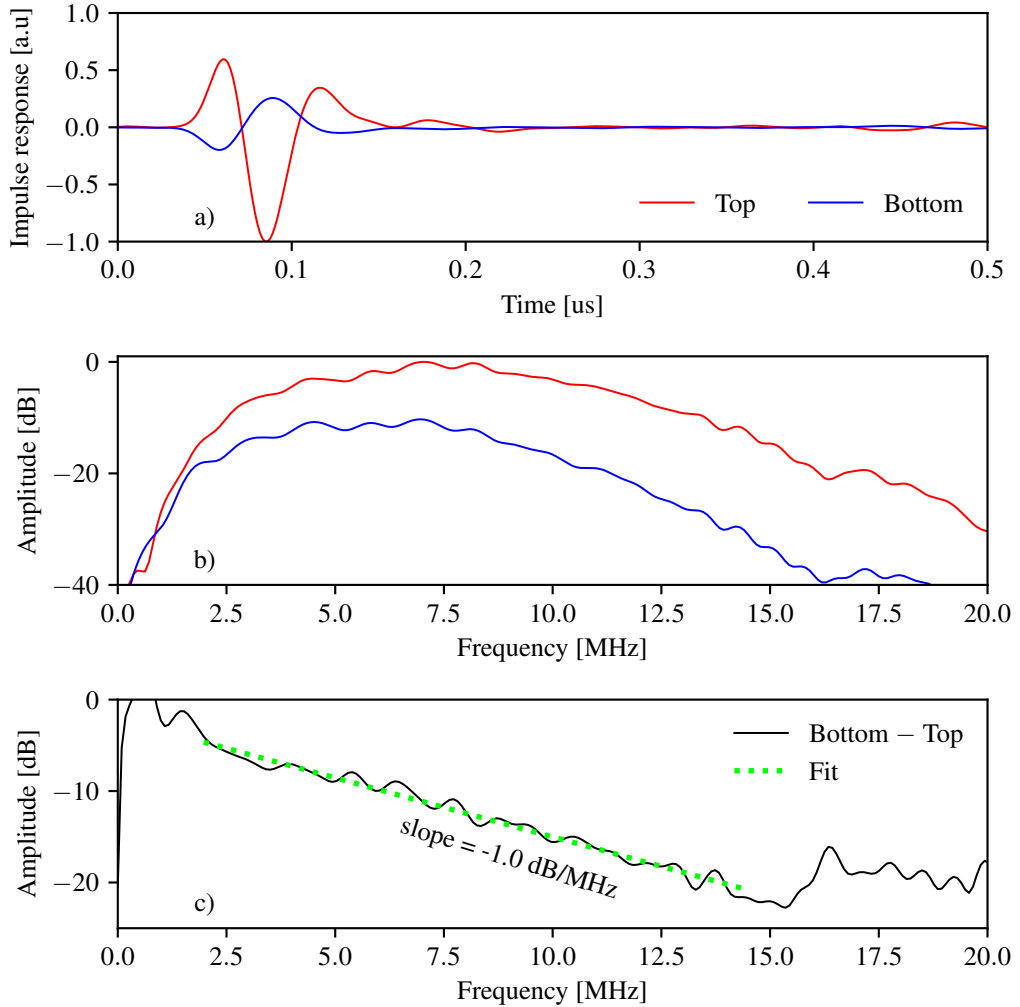


**Figure 5.6:** Impulse response for rows and columns in both time and frequency domain. a) The average transmit impulse response for both top and bottom electrodes. The impulse response magnitude of the bottom electrode is approximately reduced by a factor of 3 compared with top. b) The corresponding transmit transfer function for the top and bottom electrodes. The shape of the transfer functions are similar despite the reduced amplitude for the bottom electrodes. c) The transfer function for the top electrodes subtracted from the transfer function of the bottom electrodes. In the region between 2.5 MHz and 15 MHz an exponential tendency (dB scale) is observed, and attenuation is estimated by fitting a linear function to the dB compressed data. The calculated impulse responses are averaged from 50 measurements.

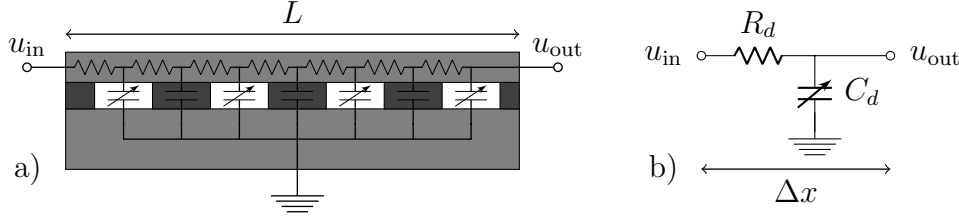


**Figure 5.7:** Model of the Row-Column addressed CMUT array. a) Idealized model of a Row-Column element. The resistance through the element is modelled by resistors, the CMUTs cells are modelled as variable capacitors, and the parasitic capacitance is modelled as constant capacitors. b) When the capacitance of the CMUTs and the parasitic capacitance are merged together, the circuit is described as a Resistor Capacitor (RC) delay line.  $R_d$  and  $C_d$  are the resistance and capacitance of a distributed segment of length  $\Delta x$  and are related to the total resistance and capacitance by  $R_d = R/L \cdot \Delta x$  and  $C_d = C/L \cdot \Delta x$ .

itors are assumed to be evenly distributed along the element,  $R_d$  and  $C_d$ , are resistance and capacitance of a distributed segment of length  $\Delta x$ . These quantities are related to the total resistance,  $R$ , and the total capacitance  $C$ , by

$$R_d = \frac{R}{L} \Delta x \quad C_d = \frac{C}{L} \Delta x, \quad (5.3)$$

where  $L$  is the length of the element. The capacitance and resistance of a CMUT element can be mathematically formulated as

$$C = \frac{\varepsilon W L}{g}, \quad (5.4)$$

and the resistance of an element with an uniform cross-sectional area is [94]

$$R = \frac{\rho L}{HW}, \quad (5.5)$$

where  $\varepsilon$  is the relative permittivity,  $W$  is the width of the element, and  $g$  is the gap height,  $H$  is the electrode thickness. The resistivity  $\rho$  of silicon can vary eight orders of magnitude depending on the doping level, and is therefore a crucial parameter in the electrical design process of a CMUT. Under the assumption of constant capacitance and resistance and in the limit where  $\Delta x \rightarrow 0$ , the voltage distribution  $u(x, t)$  in a delay line is governed by the diffusion equation

$$\frac{\partial u(x, t)}{\partial t} = \frac{L^2}{RC} \frac{\partial^2 u(x, t)}{\partial x^2}. \quad (5.6)$$

During operation will a CMUT element be subject to the following boundary conditions and initial condition

$$u(0, t) = U_0 g(\omega t) \quad (5.7)$$

$$\left. \frac{\partial u(x, t)}{\partial x} \right|_{x=L} = 0 \quad (5.8)$$

$$u(x, 0) = 0, \quad (5.9)$$

where  $U_0$  is the amplitude of the excitation, and  $\omega$  and  $g(\omega t)$  are the angular excitation frequency and excitation function, respectively. The first boundary condition (5.7) corresponds to the input signal at the electrode pad. The second boundary condition (5.8) states that the current density is zero at the end of the electrode, hence, the flux is zero. The initial condition (5.9) implies zero AC voltage at  $t = 0$ . The system contains some intrinsic characteristic parameters and by introducing  $\hat{x} = x/L$ ,  $\hat{t} = \omega t$ , and  $\hat{u} = u/U_0$  allow Eqn. 5.6 to be rewritten on a dimensionless form

$$\frac{\partial \hat{u}}{\partial \hat{t}} = \hat{D} \frac{\partial^2 \hat{u}}{\partial \hat{x}^2} \quad \text{where} \quad \hat{D} = \frac{1}{\omega RC}. \quad (5.10)$$

The product  $\omega RC$  is here seen to be the determining parameter of this system, and can be interpreted as an inverse diffusion coefficient. The  $\omega RC$  product can be expressed in terms of geometry and material properties by using Eqn. 5.4 and Eqn. 5.5, that provides the following scaling properties

$$\omega RC = \omega \frac{\varepsilon WL}{g} \frac{\rho L}{HW} = \omega \frac{\varepsilon \rho L^2}{gH} \propto \frac{L^2}{H}. \quad (5.11)$$

The length of an electrode has a square dependence on the  $\omega RC$  product, and the height of the electrode has an inverse dependence, whereas the width of the element cancels out. Hence, the parameter space suitable for a short CMUT elements are much larger than the parameter space of long element. Typical sizes of the different types of CMUT elements are sketched in Fig. 5.8.

A more quantitative analysis requires a solution to Eqn. 5.10, which will be given in both the frequency and time domain. The frequency domain analysis provides a significant reduced complexity, that enables a closed form solution that is used to define a criterion for the upper bound of  $\omega RC$ . Eigenfunction expansion is used for the analysis in time domain analysis, and an infinite series representations is used to evaluate transient response of the system.

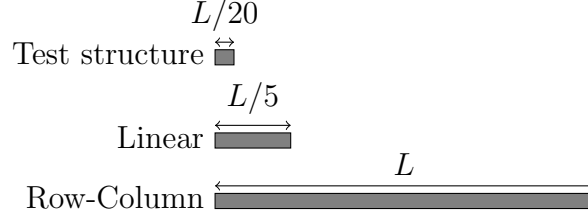


**Figure 5.8:** The size difference between a common RCA element, a linear element and a test structure.

The diffusion equation does not have a closed-form solution when the particular initial and boundary conditions (Eqn. 5.7 to Eqn. 5.9) are imposed. However, a closed form solution of the transfer function can be found in the frequency domain. After a Fourier transform,  $\mathcal{F}$ , Eqn. 5.6 can be expressed as

$$\frac{\partial^2 U}{\partial x^2} - \frac{\kappa^2}{L^2} U = 0 \quad (5.12)$$

where

$$\mathcal{F}\{u\} = U \quad \text{and} \quad \kappa^2 = i\omega RC. \quad (5.13)$$

By imposing the transformed boundary conditions

$$\mathcal{F}\{u(0, t)\} = V_0 G(\omega) \quad (5.14)$$

$$\mathcal{F}\left\{\left.\frac{\partial u(x, t)}{\partial x}\right|_{x=L}\right\} = 0 \quad (5.15)$$

the final solution becomes

$$U(x, \omega) = V_0 G(\omega) \underbrace{\frac{\cosh\left(\kappa\left(1 - \frac{x}{L}\right)\right)}{\cosh(\kappa)}}_{H(x, \omega)}, \quad (5.16)$$

where  $H(x, \omega)$  is the transfer function of the system. The product  $\omega RC$  appears again in the frequency domain analysis, and its impact on the transfer function is plotted for different values in Fig. 5.9 a) and b), for both the absolute magnitude and phase, respectively.

The absolute magnitude decays along the element, and it translates into a decreasing AC magnitude along the element. Hence, the emitted pressure will be highest near the contact pad and then attenuate along the element. The attenuating effect becomes more pronounced as  $\omega RC$  increases. The

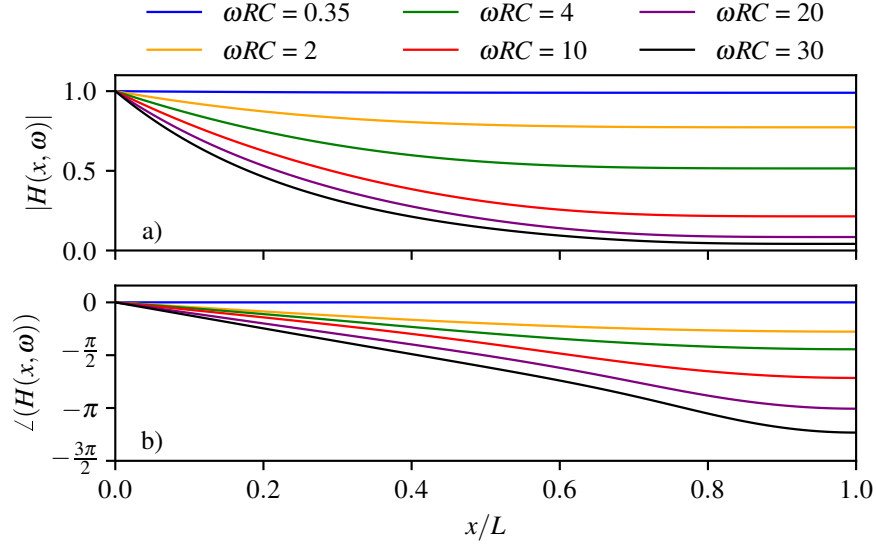


**Figure 5.9:** The transfer function as function of normalized distance for six different values of  $\omega RC$ . a) The magnitude of the transfer function, in the DC case where  $\omega RC \rightarrow 0$  the potential becomes uniformly distributed along the element. As  $\omega RC$  increases, the AC potential drop along the element, becomes larger. b) The phase of the transfer function. For  $\omega RC \ll 1$  the pressure will approximately be emitted simultaneously along the element, however, for larger values of  $\omega RC$  a significant delay is predicted along the element.

phase shift along the element is also influenced by  $\omega RC$ , so a transmitted pulse will be time delayed along the element. Equivalently to the magnitude, the higher  $\omega RC$  value the more pronounced effect. Consequently, at the end of an element, the applied AC signal becomes increasingly time delayed and attenuated as  $\omega RC$  increases. The design criterion is found by evaluating the absolute magnitude of the transfer function at the end of an element, where  $H(x, \omega)$  simplifies to

$$H(L, \omega) = \frac{1}{\cosh(\kappa)}. \quad (5.17)$$

A criterion of a 1% potential drop is used as a guideline to get close to a uniform acoustic pressure along the element. In terms of phase shift along the element, this criterion corresponds to a delay of  $-0.17$  rad or  $-9.7^\circ$ . The

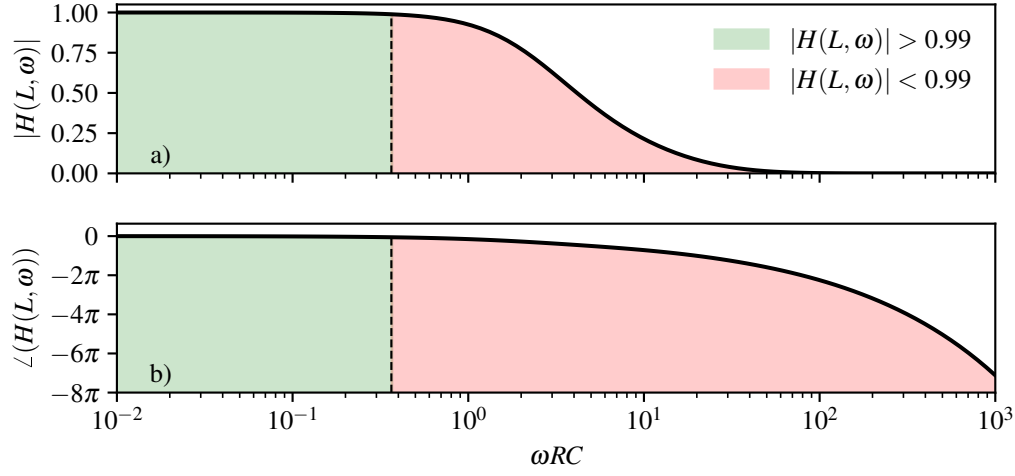


**Figure 5.10:** The transfer function at the end of the element ( $x = L$ ) as function of the product  $\omega RC$ . a) The absolute magnitude at the end of an element, where at 0.99 is indicated with a dashed line. The green region indicates that the magnitude of the transfer function is above above 0.99 and the red region indicates a magnitude less than 0.99. b) The phase delay at the end of an element. The 0.99 magnitude threshold is also indicated on this plot, and the criterion corresponds to a delay at the end of  $-0.17$  radians or  $-9.7$  degrees.

magnitude and phase of the transfer function at the end of the element are plotted as a function of  $\omega RC$  in Fig. 5.10 a) and b), respectively.

The green area indicates the regime where this criterion is satisfied and red where it is not. A numerical solution of Eqn. 5.17 shows that the criterion is met when

$$\omega RC < 0.35. \quad (5.18)$$

This criterion limits the acceptable parameter space for RCA arrays. The specified imaging properties such as center frequency and channel count determine the size of a row-column array. Consequently, the electrode thickness and resistivity are the only design variables, are two options are possible, either a low resistivity or a thick electrode, which can be concluded from Fig. 5.11 where the expression for  $\omega RC$  is in a contour plot.

Highly doped silicon is necessary to satisfy the 0.35 criterion and preferably combined with a thick electrode. A thick electrode is desired from an electrical point of view, but, thick electrodes require additional dry etching in the fabrication process. Long dry etch processes are not necessarily problematic, however, the probability of particle redeposition increases with the



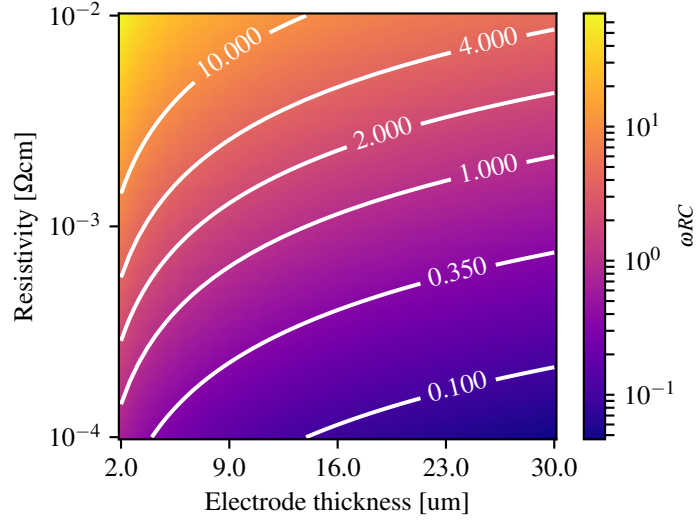


**Figure 5.11:**  $\omega RC$  parameter space. Assumed values for calculation of  $\omega RC$ :  $L = 2$  cm,  $W = 90$   $\mu\text{m}$ ,  $C_0 = 100$  pF, and  $f_{max} = 10$  MHz.

etching time, that later can lower the bonding yield. SOI wafers that satisfy the  $\omega RC$  criterion are highly specialized wafers and not a common product in the SOI wafer industry. This statement is illustrated on the scatter plot in Fig. 5.12. The scatters represents the SOI wafer stock list from Ultrasil. The size of the scatter indicates the quantity of the given wafer batch, and a transparent color scheme has been used to enable visualization of multiple batches with similar properties. The dashed lines outline different values of  $\omega RC$ , and the green region indicates the parameter space that satisfies the developed criterion. The majority of the stock list wafers are observed violate the criterion, and only few wafer batches satisfy the criterion. Additional SOI parameters have been omitted in this analysis. These parameters include thickness of the BOX and handle layers, wafer bow, doping type, and crystal orientation are also influential on the CMUT fabrication.

The developed  $\omega RC$  criterion is difficult to verify directly, especially for the bottom electrodes. The attenuation along the bottom electrode cannot be probed using common electrical characterization, since the bottom electrodes are beneath the surface of the array. An indirectly verification of this effect can be done by measuring the transmit pressure along the element.

By using the RCA scheme, it is possible to actuate the same CMUTs cells, either using the rows or the columns. Thus, effects that do not originate from the electrode configuration should be present in both cases. The transmit pressure field is measured for all elements individually at a distance

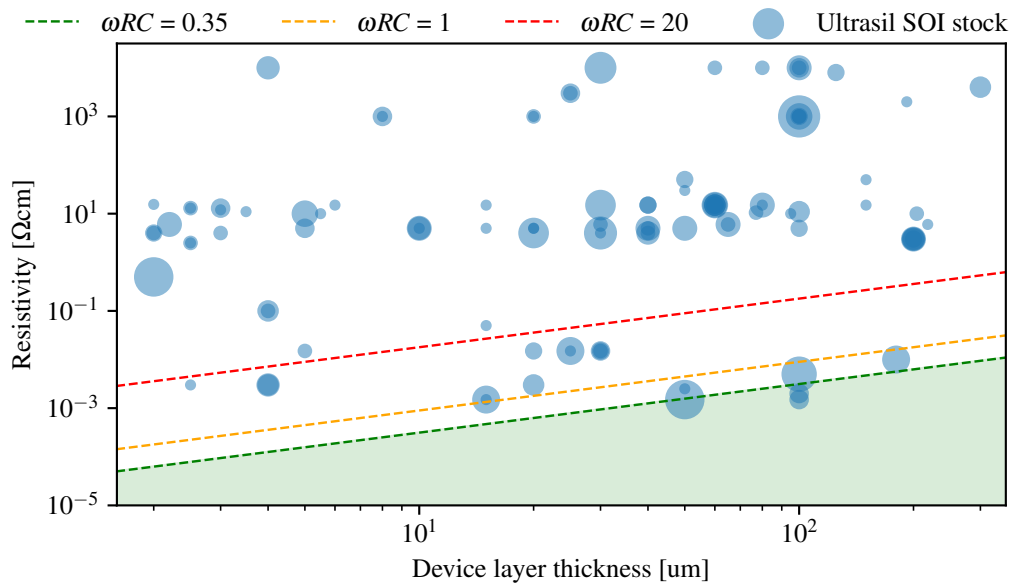


**Figure 5.12:** Available 4" SOI wafer stock list from Ultrasil mapped in the resistivity versus device layer thickness parameter space. The size of the scatters indicates quantity of the available SOI wafer batch, and scatter are made transparent to enable visualization of multiple batches with the same resistivity and device layer thickness. The green area indicates the region that satisfies the  $\omega RC$  criterion. The used wafer stock list is from the 23<sup>th</sup> of august 2019. Assumed values for calculation of  $\omega RC$ :  $L = 2$  cm,  $W = 90$   $\mu\text{m}$ ,  $C_0 = 100$  pF, and  $f_{max} = 10$  MHz.

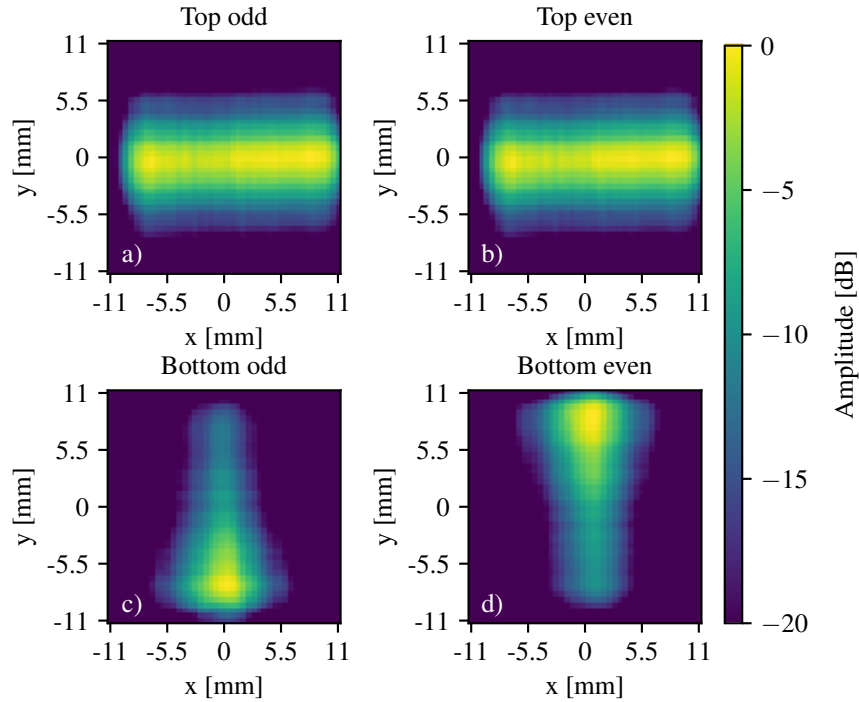


**Figure 5.13:** Average peak-to-peak pressure field for the 92+92 RCA transducer. The numbering scheme of the elements is important, even and odd elements are averaged separately. The pressure fields from the top electrodes are shown in a) and b), and the pressure fields from the bottom electrode are shown in c) and d). The top electrodes are unaffected by the numbering scheme, whereas an anti-symmetry is observed for the bottom electrodes between the odd and even elements. The maximum pressure is measured near the edge closest to the electrical connection and the pressure decreases along the element.

of 1 cm using an AIMS III intensity measurement system (Onda Corporation, Sunnyvale, CA, USA) with an Onda HGL-0400 Hydrophone connected to the experimental research ultrasound scanner, SARUS [95]. The elements are excited by a six-cycle sinusoidal pulse at different frequencies. Six cycles were chosen to ensure the correct excitation frequency by minimizing transient effects. The pressure field is mapped by moving the hydrophone in the x-y plane in front of the transducer, and resolved in a  $45 \times 45$  grid with a spacing of 0.5 mm. The pressure fields of all elements (both top and bottom) have been measured by probing all frequencies in each grid point. The averaged peak-to-peak pressure fields for the top and bottom electrodes are shown in Fig. 5.13. The probe is excited at the center frequency of 4.5 MHz and each plot has been normalized to its own maximum and dB compressed. The odd and even refer to numbering scheme of the elements,

and it becomes important since the all even elements are wire bonded on one side of the array and the odd elements are wire bonded to the opposite side. The top electrodes are unaffected by the numbering scheme, whereas a significant change is observed for bottom electrodes. The bottom electrodes emit pressure unevenly along the element, and the pressure output is attenuated along the element. Most pressure is emitted at near the contact and least pressure is emitted in the opposite end. The top electrodes shown in Fig. 5.13 a) and b) have an  $\omega RC$  value of 0.03 and thereby satisfying the developed criterion of Eqn. 5.18, and the pressure distribution is observed to be uniformly distributed along the element. The bottom electrodes shown in Fig. 5.13 c) and d) have an  $\omega RC$  value of 21.4 and violate the criterion. Hence, the measured attenuation in the pressure field is expected according to the developed theory. The pressure drop along an element should be qualitatively comparable with the theory from the delay line model, and the transfer function is compared to measurements in Fig. 5.14.

The delay line model is plotted in Fig. 5.14 a) for comparable values of  $\omega RC$ . The mean and standard deviation of the peak-to-peak pressure fields along the center of an element are plotted in Fig. 5.14 b) and c) for the 92+92 and 62+62 RCA CMUT probes, respectively. The solid lines represent the bottom electrodes and the dashed lines the top electrodes. Only one pressure profile has been plotted for the top electrodes due to the same behaviour for the other excitation frequencies. The highest frequency of 7 MHz is used as a representation for the worst case scenario in terms of  $\omega RC$ . Each pressure profile has been normalized to its own maximum to obtain a fair comparison between the different frequencies. Higher values of  $\omega RC$  is observed to increase the attenuation along the electrode in good agreement with the transfer function model. The expected pressure drop at the end of an element are according to the model 76%, 92%, and 96% for 2 MHz, 4.5 MHz, and 7 MHz, respectively. However, the measured pressure drop is observed to be 63%, 74%, and 82% for the same excitation frequencies, and the model does therefore overestimate the measured values. The discrepancy between Fig. 5.14 a) and b) could partly be due to an excitation voltage  $U_{ac}$  of 75 V, corresponding to 41% of the 180 V applied DC bias, in which case  $U_{ac}^2$  becomes non-negligible. Nonlinear effects could be reduced by lowering the applied AC voltage, however, these parameters are chosen to imitate real operation conditions for medical imaging. Another reason for the discrepancy is the estimation of  $\omega RC$ , where in particular the resistance is uncertain. The SOI wafer used for the bottom electrodes is specified with an upper bound on the resistivity of 0.1  $\Omega$  cm, and this was used for estimating  $\omega RC$ . The true  $\omega RC$  value could, therefore, be lower, and thereby decrease the discrepancy between theory and experiment. Yet another reason could be transient effects

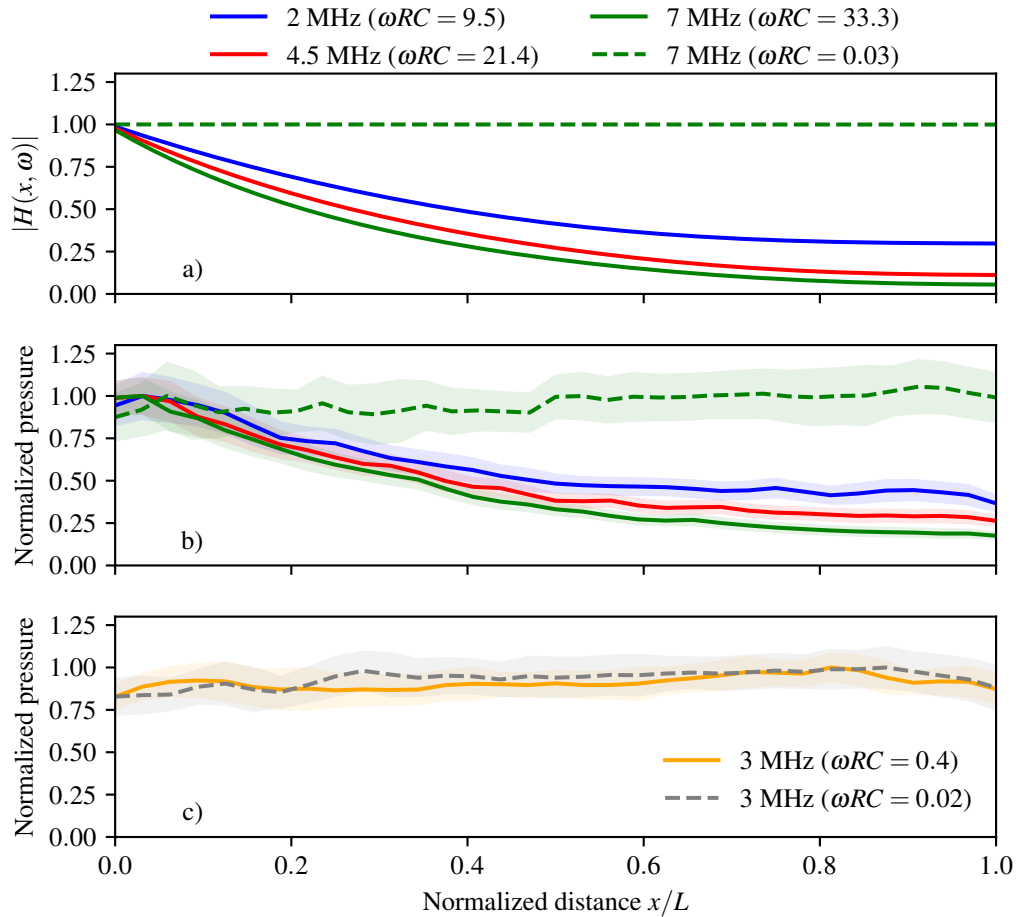


**Figure 5.14:** Comparison between measurements and theory. a) Transfer function of the delay line model. b) Measured average peak-to-peak pressure drops along elements for the probe 92+92 RCA probe. c) Measured average peak-to-peak pressure drops along elements for the 62+62 RCA probe from [31]. Solid lines: bottom electrode. Dashed lines: top electrode. Shaded area: one standard deviation. The same qualitative tendency is observed in a) and b), which demonstrates the consistency between measurement and theory.

which are not accounted for in the frequency domain analysis. These effect can, however, be included if Eqn. 5.10 is solved in the time domain. An analysis performed by EigenFunction Expansion (EFE) can be used to find an infinite series solution. A harmonic excitation is needed if the time and frequency analysis are to be compared. A continuous sinusoidal excitation is used instead of the general excitation function  $g(\omega t)$  which therefore alters the initial condition to

$$\hat{u}(0, \hat{t}) = \sin(\hat{t}). \quad (5.19)$$

Apart from the nondimensionalization the two boundary conditions are unchanged. Under these conditions the solution to the diffusion equation is found to be

$$u(x, t) = \sin(t) + \sum_{n=1}^{\infty} \frac{A_n}{1 + \left(\frac{\lambda_n}{\omega RC}\right)^2} \left[ \sin(t) + \frac{\lambda_n}{\omega RC} \left[ \cos(t) - \exp\left(-\frac{\lambda_n t}{\omega RC}\right) \right] \right] \times \sin\left(\frac{(2n-1)\pi x}{2}\right). \quad (5.20)$$

Where an amplitude parameter,  $A_n$ , and the eigenvalues of the system,  $\lambda_n$ , are defined as

$$A_n = \frac{4}{\pi(1-2n)} \quad \text{and} \quad \lambda_n = \frac{(2n-1)^2 \pi^2}{4}. \quad (5.21)$$

Valuable information can still be extracted despite the complexity of the infinite series solution provided by EFE. The first  $\sin(t)$  term is completely independent of the position, and will therefore provide a uniform voltage distribution along the element. Voltage variations along the elements are therefore solely determined by the sum, and the magnitude of the sum depends strongly on the  $\omega RC$  product. The contribution from the infinite sum vanishes for small values of  $\omega RC$  in excellent agreement with the frequency domain analysis. The transient dynamics is observed to be determined by an exponential decay with a rate parameter or characteristic time scale that also depends on  $\omega RC$ . All these effects can be summarized by investigating the first cycle of the sinusoidal excitation which is plotted in Fig. 5.15 a) to h) for  $\omega RC = 20$ .

The colored line the EFE solution and the black dashed line is the frequency domain model. An overshoot is observed during the first cycle of the EFE solution relative to the frequency model. The peak-to-peak pressure are therefore expected to be higher according the EFE analysis, which could

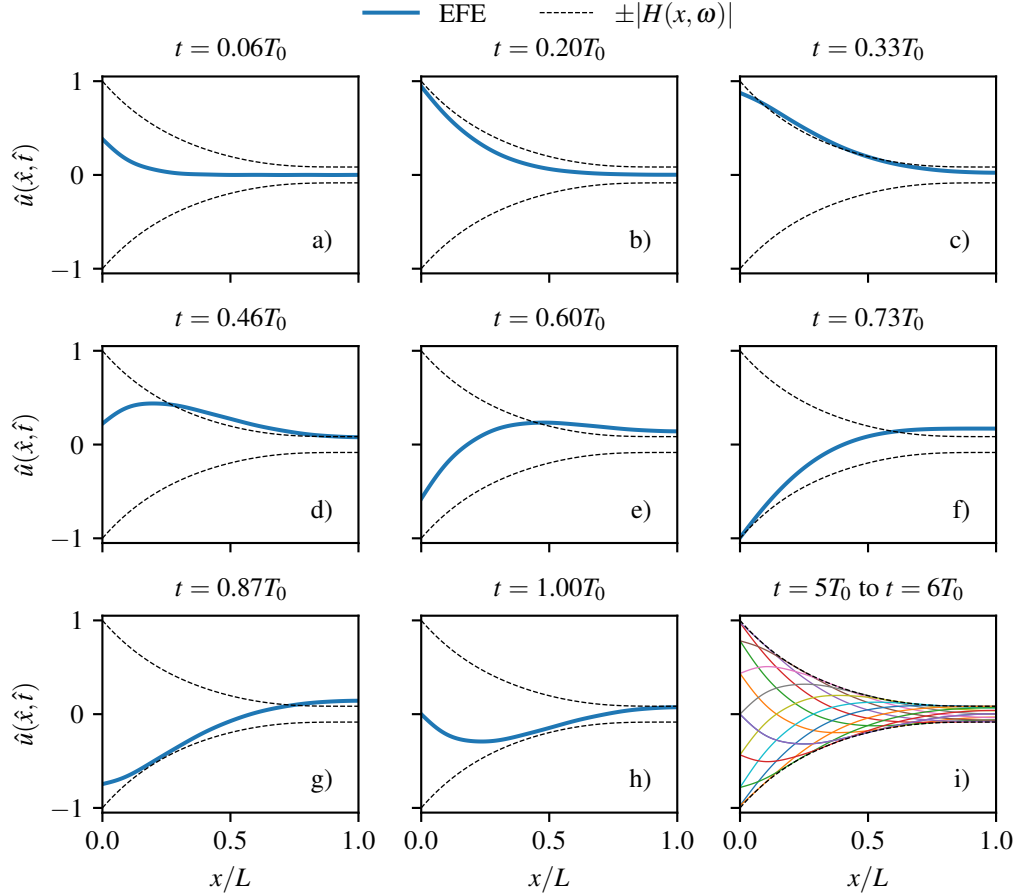


**Figure 5.15:** Time domain solutions the Eqn. 5.10 for  $\omega RC = 20$ . The solid lines are the EFE solution and the black dashed lines are the frequency domain transfer function (Eqn. 5.16). Snapshots of the first sinusoidal cycle are plotted between a) and h), and the time stamp of the snapshot is shown above each plot and defined in terms of the period  $T_0$ . Multiple snapshots are shown in i) for 15 different times between  $5T_0$  and  $6T_0$ . The transient effects are highly suppressed and the frequency transfer function confines the upper and lower bound as expected.

explain the discrepancy between measurements and theory in Fig. 5.14. The maximum amplitude of the time and frequency model must equal in the limit where  $t \rightarrow \infty$  or when the transient contributions vanishes as shown in Fig. 5.15 i), where the EFE solution is observed to be confined within the bounds of the frequency transfer model as expected.

### 5.3 Ultrasound imaging results

Two of the 92+92 RCA arrays from section 4.1 have been assembled into probes, one with and one without an integrated compound diverging lens. Both arrays suffers from too large electrode resistance in the bottom electrodes, and the imaging capabilities are therefore limited. The compound lens introduces an additional frequency dependent loss mechanism that reduces the output pressure and SNR even further and images were therefore not generated by this probe, but characterization of the lens properties and transmit impulse response of this probe can be found in paper E.

A set of volumetric images were acquired by the 92+92 RCA probe without lens. The RF data was acquired by the SARUS experimental scanner [95]. The CMUT probe was biased with 190 V corresponding to 83% of the pull-in voltage, and excited with an  $\pm 75$  V AC pulse. The pulse for the imaging sequence was four cycled 4.5 MHz sinusoidal pulse.

The three spatially orthogonal images planes of a multi wire phantom has been imaged by the developed RCA probe and shown in Fig. 5.16. The wires are resolved at a depth of 14 cm and detected in all three planes. Distinguishable wires are observed for all depths in the elevation plane, however, the first five layers of wires are not detected in azimuth plane due to a misalignment between transducer and phantom. The C-plane image is acquired at a depth of 40 mm and confirms the missing wires in the azimuth plane are caused by misalignment. Row-column images of cyst phantoms have also been acquired and showed in Fig. 5.17. Cysts are detected in all three planes, but due to a significant misalignment between transducer and phantom are some of the cysts only partially in the field of view. Three cysts are observed in the azimuth plane, all indicated with dashed yellow circles. The third cyst is just barely in the field of view, but the circumference is observable, which thereby demonstrates 3D imaging capabilities down to a depth of 70 mm. The C-plane image is acquired at a depth of 50 mm, and yellow dash lines are imposed on top of the image to indicate the shape of the cyst.



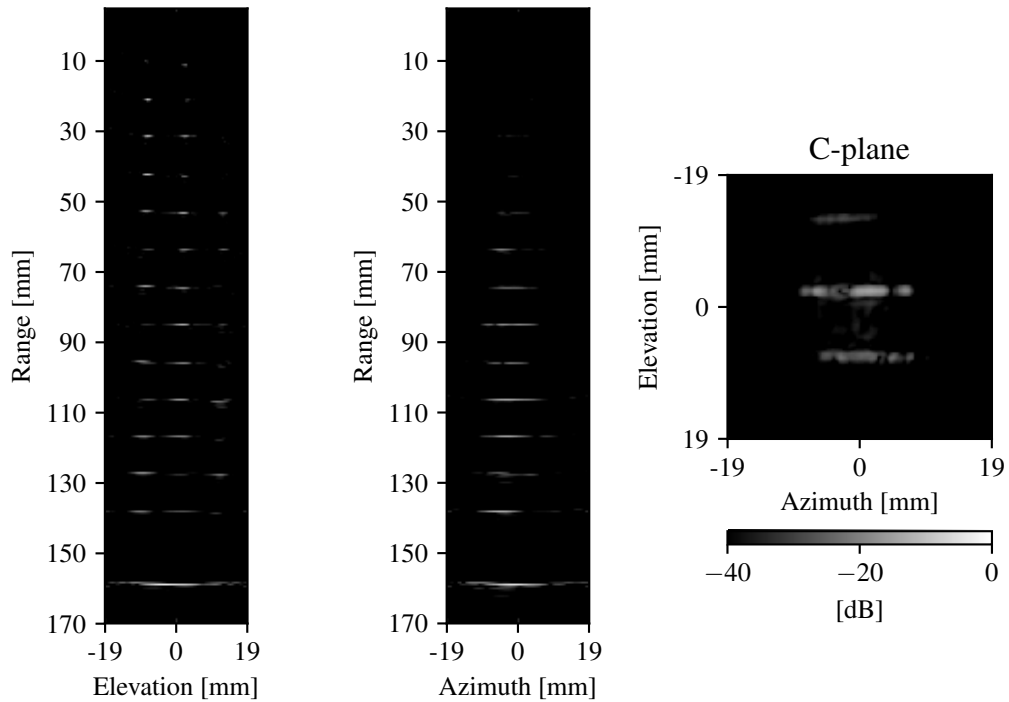


**Figure 5.16:** Volumetric imaging of a wire phantom. The images were acquired by the developed 92+92 RCA CMUT probe w/o lens. Three orthogonal planes (azimuth, elevation, and the C-plane) are shown from a volume of  $3.8 \text{ cm} \times 3.8 \text{ cm} \times 17 \text{ cm}$  using a dynamic range of 40 dB. The C-plane is acquired at depth of 40 mm.

## 5.4 Chapter summery

An acoustic white noise analysis was presented. The white noise analysis was used to characterize the frequency response of the overall CMUT system including electronics and instruments. A flat frequency spectrum between 0 MHz up to 15.3 MHz was demonstrated for a developed single channel acoustic experimental set-up. The transmit impulse response of the characterized CMUT was calculated using the white noise data. The ring-down amplitude was observed less than  $-30 \text{ dB}$  for all times after the main peak. Additionally, the parameters transmit pressure, center frequency, and bandwidth were estimated as function of the applied bias. The result showed an expected pressure increase, a reduced center frequency, and a fractional bandwidth increase from 115% of 130%. A criterion of how to design to design row-column electrodes were derived and demonstrated experimentally.

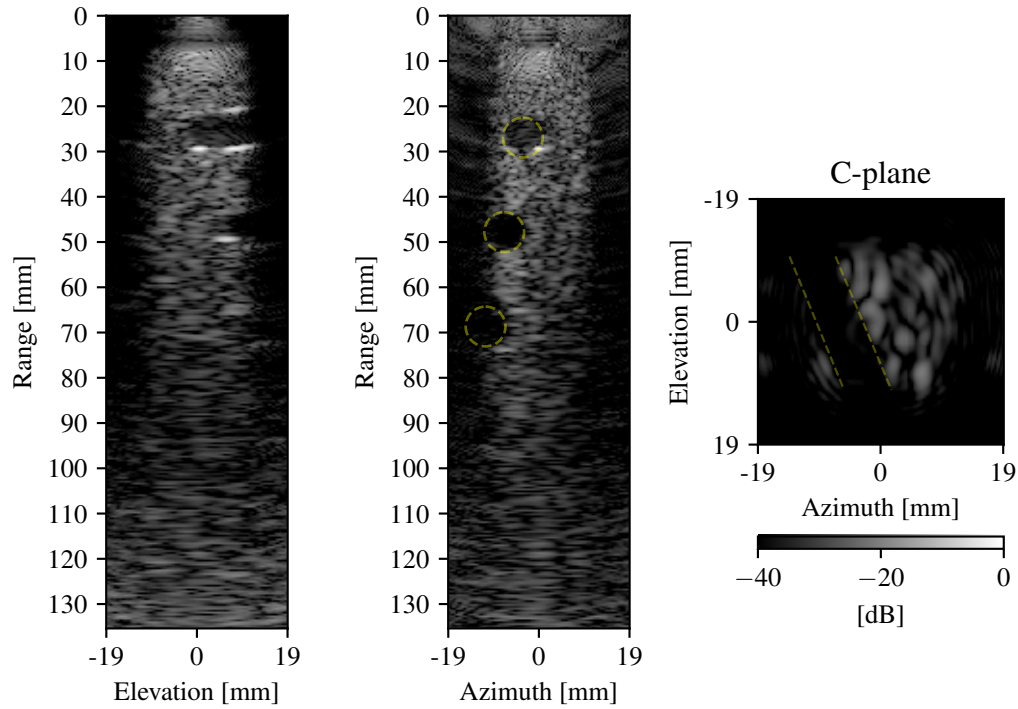


**Figure 5.17:** Volumetric imaging of a cyst phantom. The ultrasound images were acquired by the developed 92+92 RCA CMUT probe w/o lens. Three orthogonal planes (azimuth, elevation, and the C-plane) are shown from a volume of  $3.8\text{ cm} \times 3.8\text{ cm} \times 17\text{ cm}$  using a dynamic range of 40 dB. Three cysts are detectable in the azimuth plane which is indicated with transparent dashed yellow circles. The C-plane is acquired at depth of 45 mm.

The developed criterion was used to characterize the acoustic performance of a developed 92+92 row-column probe. The criterion can be used to ensure less than 1% attenuation of AC signals along a row-column element, which mathematically is formulated as  $\omega RC < 0.35$ . Finally, volumetric ultrasound images acquired by one of the developed 92+92 row-column addressed CMUT probe were presented. 3D images of a wire phantom showed a clear separation between wires in all three dimensions, and the wires were distinctly resolved down to a depth of 14 cm. In addition, images of a cyst phantom demonstrated visualization of cysts down to depth of 7 cm in all three dimensions.



## CHAPTER 6

---

### Conclusion

---

This thesis has presented the results of the PhD project entitled Micromachined Integrated 2D Transducers for Ultrasound Imaging. The main goal of the project was to develop ultrasound transducer technology for three dimensional ultrasound imaging, and more specifically development of large row-column arrays. This goal has been attained.

The scaling laws for row-column addressed arrays are highly favourable as the channel count increases linearly with the number of elements, whereas conventional fully populated matrix arrays have a quadratic dependency. A Capacitive Micromachined Ultrasonic Transducer (CMUT) technology platform was chosen as the transducers technology in this work due to the design flexibility and the desirable imaging properties offered by this technology.

In chapter 2, a theoretical analysis of the a single CMUT cell was given. All derived equations were non dimensionalized to provide valuable information regarding the scaling law of relevant CMUT characteristics. The scaling law of the pull-in voltage was derived for a non-linear spring model and for a non-linear clamped plate applied to an electrostatic pressure. A perturbative solution to the deflection of the clamped plate problem and the scaling properties of pull-in voltages were determined. The dynamics of a single CMUT cell was analyzed using a non-linear harmonic oscillator model in the low and high  $ka$  regimes. The low  $ka$  analysis demonstrated a reduction of the resonance frequency due to an additional mass loading. This frequency reduction was observed to depend on the aspect ratio of the CMUT plate and the density ratio between the medium and the plate material. A phase portrait analysis was used for the high  $ka$  regime to rapidly visualize the dy-

namics of various initial conditions. The parameter space was from the phase portrait analysis observed to depend on the applied bias and the damping of the CMUT plate.

Various concepts of the row-column addressing scheme were described in Chapter 3. A brief literature review was first given followed by the scaling laws of the transducer area and imaging resolution capabilities (FWHM) for both row-column arrays and conventional fully populated matrix arrays. An explanation of an undesired row-column specific edge wave phenomenon was given, and an integrated apodization scheme was implemented into all CMUT designs in this work to reduce the effect from edge waves. The last part of the chapter described a capacitive substrate coupling, which lead to increased parasitic capacitance for the columns. A 62+62 CMUT row-column probe from the literature was used as a reference for this work. The capacitance of the columns was observed to be by a factor of 2.5 higher than the rows for this probe. The capacitance difference was caused by capacitive substrate coupling, and the substrate coupling factor of 2.5 was used as a benchmark throughout the thesis.

In chapter 4 four different microfabrication processes of row-column addressed CMUT arrays were described. Two 92+92 row-column transducers with integrated apodization were fabricated and assembled into ultrasound probes, one with a divergent lens and one without. The used fabrication method relied on Local oxidation of silicon (LOCOS) and the process was observed to be unsuitable for fabrication of row-column arrays due to a low array yield. The substrate coupling factor of these arrays were reduced to 1.6, and impedance measurements showed a coupling coefficient of 15.8% for the LOCOS arrays. The diverging properties of the row-column probe with lens are discussed in paper E. A polymer based CMUT fabrication using polymer BenzoCycloButene (BCB) as spacer and post material was also developed. An electrically insulating glass substrate was used for the BCB CMUT to reduce to substrate coupling, the reduction was demonstrated a 62+62 row-column CMUT array with integrated apodization. The capacitance measurements of the rows and columns showed a substrate coupling factor of 1.1, hence a significant reduction compared to the LOCOS process. Stability tests and acoustic characterization of linear BCB CMUT arrays are reported in paper A. However, the dielectric properties of the BCB polymer was characterized and showed a median breakdown voltage of 0.08 V/nm. The BCB fabrication process was therefore not suitable for medical imaging applications where breakdown field strengths of 0.5 V/nm or even higher are required. The third demonstrated row-column fabrication process was based on principle of the anodic bonding. Multiple row-column arrays were fabricated and the developed process showed to be well suited fabrication of

large area structures such as row-column addressed arrays. Electrical characterization showed an issue with short circuiting between the top and bottom electrodes. This issue was addressed by introducing a nitride film at the bonding interface, and preliminary measurements implied the new approach solved the problem. The acoustic performance of the anodic bonded CMUTs are yet to be determined, and measurement strategies are currently being planned. The best properties from the LOCOS process and the anodic bonding process were combined in the fourth and final fabrication process where the intended application was a large 188+188 row-column addressed CMUT probe. A novel zig-zag element configuration was developed for this probe to fulfill a  $\lambda/2$  pitch constraint while preserving a closely packed CMUT cell layout. A simulation study of the zig-zag element configuration can be found in paper B. The fabrication of the 188+188 row-column arrays are still being developed. The fabrication of the row-column arrays were not fully successful due to rupture of the CMUT plate. However, impedance measurements on linear arrays was demonstrated where an expected CMUT behaviour was observed and the electromechanical coupling coefficient was estimated to be 7.8%.

The last part of the chapter described a novel fabrication method of a Poly-Silicon-On-Insulator (PSOI) wafer suited for CMUT applications. Purchasing conventional 4" SOI wafers, for CMUT fabrication at a university level, has gotten increasingly more difficult during the last couple of years. The developed PSOI technology is intended as a substitution for conventional SOI wafers, and multiple PSOI wafers were demonstrated in this work. The PSOI wafers were shown to be applicable to both fusion bonded and anodically bonded CMUTs. The surface roughness of the PSOI device layer was measured to 0.47 nm, and the device layer resistivity was measured to  $0.036 \Omega \text{ cm} \pm 0.019 \Omega \text{ cm}$ . Additional results and findings are presented in paper D.

In chapter 5, an acoustic white noise analysis was presented. The white noise analysis was used to characterize the frequency response of the overall CMUT system including electronics and instruments. A flat frequency spectrum between 0 MHz up to 15.3 MHz was demonstrated for a developed single channel acoustic experimental set-up. The white noise analysis was additionally used to acoustically characterize a linear CMUT array fabricated by the combined LOCOS and anodic bonding method. The transmit impulse response was calculated, and the amplitude of the ringing was observed less than -30 dB. Additionally, an analysis of relevant CMUT parameters was provided as function of the applied bias. The result showed an expected pressure increase, a reduced center frequency, and a fractional bandwidth increase from 115% of 130%.

Finally, an acoustical characterization of the 92+92 row-columns probes was described. The analysis showed a constant pressure field along rows, but a decreasing pressure field along the columns. The phenomenon of decreasing pressure was explained by a developed delay line model. The resistance of the columns was in this design too high, which caused attenuation of high frequency content. The developed delay line model was used to define a design criterion  $\omega RC < 0.35$  that ensures less than 1% attenuation along an element. Additional results and findings regarding electrode resistance can be found in paper C.

Volumetric ultrasound images acquired by the developed 92+92 row-column addressed CMUT probe were presented in the last part of the chapter. The acquired 3D ultrasound images had a volume of  $170 \times 3.8 \times 3.8 \text{mm}^3$ . Volumetric ultrasound images of a wire phantom showed a clear separation between wires in all three dimensions. The wires were distinctly resolved down to a depth of 14 cm. The 92+92 row-column probe was also used to image a cyst phantom, where cysts were detectable down to depth of 7 cm in all three dimensions.

The work of this PhD has addressed theoretical consideration and experimental fabrication of row-column addressed CMUT technology. The row-column technology scales more efficient with the channel count than the conventional fully populated matrix array. However, the complexity of the clean room fabrication increases with the surface area of a given device, thus, the fabrication of large row-column CMUT arrays becomes more difficult as the channel count goes up.

Additional concepts are introduced for the row-column CMUT technology compared to conventional linear ultrasound transducers, that includes challenges related to the clean room fabrication, acoustics, and electronics. Multiple CMUT fabrication platforms have been investigated during this thesis, and the anodic bonding technique presented in chapter 4 is believed to best be suited process for large area row-column addressed arrays despite the lack of acoustic characterization. The anodic bonding process has no substrate coupling, low resistivity in metal electrodes for both rows and columns, a low parasitic capacitance due to a structured bottom electrode, and the process has shown to be structurally stable during the clean room fabrication. Additional process and development is currently believed to solve the current electrical issues associated with the developed anodic bonding process. Hence, fabrication of large row-column arrays can begin as soon as this problem has definitely been eliminated.

---

## Bibliography

---

- [1] J. Wild, “The use of ultrasonic pulses for the measurement of biologic tissues and the detection of tissue density changes.” *Surgery*, 1950.
- [2] D. G. Wildes and L. S. Smith, “Advanced ultrasound probes for medical imaging,” in *AIP Conference Proceedings*, vol. 1430, no. 1. AIP, 2012, pp. 801–808.
- [3] M. I. Haller and B. T. Khuri-Yakub, “A surface micromachined electrostatic ultrasonic air transducer,” in *Proc. IEEE Ultrason. Symp.*, vol. 2, 1994, pp. 1241–1244.
- [4] ———, “A surface micromachined electrostatic ultrasonic air transducer,” *IEEE Transactions on Ultrasonics, Ferroelectrics, and Frequency Control*, 1996.
- [5] A. Debray, J. Mouly, and M. Villien, “New applications along with manufacturing capabilities and technological readiness are driving the takeoff of micro-machined ultrasonic transducers,” Yole Développement, Tech. Rep., 2018.
- [6] C. Daft, P. Wagner, B. Bymaster, S. Panda, K. Patel, and I. Ladabaum, “CMUTs and electronics for 2D and 3D imaging: Monolithic integration, in-handle chip sets and system implications,” in *Proceedings - IEEE Ultrasonics Symposium*, 2005, pp. 463—474.
- [7] D. Gross, C. Coutier, M. Legros, A. Bouakaz, and D. Certon, “A cMUT probe for ultrasound-guided focused ultrasound targeted therapy,” *IEEE*



- transactions on ultrasonics, ferroelectrics, and frequency control*, vol. 62, no. 6, pp. 1145–1160, 2015.
- [8] A. S. Savoia, G. Caliano, and M. Pappalardo, “A CMUT Probe for Medical Ultrasonography: From Microfabrication to System Integration,” *IEEE Transactions on Ultrasonics Ferroelectrics and Frequency Control*, vol. 59, no. 6, pp. 1127–1138, 2012.
- [9] K. Karadayi, Y. Kim, R. Managuli, and R. Managuli, “Three-Dimensional Ultrasound: From Acquisition to Visualization and from Algorithms to Systems,” 2009.
- [10] S. Holbek, T. L. Christiansen, M. B. Stuart, C. Beers, E. V. Thomsen, and J. A. Jensen, “3-D Vector Flow Estimation with Row-Column Addressed Arrays,” *IEEE transactions on ultrasonics, ferroelectrics, and frequency control*, vol. 63, no. 11, pp. 1799–1814, 2016.
- [11] D. Certon, F. Teston, and F. Patat, “A finite difference model for cMUT devices,” *IEEE transactions on ultrasonics, ferroelectrics, and frequency control*, vol. 52, no. 12, pp. 2199–2210, 2005.
- [12] B. Bayram, G. G. Yaralioglu, A. S. Ergun, M. Oralkan, and B. T. Khuri-Yakub, “Dynamic FEM analysis of multiple cMUT cells in immersion,” in *IEEE Ultrasonics Symposium, 2004*, vol. 1. IEEE, 2004, pp. 252–255.
- [13] H. Köymen, A. Atalar, E. Aydoğdu, C. Kocabaş, H. K. Oğuz, S. Olçum, A. Ozgurluk, and A. Ünlügedik, “An improved lumped element nonlinear circuit model for a circular CMUT cell,” *IEEE Transactions on Ultrasonics, Ferroelectrics, and Frequency Control*, 2012.
- [14] S. Satir, J. Zahorian, and F. L. Degertekin, “A large-signal model for CMUT arrays with arbitrary membrane geometry operating in non-collapsed mode,” *IEEE Transactions on Ultrasonics, Ferroelectrics, and Frequency Control*, 2013.
- [15] A. Lohfink and P. C. Eccardt, “Linear and Nonlinear Equivalent Circuit Modeling of CMUTs,” *IEEE Transactions on Ultrasonics, Ferroelectrics, and Frequency Control*, 2005.
- [16] A. S. Ergun, G. G. Yaralioglu, and B. T. Khuri-Yakub, “Capacitive Micromachined Ultrasonic Transducers: Theory and Technology,” *Journal of Aerospace Engineering*, vol. 16, pp. 76–84, 2003.

- [17] S. H. Strogatz, *Nonlinear Dynamics and Chaos with Student Solutions Manual: With Applications to Physics, Biology, Chemistry, and Engineering*. CRC Press, 2018.
- [18] M. F. La Cour, T. L. Christiansen, J. A. Jensen, and E. V. Thomsen, “Electrostatic and small-signal analysis of CMUTs with circular and square anisotropic plates,” *IEEE Transactions on Ultrasonics, Ferroelectrics, and Frequency Control*, 2015.
- [19] P. R. Stepanishen, “The impulse response and time dependent force on a baffled circular piston and a sphere,” *Journal of Sound and Vibration*, 1973.
- [20] J. A. Jensen, *Estimation of Blood Velocities Using Ultrasound: A Signal Processing Approach*. New York: Cambridge University Press, 1996.
- [21] A. H. Nayfeh, *Introduction to perturbation techniques*. John Wiley & Sons, 2011.
- [22] C. E. Morton and G. R. Lockwood, “Theoretical assessment of a crossed electrode 2-D array for 3-D imaging,” in *Proc. IEEE Ultrason. Symp.*, 2003, pp. 968–971.
- [23] C. H. Seo and J. T. Yen, “64 × 64 2-D array transducer with row-column addressing,” in *Proceedings - IEEE Ultrasonics Symposium*, 2006.
- [24] M. F. Rasmussen and J. A. Jensen, “3D ultrasound imaging performance of a row-column addressed 2D array transducer: a simulation study,” in *Medical Imaging 2013: Ultrasonic Imaging, Tomography, and Therapy*, 2013.
- [25] ———, “3-D ultrasound imaging performance of a row-column addressed 2-D array transducer: A measurement study,” in *IEEE International Ultrasonics Symposium, IUS*, 2013.
- [26] A. Sampaleanu, P. Zhang, A. Kshirsagar, W. Moussa, and R. Zemp, “Top-orthogonal-to-bottom-electrode (TOBE) CMUT arrays for 3-D ultrasound imaging,” *IEEE Transactions on Ultrasonics, Ferroelectrics, and Frequency Control*, 2014.
- [27] M. F. Rasmussen, T. L. Christiansen, E. V. Thomsen, and J. A. Jensen, “3-D Imaging Using Row-Column-Addressed Arrays With Integrated Apodization. Part I: Apodization Design and Line Element Beamforming,” *IEEE Transactions on Ultrasonics, Ferroelectrics, and Frequency Control*, vol. 62, no. 5, pp. 947–958, 2015.

- [28] T. L. Christiansen, M. F. Rasmussen, J. P. Bagge, L. N. Moesner, J. A. Jensen, and E. V. Thomsen, “3-D Imaging Using Row-Column-Addressed Arrays With Integrated Apodization. Part II: Transducer Fabrication and Experimental Results,” *IEEE Transactions on Ultrasonics, Ferroelectrics and Frequency Control*, vol. 62, no. 5, pp. 959–971, 2015.
- [29] C. Ceroici, T. Harrison, and R. J. Zemp, “Fast Orthogonal Row-Column Electronic Scanning With Top-Orthogonal-to-Bottom Electrode Arrays,” *IEEE Transactions on Ultrasonics, Ferroelectrics, and Frequency Control*, 2017.
- [30] A. Stuart Savoia, B. Mauti, L. Fanni, G. Caliano, E. Boni, P. Mattesini, M. Scaringella, and P. Tortoli, “A 120+ 120- Element Crisscross CMUT Probe’s with Real-Time Switchable Electronic and Fresnel Focusing Capabilities,” in *IEEE International Ultrasonics Symposium, IUS*, 2018.
- [31] M. Engholm, H. Bouzari, T. L. Christiansen, C. Beers, J. P. Bagge, L. N. Moesner, S. E. Diederichsen, M. B. Stuart, J. A. Jensen, and E. V. Thomsen, “Probe development of CMUT and PZT row-column-addressed 2-D arrays,” *Sensors and Actuators, A: Physical*, 2018.
- [32] J. Song, S. Jung, Y. Kim, K. Cho, B. Kim, S. Lee, J. Na, I. Yang, O.-k. Kwon, and D. Kim, “Reconfigurable 2D cMUT-ASIC arrays for 3D ultrasound image,” in *Medical Imaging 2012: Ultrasonic Imaging, Tomography, and Therapy*, 2012.
- [33] C. Chen, Z. Chen, D. Bera, S. B. Raghunathan, M. Shabanimotlagh, E. Noothout, Z. Y. Chang, J. Ponte, C. Prins, H. J. Vos, J. G. Bosch, M. D. Verweij, N. De Jong, and M. A. Pertijs, “A Front-End ASIC with Receive Sub-array Beamforming Integrated with a  $32 \times 32$  PZT Matrix Transducer for 3-D Transesophageal Echocardiography,” *IEEE Journal of Solid-State Circuits*, 2017.
- [34] D. H. Turnbull, P. K. Lum, A. T. Kerr, and F. S. Foster, “Simulation of b-scan images from two-dimensional transducer arrays: Part i - methods and quantitative contrast measurements,” *Ultrasonic Imaging*, 1992.
- [35] A. Austeng and S. Holm, “Sparse 2-D arrays for 3-D phased array imaging - Design methods,” *IEEE Transactions on Ultrasonics, Ferroelectrics, and Frequency Control*, 2002.

- [36] A. Ramalli, E. Boni, A. S. Savoia, and P. Tortoli, “Density-tapered spiral arrays for ultrasound 3-D imaging,” *IEEE Transactions on Ultrasonics, Ferroelectrics, and Frequency Control*, 2015.
- [37] J. A. Jensen and N. B. Svendsen, “Calculation of Pressure Fields from Arbitrarily Shaped, Apodized, and Excited Ultrasound Transducers,” *IEEE Trans. Ultrason., Ferroelec., Freq. Contr.*, vol. 39, no. 2, pp. 262–267, 1992.
- [38] J. A. Jensen, “Field: A Program for Simulating Ultrasound Systems,” *Med. Biol. Eng. Comp.*, vol. 10th Nordi, pp. 351–353, 1996.
- [39] D. T. Blackstock, *Fundamentals of Physical Acoustics*, ser. A Wiley-Interscience publication. John Wiley & Sons, 2000.
- [40] I. B. Daya, A. I. Chen, M. J. Shafiee, A. Wong, and J. T. Yeow, “Compensated Row-Column Ultrasound Imaging System Using Fisher Tippet Multilayered Conditional Random Field Model,” *PLoS ONE*, 2015.
- [41] I. Ben Daya, A. I. Chen, M. J. Shafiee, A. Wong, and J. T. Yeow, “Compensated Row-Column Ultrasound Imaging System Using Multilayered Edge Guided Stochastically Fully Connected Random Fields,” *Scientific Reports*, 2017.
- [42] I. Ben Daya, A. I. Chen, M. J. Shafiee, J. T. Yeow, and A. Wong, “Compensated Row-Column Ultrasound Imaging System Using Edge-Guided Three Dimensional Random Fields,” *Journal of Computational Vision and Imaging Systems*, 2018.
- [43] I. B. Daya, J. T. W. Yeow, and A. Wong, “Compensated Row-Column Ultrasound Imaging Systems with Data-Driven Point Spread Function Learning,” in *International Conference on Image Analysis and Recognition*. Springer, 2019, pp. 429–441.
- [44] J. Jung, S. Kim, W. Lee, and H. Choi, “Fabrication of a two-dimensional piezoelectric micromachined ultrasonic transducer array using a top-crossover-to-bottom structure and metal bridge connections,” *Journal of Micromechanics and Microengineering*, 2013.
- [45] B. A. Greenlay and R. J. Zemp, “Fabrication of linear array and top-orthogonal-to-bottom electrode CMUT arrays with a sacrificial release process,” *IEEE Transactions on Ultrasonics, Ferroelectrics, and Frequency Control*, 2017.

- [46] J. L. Sanders, X. Wu, O. J. Adelegan, M. M. Mahmud, F. Yalcin Yamaner, C. M. Gallippi, and O. Oralkan, "A Row-Column (RC) Addressed 2D Capacitive Micromachined Ultrasonic Transducer (CMUT) Array on a Glass Substrate: Preliminary Results," in *Proceedings of the Annual International Conference of the IEEE Engineering in Medicine and Biology Society, EMBS*, 2018.
- [47] M. Engholm, H. Bouzari, J. A. Jensen, and E. V. Thomsen, "Capacitive Substrate Coupling of Row-Column-Addressed 2-D CMUT Arrays," *Proceedings of 2016 Ieee International Ultrasonics Symposium*, vol. 2016-, p. 7728384, 2016.
- [48] O. Ahrens, A. Buhrdorf, D. Hohlfeld, L. Tebje, and J. Binder, "Fabrication of gap-optimized CMUT," *IEEE Transactions on Ultrasonics, Ferroelectrics, and Frequency Control*, 2002.
- [49] A. S. Ergun, Y. Huang, X. Zhuang, Ö. Oralkan, G. G. Yaralioglu, and B. T. Khuri-Yakub, "Capacitive Micromachined Ultrasonic Transducers: Fabrication Technology," *IEEE Transactions on Ultrasonics, Ferroelectrics, and Frequency Control*, 2005.
- [50] E. Cianci, A. Schina, A. Minotti, S. Quaresima, and V. Foglietti, "Dual frequency PECVD silicon nitride for fabrication of CMUTs' membranes," *Sensors and Actuators, A: Physical*, 2006.
- [51] T. Xu, C. Tekes, and F. Degertekin, "CMUTs with high-K atomic layer deposition dielectric material insulation layer," *IEEE Transactions on Ultrasonics, Ferroelectrics, and Frequency Control*, 2014.
- [52] E. Bahette, J. F. Michaud, D. Certon, D. Gross, and D. Alquier, "Progresses in cMUT device fabrication using low temperature processes," *Journal of Micromechanics and Microengineering*, 2014.
- [53] U. Gösele and Q. Tong, "Semiconductor wafer bonding," *Annual review of materials science*, vol. 28, no. 1, pp. 215–241, 1998.
- [54] M. A. Schmidt, "Wafer-to-wafer bonding for microstructure formation," *Proceedings of the IEEE*, vol. 86, no. 8, pp. 1575–1585, 1998.
- [55] Y. Huang, A. Sanli Ergun, E. Hægström, M. H. Badi, and B. T. Khuri-Yakub, "Fabricating capacitive micromachined ultrasonic transducers with wafer-bonding technology," *Journal of Microelectromechanical Systems*, 2003.

- [56] X. Zhuang, I. O. Wygant, D. S. Lin, M. Kupnik, O. Oralkan, and B. T. Khuri-Yakub, “Wafer-bonded 2-D CMUT arrays incorporating through-wafer trench-isolated interconnects with a supporting frame,” *IEEE Trans. Ultrason., Ferroelec., Freq. Contr.*, vol. 56, no. 1, pp. 182–192, jan 2009.
- [57] A. S. Logan, L. L. P. Wong, and J. T. W. Yeow, “2-D CMUT wafer bonded imaging arrays with a row-column addressing scheme,” in *Proc. IEEE Ultrason. Symp.*, sep 2009, pp. 984–987.
- [58] D. Gross, M. Perroteau, D. Certon, C. Coutier, and M. Legros, “Fabrication and characterization of wafer-bonded cMUT arrays dedicated to ultrasound-image-guided FUS,” in *2014 IEEE International Ultrasonics Symposium*. IEEE, 2014, pp. 181–184.
- [59] A. I. H. Chen, L. L. P. Wong, Z. Li, S. Na, and J. T. W. Yeow, “Practical CMUT fabrication with a nitride-to-oxide-based wafer bonding process,” *Journal of Microelectromechanical Systems*, vol. 26, no. 4, pp. 829–836, 2017.
- [60] K. K. Park, H. Lee, M. Kupnik, and B. T. Khuri-Yakub, “Fabrication of capacitive micromachined ultrasonic transducers via local oxidation and direct wafer bonding,” *Journal of Microelectromechanical Systems*, 2011.
- [61] M. J. Molgaard, J. M. Hansen, M. H. Jakobsen, and E. V. Thomsen, “Sensitivity optimization of wafer bonded gravimetric CMUT sensors,” *Journal of Microelectromechanical Systems*, 2018.
- [62] M. Engholm, “Capacitive Micromachined Ultrasonic Transducers for 3-D Imaging,” Ph.D. dissertation, The Technical University of Denmark, 2018.
- [63] K. R. Williams and R. S. Muller, “Etch rates for micromachining processing,” *Journal of Microelectromechanical Systems*, 1996.
- [64] G. G. Yaralioglu, A. S. Ergun, B. Bayram, E. Hægström, and B. T. Khuri-Yakub, “Calculation and measurement of electromechanical coupling coefficient of capacitive micromachined ultrasonic transducers,” *IEEE Trans. Ultrason., Ferroelec., Freq. Contr.*, vol. 50, no. 4, pp. 449–456, 2003.

- [65] M. M. W. Chang, M. T. Deng, J. T. Gwo, J. D. Mai, and E. Hsu, "Polymer-based capacitive micromachined ultrasonic transducers (CMUT) for micro surgical imaging applications," in *Proceedings of 1st IEEE International Conference on Nano Micro Engineered and Molecular Systems, 1st IEEE-NEMS*, 2006.
- [66] Z. Li, A. I. Chen, L. L. Wong, S. Na, and J. T. Yeow, "Fabrication of Polymer-Based Wafer-Bonded Capacitive Micromachined Ultrasonic Transducers," in *2015 IEEE International Ultrasonics Symposium, IUS 2015*, 2015.
- [67] R. Manwar, T. Simpson, A. Bakhtazad, and S. Chowdhury, "Fabrication and Characterization of a High Frequency and High Coupling Coefficient CMUT Array," *Microsystem Technologies*, pp. 1–13, 2016.
- [68] D. C. Pang and C. M. Chang, "Development of a novel transparent flexible capacitive micromachined ultrasonic transducer," *Sensors (Switzerland)*, 2017.
- [69] X. Zhang, O. Adelegan, F. Y. Yamaner, and O. Oralkan, "An optically transparent capacitive micromachined ultrasonic transducer (CMUT) fabricated using SU-8 or BCB adhesive wafer bonding," in *IEEE International Ultrasonics Symposium, IUS*, 2017.
- [70] C. D. Gerardo, E. Cretu, and R. Rohling, "Fabrication and testing of polymer-based capacitive micromachined ultrasound transducers for medical imaging," *Microsystems and Nanoengineering*, 2018.
- [71] A. S. Savoia, B. Mauti, G. Caliano, G. Matrone, M. Piastra, R. Bardelli, F. Toia, F. Quaglia, and A. Ramalli, "A 3D packaging technology for acoustically optimized integration of 2D CMUT arrays and front end circuits," in *IEEE International Ultrasonics Symposium, IUS*, 2017.
- [72] A. I. H. Chen, L. L. P. Wong, S. Na, Z. Li, M. Macecek, and J. T. W. Yeow, "Fabrication of a Curved Row-Column Addressed Capacitive Micromachined Ultrasonic Transducer Array," *J. Microelectromech. S.*, vol. 25, no. 4, pp. 675–682, 2016.
- [73] F. Niklaus, G. Stemme, J. Q. Lu, and R. J. Gutmann, "Adhesive wafer bonding," 2006.
- [74] S. Olcum, K. Oğuz, M. N. Şenlik, F. Y. Yamaner, A. Bozkurt, A. Atalar, and H. Köymen, "Wafer bonded capacitive micromachined underwater transducers," in *Proceedings - IEEE Ultrasonics Symposium*, 2009.

- [75] F. Y. Yamaner, X. Zhang, and Ö. Oralkan, “A three-mask process for fabricating vacuum-sealed capacitive micromachined ultrasonic transducers using anodic bonding,” *IEEE Transactions on Ultrasonics, Ferroelectrics, and Frequency Control*, 2015.
- [76] X. Zhang, O. Adelegan, F. Y. Yamaner, and O. Oralkan, “CMUTs on glass with ITO bottom electrodes for improved transparency,” in *IEEE International Ultrasonics Symposium, IUS*, 2016.
- [77] X. Zhang, F. Y. Yamaner, and O. Oralkan, “Fabrication of Vacuum-Sealed Capacitive Micromachined Ultrasonic Transducers with Through-Glass-Via Interconnects Using Anodic Bonding,” *Journal of Microelectromechanical Systems*, 2017.
- [78] G. Wallis and D. I. Pomerantz, “Field assisted glass-metal sealing,” *Journal of Applied Physics*, 1969.
- [79] L. Möckl, D. C. Lamb, and C. Bräuchle, “Super-resolved Fluorescence Microscopy: Nobel Prize in Chemistry 2014 for Eric Betzig, Stefan Hell, and William E. Moerner,” *Angewandte Chemie International Edition*, 2014.
- [80] C. Errico, J. Pierre, S. Pezet, Y. Desailly, Z. Lenkei, O. Couture, and M. Tanter, “Ultrafast ultrasound localization microscopy for deep super-resolution vascular imaging,” *Nature*, vol. 527, no. 7579, pp. 499–502, 2015.
- [81] B. Chang, P. Leussink, F. Jensen, J. Hübner, and H. Jansen, “DREM: Infinite etch selectivity and optimized scallop size distribution with conventional photoresists in an adapted multiplexed Bosch DRIE process,” *Microelectronic Engineering*, 2018.
- [82] J. Wibbeler, G. Pfeifer, and M. Hietschold, “Parasitic charging of dielectric surfaces in capacitive microelectromechanical systems (MEMS),” *Sensors and Actuators A: Physical*, vol. 71, no. 1-2, pp. 74–80, 1998.
- [83] P. J. French, “Polysilicon: A versatile material for microsystems,” in *Sensors and Actuators, A: Physical*, 2002.
- [84] E. Ibok and S. Garg, “A Characterization of the Effect of Deposition Temperature on Polysilicon Properties Morphology, Dopability, Etchability, and Polycide Properties,” *Journal of the Electrochemical Society*, vol. 140, no. 10, pp. 2927–2937, 1993.



- [85] F. C. Eversteyn and B. H. Put, "Influence of AsH<sub>3</sub>, PH<sub>3</sub>, and B<sub>2</sub>H<sub>6</sub> on the Growth Rate and Resistivity of Polycrystalline Silicon Films Deposited from a SiH<sub>4</sub>-H<sub>2</sub> Mixture," *Journal of the Electrochemical Society*, vol. 120, no. 1, pp. 106–110, 1973.
- [86] B. Loisel, L. Haji, and M. Guendouz, "LPCVD SILICON FOR ACTIVE DEVICES," *Journal de Physique Colloques*, vol. 50, pp. C5-467–C5-477, 1989.
- [87] L. Chen, J. Miao, L. Guo, and R. Lin, "Control of stress in highly doped polysilicon multi-layer diaphragm structure," *Surface and Coatings Technology*, 2001.
- [88] J. Yang, H. Kahn, A.-Q. He, S. M. Phillips, and A. H. Heuer, "A new technique for producing large-area as-deposited zero-stress LPCVD polysilicon films: the multipoly process," *Journal of Microelectromechanical Systems*, vol. 9, no. 4, pp. 485–494, 2000.
- [89] J. B. Lasky, S. R. Stiffler, F. R. White, and J. R. Abernathy, "Silicon-on-insulator (SOI) by bonding and etch-back," in *1985 International Electron Devices Meeting*. IEEE, 1985, pp. 684–687.
- [90] I. T. Johansen, "Electrical conductivity in evaporated silicon oxide films," *Journal of Applied Physics*, vol. 37, no. 2, pp. 499–507, 1966.
- [91] J. Vermeer, "The impulse breakdown strength of pyrex glass," *Physica*, vol. 20, no. 1-6, pp. 313–326, 1954.
- [92] J. A. Jensen, "Safety assessment of advanced imaging sequences II: Simulations," *IEEE transactions on ultrasonics, ferroelectrics, and frequency control*, vol. 63, no. 1, pp. 120–127, 2015.
- [93] C. Kittel, *Introduction to solid state physics*. Wiley New York, 1976.
- [94] D. A. Neamen, *Semiconductors Physics and Devices: Basic Principles*. McGraw-Hill, 2012.
- [95] J. A. Jensen, H. Holten-Lund, R. T. Nilsson, M. Hansen, U. D. Larsen, R. P. Domsten, B. G. Tomov, M. B. Stuart, S. I. Nikolov, M. J. Pihl, Y. Du, J. H. Rasmussen, and M. F. Rasmussen, "SARUS: A Synthetic Aperture Real-Time Ultrasound System," *IEEE Trans. Ultrason., Ferroelec., Freq. Contr.*, vol. 60, no. 9, pp. 1838–1852, sep 2013.

## APPENDIX A

---

Paper A - BCB polymer based row-column addressed  
CMUT

---

# BCB polymer based row-column addressed CMUT

Andreas Spandet Havreland\*, Martin Lind Ommen\*, Chantal Silvestre\*, Mathias Engholm\*,  
Jørgen Arendt Jensen† and Erik Vilain Thomsen\*

\* Department of Micro and Nanotechnology, Technical University of Denmark, DK-2800 Kgs. Lyngby, Denmark

† Center for Fast Ultrasound Imaging, Department of Electrical Engineering,  
Technical University of Denmark, DK-2800 Lyngby, Denmark

**Abstract**—This paper presents an inexpensive, low temperature and rapid fabrication method for capacitive micromachined ultrasonic transducers (CMUT). The fabrication utilizes the bonding and dielectric properties of the photosensitive polymer Benzocyclobutene (BCB). A BCB based row-column addressed CMUT with integrated apodization has been fabricated and characterized with initial impedance measurement. Furthermore, two linear BCB CMUT arrays have been fabricated with different bottom electrode designs and characterized acoustically. All the fabricated arrays have a center frequency of 2.5 MHz when immersed into water and a pull-in voltage of 75 V. Stability tests have showed a stable coupling coefficient of approximately 0.1 during 10 hours of biased operation. Acoustic measurements, with a hydrophone positioned 1 cm from the CMUTs, have showed a peak-to-peak pressure of 14 kPa.

## I. INTRODUCTION

Ultrasound transducers have for decades been based on piezoelectric technology, which today is a highly optimized technology. A promising alternative technology is the Capacitive Micromachined Ultrasonic Transducer (CMUT), which has the advantages of a wider bandwidth, and less acoustic impedance mismatch between transducer and tissue compared to a piezo transducer among others. The CMUT technology has furthermore higher design flexibility and allows for more closely packed active elements, thus, enabling the possibility for high frequency transducers. CMUTs are made by conventional MEMS (microelectromechanical systems) fabrication techniques. A CMUT transducer relies on having thousands of tightly sealed cavities, which can be obtained by either bonding or sacrificial release [1], [2]. If a bonding method is used the bonding process becomes one of the more critical steps in the fabrication process. Several methods have been demonstrated in the literature with different wafer-bonding techniques, where fusion/direct bonding and anodic bonding are among the more common methods [1], [3].

A third option is to use Benzocyclobutene (BCB) as a spacer and adhesive bonding material. CMUTs fabricated by adhesive wafer bonding using BCB have been demonstrated by [4]–[7]. BCB, from the Dow Chemical Company’s Cyclotene 4000 series, is a spin and spray coatable photosensitive polymer and at the same time being an excellent bonding material, with a reported mean bonding strength up to  $35\text{Jm}^{-2}$  [8]. Furthermore, BCB exhibits a high chemical resistance when fully cured, which becomes an apparent advantage in the presented fabrication process. A BCB based CMUT fabrication has the advantage of being less sensitive to parti-

cles during the bonding process compared to fusion bonding. Hence, transducer arrays with large footprints such as a Row-Column Addressed (RCA) CMUT arrays can benefit from this fabrication technique. A RCA array is a 2-D transducer configuration for 3D ultrasound imaging [9]. Compared with conventional 2-D arrays RCA significantly reduces the required number of connections from  $N^2$  to  $2N$ , with  $N$  being the number of channels.

In the presented CMUT design, BCB is used as a spacer defining the gap in the CMUT. However, BCB is inferior to the typical CMUT spacers  $\text{SiO}_2$  and  $\text{Si}_3\text{N}_4$  in terms of breakdown voltage, Young’s modulus, and thickness uniformity. High quality  $\text{SiO}_2$  and  $\text{Si}_3\text{N}_4$  thin films have a breakdown field of approximately  $1\text{Vnm}^{-1}$  [10] whereas the breakdown field of BCB is  $0.53\text{Vnm}^{-1}$  according to the data sheet. Hence, to make the breakdown voltage of BCB competitive towards  $\text{SiO}_2$  new designs must be incorporated.

This paper addresses an inexpensive and fast BCB fabrication, which is a suitable rapid prototyping platform for different CMUT designs, and in the long term potentially a candidate for ultrasound imaging. This prototyping platform has, however, some challenges with hermetically sealing the cavities, less thin film uniformity, and softer clamping conditions. These effects lead to increased squeeze flow damping, variations in pull-in voltage across the wafer, and presumably more mechanical cross talk between CMUT cells.

## II. FABRICATION AND ARRAY DESIGN

The BCB CMUT fabrication is entirely based on MEMS fabrication techniques. The fabrication is a three mask process schematically shown in Fig 1. A quartz wafer substrate is chosen in order to reduce the number of required masks by enabling backside alignment after the bonding process. In addition, the dielectric properties of the quartz substrate have the benefit of lowering substrate coupling [11].

Step 1 is a lithography step with a negative tone resist (AZ nLOF 2020) followed by 400 nm aluminum deposition and lift-off in Microposit™ remover 1165. CYCLOTENE resin 4022-25 BCB from Dow Chemical Company is, in step 2, spin coated on top of the structured bottom electrode followed by a  $60^\circ\text{C}$  bake for 90 s. The BCB is afterwards exposed (@ 365 nm) for 3.2 s with an intensity of  $13\text{mWcm}^{-1}$  resulting in a dose of  $41.6\text{mJcm}^{-2}$ . A post exposure bake at  $60^\circ\text{C}$  for 90 s is done subsequently. Development is carried out in two beakers using DS3000 from Dow Chemical Company.

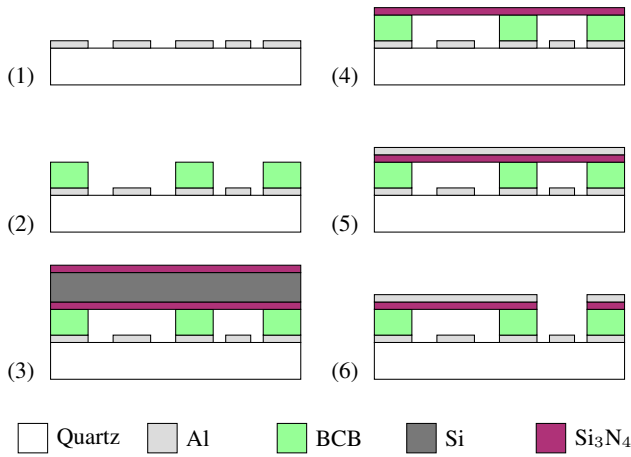


Fig. 1. BCB CMUT fabrication process. Step 1: Lithography, metallization and lift-off. Step 2: BCB lithography on top of patterned metal. Step 3: A double side polished wafer with silicon nitride is bonded to the BCB. Step 4: Top nitride layer and the silicon are etched away in a dry etch and potassium hydroxide (KOH) respectively. Step 5: Metal deposition. Step 6: Lithography followed by an etch through metal and Silicon. Figure is not to scale.

The development time and temperature in the first beaker are approximately 1 min at 30 °C, next in the second beaker for 2 min at room tempered DS3000 which stops the development. A final 90 °C bake for 1 min is performed after development resulting in an approximate final BCB thickness of 450 nm. Notice that the BCB is on top of aluminum pads. The purpose of these pads are to planarize the surface, and thereby achieve the best possible condition for the spin coating process. The planarization pads are not electrically connected in the final device. The plate of the CMUT is made of silicon nitride, and can be fabricated in a cleanroom with a Low Pressure Chemical Vapour Deposition (LPCVD) nitride furnace. The top-wafer consist of a 350  $\mu\text{m}$  double side polished wafer with a 350 nm low stress LPCVD silicon nitride on both sides. To lower the stress-induced curvature across the wafer, the nitride is kept on both sides during bonding in step 3. The nitride top-wafer is bonded to the patterned BCB in a CNI v2.0 desktop nanoimprint tool from NIL Technology. During bonding the temperature is first ramped to 125 °C and kept for 15 min and subsequently raised to 240 °C and kept constant for 1 h. This step is a combined bonding and curing step.

A nitride plate serves two purposes. First, it lowers the fabrication cost compared to a SOI based method, and second the dielectric properties of the nitride increases the overall breakdown voltage and allows the plate to go into pull-in without short circuiting. The top nitride layer and the silicon are etched away in step 4. The nitride is removed in a fluorine plasma and the silicon is etched in potassium hydroxide (KOH). The silicon has a thickness of 350  $\mu\text{m}$  and requires approximately 4.5 h of etching in 28wt.% KOH at 80 °C. The bonded wafers are etched without any backside or edge protection and the BCB will therefore be directly exposed to KOH at the edges. The transparent quartz substrate

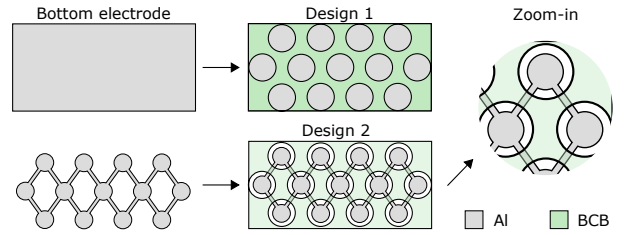


Fig. 2. A top view of two different array designs. Design 1 has a full bottom electrode. Design 2 has a structured bottom electrode and the overlapping region with BCB is significantly reduced (see the zoom-in figure). The planarization pads are for simplicity not included in this sketch.

enables visual inspection of potential damages of the CMUT structures, and it has by visual inspection been observed that KOH etches BCB at the edges with a rate of approximate 1 mm  $\text{h}^{-1}$ . Hence, a safety margin of 1 cm should be sufficient for this process.

In step 5, 400 nm aluminum is deposited on top of the remaining nitride device layer and followed by a lithography step, which later defines the top electrode. In step 6, aluminum is first etched in a wet solution of  $\text{H}_2\text{O}:\text{H}_3\text{PO}_4$  in the volume ratio 1:2. Finally, the nitride is removed in a dry etch process to access the bottom electrode.

The highest temperature during fabrication is 240 °C, which makes this process CMOS compatible. The low process temperature allows for a metal bottom electrode, which can be structured. Two different bottom electrodes designs have been fabricated and are shown schematically in Fig 2. Design 1 has a full bottom electrode. It has the disadvantage of increased parasitic capacitance, however, this design reduces the required masks from three to two. Design 2, inspired by [4], has a structured bottom electrode, which serves two purposes. First, it provides a reduction in parasitic capacitance and second less BCB will be exposed to a high electric field. The BCB on top of the connecting wires must be able to withstand the direct electric field between top and bottom electrodes. However, as opposed to Design 1, it is only in a very small area where BCB should withstand the direct electric field. Hence, the probability of trapping particles or other breakdown lowering defects is reduced.

Often, CMUT transducers for medical imaging are designed to be operated with a DC bias voltage of approximately 200 V [12], [13]. The presented CMUT is a rapid prototype of a BCB CMUT, and the nitride plate is too thin with respect to the mask layout, resulting in a lowered pull-in voltage and resonant frequency. The pull-in voltage is measured to be approximately 75 V. The resonance frequency in air is 4 MHz and reduces to 2.5 MHz when immersed into water.

A BCB RCA CMUT with integrated apodization [14], [15] has been fabricated along with two linear arrays. The RCA CMUT array has a footprint of  $2.6 \times 2.6 \text{ cm}^2$ , and design 2 bottom electrode configuration. The footprint of the two linear arrays are  $5.4 \times 25.4 \text{ mm}^2$ , where one of them is design 1 and the other is design 2.

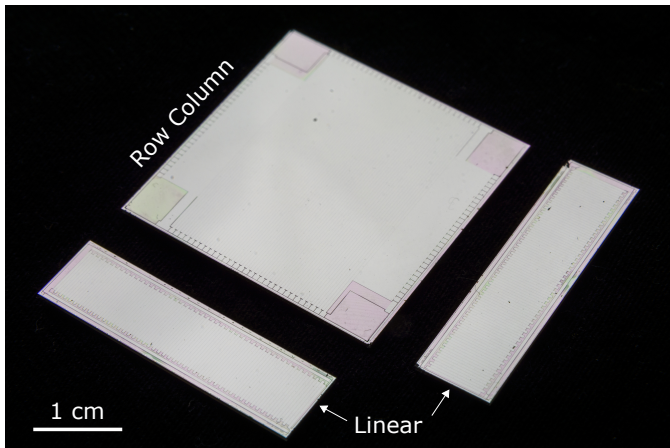


Fig. 3. Image of the presented BCB CMUTs. 62+62 BCB Row-Column addressed CMUT array with integrated apodization and two 92-element linear BCB CMUT arrays with different bottom electrode configurations.

TABLE I  
CMUT ARRAY PARAMETERS

Parameter	Value	
	1D	2D
Array	94	62+62
Number of elements	94	62+62
Element width	270 $\mu\text{m}$	270 $\mu\text{m}$
Element length	5.4 mm	26 mm
Element pitch	270 $\mu\text{m}$	270 $\mu\text{m}$
Cell diameter	60 $\mu\text{m}$	
Electrode diameter (design 2)	40 $\mu\text{m}$	
Cell to cell distance	7.5 $\mu\text{m}$	
BCB cavity height	45 nm	
Nitride plate thickness	350 nm	

The final transducers are shown in Fig 3. The 1-D linear arrays consist of 94 elements each with 288 CMUT cells and the RCA array consists of 62 rows and 62 columns each having 1254 CMUT cells with apodization included. All array parameters can be found in Table I.

### III. RESULTS

For this BCB fabrication technique to be of interest the performance has to be constant in time. Hence, operational stability is a key parameter, and a Row-Column element with integrated apodization has been stability tested by impedance measurements during 10 hours of biased operation. The measurements were performed using an Agilent 4294A Precision Impedance Analyzer with a varying DC voltage and an AC voltage of 50 mV. The stability results can be found in Fig 4. The figure contains four plots where a) is the applied voltage sequence. The voltage steps of 0 V, 65 V and -65 V are applied to the CMUT in a sequence such all transition combinations are present. 65 V corresponds to  $\sim 85\%$  of the pull-in voltage. The capacitance and the coupling coefficient  $\kappa^2$  are depicted in b) and c). The capacitance and coupling coefficient have the same qualitative behavior. An increasing tendency over time is observed for both biased polarities. The underlying reason for this increasing behavior is not yet understood. However, it is

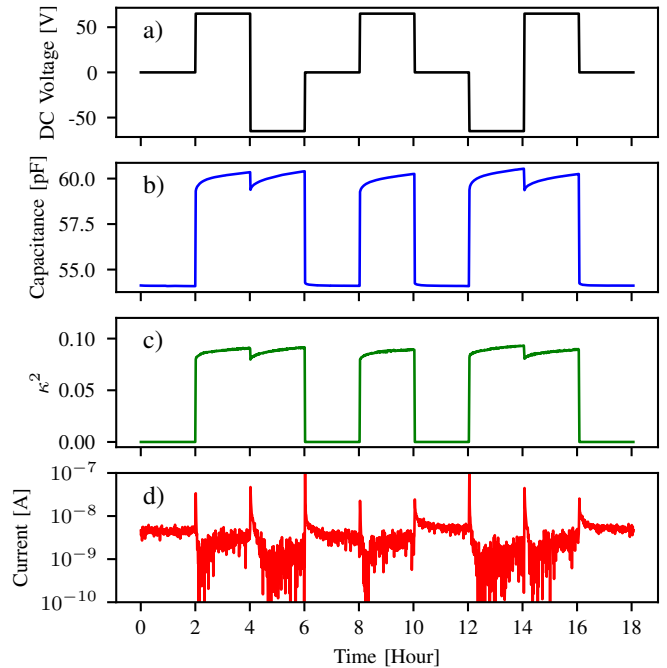


Fig. 4. Stability measurements during 10 hours of operation on a Row test element having a design 2 bottom electrode configuration. a) The applied DC voltage sequence. b) The measured capacitance. c) The fitted coupling coefficient. A slow increasing tendency during 2 hours of operation is observed in both plots. d) The measured current. Notice none of the measured parameters show any polarity depended characteristics.

not believed to be dielectric charging, since these parameters would then be expected to decay in time in one of the biased polarities or both. The coupling coefficient is estimated by fitting a lumped element model to the impedance spectra. The magnitude of the coupling coefficient is approximately 0.1 during operation, and is furthermore observed to be equal for both polarities.

To verify the absence of dielectric charging the leak current through the CMUT is shown in d). The current in a polymer depends on several parameters and has multiple regimes in its IV characteristic [16]. The measured current stabilizes in the nA range for both polarities, and does not show any signs of dielectric charging.

The two 1-D linear arrays have been acoustically characterized. Hydrophone measurements were performed in water, using a calibrated ONDA HGL-0400 hydrophone positioned 1 cm from the CMUT. Prior to the measurement, PDMS has been coated on top of the arrays to ensure electrical isolation of the elements during operation. A 2.5 MHz two-cycle sine pulse was used to excite the CMUTs with a 70 V DC bias and an AC peak-to-peak voltage of 10 V. The acoustic results are shown in Fig 5. The two upper plots show the hydrophone response and the lower plot shows the Fourier spectrum of the two signals. The hydrophone responses are an average of 30 measurements of the same element during a time period of 3 min. The averaged hydrophone responses show a small

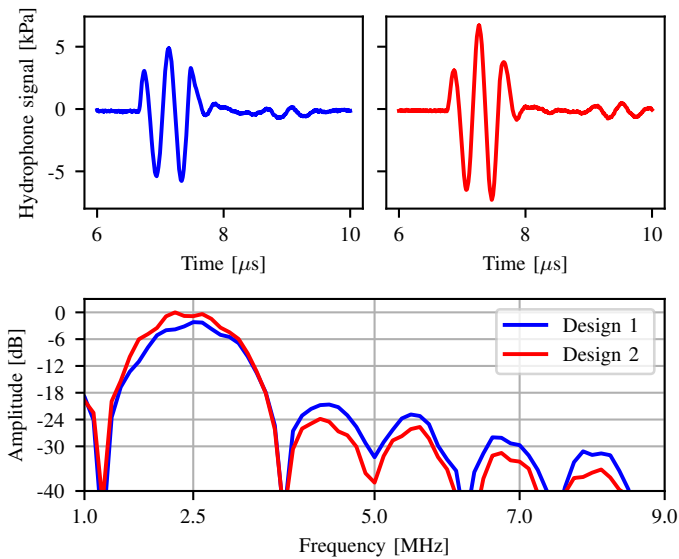


Fig. 5. Acoustic measurements of linear CMUT elements. Upper figures: Hydrophone response for the two array designs. To reduce noise 30 signals have been averaged. The smaller signal at  $9\mu\text{s}$  corresponds to the reflection from the PDMS. Lower figure: Fourier spectrum for a two period sine pulse with a DC bias voltage of 70 V and a peak-to-peak AC voltage of 10 V.

amplitude increase for Design 2. The peak-to-peak pressure is measured to be 10 kPa and 14 kPa for design 1 and 2, respectively, which might suggest the amplitude is design depend. The current output pressure is too low and noisy to be used for medical imaging, and further optimization will be needed to increase the output pressure. In the Fourier spectrum it is seen that the side lobes from the higher harmonics starts in the range between -18 dB and -24 dB, thus, not nearly as good as other CMUT in the literature, where a -40 dB suppression of the second and third harmonic can be found [17]. In conclusion structuring the bottom electrode does not only reduce the parasitic capacitance and thereby increase the sensitivity in receive, but it might also have the advantage of an increased peak-to-peak pressure. However, despite improvements in the design, more optimization is needed to make BCB CMUTs competitive towards other CMUT fabrication techniques and ultimately the piezoelectric technology.

#### IV. CONCLUSION

An inexpensive and rapid BCB fabrication process for 1-D and 2-D CMUT array is proposed. Functional 2.5 MHz BCB CMUTs have been fabricated and demonstrated. Two linear arrays with different bottom electrode configuration have been characterized one with a uniform bottom electrode and another with a structured bottom electrode. The presented BCB CMUTs have been stability tested during 10 hours of operation, and a coupling coefficient  $\kappa^2$  of approximately 0.1 has been observed. BCB based 1-D linear elements have been acoustically characterized with a 2-cycle sine pulse, where the peak-to-peak pressure, at 1 cm, was measured to be 14 kPa.

#### V. ACKNOWLEDGEMENT

We would like to thank the Danish Innovation Fund and BK Ultrasound for funding this research, and the Otto Mønsted fund for financial support of travel expenses.

#### REFERENCES

- [1] Y. Huang, A. Sanli Ergun, E. Hægström, M. H. Badi, and B. T. Khuri-Yakub, "Fabricating capacitive micromachined ultrasonic transducers with wafer-bonding technology," *Journal of Microelectromechanical Systems*, vol. 12, no. 2, pp. 128–137, 2003.
- [2] A. S. Ergun, G. G. Yaralioglu, and B. T. Khuri-Yakub, "Capacitive micromachined ultrasonic transducers: Theory and technology," *Journal of Aerospace Engineering*, vol. 16, pp. 76–84, 2003.
- [3] S. Olcum, K. Ouz, M. N. enlik, F. Y. Yamaner, A. Bozkurt, A. Atalar, and H. Köymen, "Wafer bonded capacitive micromachined underwater transducers," *Proceedings - IEEE Ultrasonics Symposium*, p. 5441699, 2009.
- [4] Z. Li, A. I. Chen, L. L. Wong, S. Na, and J. T. Yeow, "Fabrication of polymer-based wafer-bonded capacitive micromachined ultrasonic transducers," in *2015 IEEE International Ultrasonics Symposium, IUS 2015*, 2015.
- [5] Z. Li, L. L. P. Wong, A. I. H. Chen, S. Na, J. Sun, and J. T. W. Yeow, "Fabrication of capacitive micromachined ultrasonic transducers based on adhesive wafer bonding technique," *Journal of Micromechanics and Microengineering*, vol. 26, no. 11, p. 115019, 2016.
- [6] R. Manwar, T. Simpson, A. Bakhtazad, and S. Chowdhury, "Fabrication and characterization of a high frequency and high coupling coefficient CMUT array," *Microsystem Technologies*, pp. 1–13, 2016.
- [7] R. Manwar and S. Chowdhury, "Experimental analysis of bisbenzocyclobutene bonded capacitive micromachined ultrasonic transducers," *Sensors*, vol. 16, no. 7, p. 959, 2016.
- [8] F. Forsberg, F. Saharil, T. Haraldsson, N. Roxhed, G. Stemme, W. van der Wijngaart, and F. Niklaus, "A comparative study of the bonding energy in adhesive wafer bonding," *Journal of Micromechanics and Microengineering*, vol. 23, no. 8, p. 85019, 2013.
- [9] C. C. E. Morton and G. R. G. Lockwood, "Theoretical assessment of a crossed electrode 2-D array for 3-D imaging," *IEEE Symposium on Ultrasonics*, 2003, vol. 1, no. c, pp. 968–971, 2003.
- [10] C. M. Osburn and E. J. Weitzman, "Electrical conduction and dielectric breakdown in silicon dioxide films on silicon," *Journal of The Electrochemical Society*, vol. 119, no. 5, p. 603, 1972.
- [11] M. Engholm, H. Bouzari, J. A. Jensen, and E. V. Thomsen, "Capacitive substrate coupling of row-column-addressed 2-D CMUT arrays," *Proceedings of 2016 IEEE International Ultrasonics Symposium*, vol. 2016-, p. 7728384, 2016.
- [12] M. Engholm, T. L. Christiansen, C. Beers, J. P. Bagge, L. N. Moesner, H. Bouzari, A. Lei, M. Berkheimer, M. B. Stuart, J. A. Jensen, and E. V. Thomsen, "A hand-held row-column addressed CMUT probe with integrated electronics for volumetric imaging," *Proceedings of 2015 IEEE International Ultrasonics Symposium*, p. 7329132, 2015.
- [13] A. S. Savoia, G. Caliano, and M. Pappalardo, "A CMUT probe for medical ultrasonography: From microfabrication to system integration," *IEEE Transactions on Ultrasonics Ferroelectrics and Frequency Control*, vol. 59, no. 6, pp. 1127–1138, 2012.
- [14] M. F. Rasmussen, T. L. Christiansen, E. V. Thomsen, and J. A. Jensen, "3-D imaging using row-column-addressed arrays with integrated apodization. Part I: Apodization design and line element beamforming," *IEEE Transactions on Ultrasonics, Ferroelectrics, and Frequency Control*, vol. 62, no. 5, pp. 947–958, 2015.
- [15] T. L. Christiansen, M. F. Rasmussen, J. P. Bagge, L. N. Moesner, J. A. Jensen, and E. V. Thomsen, "3-D imaging using row-column-addressed arrays with integrated apodization. Part II: Transducer fabrication and experimental results," *IEEE Transactions on Ultrasonics, Ferroelectrics and Frequency Control*, vol. 62, no. 5, pp. 959–971, 2015.
- [16] L. A. Dissado and J. C. Fothergill, *Electrical degradation and breakdown in polymers*. London: Peter Peregrinus, 1992.
- [17] A. Lei, S. E. Diederichsen, S. M. Hansen, M. B. Stuart, J. P. Bagge, J. A. Jensen, and E. V. Thomsen, "Elimination of second-harmonics in CMUTs using square pulse excitation," *Proceedings of 2016 IEEE International Ultrasonics Symposium*, vol. 2016-, p. 7728824, 2016.



## APPENDIX B

---

Paper B - Design of a novel zig-zag 192+192 Row  
Column Addressed Array Transducer: A simulation study.

---



# Design of a novel zig-zag 192+192 Row Column Addressed Array Transducer: A simulation study.

Mikkel Schou<sup>1</sup>, Andreas Spandet Havreland<sup>2</sup>, Mathias Engholm<sup>2</sup>, Matthias Bo Stuart<sup>1</sup>,  
Erik Vilain Thomsen<sup>2</sup> and Jørgen Arendt Jensen<sup>1</sup>

<sup>1</sup>Center for Fast Ultrasound Imaging, Dept. of Elec. Eng., Bldg. 349. <sup>2</sup> Department of Micro and Nanotechnology, Technical University of Denmark, 2800 Kgs. Lyngby, Denmark

**Abstract**—Super resolution imaging (SRI) can benefit greatly from full 3D imaging to compensate for vessel structures moving out of the image plane. Row Column Addressed (RCA) arrays can provide such 3D imaging with low-complexity probe design. A RCA probe is being designed for a rat kidney with 192 + 192 elements to ensure low sidelobes and an imaging volume of 15x15x15 mm<sup>3</sup>. The design space of such a transducer is investigated with this in mind. Capacitive micromachined ultrasonic transducer (CMUT) technology allows for new geometric shapes, including a near kerf-less zig-zag interwoven structure, which provides flexibility in the design process of new RCA. This work compares the image quality of a straight element RCA array with an RCA array with an interwoven zig-zag structure by simulations, to assess the image quality of a zig-zag structured RCA. The Point Spread Function (PSF) showed symmetry in both the azimuth and elevation direction. Both the straight and interwoven design had a lateral Full Width Half Maximum (FWHM) of approximately 0.6  $\lambda$ , close to the ideal FWHM without apodization. The interwoven design showed a slight contrast loss over the straight design, which was quantified with the Cystic Resolution (CR). The CR at 20 dB for the straight design was 1.3  $\lambda$ , compared to 1.4  $\lambda$  of the interwoven design. The two designs had comparable PSF metrics. The interwoven zig-zag structure is therefore a viable solution to meet the requirements of the rodent experiments and provides a new level of design flexibility for manufacturing RCA transducer arrays.

## I. INTRODUCTION

Super Resolution Imaging (SRI) can become an invaluable tool for understanding and diagnosing various disease processes that influences the microvascular blood flow, such as cancer, stroke, and arteriosclerosis [1]. SRI combines the use of microbubbles, a long known contrast agent used in medical ultrasound, with precise tracking of their temporal movement through a series of ultrasound frames to enhance the spatial resolution beyond the diffraction limit of the ultrasound system. The 2-D SRI method in its current state is prone to errors. This include movement artifacts from tissue, respiration and movement of the transducer probe itself [2], which complicates the microbubble tracking even more. The errors due to motion are often solved by fixating the subject and the transducer probe, which is unrealistic in a real clinical setting.

Another suspected source of error is vessel structures moving in and out of the image plane the in elevation plane [2]. 2-D ultrasound systems often uses a 1-D array, which have a broad beam in elevation, thereby receiving echoes from microbubble outside the image plane [3]. 3-D ultrasound can capture a full

3-D volume and is in principle not limited to a single plane in elevation. However implementation of 3-D ultrasound have proven itself difficult. 3-D imaging techniques can in general be performed using either one of two methods. Either using a translating 1-D array or a 2-D array. 2-D arrays can further be divided into fully populated arrays, using microbeamformers, or as Row-Column Addressed Arrays (RCA) [4]. Methods such as translating the ultrasound probe from emission to emission have shown 3-D volumes, but when looking at vessel structures at around 2-20  $\mu\text{m}$  in size [3], translation must be performed in a highly precise manner. Combining this with the long acquisition time required for SRI makes the method highly impractical for SRI. A matrix probe has shown great resolution in 3-D, this however requires  $N^2$  number of connections where  $N$  is the number of elements in each dimension of the 2-D array, or by microbeamforming which puts high demand on the front end electronics [5]. RCA have shown potential for lower production cost and the use of fewer connections allows for a simpler setup.

An in-vivo measurement of a rat kidney is in development to test the feasibility of 3-D SRI. The dimension of the rat kidney requires an acoustical window of approximately 15 by 15 mm, which is assumed to be the desired dimensions of the RCA probe [6]. The intended technology for the probe is Capacitive Micromachined Ultrasonic Transducer (CMUT) elements, which allows for manufacturing of new structures. The channel count of 192+192 combined with a high frequency necessitates flexibility in the manufacturing process of the CMUT array. For this reason a new kerf-less interwoven zig-zag structure is introduced. The new interwoven zig-zag RCA design allows for different implementation method and is therefore investigated here. In this work we present a simulation model and results of a 192+192, 8 MHz interwoven RCA design, to evaluate whether it carries a penalty in imaging performance compared to a traditional geometry.

## II. METHODS

### A. Row Column addressed arrays

The standard RCA probe is constructed as a matrix array where only the rows and columns can be addressed, limiting the number of connections to  $2N$ . A cutout of the straight RCA is visualized in Fig. 1 to the left. The row and columns of the RCA are connected such that a single element is comprised of  $M$  cells, and  $N = M$ . For the interwoven design two

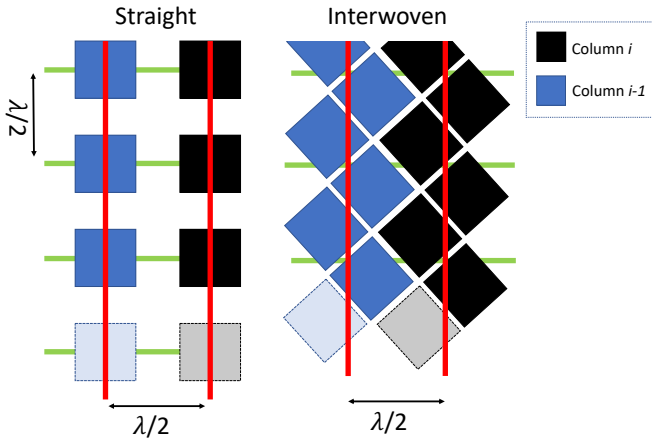


Fig. 1: Simulation setup. To the left the straight element RCA is visualized, the cells have  $\lambda/2$  spacing which matches the inter-element spacing. To the right the interwoven structure is visualized. The red lines symbolizes the assumed acoustic center of the column elements, the green likewise for the rows.

cells are acting as a single unit, by arranging the dual cells in a zig-zag like structure, one element is then comprised of  $2M$  cells. The interwoven design gives an overlapping region between two neighboring elements causing an almost kerf-less like structure as seen to the right in Fig. 1. A larger aperture size provides a method of maintaining a constant resolution in a deeper region, and it has been observed that the resolution and contrast of RCA transducers scales with number of channels [7]. The RCA array offers a linear scale of number of channels as oppose to the matrix probe making it ideal for larger aperture sizes. Grating lobes arises when the spacing of the elements are too big [7]. To avoid grating lobes an element spacing of half the wavelength ( $\lambda/2$ ) is necessary, and this applies for both the straight element and the interwoven. A  $192 + 192$  RCA probe with a center frequency of 8 MHz meets the requirement for the rodent experiment but is difficult to manufacture. The interwoven design is more flexible in the manufacturing process and therefore needs to be evaluated from an imaging perspective.

### B. Imaging sequence

Synthetic Aperture imaging (SAI) have been widely used to enhance resolution and contrast in 2-D ultrasound imaging and increased frame rate [8]. For RCA SAI provides a method for insonifying an entire volume and collect backscattered signals from that region without being limited to a single plane. The simple SAI approach is to use a single element emission scheme where one single line element transmit at a time. All the  $N$  orthogonal line elements are then active in receive and the data is beamformed through a delay-and-sum technique developed by Rasmussen et al [9]. The beamformed data for a single emission is referred to as a low resolution

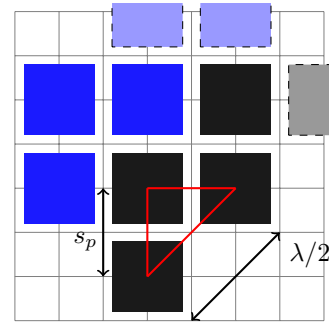


Fig. 2: Section of the interwoven structure, rotated 45 degrees.  $s_p$  is the cell pitch. The red triangle displays the right-angle triangle used to estimate the cell pitch in eq. 1 for the zig zag structure. The interwoven structure have an cell spacing of  $\lambda/\sqrt{8}$ .

TABLE I: Parameters used in simulation

Straight	
Number of cells ( $M$ )	$192 \times 192$
Number of elements/connections	$192+192$
Center frequency	8 MHz
Wavelength ( $\lambda$ )	$192.5 \mu\text{m}$
Line element pitch	$96.25 \mu\text{m}$
Zig Zag structure	
Number of cells ( $M$ )	$(2 \cdot 192) \times (2 \cdot 192)$
Number of elements/connections	$192+192$
Center frequency	8 MHz
Wavelength ( $\lambda$ )	$192.5 \mu\text{m}$
Line element pitch	$96.25 \mu\text{m}$
Cell pitch ( $s_p$ )	$68.05 \mu\text{m}$
Imaging parameters	
No. Transmit events	192
Emission Pulse type	2 cycles of a sinusoid
Roll of apodization	15 pitch lengths of a Hanning
Speed of sound ( $c$ )	$1540 \text{ m/s}$

volume (LRV), as there is no focusing in transmit. A new LRV is formed by emitting with the next line element in the transmit direction. Summing the contribution from all emissions reveals a high resolution volume (HRV), and the dynamic transmit focus is generated synthetically. This scheme is called single element RCA SAI.

The final HRV is comprised of  $N$  transmit events corresponding to the number of elements in one of the two RCA dimensions. The transmit plane is referred to as the azimuth-range plane as steering in transmit is only performed using one side of the RCA array. The receive plane is referred to as the elevation-range plane. The delay-and-sum technique used here assumes that the time of flight is calculated as the distance from a point to a line, and the elongated row and column elements are assumed to be line elements. For the straight element RCA, the reference lines are defined as the center line of the element limited by the edges. For the interwoven design the acoustical center is assumed to be the geometric center line of the zig-zag element. This is visualized in Fig. 1. Here the green line symbolizes the row elements and column lines are marked with red. The zig zag structure will be further

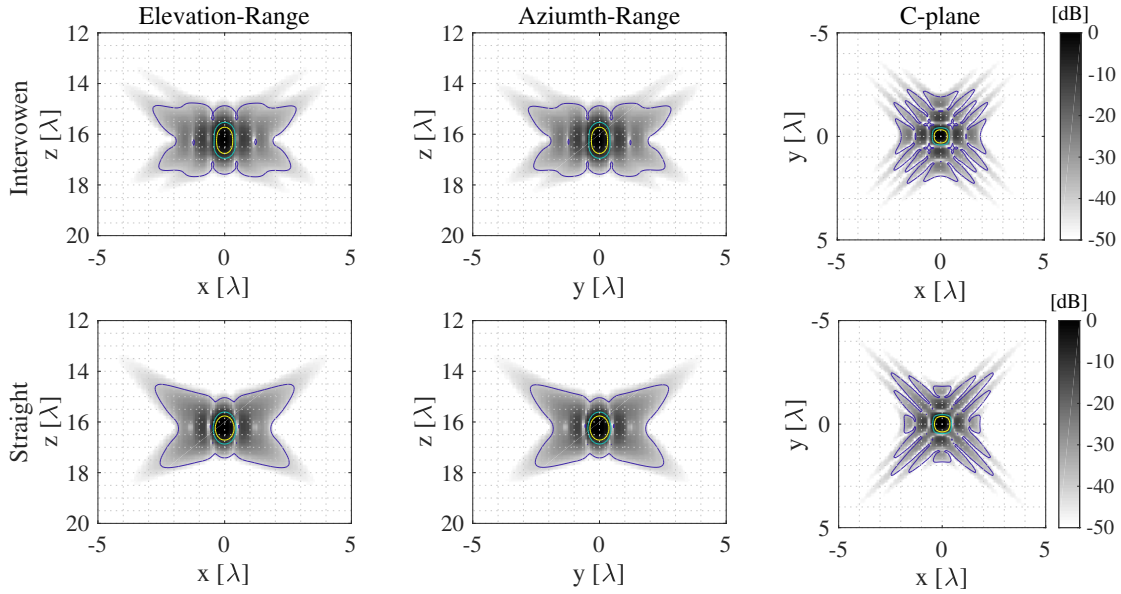


Fig. 3: Figure shows the range-elevation, range-azimuth, and elevation-azimuth planes beamformed from 192 emissions. Simulations parameters can be found in Table I. The top panel shows the results of the interwoven RCA beamformed planes and the bottom panel shows the same three planes for the straight RCA. The contour lines on top shows: 6 dB (yellow), 20 dB (green), and 40 dB (blue). The dynamic range is 50 dB.

described in II-C.

### C. Implementation in Field II

The straight RCA was implemented in Field II ([10], [11]) as  $N$  row elements and  $N$  column elements placed orthogonal to each other in space. The elements were implemented as elongated elements and the row aperture and column aperture was defined separately but spatially on top of each other. The interwoven structure was defined as the individual cells. The simulated received signals from the individual cells were summed without beamforming to emulate the expected responses from a zig-zag element. The line element pitch of the two models was the same for comparison reasons. The spacing in the zig-zag structure was determined by a right-angle triangle, shown in red in Fig. 2.:

$$s_p^2 + s_p^2 = \left(\frac{\lambda}{2}\right)^2 \Leftrightarrow s_p = \frac{\lambda}{\sqrt{8}}. \quad (1)$$

Here  $s_p$  is the cell pitch. To avoid ghost echos, integrated edge apodization was applied to the modelled as a drop in intensity corresponding to a Hanning weighted drop-off in intensity [9]. The parameters used can be found in Table I.

### D. Performance estimators

A point spread function (PSF) was simulated for each of the two transducer models in Field II to estimate the performances. The quantifiable measures used were the full-width-half-maximum (FWHM) and the cystic radius at 20 dB

TABLE II: Estimated metrics

<b>FWHM</b>	Azimuth-Range	Elevation - Range	C-plane
Straight	$0.62 \lambda$	$0.60 \lambda$	$0.60 \lambda$
Interwoven	$0.61 \lambda$	$0.62 \lambda$	$0.62 \lambda$
<b>CR20dB</b>	Azimuth-Range	Elevation-Range	C-plane
Straight	$1.42 \lambda$	$1.42 \lambda$	$1.43 \lambda$
Interwoven	$1.34 \lambda$	$1.34 \lambda$	$1.30 \lambda$

(CR20dB). Cystic resolution can be defined as [12]:

$$CR(r) = \sqrt{\frac{E_{t0}^{out}(r)}{E_{t0}^{tot}}} \quad (2)$$

where  $E^{tot}$  is the total PSF energy in an area and  $E^{out}$  refers to the PSF energy outside the region of interest. In this case the region of interest is a growing sphere as a function of radius  $r$ . The reported value is the radius at which the  $CR$  measure drops below 20 dB. In case of a 3-D PSF, the ideal metric should be in 3-D. However such a measure have yet to be defined, so the two measures were calculated on the three orthogonal planes centered around the PSF. All metrics were normalized by the wavelength, as were the plots.

## III. RESULTS & DISCUSSION

A simulation of a point scatter located at  $[0,0,16.2] \lambda$  was performed for the two setups to extract the PSFs. The results are seen in Fig. 3. The two PSFs are showed using the same RCA SAI without apodization. Three orthogonal planes were beamformed and used to extract metrics to quantify performance. The metrics are found in Table II. The interwoven RCA showed similar resolution as to that of straight RCA with

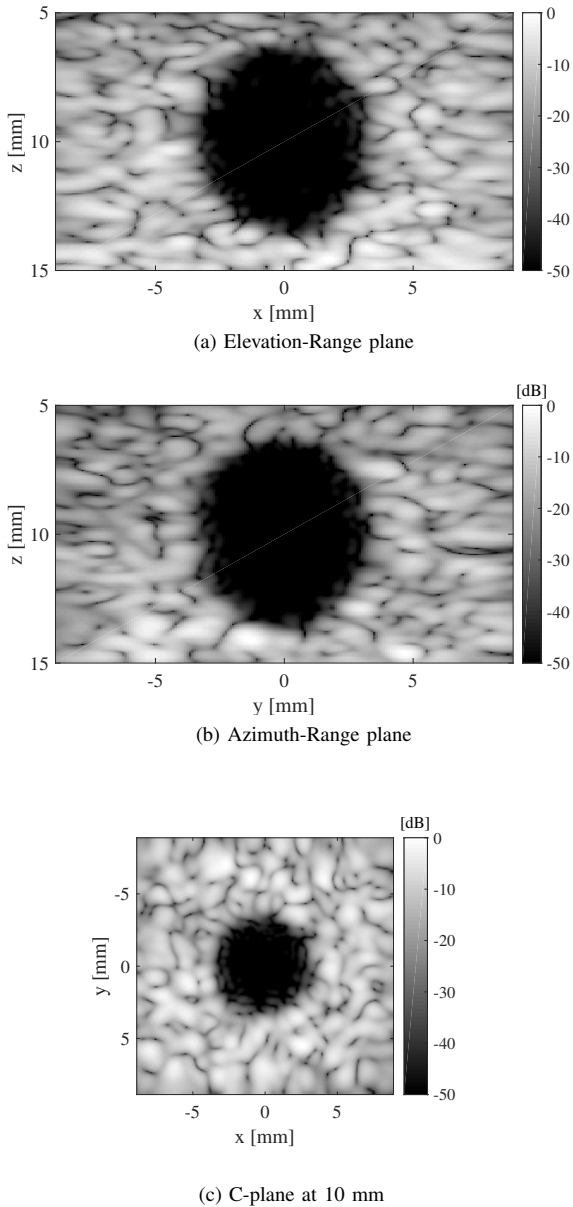


Fig. 4: Three images shows a simulated cyst phantom, here imaged with SA single emission. The round shape of the cyst is maintained in both directions. a) shows the Elevation-Range plane, b) shows the Azimuth-Range plane and c) shows the C-plane at depth 10 mm. All have a dynamic range of 50 dB.

FWHM of approximately  $0.61 \lambda$ , which is close to the limit of the ideal diffraction limited resolution of  $\lambda/2$ . The contrast quantified by CR20dB revealed a slightly better contrast for the straight RCA at 1.34 over 1.42  $\lambda$ . The PSFs showed symmetry in both the Azimuth-Range and Elevation-Range plot suggesting a symmetric geometry of the PSF, which is ideal for 3-D imaging. A spherical cyst phantom was simulated using zig-zag structured RCA model, with an optimized RCA SAI scheme. The cyst phantom consisted of a collection of

scatters in a  $10 \times 10 \times 10 \text{ mm}^3$  region, a region corresponding to a sphere of radius 3 mm and a center of [0,0, 10] mm. The result can be seen in Fig.4.

#### IV. CLOSING STATEMENT

Simulations showed similar imaging performance for the interwoven and the straight RCA, close to the theoretical ideal FWHM of  $\lambda/2$ . This proves that interwoven RCA design, from an imaging perspective, can be implemented instead of the straight one. The interwoven design allows for more flexibility in the manufacturing process. Having a 8 MHz, 192+192 RCA array can provide constant resolution in both directions of the 3-D volumes, which is ideal for SRI. It also allows for more advanced RCA SAI imaging schemes in the future.

#### ACKNOWLEDGMENT

This work was financially supported by the Danish National Advanced Technology Foundation (82-2012-4), Innovation Fund Denmark (7050-00004B) and by BK Medical, Herlev, Denmark.

#### REFERENCES

- [1] C. Errico, J. Pierre, S. Pezet, Y. Desailly, Z. Lenkei, O. Couture, and M. Tanter, "Ultrafast ultrasound localization microscopy for deep super-resolution vascular imaging," *Nature*, vol. 527, pp. 499–502, November 2015.
- [2] K. Christensen-Jeffries, S. Harput, J. Brown, P. N. T. Wells, P. Aljabar, C. Dunsby, M. Tang, and R. J. Eckersley, "Microbubble axial localization errors in ultrasound super-resolution imaging," *IEEE Trans. Ultrason., Ferroelec., Freq. Contr.*, vol. 64, no. 11, pp. 1644–1654, 2017.
- [3] K. Christensen-Jeffries, R. J. Browning, M. Tang, C. Dunsby, and R. J. Eckersley, "In vivo acoustic super-resolution and super-resolved velocity mapping using microbubbles," *IEEE Trans. Med. Imag.*, vol. 34, no. 2, pp. 433–440, February 2015.
- [4] C. E. Morton and G. R. Lockwood, "Theoretical assessment of a crossed electrode 2-D array for 3-D imaging," in *Proc. IEEE Ultrason. Symp.*, 2003, pp. 968–971.
- [5] U. lok and P. C. Li, "Microbeamforming with error compensation," *IEEE Trans. Ultrason., Ferroelec., Freq. Contr.*, vol. 65, no. 7, pp. 1153–1165, July 2018.
- [6] K. B. Hansen, C. A. Villagomez-Hoyos, J. Brasen, K. Diamantis, V. Sboros, C. M. Sørensen, and J. A. Jensen, "Robust microbubble tracking for super resolution imaging in ultrasound," in *Proc. IEEE Ultrason. Symp.*, 2016, pp. 1–4.
- [7] M. F. Rasmussen and J. A. Jensen, "3-D ultrasound imaging performance of a row-column addressed 2-D array transducer: A measurement study," in *Proc. IEEE Ultrason. Symp.*, July 2013, pp. 1460–1463.
- [8] J. A. Jensen, S. Nikolov, K. L. Gammelmark, and M. H. Pedersen, "Synthetic aperture ultrasound imaging," *Ultrasonics*, vol. 44, pp. e5–e15, 2006.
- [9] M. F. Rasmussen, T. L. Christiansen, E. V. Thomsen, and J. A. Jensen, "3-D imaging using row-column-addressed arrays with integrated apodization — Part I: Apodization design and line element beamforming," *IEEE Trans. Ultrason., Ferroelec., Freq. Contr.*, vol. 62, no. 5, pp. 947–958, 2015.
- [10] J. A. Jensen, "Field: A program for simulating ultrasound systems," *Med. Biol. Eng. Comp.*, vol. 10th Nordic-Baltic Conference on Biomedical Imaging, Vol. 4, Supplement 1, Part 1, pp. 351–353, 1996.
- [11] J. A. Jensen and N. B. Svendsen, "Calculation of pressure fields from arbitrarily shaped, apodized, and excited ultrasound transducers," *IEEE Trans. Ultrason., Ferroelec., Freq. Contr.*, vol. 39, pp. 262–267, 1992.
- [12] K. Ranganathan and W. F. Walker, "Cystic resolution: A performance metric for ultrasound imaging systems," *IEEE Trans. Ultrason., Ferroelec., Freq. Contr.*, vol. 54, no. 4, pp. 782–792, 2007.



## APPENDIX C

---

Paper C - CMUT Electrode Resistance Design: Modeling  
and Experimental Verification by a Row-Column Array

---

# CMUT Electrode Resistance Design: Modelling and Experimental Verification by a Row-Column Array

Andreas Spandet Havreland, Mathias Engholm, Borislav Gueorguiev Tomov, Jørgen Arendt Jensen, Ole Hansen  
and Erik Vilain Thomsen

**Abstract**—This paper addresses the importance of having control over the resistivity of the electrodes for capacitive micromachined ultrasonic transducers (CMUT) devices. The electrode resistivity can vary depending on the fabrication technology used, and resistivity control becomes especially important in the cases where metal electrodes can not be used. This raises the question: When is the resistivity of an electrode sufficiently low? To answer this question we have developed a simple design criterion. The criterion describes the attenuation of AC signals along a CMUT element. It is shown that the non-dimensional product between angular excitation frequency, resistance, and capacitance  $\omega RC$  of an element has to be smaller than 0.35 to ensure an AC potential drop along the element of less than 1%. The optimal magnitude and directionality of the transmit pressure will be achieved if CMUT elements are designed according to the developed criteria. Hence, the model can be used to estimate device parameters that will ensure the CMUT is suitable for generating ultrasound images. An example is given where the model is used to predict the required electrode thickness for structured electrodes made of Gold, Aluminium, and Indium-Tin-Oxide, respectively. To verify the model, two Row-Column addressed (RCA) CMUT transducers were used to illustrate the effect of high and low electrode resistivity. One transducer had a sufficient electrode resistivity, and the other had an insufficient electrode resistivity. The RCA CMUT transducers were fabricated using fusion bonding, where the top electrode is made of aluminium and the bottom electrode is made of doped silicon. The resistivity of the aluminium top electrode is  $2 \times 10^{-6} \Omega\text{cm}$  for both transducers, whereas the resistivity for the bottom electrode is  $0.1 \Omega\text{cm}$  for the first transducer and  $0.005 \Omega\text{cm}$  for the second transducer. The transducer with low resistivity emits pressure uniformly along both the rows and columns, whereas the transmit pressure field from the other transducer has a uniformly distributed pressure field along the rows, but a decreasing pressure field along the columns due to the high resistivity in the bottom electrode. The pressure drop, along the columns is frequency dependent and has been observed to be 63%, 74%, and 82% for the excitation frequencies 2 MHz, 4.5 MHz, and 7 MHz, respectively.

## I. INTRODUCTION

Capacitive Micromachined Ultrasonic Transducers (CMUT) have shown promising results within the field of ultrasonic medical imaging [1]. Several CMUT papers have been published demonstrating fabrication [2], theoretical models [3], electronics [4], assembly of transducers [1], and safety concerns [5]. The fabrication process of CMUTs can vary significantly from one transducer design to another. However, common for all CMUTs is the overall structure consisting of a substrate, a cavity, and a vibrating plate or membrane. Furthermore, CMUTs have two electrodes, a top and a bottom electrode. The top electrode is typically a metal electrode, whereas the bottom electrode mostly is made of either a metal or doped silicon.

The resistivity of metal electrodes is on the order of  $10^{-6} \Omega\text{cm}$  [6], while the resistivity of a silicon electrode varies from  $10^4$  to  $10^{-4} \Omega\text{cm}$  depending on the doping level [7]. The resistance in the electrode has to be sufficiently low to achieve acceptable performance of the CMUTs, which in most cases never becomes an issue for metal electrodes due to their low resistivity. However, in special cases it can become challenging to use even highly doped silicon, particularly for long elements such as elements in a Row-Column Addressed (RCA) array. If the resistivity in an electrode becomes too high, the overall system will behave as a low pass filter, and during operation the applied AC signals will be significantly attenuated along the electrode, leading to variations in the transmit pressure. A non-uniform transmitting element will skew the transmitted field and seriously degrade the receive focusing. Additionally, a larger element resistance decreases the received energy leading to an overall degradation of the SNR in the ultrasound image. Another example where limited electrode resistivity can occur is transparent CMUTs [8], [9]. In such applications the transparent conductor Indium-Tin-Oxide (ITO) is typically used as electrode material, due to its optical transparency and low electrical resistivity. However, the resistivity of ITO is on the order of  $10^{-4} \Omega\text{cm}$ , hence, two orders of magnitude higher than that of aluminium and gold films, and electrode resistance can therefore become a significant problem in such devices.

To eliminate problems with electrode resistance it would be natural to design a given CMUT device such that the bottom electrode is made of metal. However, this is not always an option, due to process compatibility as high temperature processes do not permit the use of metals. In the literature

This work is financially supported by the Innovation Fund Denmark (7050-00004B) and by BK Medical (Herlev, Denmark).

A. S. Havreland, M. Engholm and E. V. Thomsen are with the Department of Health Technology, Technical University of Denmark, Kgs. Lyngby, Denmark.

O. Hansen is with the Nanolab Department, Technical University of Denmark, Kgs. Lyngby, Denmark.

B. G. Tomov and J. A. Jensen are with the Center for Fast Ultrasound Imaging, Department of Health Technology, Technical University of Denmark, Kgs. Lyngby, Denmark.

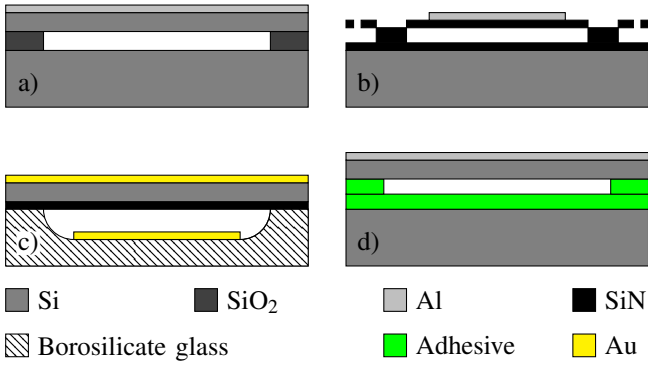


Figure 1. Cross sectional view of different CMUT technologies. a) Fusion bonding [10]. b) Sacrificial release [11]. c) Anodic bonding [12]. d) Adhesive polymer bonding [13].

multiple approaches have been reported, and the four most important techniques are fusion/direct bonding [10], sacrificial release [11], anodic bonding [12], and adhesive polymer bonding [13]. Cross sectional views of a CMUT cell fabricated using the four techniques are shown in Fig. 1. A fusion bonded CMUT is sketched in a). This process requires a post annealing temperature on the order of 1000 °C, which excludes the use of a metal bottom electrode. A doped silicon bottom electrode is therefore commonly used instead. A sacrificial release fabricated CMUT is shown in b). This method allows both metal [1] and silicon [11] bottom electrodes. Thus, resistivity problems can be present in this type of CMUTs, if a silicon electrode is used. An anodically bonded CMUT is shown in c), and a gold electrode will be the natural choice for the bottom electrode. Electrode resistance considerations can also be relevant for transparent applications, when ITO is used as electrode material. Finally, an adhesive polymer bonded CMUT is shown in d). This technique is flexible with respect to design, and enables low temperature bonding between all common semiconductor materials. Similar to the sacrificial release an adhesive bonded CMUT can be designed with both a silicon [13], [14] and a metal bottom electrode [15]. This technology has also been used for transparent applications [16], [17], where electrode resistance again can become an issue. In the CMUT applications where problems with electrode resistance can occur, the resistivity and electrode dimensions have to be chosen correctly to obtain full functionality. The minimum required resistivity and electrode dimensions, such as thickness and length, can be estimated by a simple criterion developed in this paper.

The criterion is developed from delay line theory, which is used to predict the attenuation of AC signals along an element, and experimental data, from two RCA transducers, are used to validate the theory. The RCA transducer has two electrodes perpendicular to each other with different resistivities [18]. A RCA transducer is therefore ideal to evaluate the effect of electrode resistance, since the same CMUT cells can be excited by two different electrode configurations. Measuring the AC potential along the bottom electrode is not easy experimentally, however, the effect can be quantified by measuring the transmit pressure along an element. The

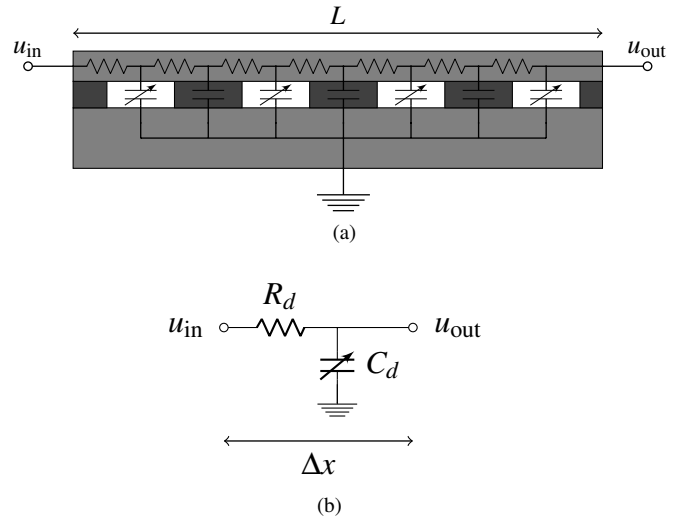


Figure 2. Model of the Row-Column addressed CMUT array. a) Idealized model of a Row-Column element. The resistance through the element is modelled by resistors, the CMUTs cells are modelled as variable capacitors, and the parasitic capacitance is modelled as constant capacitors. b) When the capacitance of the CMUTs and the parasitic capacitance are merged together, the circuit is described as a Resistor Capacitor (RC) delay line.  $R_d$  and  $C_d$  are the resistance and capacitance of a distributed segment of length  $\Delta x$  and are related to the total resistance and capacitance by  $R_d = R/L \cdot \Delta x$  and  $C_d = C/L \cdot \Delta x$ .

model will later be used to estimate the required thickness for different electrode materials. The discussed theory can be used regardless of the fabrication method and applied to both top and bottom electrodes. Publications regarding electrode resistance for CMUTs are limited, and only a brief discussion have been found in [11]. The paper is organized as follows: Section II introduces a delay line theory for CMUT arrays and an explanation of the measurement set-up. Results are discussed and compared to the developed theory in Section III. Finally, Section IV concludes the paper.

## II. METHOD

### A. Modelling

The potential along CMUT elements can be modelled as a delay line as shown in Fig. 2, where (a) shows a common CMUT design with an equivalent circuits on top. The resistivity of the electrode determines the magnitude of the resistors. The variable capacitors represent CMUTs and the constant capacitors represent the parasitic capacitance. By merging the capacitive components, the electronic circuit can be described by Resistor Capacitor (RC) delay lines as shown in Fig. 2 (b). In this model the resistors and capacitors are assumed to be evenly distributed along the element,  $R_d$  and  $C_d$ , are resistance and capacitance of a distributed segment of length  $\Delta x$ . These quantities are related to the total resistance,  $R$ , and the total capacitance  $C$ , by

$$R_d = \frac{R}{L} \Delta x \quad C_d = \frac{C}{L} \Delta x, \quad (1)$$

where  $L$  is the length of the element. The capacitance of a CMUT element can be mathematically formulated as



$$C = C_p + nC_{\text{cell}}, \quad (2)$$

where  $C_p$  is the total parasitic capacitance and  $C_{\text{cell}}$  is the capacitance of each of the  $n$  CMUT cells. The device capacitance of a CMUT cell can be calculated as described in several papers [11], [19], [20], and is determined by cell geometry and gap height. These parameters are fixed depending on the application. The resistance of an element with a uniform cross-sectional area,  $A$ , is [7]

$$R = \frac{\rho L}{A}, \quad (3)$$

where  $\rho$  is the resistivity and  $L$  is the length of the element. The resistivity in silicon can vary eight orders of magnitude depending on the doping level [7], hence it is a crucial parameter from a design perspective.

In the limit where  $\Delta x \rightarrow 0$  and under the assumption of constant capacitance and resistance the voltage distribution  $u(x, t)$  in a RC delay line is governed by the diffusion equation [21]

$$\frac{\partial u(x, t)}{\partial t} = \frac{L^2}{RC} \frac{\partial^2 u(x, t)}{\partial x^2}, \quad (4)$$

where  $x$  is the position along the length of the element,  $t$  is time, and the diffusion coefficient is described by the product  $L^2/RC$ . During operation a CMUT will be subject to the following boundary conditions and initial condition

$$u(0, t) = V_0 g(2\pi f t) \quad (5)$$

$$\left. \frac{\partial u(x, t)}{\partial x} \right|_{x=L} = 0 \quad (6)$$

$$u(x, 0) = 0, \quad (7)$$

where  $V_0$  is the amplitude of the excitation voltage, and  $f$  and  $g(2\pi f t)$  are the excitation frequency and function, respectively. The first boundary condition (5) corresponds to the input signal at the electrode pad. The second boundary condition (6) states that the current density is zero at the end of the electrode, hence, the flux is zero. The initial condition (7) implies zero AC voltage at  $t = 0$ . The diffusion equation does not have a closed form solution for these particular initial and boundary conditions. However, a closed form solution of the transfer function can be found in the frequency domain. After a Fourier transform,  $\mathcal{F}$ , the diffusion equation (4) can be expressed as:

$$\frac{\partial^2 U}{\partial x^2} - \frac{\kappa^2}{L^2} U = 0 \quad (8)$$

where

$$\mathcal{F}\{u\} = U \quad \text{and} \quad \kappa^2 = i\omega RC. \quad (9)$$

By imposing the transformed boundary conditions

$$\mathcal{F}\{u(0, t)\} = V_0 G(\omega) \quad (10)$$

$$\mathcal{F}\left\{\left.\frac{\partial u(x, t)}{\partial x}\right|_{x=L}\right\} = 0 \quad (11)$$

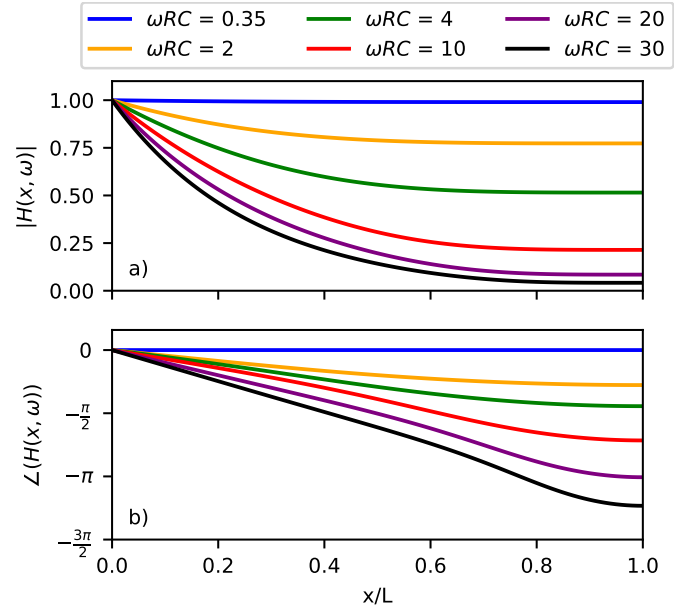


Figure 3. The absolute magnitude and phase of the transfer function as function of normalized distance for six different values of  $\omega RC$ . a) The magnitude of the transfer function, in the DC case where  $\omega RC \rightarrow 0$  the potential becomes uniformly distributed along the element. As  $\omega RC$  increases, the AC potential drop along the element, becomes larger. b) The phase of the transfer function. For  $\omega RC \ll 1$  the pressure will approximately be emitted simultaneously along the element, however, for larger values of  $\omega RC$  a significant delay is predicted along the element.

the final solution becomes:

$$U(x, \omega) = V_0 G(\omega) \underbrace{\frac{\cosh\left(\kappa\left(1 - \frac{x}{L}\right)\right)}{\cosh(\kappa)}}_{H(x, \omega)}, \quad (12)$$

where  $H(x, \omega)$  is the transfer function of the system.

The product  $\omega RC$  is the determining factor for this system, and the product can be understood as an inverse dimensionless diffusion coefficient, see explanation in Appendix A. A visualization of the transfer function is plotted for different values of  $\omega RC$  in Fig. 3, for both the absolute magnitude a) and phase b). The absolute magnitude decays along the element, and it translates into a decreasing AC magnitude along the element, hence, the emitted pressure is highest near the contact pad and then attenuated along the element. The attenuating effect becomes more pronounced as  $\omega RC$  increases. The phase shift along the element is also influenced by  $\omega RC$ , so the emission will be time delayed along the element. Equivalently to the magnitude, the higher  $\omega RC$  value the more pronounced effect. Consequently, at the end of an element the applied AC signal becomes increasingly attenuated and delayed in time as  $\omega RC$  increases. The design criterion is found by evaluating the absolute magnitude of the transfer function at the end of an element, where  $H(x, \omega)$  simplifies to

$$H(L, \omega) = \frac{1}{\cosh(\kappa)}. \quad (13)$$

A criterion of a 1% potential drop at the end of an element is used as a guideline to get close to a uniform acoustic pressure

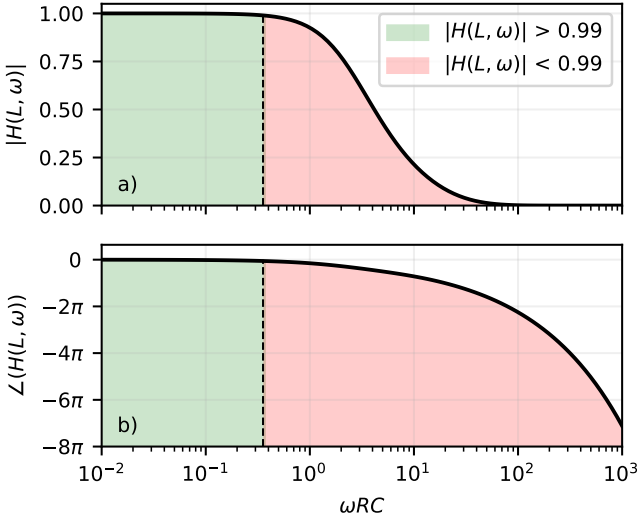


Figure 4. The transfer function at the end of the element ( $x=L$ ) as function of  $\omega RC$ . a) The absolute magnitude at the end of an element, where  $|H(L, \omega)| = 0.99$  is indicated with a dashed line. The green region indicates that the magnitude of the transfer function is above 0.99 and the red region indicates a magnitude less than 0.99. b) The phase delay at the end of an element. The 0.99 magnitude threshold is also indicated on this plot, and the criterion corresponds to a delay at the end of  $-0.17$  radians or  $-9.7$  degrees.

along the element. In terms of phase shift along the element this criterion corresponds to a delay of  $-0.17$  radians or  $-9.7$  degrees. The magnitude and phase of the transfer function at the end of the element are plotted as a function of  $\omega RC$  in Fig. 4 a) and the phase delay is plotted in b). The green area indicates the regime where this criterion is satisfied and red where it is not. A numerical solution of (13) shows that the criterion is met when

$$\omega RC < 0.35. \quad (14)$$

CMUTs can be considered as a voltage dependent capacitor, thus, a time dependent voltage signal yields a time dependent capacitance. The time dependence of the capacitance gives rise to non-linearity in this delay line model, and these effects are assumed to be negligible, therefore, all capacitive effects are modelled into a constant capacitor. The capacitance is inversely proportional to the gap height, and during operation of a CMUT the top plate is displaced to either transmit or receive a signal. Hence, changes in capacitance is a necessity for an operational CMUT. However, a constant capacitance assumption is used to obtain a simple analytical closed form model. The largest change in gap size occurs at the resonance frequency, where the constant capacitance assumption is violated most. Away from the resonance the displacement of the top plate decreases, and the validity of the constant capacitance assumption increases. The lower bound of the model where  $\omega RC \rightarrow 0$  corresponds to the stationary DC case and is well described by the model. The upper bound where  $\omega RC \rightarrow \infty$  will first of all be limited by the underlying assumptions of ideal resistors and capacitors, since inductive components will start to dominate as the frequency increases.

The capacitance and resistance can be measured after the CMUT array has been fabricated. However, estimating  $\omega RC$  before fabrication can be cumbersome, especially if the doping profile is varying though the substrate. By introducing the concepts of sheet resistance  $R_{\square}$  and capacitance per area  $C'$ , (14) can be rewritten as

$$\omega R_{\square} C' L^2 < 0.35. \quad (15)$$

This expression shows a square dependency on the element length, hence, long elements will be influenced significantly by this effect if not designed correctly. The elevation length of 1D arrays is designed by the wavelength multiplied by a factor (typically in the range between 20-30). However, the element length in a RCA array is determined by the number of channels. Thus, by linearly increasing the number of channels the product  $\omega RC$  increases with a square dependency. Therefore, problems with resistivity will be much more pronounced in RCA arrays compared to 1D arrays, where these effects rarely will be a problem. Derivation of (15) and an analysis of a varying doping profile can be found in Appendix B.

### B. CMUT transducer

The two transducers used in this work are fully assembled CMUT probes, with identical footprints, and 16.6 mm long elements. Details of the design, fabrication, and assembly of such probes can be found in the publications [22], [23]. The top electrode is identical for the two probes and made of 400 nm aluminium with a resistivity on the order of  $2 \times 10^{-6} \Omega \text{cm}$ . The resistivity for the bottom electrodes differs between the two probes. To distinguish between the two probes, the probe with high resistivity is denoted probe 1 and the probe with lower resistivity is denoted probe 2. Both probes have a pull-in voltage of 220 V and  $\lambda/2$  pitch. Probe 1 is a 92+92 RCA array with a center frequency of 4.5 MHz and probe 2 is a 62+62 RCA array with a center frequency of 3.0 MHz. Additional details can be found in Table I. The capacitance is estimated from impedance measurements, and the resistance is calculated using (3) and estimated as the worst-case scenario with respect to the resistivity provided by the SOI-wafer supplier. The difference in capacitance, between the top and bottom electrode, is due to capacitive substrate coupling, as detailed in [24]. The top electrode satisfies in all cases the criterion of  $\omega RC < 0.35$ . However, the bottom electrode has an  $\omega RC$  ranging from 9.5 to 33.3 for probe 1 leading to an expected potential drop of 76%, 92%, and 96% for 2 MHz, 4.5 MHz, and 7 MHz, respectively.

The bottom electrode for probe 2 has  $\omega RC = 0.4$ , corresponding to an attenuation of 1.2% along the element. This value does not strictly satisfy the developed criterion, but in an experimental setting, the additional 0.2% attenuation will not be critical for the overall performance.

### C. Acoustic characterization

The AC potential drop along the bottom electrode is difficult to measure experimentally due to the encapsulation of CMUTs, so to indirectly verify this effect the transmit pressure field has been measured instead. By using the Row-Column addressing

Table I  
DETAILS ABOUT TOP AND BOTTOM ELECTRODES FOR THE TWO PROBES.

Probe 1		
	Top	Bottom
Resistance	10 $\Omega$	<6.3 k $\Omega$
Capacitance	80 pF	120 pF
Resistivity	$3.9 \times 10^{-6}$ $\Omega\text{cm}$	<0.1 $\Omega\text{cm}$
$\omega RC$ @ 4.5 MHz	0.02	21.4
Probe 2		
	Top	Bottom
Resistance	10 $\Omega$	<62 $\Omega$
Capacitance	136 pF	339 pF
Resistivity	$3.9 \times 10^{-6}$ $\Omega\text{cm}$	<0.005 $\Omega\text{cm}$
$\omega RC$ @ 3 MHz	0.03	0.4

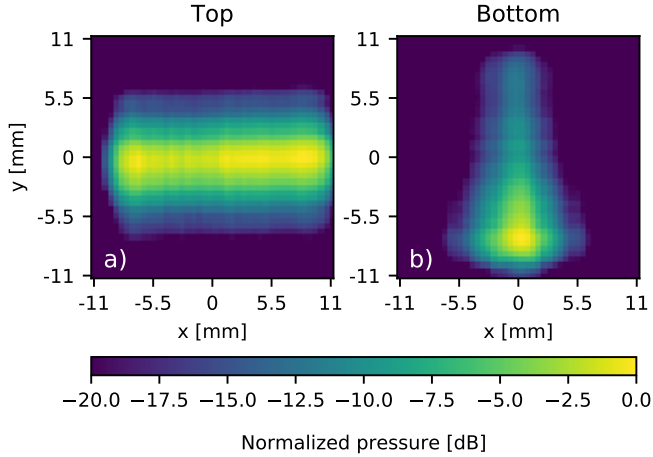


Figure 5. Average peak-to-peak pressure field at 4.5 MHz for probe 1. Pressure field measurement of single top a) and bottom b) electrode. The pressure distribution for the top electrode is uniform along the element. For the bottom electrode the pressure reaches its maximum value near the contact followed by a decaying tendency along the element due to the high resistivity.

scheme, it is possible to actuate the same CMUTs cells, but with two different electrode configurations. The transmit pressure field is measured for all elements individually at a distance of 1 cm using an AIMS III intensity measurement system (Onda Corp., California, USA) with an Onda HGL-0400 Hydrophone connected to the experimental research ultrasound scanner, SARUS [25]. The elements are excited by a 6 cycle sinusoidal pulse at different frequencies. Six cycles were chosen to ensure the correct excitation frequency by minimizing transient effects. The pressure field is mapped by moving the hydrophone in the  $x$ - $y$  plane in front of the transducer. The  $x$ - $y$  plane is resolved in a  $45 \times 45$  grid with a spacing of 0.5 mm. This grid is large enough to capture the entire footprint of the transducer. The pressure fields of all elements (both top and bottom) have been measured by probing all frequencies in each grid point.

### III. RESULTS AND DISCUSSION

The mean and standard deviation of the peak-to-peak pressure including harmonics have been estimated by spatially cross-correlating the pressure field from Row element 1 with all other Row elements and likewise for the columns. The averaged peak-to-peak pressure field, of single top and bottom electrodes for probe 1, is shown in Fig. 5. The probe is excited at the center

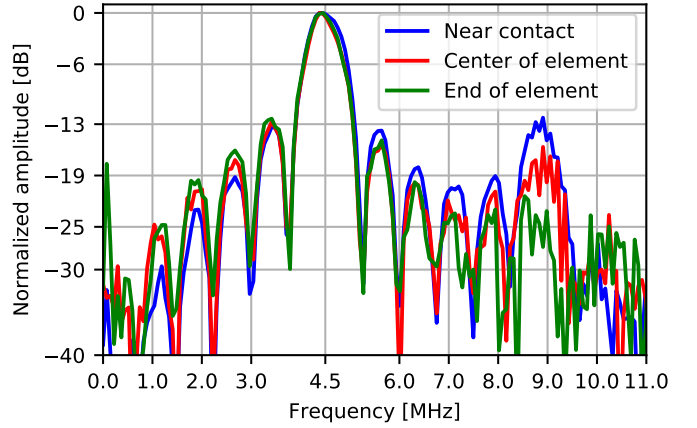


Figure 6. Normalized frequency content for three different positions along an element. The measurement is carried out with probe 1 at 4.5 MHz corresponding to  $\omega RC = 21.4$ . The fundamental to harmonic ratio decreases along the element. Near the contact the second harmonic is suppressed  $-13$  dB, whereas at the center of the element the suppression is  $-19$  dB, finally, at the end the suppression is observed to be  $-25$  dB.

frequency of 4.5 MHz and each plot has been normalized to its own maximum and dB compressed. The top electrodes a) have an  $\omega RC$  value of 0.03 satisfying the criterion in (14), and the pressure distribution is observed to be uniformly distributed along the element. The bottom electrodes b) have an  $\omega RC$  value of 21.4 and violates the criterion and is expected to attenuate high frequency signals. A significant attenuation is experimentally verified in the pressure distribution, where the maximum pressure is measured at the edge, followed by a decaying tendency along the element. The model predicts an attenuation of 92% from the electrode pad to the end of the element at 4.5 MHz.

To verify that high frequency components are attenuated along the element, the frequency components have been evaluated from three different positions, near the contact, in the center of the element, and at the end of the element. Fig. 6 shows the frequency content normalized to its own maximum for the three positions. The fundamental to harmonic ratio is, as predicted, observed to decrease along the element. The second harmonic is suppressed by  $-13$  dB closest to the contact,  $-19$  dB in the center of the element, and  $-25$  dB at the end of the element. Additionally, the low frequency content, relative to the fundamental, is more dominant away from the contact. These measurements verify the low-pass filtering properties of CMUT elements, when  $\omega RC$  is not correctly designed.

The pressure drop along an element should be qualitatively comparable with the RC delay line transfer function. The transfer function delay line model is shown for selected values of  $\omega RC$  in Fig. 7 a). The mean and standard deviation of the cross-correlated peak-to-peak pressure fields along the center of an element is plotted in Fig. 7 b) and c) for probe 1 and 2, respectively. The solid lines represent the bottom electrodes and the dashed line the top electrodes. Only one pressure profile has been plotted for the top electrodes for probe 1 due to same behavior for the other excitation frequencies. The highest frequency of 7 MHz is used as a representation of the worst-case scenario in terms of  $\omega RC$ . To

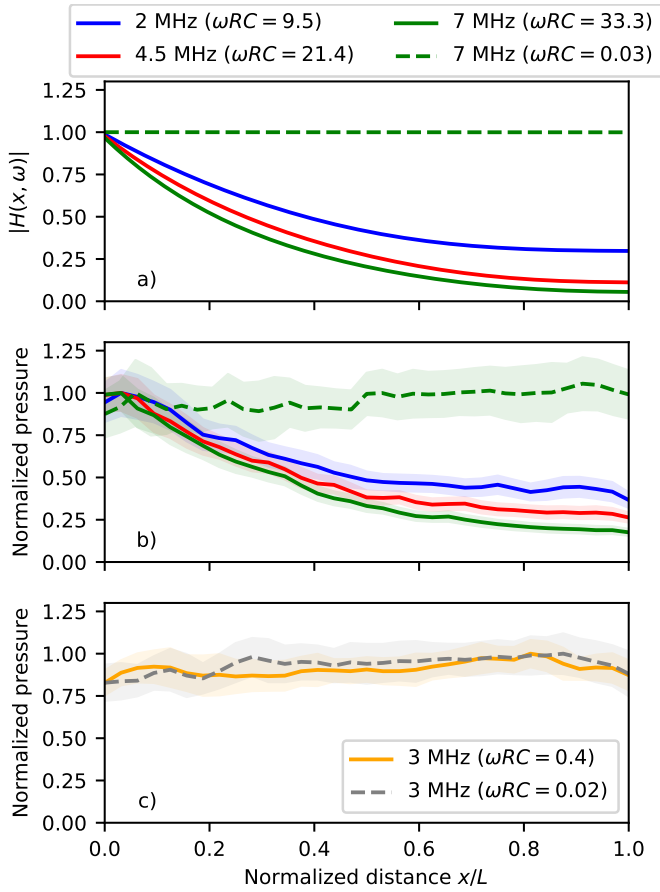


Figure 7. a) Transfer function of the delay line model. b) The measured average peak-to-peak pressure drops along elements for probe 1. c) The measured average peak-to-peak pressure drops along elements for probe 2. Solid lines indicate the bottom electrode and the dashed lines the top electrode. The shaded area represents one standard deviation. The same qualitative tendency is observed in plot a) and b), which demonstrates consistency between measurement and theory.

obtain a fair comparison between the different frequencies, each pressure profile has been normalized to its own maximum. It is observed that higher values of  $\omega RC$  lead to higher reduction of the pressure along the electrode and uniform pressure along the electrode is observed for small value of  $\omega RC$ , all in good agreement with the transfer function model. The emitted pressure using the bottom electrode from probe 1 is observed to drop 63%, 74%, and 82% for excitation frequencies of 2 MHz, 4.5 MHz, and 7 MHz, respectively.

The data acquisition time for the pressure field maps was 4 hours, and long-time-scales-effects are assumed negligible. The standard deviation would vary across the element, if long-time-scales-effects were present. The standard deviation, on Fig. 7 b) and c), is approximately constant along the element for each measurement, thus, the emitted pressure is stable in time.

Attenuation of the applied AC signal along the element will not only affect CMUT elements in transmit. In receive attenuation issues will also occur for pressure signals incident on the end of an element. In addition to attenuation, a higher electrode resistance will also increase the noise floor due to an increased thermal noise voltage, the mean square value

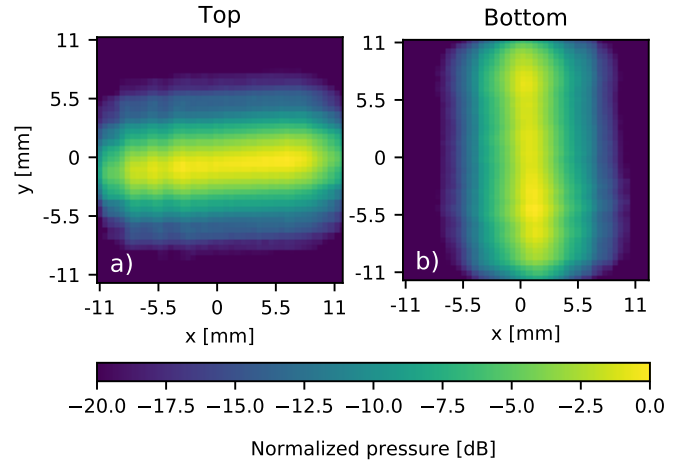


Figure 8. Average peak-to-peak pressure field at 3 MHz for probe 2. Pressure field measurement of single top a) and bottom b) electrode. The pressure field distributions for both top and bottom electrode are uniform along the element, in agreement with an  $\omega RC$  of 0.02 and 0.4 for top and bottom, respectively.

of which scales linearly with the resistance. Hence, besides attenuation and delay along the element, a reduction in SNR is also expected, due to the higher resistance.

The electrostatic force for a CMUT scales with  $(V_{DC} + V_{AC})^2$ , and whenever  $V_{AC} \ll V_{DC}$  the force will be approximately linear in  $V_{AC}$ . This is the reason why the transfer function model maps the normalized pressure quantitatively correct. The discrepancy between Fig. 7 a) and b) could partly be due to an excitation voltage  $V_{AC}$  of 75 V, corresponding to 41% of the 180 V applied DC bias, in which case  $V_{AC}^2$  becomes non negligible. Non-linear effects could be reduced by lowering the applied AC voltage, however, these parameters are chosen to imitate real operation conditions for medical imaging. Another reason for the discrepancy is the estimate of  $\omega RC$ , where in particular the resistance is uncertain. The SOI-wafer, used for the bottom electrodes, is specified with an upper bound on the resistivity, and this was used for estimating  $\omega RC$ . The true  $\omega RC$  value could therefore be lower, and thereby decrease the discrepancy between theory and experiment.

To demonstrate the predictability of the model, the same measurements have been carried out on probe 2. The average pressure field distributions at 3 MHz is shown in Fig. 8 for the top a) and bottom b) electrodes.  $\omega RC$  is in this case 0.02 and 0.4 for the top and bottom electrode, respectively. The criterion (14) is nearly satisfied in both cases, and the predicted attenuation is 0.004 % and 1.2 % for top and bottom electrodes, respectively. No significant attenuation is observed for both electrode configurations, which demonstrates that  $\omega RC$  can be used as a guideline for the resistance limitation in transducer designs.

Reducing the resistivity will always be beneficial in terms of minimizing  $\omega RC$ . However, reducing the resistivity in silicon is equivalent to increasing the doping concentration, and as the doping concentration increases, so does the intrinsic stress inside the silicon crystal. In the fabrication process, thermal mismatch after annealing between the layers introduces stress in the CMUT structure. Precise estimates of the stress distribution in the CMUT are difficult to obtain due to a wide temperature

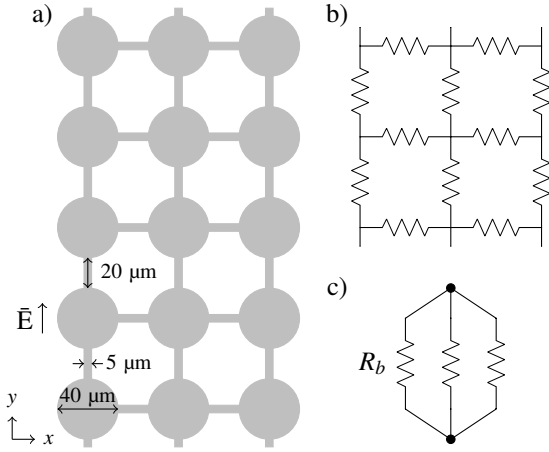


Figure 9. a) Top view sketch of a hypothetical structured electrode to fit the presented design, dimensions for the calculations are included together with assumed direction of the electric field. b) Lumped modelling of the electrode. c) Simplified lumped model.

range in the fabrication process. Thus, minimizing of stress prior to the annealing process provides a good prerequisite. CMUT fabrication processes with fusion bonding can benefit from choosing a doping concentration such that  $\omega RC$  is in the range between 0.1 – 0.35, which will ensure functional CMUTs and at the same time reduced stress in the bottom electrode. The model can be used to calculate the required electrode thickness, and an example for a transducer similar to probe 1 will be given. If the presented CMUT probes, with the same dimensions, had been fabricated using a different method that allowed another bottom electrode, it could be structured and designed as illustrated in Fig. 9 a), where all dimensions are included. The fabrication could in this case be methods based on sacrificial release or anodic bonding. The electrode is composed of circular pads and thin connecting wires, which can be modelled as a resistor network as shown in Fig. 9 b). An estimate of the resistance can be obtained by assuming the electrical field is aligned along the element ( $y$ -direction), resulting in zero current flow in the  $x$ -direction. Hence, all the horizontal resistors can be ignored. This assumption simplifies this circuit to a parallel circuit with three branches, as shown in Fig. 9 c), where a total resistance easily can be calculated. The structured electrode reduces the area of the electrode and thereby its parasitic capacitance. In all estimates of  $\omega RC$  the capacitance has been weighted with the reduced electrode area. Each of the vertical resistors in Fig. 9 b) consists of a connecting wire and one disk in series. The resistance of the connecting wires,  $R_{\text{wire}}$ , is found by (3), and the resistance of a disk can be approximated by (derivation given in Appendix C).

$$R_{\text{disk}} \approx \frac{\rho}{h} \sqrt{\frac{d+w}{d-w}} \ln \left( \frac{d}{w} \right), \quad (16)$$

where  $\rho$  is the resistivity,  $h$  is the film thickness,  $d$  is the diameter and  $w$  is the width of the connecting wires. A single element has  $3 \times 92 (= 276)$  CMUT cells along the  $y$ -direction and three CMUT cells along the  $x$ -direction. The resistance in

Table II  
RESISTIVITY OF AL, AU, AND ITO TOGETHER WITH THE MINIMUM ELECTRODE REQUIRED THICKNESS.

Material	Resistivity [ $\Omega\text{cm}$ ]	$h_{\text{min}}$ [nm] @ 4.5 MHz
Aluminium	$3.9 \times 10^{-6}$	58
Gold	$3.5 \times 10^{-6}$	50
ITO	$1.8 \times 10^{-4}$	2700

each branch,  $R_b$ , in the simplified model is then calculated by

$$R_b = 276 \times (R_{\text{wire}} + R_{\text{disk}}). \quad (17)$$

When the resistance of a single branch,  $R_b$ , is known the total resistance can be estimated as a function of electrode thickness and the established criterion (14) can be used to calculate a minimum electrode thickness  $h_{\text{min}}$ . The resistivity for aluminium, gold, and ITO for  $h_{\text{min}}$  @ 4.5 MHz can be found in Table II. Four point probe measurements have been carried out to determine the resistivity of a 100 nm aluminium- and gold film, and the ITO resistivity has been found in [26]. Given the design and dimensions in Fig. 9 the estimated minimum electrode thickness for aluminium and gold are 58 nm and 50 nm, respectively. In the literature the typical thickness of a structured electrode varies from 50 nm [27] to 200 nm [28]. Hence, typical metal electrodes will be sufficient for arrays of this size. For transparent CMUT applications the required thickness of ITO is 2.7  $\mu\text{m}$ , which is impractical in such a fabrication process.

#### IV. CONCLUSION

This paper presented a mathematical model to estimate required electrical properties to operate a functional CMUT, and the model has been verified experimentally. Two Row-Column addressed probes were used to demonstrate the effect, one probe with a high resistivity electrodes and another with a low resistivity electrodes. The CMUT probes both had aluminium top electrodes and doped silicon bottom electrodes. The doping level was varied between the two probes corresponding to a bottom electrode resistivity of 0.1  $\Omega\text{cm}$  for the first probe and 0.005  $\Omega\text{cm}$  for the second probe. High resistivity in the electrode impedes propagation of high frequency AC signals along the element, and the theory of RC delay lines was used to describe the frequency dependent attenuation. High frequency filtering was demonstrated by examining the frequency content at three different positions along an element. For an  $\omega RC$  value of 21.4 the fundamental to second harmonic ratio was observed to decrease along the element from  $-13$  dB near the contact, to  $-18$  dB in the center of the element to  $-25$  dB at the end of the element. From this work it can be concluded that a CMUT fabrication process should be designed such that  $\omega RC < 0.35$  where  $\omega$  is the angular excitation frequency,  $R$  is the element resistance, and  $C$  is the element capacitance. When CMUTs are designed according to this criterion, the amplitude attenuation of the applied AC signal will be reduced less than 1% along the element. Experimentally this effect was demonstrated for both probes. The low resistivity probe showed a uniform pressure profile along the element, and the high resistivity probe showed a significant decay in the pressure

profile along the element. For  $\omega RC$  equal to 9.5, 21.4, and 33.3 the mean transmit pressure at the end of an element was observed to drop 63%, 74%, and 82%, respectively.

#### ACKNOWLEDGEMENTS

This work is financially supported by the Innovation Fund Denmark (7050-00004B) and by BK Medical (Herlev, Denmark).

#### REFERENCES

- [1] A. S. Savoia, G. Caliano, and M. Pappalardo, "A CMUT probe for medical ultrasonography: From microfabrication to system integration," *IEEE Trans. Ultrason., Ferroelec., Freq. Contr.*, vol. 59, no. 6, pp. 1127–1138, 2012.
- [2] M. I. Haller and B. T. Khuri-Yakub, "A surface micromachined electrostatic ultrasonic air transducer," in *Proc. IEEE Ultrason. Symp.*, vol. 2, 1994, pp. 1241–1244.
- [3] C. Meynier, F. Teston, and D. Certon, "A multiscale model for array of capacitive micromachined ultrasonic transducers," *J. Acoust. Soc. Am.*, vol. 128, no. 5, pp. 2549–2561, 2010.
- [4] G. Gurun, P. Hasler, and F. L. Degertekin, "Front-end receiver electronics for high frequency monolithic CMUT-on-CMOS imaging arrays," *IEEE Trans. Ultrason., Ferroelec., Freq. Contr.*, vol. 58, no. 8, pp. 1658–1668, August 2011.
- [5] P. Zhang, G. Fitzpatrick, W. Moussa, and R. J. Zemp, "CMUTs with improved electrical safety and minimal dielectric surface charging," in *Proc. IEEE Ultrason. Symp.*, 2010, pp. 1881–1885.
- [6] C. Kittel, *Introduction to solid state physics*. Wiley, 2005.
- [7] N. A. Neamen, *Semiconductor physics and devices*. McGraw-Hill Higher Education, 2003.
- [8] X. Zhang, O. J. Adelegan, F. Y. Yamaner, and O. Oralkan, "CMUTs on glass with ITO bottom electrodes for improved transparency," in *Proc. IEEE Ultrason. Symp.*, 2016, pp. 1–4.
- [9] X. Zhang, X. Wu, O. J. Adelegan, F. Y. Yamaner, and O. Oralkan, "Backward-mode photoacoustic imaging using illumination through a CMUT with improved transparency," *IEEE Trans. Ultrason., Ferroelec., Freq. Contr.*, vol. 65, pp. 85–94, 2018.
- [10] Y. Huang, A. S. Ergun, E. Hæggeström, M. H. Badi, and B. T. Khuri-Yakub, "Fabricating capacitive micromachined ultrasonic transducers with wafer-bonding technology," *J. Microelectromech. Syst.*, vol. 12, no. 2, pp. 128–137, 2003.
- [11] A. S. Ergun, Y. Huang, X. Zhuang, Ö. Oralkan, G. G. Yaralioglu, and B. T. Khuri-Yakub, "Capacitive micromachined ultrasonic transducers: Fabrication technology," *IEEE Trans. Ultrason., Ferroelec., Freq. Contr.*, vol. 52, no. 12, pp. 2242–2258, 2005.
- [12] F. Y. Yamaner, X. Zhang, and O. Oralkan, "A three-mask process for fabricating vacuum-sealed capacitive micromachined ultrasonic transducers using anodic bonding," *IEEE Trans. Ultrason., Ferroelec., Freq. Contr.*, vol. 62, no. 5, pp. 972–982, 2015.
- [13] Z. Li, L. L. P. Wong, A. I. H. Chen, S. Na, J. Sun, and J. T. W. Yeow, "Fabrication of capacitive micromachined ultrasonic transducers based on adhesive wafer bonding technique," *J. Micromech. Microeng.*, vol. 26, no. 11, p. 115019, 2016.
- [14] R. Manwar, T. Simpson, A. Bakhtazad, and S. Chowdhury, "Fabrication and characterization of a high frequency and high coupling coefficient CMUT array," *Microsyst. Technol.*, vol. 23, no. 10, pp. 4965–4977, 2017.
- [15] A. S. Havreland, M. L. Ommen, C. Silvestre, M. Engholm, J. A. Jensen, and E. V. Thomsen, "BCB polymer based row-column addressed CMUT," in *Proc. IEEE Ultrason. Symp.*, 2017, pp. 1–4.
- [16] D. Pang and C. Chang, "Development of a novel transparent flexible capacitive micromachined ultrasonic transducer," *Sensors*, vol. 17, no. 6, p. 1443, 2017.
- [17] X. Zhang, O. Adelegan, F. Y. Yamaner, and O. Oralkan, "An optically transparent capacitive micromachined ultrasonic transducer (CMUT) fabricated using SU-8 or BCB adhesive wafer bonding," in *2017 IEEE International Ultrasonics Symposium (IUS)*, 2017, pp. 1–4.
- [18] A. S. Logan, L. L. P. Wong, and J. T. W. Yeow, "2-D CMUT wafer bonded imaging arrays with a row-column addressing scheme," in *Proc. IEEE Ultrason. Symp.*, sep 2009, pp. 984–987.
- [19] H. Köymen, A. Atalar, E. Aydogdu, C. Kocabas, H. K. Oguz, S. Olcum, A. Ozgurluk, and A. Ünlügedik, "An improved lumped element nonlinear circuit model for a circular CMUT cell," *IEEE Trans. Ultrason., Ferroelec., Freq. Contr.*, vol. 59, no. 8, pp. 1791–1799, 2012.
- [20] M. F. la Cour, T. L. Christiansen, J. A. Jensen, and E. V. Thomsen, "Electrostatic and small-signal analysis of CMUTs with circular and square anisotropic plates," *IEEE Trans. Ultrason., Ferroelec., Freq. Contr.*, p. in press, 2015.
- [21] E. Fabricius, *Introduction to VLSI design*. McGraw-Hill, 1990.
- [22] M. Engholm, T. L. Christiansen, C. Beers, J. P. Bagge, L. N. Moesner, H. Bouzari, A. Lei, M. Berkheimer, M. B. Stuart, J. A. Jensen, and E. V. Thomsen, "A hand-held row-column addressed CMUT probe with integrated electronics for volumetric imaging," in *Proc. IEEE Ultrason. Symp.*, 2015, pp. 1–4.
- [23] M. Engholm, H. Bouzari, T. L. Christiansen, C. Beers, J. P. Bagge, L. N. Moesner, S. E. Diederichsen, M. B. Stuart, J. A. Jensen, and E. V. Thomsen, "Probe development of CMUT and PZT row-column-addressed 2-d arrays," *Sens. Actuators A: Phys.*, vol. 273, pp. 121–133, 2018.
- [24] M. Engholm, H. Bouzari, J. A. Jensen, and E. V. Thomsen, "Capacitive substrate coupling of row-column-addressed 2-D CMUT arrays," in *Proc. IEEE Ultrason. Symp.*, 2016, pp. 1–4.
- [25] J. A. Jensen, H. Holten-Lund, R. T. Nilsson, M. Hansen, U. D. Larsen, R. P. Domsten, B. G. Tomov, M. B. Stuart, S. I. Nikolov, M. J. Pihl, Y. Du, J. H. Rasmussen, and M. F. Rasmussen, "SARUS: A synthetic aperture real-time ultrasound system," *IEEE Trans. Ultrason., Ferroelec., Freq. Contr.*, vol. 60, no. 9, pp. 1838–1852, 2013.
- [26] M. Gao, R. Job, D. Xue, and W. R. Fahrner, "Thickness dependence of resistivity and optical reflectance of ITO films," *Chin. Phys. Lett.*, vol. 25, no. 4, pp. 1380–1383, 2008.
- [27] S. Olcum, K. Oguz, M. N. Senlik, F. Y. Yamaner, A. Bozkurt, A. Atalar, and H. Koymen, "Wafer bonded capacitive micromachined underwater transducers," in *Proc. IEEE Ultrason. Symp.*, 2009, pp. 976–979.
- [28] A. S. Savoia, B. Mauti, G. Caliano, L. Maiolo, A. Minotti, A. Pecora, G. Fortunato, A. Bagolini, and P. Bellutti, "Optimization of the efficiency and reliability of reverse-fabricated CMUT arrays," in *Proc. IEEE Ultrason. Symp.*, 2017, pp. 1–4.
- [29] G. S. May and S. M. Sze, *Fundamentals of semiconductor fabrication*. John Wiley and Sons, Inc., 2004.

#### APPENDIX A

The delay line model can be written in a non-dimensional form by introducing the new variables  $x^* = x/L$ ,  $t^* = \omega t$  and  $u^* = u/V_0$ , where the asterisk indicates non-dimensional variables. The non-dimensional version of the differential equation then reads

$$\frac{\partial u^*}{\partial t^*} = \frac{1}{\omega RC} \frac{\partial^2 u^*}{\partial x^{*2}} \quad (18)$$

where the dimensionless diffusion coefficient is given by

$$D^* = \frac{1}{\omega RC}. \quad (19)$$

To ensure a highly responsive system, and thereby a more uniform voltage distribution along the element, the diffusion coefficient  $D^*$  has to be maximized. Notice, this is in full agreement with the parameter found in (12).

#### APPENDIX B

$\omega RC$  can be decoupled into lateral and vertical geometry dependence by introducing the concepts of sheet resistance and capacitance per area. The sheet resistance,  $R_{\square}$ , depends on junction depth  $z_j$  and the carrier mobility  $\mu$  in the following manner [29]

$$R_{\square} = \frac{1}{q \int_0^{z_j} \mu(z) N(z) dz}, \quad (20)$$

where  $q$  is the elementary charge,  $N$  is the carrier concentration and  $z$  is the depth. For SOI wafers, where the doping concentration is constant through the device layer, an analytical

solution of  $R_{\square}$  can be found. In all other cases numerical integration must be used. For an rectangular shaped element the sheet resistance is related to the resistance by

$$R = \frac{\rho}{h} \frac{L}{W} = R_{\square} \frac{L}{W}, \quad (21)$$

where  $W$  is the width of the element. The capacitance per area  $C'$  is simply the capacitance divided by the cross-sectional area

$$C = C'WL. \quad (22)$$

Thus, the product  $\omega RC$  can be rewritten by substituting (21) and (22) into (14):

$$\omega R_{\square} C' L^2 < 0.35 \quad (23)$$

$R_{\square}$  and  $C'$  only have a vertical dependence, whereas all lateral dependencies are now moved into  $L^2$ .  $\omega R_{\square} C' L^2$  represents a generalized version of  $\omega RC$ , which can be estimated for all geometries and doping profiles.

### APPENDIX C

The series resistance contribution from the disk shaped element can be calculated using finite elements for any given geometry. An approximate closed form expression, however, is useful when effects of geometrical changes are evaluated. The resistance of the disk shaped element is well approximated by the resistance of two trapezoidal resistance elements in series as illustrated in Fig. 10; each trapezoidal element has a base width equal to the diameter  $d$  of the disk, while the top width equals the width  $w$  of the connecting wire and the height of the trapezoidal element is  $H = \frac{1}{2} \sqrt{d^2 - w^2} = \frac{1}{2} \sqrt{(d-w)(d+w)}$  as seen from elementary geometry.

The cross-section of the conduction path then varies linearly along the element, and the incremental resistance contribution  $dR$  for an element of length  $dy$  becomes

$$dR = \frac{\rho}{h} \frac{dy}{f(y)} = \frac{\rho}{h} \frac{dy}{w + (d-w) \frac{y}{H}}$$

where  $h$  is the thickness of the conducting material of resistivity  $\rho$ .

The total resistance of the disk is then approximately

$$R_{\text{disk}} \approx \frac{2\rho}{h} \int_0^H \frac{dy}{w + (d-w) \frac{y}{H}} = \frac{\rho}{h} \sqrt{\frac{d+w}{d-w}} \ln \left( \frac{d}{w} \right), \quad (24)$$

where the factor of 2 is due to series connection of two trapezoidal elements.

Compared to Comsol FEM calculations the resistance is overestimated by  $\sim 4\%$  when (24) is used on the geometry of this paper.

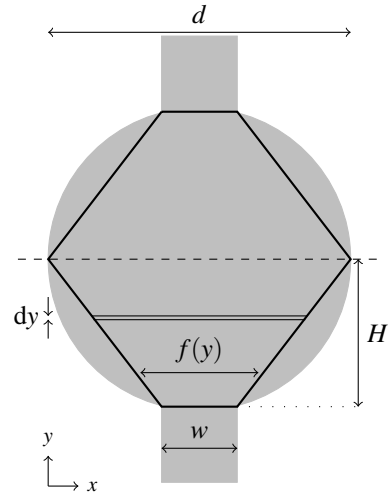


Figure 10. Trapezoidal resistor elements in the disk shaped element. Grey area is the ideal geometry and the solid black lines indicates the approximate disk geometry.

## APPENDIX D

---

Paper D - Wafer bonded CMUT technology utilizing  
Poly-Silicon-on-Insulator wafers

---



# Wafer bonded CMUT technology utilizing a Poly-Silicon-on-Insulator wafer

Andreas Spandet Havreland, Mathias Engholm, Rune Sixten Grass,  
Jørgen Arendt Jensen and Erik Vilain Thomsen

Department of Health Technology, Technical University of Denmark, DK-2800 Kgs. Lyngby, Denmark

**Abstract**—This paper presents a fabrication process of a Poly-Silicon-On-Insulator (PSOI) wafer that can be used as an alternative to conventional Silicon-On-Insulator (SOI) wafers for fabrication of Capacitive Micromachined Ultrasound Transducers (CMUT). The fabrication of PSOI wafers does, unlike the conventional SOI fabrication, not involve any bonding steps. A batch of PSOI wafers having a 400 nm BOX layer and a  $2.6 \mu\text{m} \pm 0.04 \mu\text{m}$  ( $1\sigma$ ) device layer is fabricated and characterized. A surface roughness of 0.47 nm is measured for the PSOI device layer, and successful fusion bonds (direct bonds) are demonstrated between PSOI wafers and oxidized silicon wafers. A wafer-bonded CMUT using a PSOI wafer is fabricated and electrically characterized, and the expected CMUT performance is observed. Impedance spectra are demonstrated at five different DC biases, the expected spring softening effect is observed when the magnitude of the DC bias is increased.

## I. INTRODUCTION

Silicon-On-Insulator (SOI) wafers are today routinely used in the semiconductor industry and have been applied for numerous applications ranging from P/N junctions [1], Optical applications [2], and in particular for applications in the industry of Micro Electrical Mechanical Systems (MEMS) [3]. The target application for this paper is the Capacitive Micromachined Ultrasound Transducer (CMUT), a technology developed in the 1990's [4] that falls into the category of MEMS devices where SOI wafers are commonly used. The basic structure of a SOI wafer consists of a device layer, a buried oxide layer (BOX), and a handle wafer (substrate). The device layer of the SOI wafer is used in CMUT applications as the vibrating plate or membrane. The device layer of SOI wafers used for wafer bonded CMUTs are required to have bondable surfaces, low electrical resistivity, predictable mechanical stiffness, and preferably a uniform device layer thickness,  $h$ . Monocrystallinity of the device layer is not important for CMUT applications, but, it is essential for other SOI based applications. The ability to customize the thickness and resistivity of the individual layer provides great freedom in a MEMS design. The fabrication processes of CMUTs are either based on a sacrificial release [5] and wafer bonding step, where the latter is the main focus of this work. Several wafer bonding techniques have been demonstrated for CMUT applications [6]–[8]. The device layer thickness, of conventional SOI wafers, can be specified from hundreds of microns down to  $2 \mu\text{m}$  with a uncertainty of  $0.3 \mu\text{m}$ . The SOI wafers used for CMUT applications are typically close to the lower limit, and have typically device layers less than  $10 \mu\text{m}$ .

However, CMUT plates (device layer) thinner than  $2 \mu\text{m}$  plate are highly desirable in some CMUT designs, especially for high frequency or high bandwidth applications. Hence, it becomes challenging for such applications to get the desired wafer specification when conventional SOI wafers are used. A thinner device layer can be obtained by thermally oxidize the SOI wafers and remove the grown oxide subsequently. This process can be controlled with high precision, but, the relative thickness variation increases, since, the uncertainty of the device layer thickness is unaffected by the oxidation process. Variations of the plate thickness,  $h$ , across a CMUT array influence important characteristic CMUT parameters such as resonance frequency and pull-in voltage, which scales with  $h$  and as  $h^{3/2}$ , respectively. Thus, tight control of the plate thickness is necessary for having equal performance of all CMUT in an array. The objective of this paper is to demonstrate the Poly-silicon-On-Insulator wafer as a rapid prototyping tool for CMUT fabrication. The PSOI technology is required to be non-inferior to the already existing SOI technology measured by important CMUT characteristics, such as reliable bonding properties, sufficient electrical properties and uniform device layer thickness across the wafer. Fusion bonded CMUTs must be demonstrated to verify non-inferiority of the PSOI technology, since fusion bonding is more sensitivity in terms of surface roughness and cleanliness compared to other techniques such as anodic bonding and polymer bonding. The majority of the CMUTs demonstrated found in the literature have plate thicknesses less than  $5 \mu\text{m}$  and it will therefore be considered as the upper bound of the device layer. In addition, the device layer resistivity should be less than  $1 \Omega \text{cm}$  to be interesting for CMUT applications.

## II. FABRICATION

### A. Fabrication of PSOI wafers

The fabrication process of conventional SOI wafers consists of few steps, first an oxide is grown on a silicon substrate (wafer A) and the oxide surface is thereafter fusion bonded to a new silicon wafer (wafer B). The oxide defines the BOX layer and wafer A defines the handle layer. The device layer is made by wafer B, the thickness is adjusted to match the desired specifications by removing silicon in a grinding process. Finally, a chemical mechanical polishing (CMP) is carried out to obtain the same surface standard as conventional silicon wafers [9]. The fabrication process of PSOI wafers are similar to the fabrication of conventional SOI. However, the

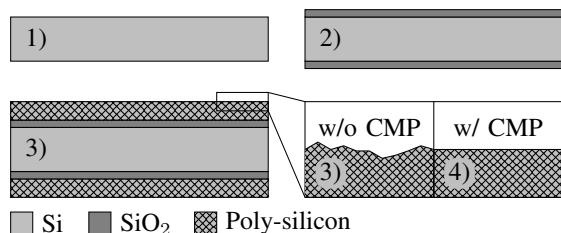


Fig. 1. Fabrication process of PSOI wafers. 1) A standard silicon wafer is RCA cleaned. 2) A thermal oxide is grown. 3) Poly-silicon is deposited in an LPCVD process. 4) The poly-silicon layer is polished (CMP) to reduce surface roughness. Figure is not to scale.

device layer is deposited using a Low Pressure Chemical Vapor Deposition (LPCVD) process instead of being bonded to the oxide surface. The fabrication of PSOI wafers consists of four steps as shown in Fig. 1.

The first step in the PSOI fabrication is a RCA clean of a silicon wafer. This wafer will end up as the handle layer and electrical properties, doping type, and wafer thickness should therefore match desired specifications. In step 2, an oxide is thermally grown that constitutes the BOX layer. A 400 nm dry oxide grown at 1100 °C is used for the PSOI wafers fabrication in this work. The device layer is created in step 3, where a boron doped poly-silicon is deposited using a LPCVD process. The equivalent could be obtained by a phosphor doped poly-silicon, but the deposition rate is substantially lower.

Finally, in step 4, the poly-silicon surface is polished using a Logitech CM62 Orbis CMP machine. The final poly-silicon thickness of a fabricated PSOI has been measured across the wafer using multi-angle reflectometry measurements, the resulting thickness map is shown in Fig. 2. A mean thickness of 2.60 μm with a standard deviation of 0.04 μm has been measured. Additionally, the difference between minimum and maximum thickness is measured to be 0.26 μm, hence, in full compliance with the non-inferior constraint. The surface roughness, of the deposited LPCVD poly-silicon, has been measured using a PLu neox Optical Profiler (confocal microscope) to 6.98 nm prior to the CMP process and 0.47 nm after the CMP process. The true surface roughness could be lower, since these measurements are at the resolution limitation of the confocal microscope. A surface roughness of approximately 0.5 nm has also been measured on a reference silicon wafer. A surface roughness of less than 1 nm is required to achieve successful fusion bond and preferably even lower [10]. The CMP process is therefore essential for fusion bonding to be successful.

The mechanical and electrical properties of a LPCVD poly-silicon are influenced by multiple parameters, including deposition temperature, deposition time, gas composition, tube pressure, and flow conditions among other. The deposition rate of the LPCVD poly-silicon should be high enough to produce 5 μm poly-silicon layer within a reasonable time. At the same time the built-in stress should preferably be tensile and the resistivity should be low. A tensile stress in the poly-

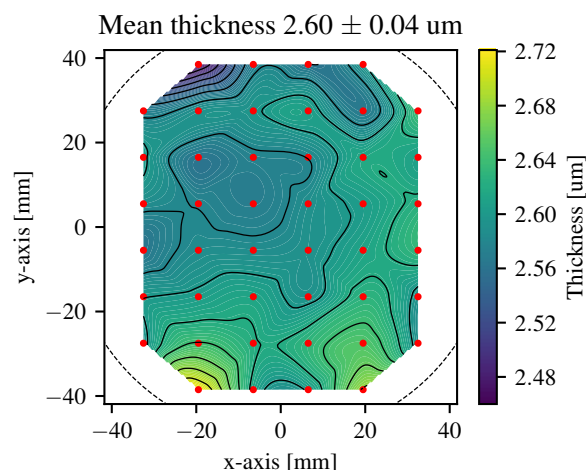


Fig. 2. Interpolated thickness map of a PSOI device layer measured using multi-angle reflectometry. The circumference of the wafer is indicated by the dashed black line, and the 44 red dots indicate the spatial positions of the data points used to generate the thickness map.

silicon prohibits buckling effects in the final CMUT structure. An acceptable resistivity parameter space depends on the CMUT application, and a criterion that describes when the resistivity is low enough for acceptable CMUT performance can be found in [11]. Four point probe measurements of 19 PSOI wafers have been conducted to estimate the resistivity of the device layer, the mean and standard deviation were  $0.036 \Omega \text{ cm} \pm 0.019 \Omega \text{ cm}$ , and the highest measured resistivity was  $0.062 \Omega \text{ cm}$ . Depositing rate, thin film stress, and resistivity do all depend on the deposition temperature [12]–[17], and quantitative values of these parameters are plotted in Fig. 3.

The material properties of the deposited poly-silicon varies from lab to lab, and the data should be interpreted as tendencies and not absolute values. The deposition rate is seen, in Fig. 3 a), to increase as the deposition temperature increases, whereas a reduction in the resistivity is observed in Fig. 3 b) (notice the log y-scale). Hence, rapid fabrication time and low resistivity are obtained by an increased deposition temperature. However, the temperature dependency of the stress is not unambiguous as the deposition rate and resistivity, and extrapolation is therefore difficult. Fusion bonded CMUTs require an annealing step at temperatures on the order of 1000 °C, and annealing time and temperature do also influence the stress and resistivity. The highest process temperature is, however, significantly lower for other CMUT fabrication methods such as anodically bonded CMUTs, where the highest process temperature is on the order of 350 °C [7]. The resistivity and stress values from Fig. 3 b) and c) are therefore directly applicable for anodically bonded CMUTs, but are perturbed during annealing for fusion bonded CMUTs. The minimum device layer thickness for conventional SOI wafers are limited to 2 μm, but, the PSOI technology can provide a device layer

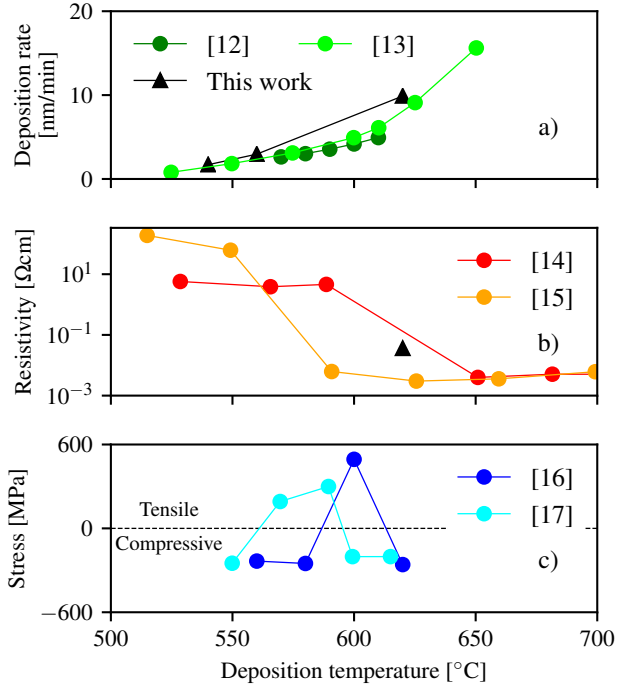


Fig. 3. The deposition rate, resistivity, and stress as function of deposition temperature. The circular markers are from the literature and represents either boron doped or undoped LPCVD poly-silicon and triangular markers indicate measurements of LPCVD boron doped poly-silicon from this work.

TABLE I  
VARIOUS MEASURED PSOI PARAMETERS

Parameter	Samples [#]	Upper bound
Device layer thickness variations	2	$<0.3 \mu\text{m}$
Surface roughness	1	$0.47 \text{ nm}$
Wafer bow	10	$<20 \mu\text{m}$
Device layer resistivity	19	$<0.062 \Omega \text{ cm}$

ranging from approximately 10 nm to 5  $\mu\text{m}$ , and is limited by how thin or how thick layers the LPCVD system can deposit. But, the PSOI technology is also applicable for applications that require device layers of less than 2  $\mu\text{m}$ . The fabrication time of PSOI wafers is two-three days under the assumption of availability of an oxidation furnace, a LPCVD poly-furnace and a CMP machine. The PSOI technology provides a rapid and flexible technology platform for CMUT research and development, as an alternative to the conventional SOI wafers where the delivery time (months) can limit iteration of various CMUT designs.

An overview of various measured PSOI parameters can be found in Table I.

### B. Fabrication of CMUTs

The CMUTs in this work have been fabricated using a LOCAL Oxidation of Silicon (LOCOS) process, first demonstrated in 2009 by [18]. The LOCOS process has numerous beneficial properties for CMUT fabrication such as high dielectric strength, reduced parasitic capacitance, good uniformity, and

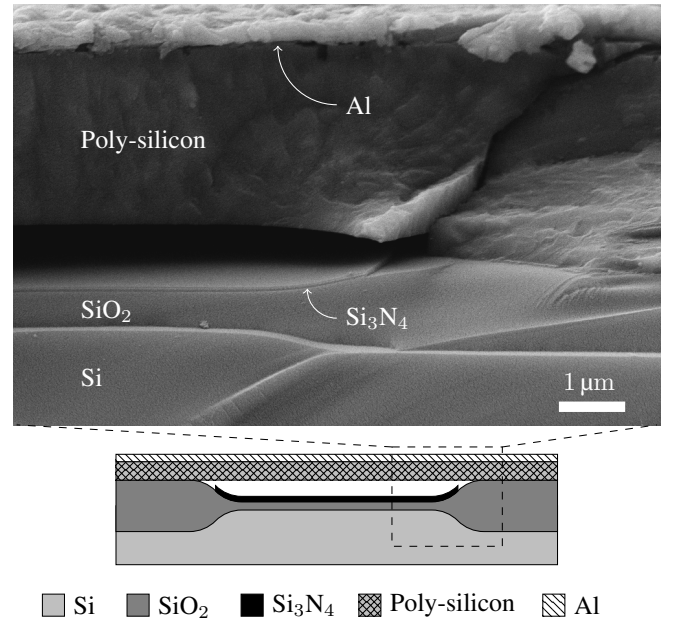


Fig. 4. Cross sectional SEM image of a CMUT fabricated using a PSOI wafer. A thin gold layer of a few nanometer has been sputter to reduce charging effects in the dielectric layers. A sketch of the designed LOCOS CMUT is inserted below the SEM image.

the gap height can be controlled with nanometer precision. The PSOI wafer and the processed LOCOS substrate wafer were both RCA cleaned prior to the fusion bonding process, and pre-bonded using a Süss SB6 wafer bonder, followed by an annealing step at 1100  $^{\circ}\text{C}$  for 70 min. A cross sectional image of a fabricated CMUT has been acquired by a Scanning Electron Microscope (SEM) and shown in Fig. 4. A sketch of the structure has been inserted below the SEM image to illustrate the designed LOCOS structure. The CMUT plate is as expected composed of a polycrystalline material separated from the bottom of the CMUT cavity by the LOCOS bird's beak structure. The CMUT has been diced by an automatic dicing saw and the surface is observed to be frayed as a result of the dicing process.

### III. CMUT CHARACTERIZATION

The fabricated CMUTs have been electrically characterized by impedance measurements. The measurements were performed using an Agilent 4294A Precision Impedance Analyzer with five different DC biases and an AC voltage of 100 mV. The impedance magnitude and phase are plotted in Fig. 5 a) and b), respectively, where the expected CMUT behaviour is observed. A distinct resonance frequency is observed in the frequency range between 5 MHz and 6.5 MHz, and the spring softening effect is confirmed by the frequency shift towards lower frequencies as the magnitude of the DC bias is increased. In addition the phase is approximately, in Fig. 5 b),  $-90^{\circ}$  for all off-resonance frequencies up to 10 MHz, which verifies the expected capacitive properties for the CMUT. The impedance

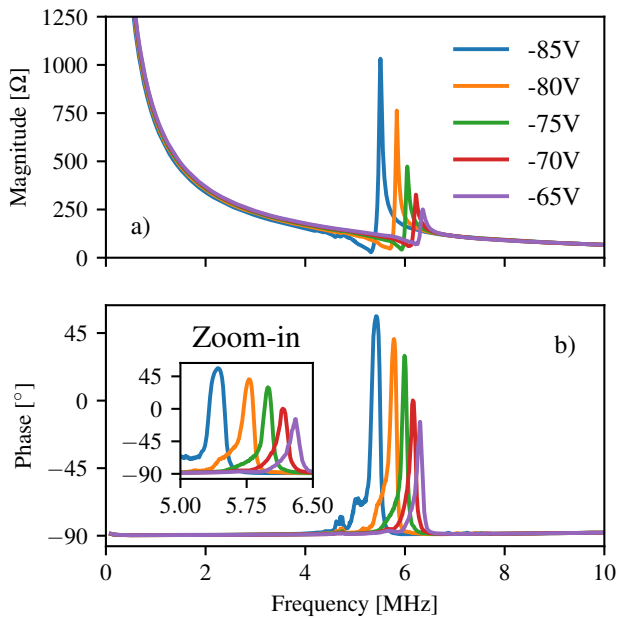


Fig. 5. Impedance measurements of a fabricated CMUT at five different DC biases. The expected spring softening effect is observed for increased DC magnitude. The applied bias ramp corresponds to 72.2%, 77.8%, 83.3%, 88.9%, 94.4% of the pull-in voltage.

measurements demonstrate the technological potential of PSOI wafers as an alternative to conventional SOI wafer for MEMS devices.

#### IV. CONCLUSION

This paper presented a fabrication method of a Poly-Silicon-On-Insulator (PSOI) wafer. A PSOI wafer was demonstrated applicable for CMUT applications as an alternative to conventional Silicon-On-Insulator (SOI) wafers. Fabrication of PSOI wafers can reduce iteration time for wafer bonded CMUTs, and the device layer of a PSOI wafer can be fabricated thinner than a conventional SOI. The device layer thickness of a fabricated PSOI wafer was measured using multi-angle reflectometry and yielded a mean thickness of  $2.60\ \mu\text{m}$  with a standard deviation of  $0.04\ \mu\text{m}$ . A mean resistivity of 19 PSOI wafers were characterized by four point probe measurements and measured to  $0.36\ \Omega\text{cm} \pm 0.19\ \Omega\text{cm}$  ( $1\sigma$ ). A surface roughness of  $0.47\ \text{nm}$  was determined by confocal microscopy, and a bondable surface properties was demonstrated by fabrication of a functional fusion bonded CMUT. An impedance analysis of the fabricated CMUT showed the expected CMUT behaviour. A distinct resonance frequency was observed for five different DC biases, and the spring softening effect was confirmed by a frequency shift as the magnitude of the applied DC bias was increased.

#### V. ACKNOWLEDGEMENT

We would like to thank the Danish Innovation Fund and BK Medical for funding this research.

#### REFERENCES

- [1] J. B. Lasky, "Wafer bonding for silicon-on-insulator technologies," *Applied Physics Letters*, vol. 48, no. 1, pp. 78–80, 1986.
- [2] W. Noell, P. A. Clerc, L. Dellmann, B. Guldemann, H. P. Herzig, O. Manzardo, C. R. Marxer, K. J. Weible, R. Dändliker, and N. De Rooij, "Applications of SOI-based optical MEMS," *IEEE Journal on Selected Topics in Quantum Electronics*, vol. 8, no. 1, pp. 148–158, 2002.
- [3] K. Mitani and U. M. Gösele, "Wafer bonding technology for silicon-on-insulator applications: A review," *Journal of Electronic Materials*, vol. 21, no. 7, pp. 669–676, 1992.
- [4] M. I. Haller and B. T. Khuri-Yakub, "A surface micromachined electrostatic ultrasonic air transducer," *IEEE Transactions on Ultrasonics, Ferroelectrics, and Frequency Control*, vol. 43, no. 1, pp. 1–6, 1996.
- [5] A. S. Ergun, G. G. Yaralioglu, and B. T. Khuri-Yakub, "Capacitive Micromachined Ultrasonic Transducers: Theory and Technology," *Journal of Aerospace Engineering*, vol. 16, pp. 76–84, 2003.
- [6] Y. Huang, A. Sanli Ergun, E. Hægström, M. H. Badi, and B. T. Khuri-Yakub, "Fabricating capacitive micromachined ultrasonic transducers with wafer-bonding technology," *Journal of Microelectromechanical Systems*, vol. 12, no. 2, pp. 128–137, 2003.
- [7] F. Y. Yamaner, X. Zhang, and Ö. Oralkan, "A three-mask process for fabricating vacuum-sealed capacitive micromachined ultrasonic transducers using anodic bonding," *IEEE Transactions on Ultrasonics, Ferroelectrics, and Frequency Control*, vol. 62, no. 5, pp. 972–982, 2015.
- [8] Z. Li, L. L. Wong, A. I. Chen, S. Na, J. Sun, and J. T. Yeow, "Fabrication of capacitive micromachined ultrasonic transducers based on adhesive wafer bonding technique," *Journal of Micromechanics and Microengineering*, vol. 26, no. 11, p. 115019, 2016.
- [9] J. B. Lasky, S. R. Stiffler, F. R. White, and J. R. Abernathy, "Silicon-on-insulator (SOI) by bonding and etch-back," in *1985 International Electron Devices Meeting*. IEEE, 1985, pp. 684–687.
- [10] M. A. Schmidt, "Wafer-to-wafer bonding for microstructure formation," *Proceedings of the IEEE*, vol. 86, no. 8, pp. 1575–1585, 1998.
- [11] A. S. Havreland, M. Engholm, B. G. Tomov, J. A. Jensen, O. Hansen, and E. V. Thomsen, "CMUT Electrode resistance design: Modeling and experimental verification by a row-column array," *IEEE Transactions on Ultrasonics, Ferroelectrics, and Frequency Control*, vol. 66, no. 6, pp. 1110–1118, 2019.
- [12] P. J. French, "Polysilicon: A versatile material for microsystems," *Sensors and Actuators, A: Physical*, vol. 99, no. 1-2, pp. 3–12, 2002.
- [13] E. Ibok and S. Garg, "A Characterization of the Effect of Deposition Temperature on Polysilicon Properties Morphology, Dopability, Etchability, and Polycide Properties," *Journal of the Electrochemical Society*, vol. 140, no. 10, pp. 2927–2937, 1993.
- [14] F. C. Eversteyn and B. H. Put, "Influence of  $\text{AsH}_3$ ,  $\text{PH}_3$ , and  $\text{B}_2\text{H}_6$  on the Growth Rate and Resistivity of Polycrystalline Silicon Films Deposited from a  $\text{SiH}_4\text{H}_2$  Mixture," *Journal of the Electrochemical Society*, vol. 120, no. 1, pp. 106–110, 1973.
- [15] B. Loisel, L. Haji, and M. Guendouz, "LPCVD SILICON FOR ACTIVE DEVICES," *Journal de Physique Colloques*, vol. 50, pp. C5–467–C5–477, 1989.
- [16] L. Chen, J. Miao, L. Guo, and R. Lin, "Control of stress in highly doped polysilicon multi-layer diaphragm structure," *Surface and Coatings Technology*, vol. 141, no. 1, pp. 96–102, 2001.
- [17] J. Yang, H. Kahn, A.-Q. He, S. M. Phillips, and A. H. Heuer, "A new technique for producing large-area as-deposited zero-stress LPCVD polysilicon films: the multiply process," *Journal of Microelectromechanical Systems*, vol. 9, no. 4, pp. 485–494, 2000.
- [18] K. K. Park, H. J. Lee, M. Kupnik, Ö. Oralkan, and B. T. Khuri-Yakub, "Fabricating capacitive micromachined ultrasonic transducers with direct wafer-bonding and locos technology," in *Proceedings of the IEEE International Conference on Micro Electro Mechanical Systems (MEMS)*, 2008.



## APPENDIX E

---

Paper E - A Row-Column-Addressed 2D Probe with and  
Integrated Compound Diverging Lens

---

# A Row–Column-Addressed 2D Probe with an Integrated Compound Diverging Lens

Mathias Engholm\*, Christopher Beers†, Andreas Spandet Havreland\*, Borislav Gueorguiev Tomov‡, Jørgen Arendt Jensen‡, and Erik Vilain Thomsen\*

\*Department of Micro and Nanotechnology, Technical University of Denmark, DK-2800 Kgs. Lyngby, Denmark

†BK Medical, PA-16803, USA.

‡Center for Fast Ultrasound Imaging, Department of Electrical Engineering, Technical University of Denmark, DK-2800 Kgs. Lyngby, Denmark

**Abstract**—Planar 2D row–column-addressed (RCA) arrays can be an attractive alternative to fully-populated arrays due to their significantly lower channel count. However, these arrays can only look straight forward, which limits their utility. One way to increase their field of view is by applying a diverging lens. However, when common lens materials are used for a single-layer diverging lens, they exhibit deficiencies in performance or form factor. A compound lens solution was integrated into a fully functioning probe to achieve a 30° field-of-view (FOV) while retaining clinically-acceptable patient contact characteristics. The compound lens was fabricated of a Bi<sub>2</sub>O<sub>3</sub> loaded RTV and an urethane, Hapflex 541.

Two similar developed probes were compared one with lens and one without. A curvilinear FOV of 28.5° was obtained, which was slightly lower than the designed and was caused by small deformation of the lens during assembly. The output pressure was lowered a factor 6 and the center frequency decreased from 8.5 MHz to 4.9 MHz due to the lens. This was caused by the lens thickness, resulting in an increased attenuation of the transmitted signal. The difference between the two dB compressed frequency responses was observed to follow a linear tendency with a fitted slope of −4 dB/MHz, which was in agreement with the estimated attenuation of the lens.

## I. INTRODUCTION

Planar 2D row–column-addressed (RCA) 2D arrays can be an attractive alternative to fully-populated matrix arrays, as they offer volumetric imaging with a greatly reduced number of electrical connections [1]–[4]. However, an inherent problem of such arrays is the field-of-view (FOV), which is limited to the forward looking rectilinear volume region in front of the transducer. For applications such as abdominal and cardiac imaging, a curvilinear volume region is necessary.

By using a diverging lens in front of the RCA transducer, the inherent rectilinear 3D imaging FOV can be extended to a curvilinear volume region [5], [6]. Joyce and Lockwood presented a diverging lens, cast onto the face of a PZT transducer, made of RTV-11. The lens material and curvature was optimized using PZFlex/OnScale (OnScale, California, USA) and the resulting lens obtained a FOV of 45° [5]. Bouzari et al. presented two concave lenses made of room temperature vulcanizing (RTV) rubber fabricated with two different radii, and it was shown that a FOV of 44.4° could be obtained [7]. The disadvantage was that the lens was formed in RTV rubber, which has a sound velocity lower than tissue. The lens shape therefore has to be concave. A

concave front curvature make patient contact very difficult, so a flat or convex front is usually a requirement, as air can be trapped between the patient and the transducer. Using a lens material with a sound velocity faster than tissue can solve this problem. The concern is that the center of the acoustic wave is attenuated more than the edge, resulting in worsened acoustic wave characteristics. Another concern is that faster materials often are stiffer, which can potentially be a problem for capacitive micromachined ultrasonic transducers (CMUTs), as this can influence the plate behavior. Another solution could be to use a compound lens of two or more materials to obtain a flat or convex front.

Such a diverging compound lens was designed and evaluated by Yang. et al. for photoacoustic computed tomography [8]. The aim was to increase the receive directivity of the detectors for photoacoustic computed tomography to avoid deformation of off-center targets. They utilized a concave shaped polydimethylsiloxane (PDMS) as one layer, and a convex shaped epoxy as the other. The −6 dB acceptance angle was increased from 11° to 55°.

Other compound lenses have been investigated for 1D transducers for elevation focusing, when a high mechanical strength or hardness are required to protect the acoustic stack, to protect the sole against cuts that can arise during surgical procedures, or if an impervious material is needed to make it easy to sterilize without compromising the array performance [9]–[11]. Such materials usually have a higher sound velocity than tissue, requiring the focusing to be achieved by making the external lens surface concave. As the market is suspicious of concave front curvature for patient contact, the acoustic stack can be curved to match a convex interior lens surface, while keeping the lens front flat. Curving the stack has manufacturing disadvantages and is sometimes prohibitive to maintaining element integrity across the entire array.

To obtain a flat or convex surface without curving the stack, a compound lens of two or more different materials can be used [9]–[11]. We have earlier presented a compound diverging add-on lens for an RCA probe which obtained a FOV of 31° [12]. The objective of this work is to integrate the developed compound lens into a fully functioning RCA probe and to compare it to a similar probe without a diverging lens.

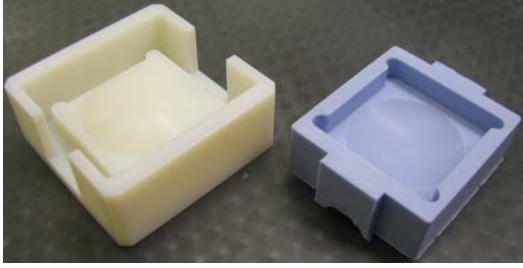


Fig. 1. The inverse mold of the inner lens is 3D printed and bead blasted (left) and a mold is cast of RTV (right).

## II. METHOD

### A. RCA array

Two 92+92 channels RCA 2D CMUT arrays with a 180  $\mu\text{m}$  element pitch were fabricated using a LOCOS process similar to the array described in [13], [14].

### B. Probe Assembly

The development of the compound lens, including the composite materials, are described in [12].

The first step of the assembly was to form the inner lens. The inverse of the mold for casting the lens was 3D printed and bead-blasted. The bead-blasting smooths any irregularities originating from the 3D print and textures the surface to obtain a better adhesion. RTV664 was cast in the 3D printed mold and cured overnight at 45  $^{\circ}\text{C}$ . RTV664 was used as the mold material, as silicones and urethanes do not adhere to each other and are commonly used in the industry for molds for the opposite material. The 3D printed inverse mold and the RTV mold are shown in Fig. 1.

The array was cleaned with IPA, plasma ashed, primed with Nusil MED1-161, blown dry with a nitrogen gun, and left in a humidity chamber for 1 hour. The array was then primed with Hapco primer 810 and blown dry with a nitrogen gun. The second primer only requires to set for a couple of minutes. Hapflex 541 was mixed in a ratio of 2:1 (A:B) in a centrifugal mixer for 2 minutes at 2000 rpm. Hapflex 541 was then directly poured into the mold and degassed for 2 minutes. The array was then pushed into the self-aligning mold and a load was placed in the backside of the array to push it completely into the mold. Hapflex 541 was then cured overnight at room temperature in a nitrogen atmosphere at 375 kPa to help reduce voids as suggested by the manufacturer. The array was then removed from the mold and post-cured for 6 hours at 45  $^{\circ}\text{C}$ . The array with the inner lens is shown in Fig. 2.

The array and the inner lens were glued to the nose piece with precision to obtain the required lens thickness as shown in Fig. 3.

A mold of RTV664 was cast around a dummy nose piece where Teflon tape was applied on its surface to avoid the RTV adhering to the nose piece and also to make the cavity in the mold a little larger than the nose piece itself. RTV615 +  $\text{Bi}_2\text{O}_3$  was mixed, in a mass mix ratio (MMR) of 1:0.9, as described in [12]. The RTV664 mold was then placed on a glass plate,

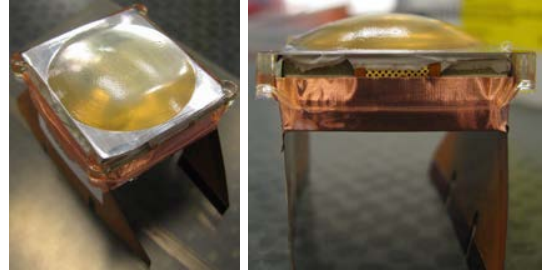


Fig. 2. The mold is filled with Hapflex 541, and after degassing the array is pushed down into it. The Hapflex is cured overnight at 375 kPa at room temperature.

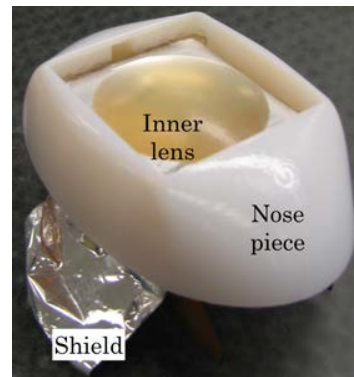


Fig. 3. The transducer with the inner lens was placed in the 3D printed nose piece and the setback was performed to obtain the required lens thickness.

filled with the RTV615 +  $\text{Bi}_2\text{O}_3$  mixture, and degassed for three minutes. The array and nose piece were then pushed into the mold and pressed against a glass plate to obtain a flat front surface. The assembly was then placed in a spring loaded holder to hold the pieces together during curing. The outer lens was cured overnight at 45  $^{\circ}\text{C}$ . The final nose piece connected to the electronics is shown in Fig. 4.

## III. CHARACTERIZATION

The transmit impulse responses of the rows of both probes were measured using an AIMS III intensity measurement



Fig. 4. The nose piece connected to the electronics after the outer lens had cured. The metal sheet sticking out of the nose piece is the electromagnetic shield.



system (Onda Corp., California, USA) with an Onda HGL-0400 hydrophone connected to the experimental research ultrasound scanner, SARUS [15]. The method used to estimate the transmit impulse response is described in [16].

The average impulse response of both probes in the time domain are shown in Fig. 5 and in the frequency domain in Fig. 6(a). The lens is seen to decrease the amplitude of the signal with a factor of six. This effect is also observed in the frequency response. Here the peak amplitude is 10.7 dB lower and the difference increases with the frequency as shown in Fig. 6(b). A linear fit of the difference between the two frequency responses resulted in a slope of  $-4$  dB/MHz, which is caused by the increased attenuation of the lens. The estimate of the one-way attenuation at 5 MHz at the center and at the edge of the lens is 9.9 dB and 18.9 dB, respectively [12]. Whereas the estimate of the one-way attenuation of the acoustic window of the probe without the lens is 3.2 dB at 5 MHz. This is consistent with the 10 dB difference at 5 MHz between the two probes.

The center frequency of the impulse response can be calculated as a weighted mean of the frequencies present in the received signal,  $S$ , as:

$$f_c = \frac{\sum_{i=0}^{N/2} S(if_s/N) \cdot if_s/N}{\sum_{i=0}^{N/2} S(if_s/N)}, \quad (1)$$

where  $N$  is the number of frequency bins in the two-sided spectrum and  $f_s$  is the sampling frequency. The center frequency decreased from 8.5 MHz to 4.9 MHz by applying the lens. The lower center frequency is also observed in the time domain as the pulse length is longer with the lens applied. These effects are caused by the attenuation of the lens. The attenuation increases with frequency, therefore the high frequency components are attenuated more. This lowers the center frequency and decreases the overall signal amplitude. The  $-6$  dB bandwidths decreased from 9.5 MHz to 5.0 MHz by applying the lens. This corresponds to the relative bandwidth decreased with seven percentage points from 109% to 102%.

The desired effect of the lens was to diverge the acoustic energy. This corresponds to applying a time delay across the transducer. The time delay of the impulse responses across the row elements relative to the average impulse response is shown in Fig. 7 for both probes. The diverging effect is visible, as signals are delayed more at the edges than at the center. The f-number,  $F_{\#}$ , of the lens can be estimated from the time delay profile. This is done by multiplying the time delay with the speed of sound to obtain the delay "distance". The radius is estimated by fitting a circle to the delay profile and dividing the radius with the width of the active footprint of the transducer. By doing so, the f-number was estimated to  $F_{\#} = 1.97$ . This corresponds to a FOV of  $28.5^\circ$ , while it was designed to  $30.1^\circ$ . A  $1.6^\circ$  lower FOV could be due to that the probe was a little deformed during curing of the last lens material, which was caused by the spring loaded holder. This could have changed the lens from being flat, to being slightly curved.

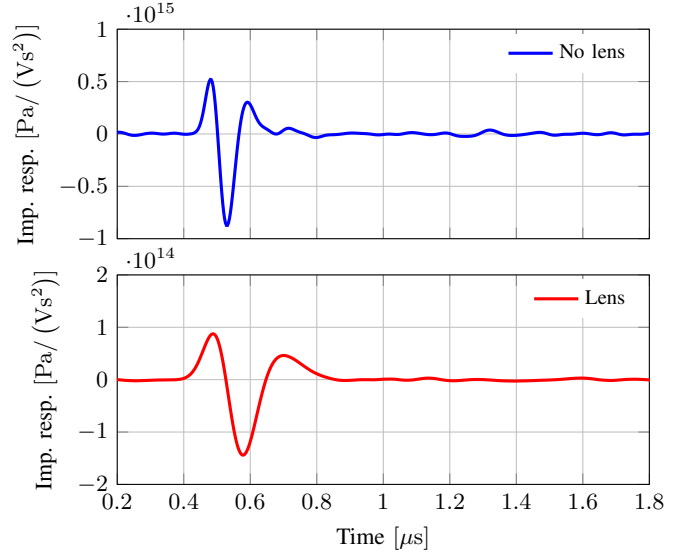


Fig. 5. Time transmit average impulse response of the two probes. The method used to estimate the transmit impulse response is described in [16].

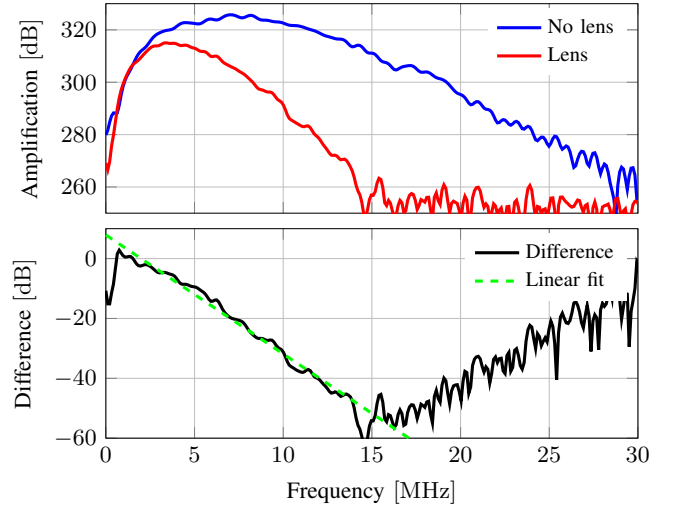


Fig. 6. Frequency impulse response derived from the time impulse response in Fig. 5. A linear fit of the difference between the two frequency responses results in a slope of  $-4$  dB/MHz

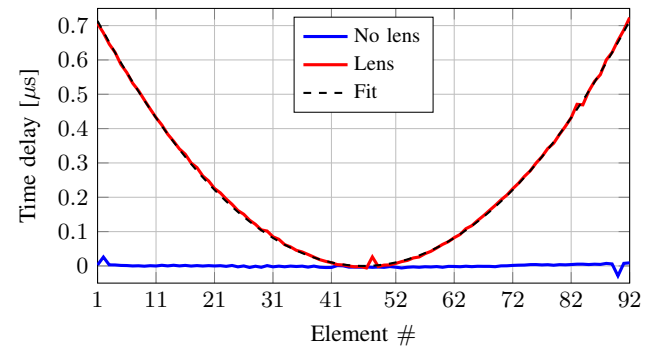


Fig. 7. Comparison of the measured time delay of the row elements of the two probes. A flat time delay profile are seen for the probe without the diverging lens, where the probe with the diverging lens has parabolic formed time delay profile. The f-number was estimated to  $F_{\#} = 1.97$ , corresponding to a FOV of  $28.5^\circ$ .

#### IV. CONCLUSION

Diverging lenses showed to be a feasible method for improving the FOV of RCA arrays. However, common lens materials have a speed of sound lower than tissue/water. The form factor of the lens therefore has to be concave to diverge the energy. A concave front makes patient contact difficult as air can be trapped between the patient and the transducer. A compound diverging lens was integrated into a fully functioning RCA probe to demonstrate the manufacturing capability. A curvilinear FOV of  $28.5^\circ$  was obtained by applying the lens.

The probe with the diverging lens was compared to a similar probe without a lens. The output pressure was a factor of 6 lower and the center frequency decreased from 8.5 MHz to 4.9 MHz by applying the lens. This was caused by the thicker lens thickness, resulting in an increased attenuation of the transmitted signal.

Compound lenses are challenged due to minimum constituent material thickness requirements and the acoustic attenuation of the materials. A compound lens will always be thicker than then the corresponding single materials lens. Alternatives to cylindrical/spherical shapes are therefore attractive to reduce the total lens thickness. However, RCA arrays might be less sensitive to the high attenuation through the lens as the element size (and therefore transmitted or received energy) is more than twice the size of 1D arrays.

#### ACKNOWLEDGMENT

This work is financially supported by the Danish National Advanced Technology Foundation (82-2012-4), Innovation Fund Denmark (7050-00004B), and by BK Medical, Herlev, Denmark.

#### REFERENCES

- [1] C. E. Morton and G. R. Lockwood, "Theoretical assessment of a crossed electrode 2-D array for 3-D imaging," in *Proc. IEEE Ultrason. Symp.*, 2003, pp. 968–971.
- [2] C. H. Seo and J. T. Yen, "A 256 x 256 2-D array transducer with row-column addressing for 3-D rectilinear imaging," *IEEE Trans. Ultrason., Ferroelec., Freq. Contr.*, vol. 56, no. 4, pp. 837–847, April 2009.
- [3] A. Sampaleanu, P. Zhang, A. Kshirsagar, W. Moussa, and R. Zemp, "Top-orthogonal-to-bottom-electrode (TOBE) CMUT arrays for 3-D ultrasound imaging," *IEEE Trans. Ultrason., Ferroelec., Freq. Contr.*, vol. 61, no. 2, pp. 266–276, 2014.
- [4] M. F. Rasmussen, T. L. Christiansen, E. V. Thomsen, and J. A. Jensen, "3-D imaging using row-column-addressed arrays with integrated apodization — Part I: Apodization design and line element beamforming," *IEEE Trans. Ultrason., Ferroelec., Freq. Contr.*, vol. 62, no. 5, pp. 947–958, 2015.
- [5] A. W. Joyce and G. R. Lockwood, "Crossed-array transducer for real-time 3D imaging," in *Proc. IEEE Ultrason. Symp.*, 2014, pp. 2116–2120.
- [6] H. Bouzari, M. Engholm, C. Beers, M. B. Stuart, S. I. Nikolov, E. V. Thomsen, and J. A. Jensen, "Curvilinear 3-D imaging using row-column-addressed 2-D arrays with a diverging lens: Feasibility study," *IEEE Trans. Ultrason., Ferroelec., Freq. Contr.*, vol. 64, no. 6, pp. 978–988, 2017.
- [7] H. Bouzari, M. Engholm, C. Beers, S. I. Nikolov, M. B. Stuart, E. V. Thomsen, and J. A. Jensen, "Curvilinear 3-D imaging using row-column addressed 2-D arrays with a diverging lens: Phantom study," *IEEE Trans. Ultrason., Ferroelec., Freq. Contr.*, vol. 65, no. 7, pp. 1182–1192, 2018.
- [8] S. Yang, W. Qin, H. Guo, T. Jin, N. Huang, M. He, and L. Xi, "Design and evaluation of a compound acoustic lens for photoacoustic computed tomography," *Biomed. Opt. Express*, vol. 8, no. 5, pp. 2756–2765, May 2017.
- [9] D. G. Miller, "Transducer acoustic lens," June 1983, US Patent 4,387,720.
- [10] J. E. Snyder, L. J. Keres, and G. W. Frey, "Compound lens for ultrasound transducer probe," Nov 1996, US Patent 5,577,507.
- [11] D. R. Dietz, C. G. Oakley, D. Morgan, and D. Patwa, "Apodizing ultrasonic lens," February 2011, US Patent 7,888,847 B2.
- [12] M. Engholm, H. Bouzari, C. Beers, J. A. Jensen, and E. V. Thomsen, "Increasing the field-of-view of row-column-addressed ultrasound transducers: implementation of a diverging compound lens," *Ultrasonics*, vol. 88, pp. 97–105, 2018.
- [13] M. Engholm, T. L. Christiansen, C. Beers, J. P. Bagge, L. N. Moesner, H. Bouzari, A. Lei, M. Berkheimer, M. B. Stuart, J. A. Jensen, and E. V. Thomsen, "A hand-held row-column addressed CMUT probe with integrated electronics for volumetric imaging," in *Proc. IEEE Ultrason. Symp.*, 2015, pp. 1–4.
- [14] M. Engholm, H. Bouzari, T. L. Christiansen, C. Beers, J. P. Bagge, L. N. Moesner, S. E. Diederichsen, M. B. Stuart, J. A. Jensen, and E. V. Thomsen, "Probe development of CMUT and PZT row-column-addressed 2-D arrays," *Sens. Actuators A: Phys.*, vol. 273, pp. 121–133, 2018.
- [15] J. A. Jensen, H. Holten-Lund, R. T. Nilsson, M. Hansen, U. D. Larsen, R. P. Domsten, B. G. Tomov, M. B. Stuart, S. I. Nikolov, M. J. Pihl, Y. Du, J. H. Rasmussen, and M. F. Rasmussen, "SARUS: A synthetic aperture real-time ultrasound system," *IEEE Trans. Ultrason., Ferroelec., Freq. Contr.*, vol. 60, no. 9, pp. 1838–1852, 2013.
- [16] J. A. Jensen, "Safety assessment of advanced imaging sequences, II: Simulations," *IEEE Trans. Ultrason., Ferroelec., Freq. Contr.*, vol. 63, no. 1, pp. 120–127, 2016.



## APPENDIX F

---

### Fabrication processes

---

#### F.1 LOCOS

Process flow title <b>2D CMUT v3.2, LOCOS</b>			Revision <b>1.0</b>
DTU Danchip National Center for Micro- and Nanofabrication	Contact email <a href="mailto:ahav@nanotech.dtu.dk">ahav@nanotech.dtu.dk</a>		Contact person Andreas Havreland
	Labmanager group MEMS(3313)	Batch name 2D CMUT LOCOS	Date of creation 13-Sep-19
			Contact phone 81711536
			Date of revision 13-Sep-19

## Objective

Batch name: **Error! Reference source not found.**

This is an example process flow to be used as a template. It should contain

- The objective of the process.
- Substrates/samples used in the flow. Both actual samples to be processed (device wafers) and monitor samples for the different process steps
- The Process flow main processes and steps
- Recommended: Figures illustrating the sample before and after each main process step.

How to use this template (works only with the .dotx template file):

- Fill out the fields in the heading!
- Add process steps in the following way:
  1. Select a process step header and one or more detail steps. Make sure to select the whole line so that the marking extends beyond the table to the right.

<b>1 Preparation</b>	1.1 Wafer selection	Wafer box	Take the wafers from the storage and put them in a wafer box.	Note the wafer IDs in the batch traveler
<b>2 SiO<sub>2</sub> deposition</b>				<b>All wafers</b>
	2.1 SiO <sub>2</sub> dry oxidation	Phosphor Drive-in (A3)	Place a test wafer in the center of the boat and place device wafers and eg. test wafers equally distributed on each side of the test wafer. No spacing between wafers. Recipe: Dry1050, time:100min Target thickness:100±10nm	Measure oxide thickness on the <u>filmtch</u> and note the result in the furnace log
<b>3 Lithography – 1.5µm standard</b>				<b>All wafers</b>
	3.1 Surface treatment	HMDS oven	Load all wafers in oven for ~30 mins Recipe: program 4	Note time in logbook

2. Press <ctrl> C to copy the part.
3. Select the step header where you want to insert the new step. Again make sure to select the whole line.
4. Press <ctrl> V to insert to new step.

- The Content (TOC) on the last page is an option, but can give a nice overview for very long process flows.

## Substrates

Substrate	Orient.	Size	Doping/type	Polish	thickness	Box	Device layer thickness	Purpose	# Sample I
SOI	<100>	4"	n (Phos.) High doping	DSP	525±25µm		20 µm	Bottom electrode	
SOI	<100>	4"	n (Phos.)	SSP	525±25µm		3 µm	Top electrode 400 nm box	

Comments: Number of wafers is for illustration only

Process flow title <b>2D CMUT v3.2, LOCOS</b>	Rev. <b>1.0</b>	Date of revision 13-Sep-19	Contact email ahav@nanotech.dtu.dk
--	--------------------	-------------------------------	---------------------------------------

Step Heading	Equipment	Procedure	Comments
<b>1 Preparation</b>			<b>Bottom electrode wafer</b>
1.1 Wafer selection	Wafer box		20 µm device layer
<b>2 Oxidation – Insulation oxide</b>			<b>Bottom electrode wafer</b>
2.1 RCA	RCA bench		All wafers
2.2 SiO <sub>2</sub> wet oxidation	Phosphorus Drive-in (A3)	Place a test wafer in the center of the boat and place device wafers and test wafers for equally distributed on each side of the test wafer. No spacing between wafers. Remember test wafers for later in the process LOCOS process  4.5 MHz Recipe: Dry1100, time:8h30min Target thickness: 400±10nm  9MHz Recipe: Dry1100, time:5h20min Target thickness: 300±10nm  Annealing time: 20min	1-3 dummies Note time in logbook
2.3 Thickness measure	Filmtek	Measure oxide thickness on dummy wafer	Dummy wafer
2.4 Break down voltage		Out of clean room	Dummy
<b>3 Nitride deposition – LOCOS nitride</b>			<b>Bottom electrode wafer</b>
3.1 Si <sub>3</sub> N <sub>4</sub> deposition	Nitride furnace (4'')	Deposit nitride Recipe: Nitride4 Time: 14 min (@ 3.4 nm/min) Target thickness: 55 nm ±5nm	
<b>4 Polysilicon deposition – Nitride etch mask</b>			<b>Bottom electrode wafer</b>
4.1 Polysilicon depositon	Polysilicon furnace (4'')	Recipe:Poly620 Time: 11 min (@8.7 nm/min) Target thickness: 100nm	
<b>5 Lithography 1.5 µm – polysilicon etch/nitrid etch</b>			<b>Bottom electrode wafer</b>
5.1 Coat wafer	Spin coater: Gamma UV	nLOF negative resist Recipe: 1.5 µm with HMDS	
5.2 Exposure	Aligner: MA6	Align to flat. Hard contact Exposure time: 8 sec Intensity: 13 mW/cm <sup>2</sup> Mask: Cavity	
5.3 Develop	TMAH UV developer	Recipe: DCH 100mm PEB60s@110C SP60s PEB 110C	
5.4 Inspection	Optical microscope	Check pattern and alignment marks	
<b>6 Polysilicon etch</b>			<b>Bottom electrode wafer</b>
6.1 Polysilicon etch	DRIE Pegasus	Recipe: 100nmPoly_SOI Process time: 12s (2 cycles)	

Process flow title <b>2D CMUT v3.2, LOCOS</b>	Rev. <b>1.0</b>	Date of revision 13-Sep-19	Contact email ahav@nanotech.dtu.dk
--	--------------------	-------------------------------	---------------------------------------

6.2	Inspection	Optical microscope	Check pattern and alignment marks	
6.3	Strip resist	Plasma asher 2	Process time: 45 min O <sub>2</sub> : 400 ml/min N: 70 ml/min Power: 1000W	
6.4	Coat wafer	Spin coater: Gamma UV	AZ 5214E positive resist Recipe: DCH 100mm 5214E 1.5um HMDS	For front side protection.
6.5	Polysilicon etch	Wet Poly Etch	Strip PolySi of backside for 2 min. Frontside is protected by resist	
6.6	Strip resist	Plasma asher 2	Process time: 45 min O <sub>2</sub> : 400 ml/min N: 70 ml/min Power: 1000W	
<b>7</b>	<b>Nitride wet etch – LOCOS nitride</b>			<b>Bottom electrode wafer</b>
7.1	Nitride etch	Wet bench	Wet silicon nitride etch H <sub>3</sub> PO <sub>4</sub> @ 160 C (2.3 nm/min) Time: ~20 min	
7.2	7up	7up	Clean wafers after wet nitride etch due to possible contamination by potassium ions from people stripping nitride after KOH	
7.3	Inspection	Optical microscope	Check pattern and alignment marks	
7.4	Strip polysilicon mask	DRIE Pegasus	Recipe: 100nmPoly_SOI Process time: 12s (2 cycles)	
<b>8</b>	<b>Lithography 1.5 μm – oxide/Si etch</b>			<b>Bottom electrode wafer</b>
8.1	Coat wafer	Spin coater: Gamma UV	Mir 701 positive resist Recipe: 1.5 μm with HMDS	
8.2	Exposure	Aligner: MA6	Align to flat. Hard contact Exposure time: 13 sec Intensity: 13 mW/cm <sup>2</sup> Mask: Bottom electrode	
8.3	Develop	TMAH UV developer	Recipe: DCH 100mm PEB60s@110C SP60s PEB 110C	
8.4	Inspection	Optical microscope	Check pattern and alignment marks	
<b>9</b>	<b>Oxide etch – insulation layer</b>			<b>Bottom electrode wafer</b>
9.1	Oxide etch	AOE	Recipe: SiO <sub>2</sub> _res Time: 2x1.5 min (@ 400nm oxide) Temp: 0C	Wait 30 min for temp to stabilize Etch 1, then 2, then 1, then 2, then O <sub>2</sub> clean chamber for a couple of min
9.2	Inspection	Optical microscope	Visual Inspection	Can you see silicon in the alignment marks?
<b>10</b>	<b>Silicon etch – insulation layer</b>			<b>Bottom electrode wafer</b>
10.1	Etching Si	Pegasus	Etch all device layer Recipe: 20um_SOI Time: 4min Temp: 20C	Check etch is all the way through the Si and you can see Oxide in the alignment marks

Process flow title <b>2D CMUT v3.2, LOCOS</b>	Rev. <b>1.0</b>	Date of revision 13-Sep-19	Contact email ahav@nanotech.dtu.dk
--	--------------------	-------------------------------	---------------------------------------

10.2 Strip resist	Plasma Asher 2	Process time: 45 min O <sub>2</sub> : 400 ml/min N: 70 ml/min Power: 1000W	
<b>11 Oxidation - LOCOS</b>			<b>Bottom electrode wafer</b>
11.1 RCA	RCA bench	Only first HF for half the time (10 sec)	20um device layer wafers
11.2 SiO <sub>2</sub> wet oxidation	Phosphorus Drive-in (A3)	Place a test wafer in the center of the boat and place device wafers and eg. test wafers equally distributed on each side of the test wafer. No spacing between wafers.  4.5 MHz Recipe: Wet1100, time: 1 Hour 35 Min Target thickness: 840 nm Total on dummy: 750 nm  9 MHz Recipe: Wet1100, time: 50 Min Target thickness: 610 nm Total on dummy: 530 nm	1-3 dummies Note time in logbook
11.3 Break down voltage		Out of clean room	Dummy
<b>12 Wafer bonding</b>			<b>All ordinary wafers</b>
12.1 RCA	RCA bench	RCA of wafers including new 3um SOI wafers	
12.2 Fusion bonding	Wafer bonder 02	Recipe: CMUT Transport wafers in dedicated box from RCA. Minimize ambient exposure and handling time. Use RCA cleaned tweezers	
12.3 Annealing	Anneal-bond furnace	Recipe: Ann1100 Time: 1h 10min	
12.4 Inspection	Pl mapper	Inspect post anneal voids Detector: Si + InGaAs Gain: x10 (corr.) Filter: 1100nm HP	
<b>13 Handle layer and box oxide etch</b>			<b>All ordinary wafers</b>
13.1 Si etch	ASE	Etch handle layer away, recipe: etchaway, ~1 hour to etch 360 μm (~6μm/min)	Etch until the oxide become visible at the circumference of the wafer. Then abort the process.
13.2 KOH	Si Etch 2: KOH	Etch the remaining of the device layer. Process time: (~40min)	If voids have been detected in the PL mapper, then make sure to puncture them with a tweezer. Then dip the wafers in the KOH again peel of the membrane.
13.3 7up	7up	Clean wafers after wet nitride etch due to possible contamination by potassium ions from people stripping nitride after KOH	



Process flow title <b>2D CMUT v3.2, LOCOS</b>	Rev. <b>1.0</b>	Date of revision 13-Sep-19	Contact email ahav@nanotech.dtu.dk
--	--------------------	-------------------------------	---------------------------------------

13.4Oxide etch	BHF	Etch box oxide away, Time: 7 min, check oxide is gone. Blue film on backside to protect oxide.	
13.5RCA	RCA bench		The wafers are fragile at this point. Make sure they do not stick to the spin dryer.
<b>14 Lithography - Access to bottom electrodes</b>			<b>Bonded wafers</b>
14.1Coat wafer	Spin coater: Gamma UV	Mir 701 positive resist Recipe: 1.5 µm with HMDS	
14.2Exposure	Aligner: MA6	Align to flat. Hard contact Exposure time: 13 sec Mask: Access to bottom electrode	
14.3Develop	TMAH UV developer	Recipe: PEB 110C 60s puddle develop	
14.4Inspection	Optical microscope	Check pattern and alignment marks	
<b>15 Etch - Access to bottom electrodes</b>			<b>Bonded wafers</b>
15.1Etch Si	DRIE- Pegasus	Etch all device layer Recipe: 2um_SOI Temp: 20C Time: 60 sec	
15.2Oxide etch	AOE	Recipe: SiO2_res Time: 4 x 2 min (@1356nm oxide) Temp: 0C	Wait 30 min for temp to stabilize
15.3Strip resist	Plasma Asher 2	Process time: 45 min O <sub>2</sub> : 400 ml/min N: 70 ml/min Power: 1000W	
<b>16 Metallization</b>			<b>Bonded wafers</b>
16.1Deposit Ti+Al	Wordentec or Alcatel	Target Ti thickness: 20nm Target Al thickness: 400nm	
<b>17 Lithography – Top electrode</b>			<b>Bonded wafers</b>
17.1Coat wafer	Spin coater: Gamma UV	AZ 5214E positive resist Recipe: 1.5 µm with HMDS	
17.2Exposure	Aligner: MA6	Align to flat. Hard contact Exposure time: 5.5 sec Mask: Top electrode	
17.3Develop	TMAH UV developer	Recipe: DCH 100nm SP 60s	
17.4Inspection	Optical microscope	Check pattern and alignment marks	
<b>18 Etch top electrode</b>			<b>Bonded wafers</b>
18.1Al etch	ICP metal	Recipe: Al etch Temp: 20C Time: 180s	Wafer has to be crystal bonded to a 6'' carrier. Remember crystal bond should be covering the entire backside of the wafer. Check in microscope of all metal is gone. Abort process when all metal is gone at the web cam. Approximately 90s.

Process flow title <b>2D CMUT v3.2, LOCOS</b>	Rev. <b>1.0</b>	Date of revision 13-Sep-19	Contact email ahav@nanotech.dtu.dk
--	--------------------	-------------------------------	---------------------------------------

18.2 Etch Si	ASE	Etch all device layer Recipe: Shallolr Time: 57s (5 cycles) Temp: 20C	
18.3 Inspection	Optical microscope	Make sure the etch is all the way through the Silicon device layer.	
18.4 Strip resist	Plasma Asher 1	Process time: 45 min O <sub>2</sub> : 400 ml/min N: 70 ml/min Power: 1000W	
<b>19 Dicing</b>			<b>Bonded wafers</b>
19.1 Coat wafers	Spin coater: Gamma UV	Recipe: 3441 DCH100 5214E 4.2 μm	Protecting resist for the dicing process.
19.2 Dicing out chips	Disco Saw	Dicing out chips	Disco Saw

**F.2 BCB**

Step	Process	Equipment	Recipe	Comments
<b>1. Defining bottom electrode</b>				
1.1	Spin on photoresist	Spin-track I	Recipe : 2.0 um nLoF with HMDS	Positiv resist
1.2	Exposure	MA6 Aligner	Time : 8 sec Dose : 112 mJ/cm2 Mask name : CMUT_BCB_Bottom Electrode	QC for MA6 13mW/cm2
1.3	Development	Developer TMAH UV-lithography	Recipe : 3001 DCH 100mm PEB60s@110C SP60s	
1.4	Inspection	Optical Microscope	Check pattern is fully developed	
1.5	Electrode deposition	Alcatel or Wordentec	Adhesion : Ti 10nm Electrode : Al 400nm	
1.6	Lift-off	Acetone bath (with metal)	Place the wafer in the acetone bath and add US	
1.7	Rinse	DI Water	Rinse wafer for 5 min and spin-dry	
1.8	Inspection	Microscope	Check lift-off is fully done	
<b>2. BCB Deposition</b>				
2.1	Adhesion promoter	Manual spinner	Promoter : AP3000 Dispense: 15sec @ 3000 rpm	
2.2	Spin on BCB	Manual spinner	Resine : BCB 4022-25 Quantity : 1 to 5 ml Spread : 5-10 sec @500 rpm Spin : 30 sec @4000 rpm	Expected thick- ness is approxima- tively 500nm ( <i>not optimized yet</i> )
2.3	Soft bake	Hot plate	Temperature : 60 °C Time : 90 sec	Dry out residual solvent
<b>NOTE:</b> According to Dow Chemical, the delay time between soft back and exposure can be up to 24h before adverse effects. BCB left-over may be thrown away in the C-waste.				

Step	Process	Equipment	Recipe	Comments
<b>3. Defining the cavities</b>				
3.1	Exposure	MA6 aligner	Time : 0.6 sec ( <i>not optimized yet</i> ) Dose : 0.015 mJ/cm <sup>2</sup> per 1 nm Mask name : CMUT_BCB_Cavities	QC of MA6 set to 13 mW/cm <sup>2</sup> . Exposure dose for 4022-25 : ~ 15 mJ/cm <sup>2</sup> per um.
3.2	Pre-develop bake	Hot plate	Temperature : 50 °C Time : 30 sec	
<b>NOTE:</b> According to Dow Chemical, the development must be done immediately after the pre-develop bake. Developer is stored in the III-V room cabinet.				
3.3	Development	Solvent Fumehood (C-1)	Technique : immersion Developer : DS3000 Temperature : 30°C-40°C ± 0.5°C Time : several minute	
3.4	Stop-development	Solvent Fumehood (C-1)	Technique : immersion Developer : DS3000 Temperature : room temp. Time : 1-2 min	Softly agitate the wafer in the becher
3.5	Rinse	DI Water	Rinse wafer for 5 min in DI water at room temp. and spin-dry	
3.6	Post-develop bake	Hot plate	Temperature : 90°C Time : 1 min	
3.7	Inspection	Microscope	Check pattern is fully developed	
3.8	Curing	Oven	Temperature : 250°C Time : 60 min	
<b>4. Wafer bonding</b>				
4.1	Adhesion promoter	Manual spinner	Promoter : AP3000 Dispense: 15sec @ 3000 rpm	Recommended by Down for metal and non organic substrate
4.2	Bonding	EVG NIL	Pressure : Temperature : Force : Time : 60 min	
4.3	Inspection	Infrared camera or Microscope	Inspect for void and cavities	

Step	Process	Equipment	Recipe	Comments
<b>5. Remove handle</b>				
5.1	Silicon etch	ASE	Recipe : etchaway Time : 1h25min	Stop etch when the handle is removed and SiO <sub>2</sub> is visible (visual inspection)
5.2	Oxide etch	BHF	Time : 14 min Etch rate : 80nm/min	
5.3	Rinse/dry	Wet bench	Time : 5 min in DI water Spin dry	No bubble or ultrasound
<b>6. Top electrode</b>				
6.1	Top electrode	Alcatel or Wordentec	Adhesion : Ti 10nm Electrode : Al 400nm	
<b>7. Access to bottom electrodes (and patterning top electrode)</b>				
7.1	Spin on photoresist	Spin-track I	Recipe : 1.5um MiR701 with HMDS	Positiv resist
7.2	Exposure	MA6 Aligner	Time : 13 sec Dose : 169 mJ/cm <sup>2</sup> Mask name : CMUT_BCB_Top Electrode Contact : hard	QC for MA6 aligner is 13mW/cm <sup>2</sup>
7.3	Development	Developer TMAH UV-lithography	Recipe : 3001 DCH 100mm PEB60s@110C SP60s	
7.4	Inspection	Optical Microscope	Check pattern is fully developed	
7.5	Dry etch Al	ICP metal etcher	Platen power : 100W Coil power : 500 W Cl <sub>2</sub> : 25 sccm HBr : 15 sccm Temperature : 20 °C Recipe name : Al etch Time : 80sec	Use end-point detection to estimate the time. Remember crystal bond.
7.6	Dry etch Si	ICP metal etcher	Platen power : 120W SF <sub>6</sub> : 30 sccm O <sub>2</sub> : 26.9 sccm Temperature : 20 °C Recipe name : Al_etch Time : 40 sec	Use end-point detection to estimate the time. Remove crystal bond with heat and DI water

Step	Process	Equipment	Recipe	Comments
7.7	Resist removal	Plasma Asher	O2 flow : 400 ml/min N2 flow : 70 ml/min Power : 1000 W Time : 30 min	
<b>8. Protective resist</b>				
8.1	Spin on photoresist	SSE	Recipe : AZ5214e_4inch_10um	
<b>9. Dicing</b>				
9.1	Chip dicing	Saw	Align wafer with x/y mark	
9.2	Resist stripping	Acetone	Fumehood (outside)	
9.3	Rinse/dry	ISO	Fumehood (outside)	Air gun dry

### **F.3 Anodic bond**



Process flow title <b>Anodic bonded CMUT</b>			Revision <b>V1</b>
	Contact email magnusgp@hotmail.com		Contact person Magnus Galsgård Petersen Contact phone +4527119550
	Labmanager group MEMS(3313)	Batch name RCABCMUT 1	Date of creation 15-May-199 Date of revision

## Objective

Batch name: RCABCMUT

The purpose of the project is to fabricate Capacitive Ultrasonic Transducers using an anodic bonding process via a homemade SOI wafer.

## Substrates

Substrate	Orient.	Size	Doping/type	Polish	thickness	Box	Purpose	#	Sample ID
Silicon	<100>	4"	n (Phos.)	DSP	350±15µm		Top plate	25	ON538-1
Boron glass		4"	p (Boron.)	DSP	500±10µm		Bottom plate	25	IB548

Comments:

Process flow title <b>Anodic bonded CMUT</b>	Rev. <b>V1</b>	Date of revision 13-Sep-19	Contact email nicolai.michaelsen@gmail.com
---	-------------------	-------------------------------	---

## Fabrication process for bottom substrate:

Step Heading	Equipment	Procedure	Comments
<b>1</b>	<b>Preparation for Bottom electrode fabrication</b>		<b>Bottom electrode wafers</b>
1.1	Wafer selection	Use the dedicated vacuum tweezer across the A-furnace stack	IB548
1.2	Dehydration	Oven 250C Place borofloat wafers in a metallic cassettes. Time: ≈24h	All borofloat wafers used for Bottom.
<b>2</b>	<b>Cr deposition as masking layer for cavity etch</b>		<b>All Bottom electrode wafers</b>
2.1	Cr deposition by E-beam evaporation	Temescal Recipe: Cr Deposition rate: 10 Å/s Final thickness: 150 nm	All borofloat wafers.
<b>3</b>	<b>Lithography process 1 – Cavities pattern</b>		<b>All Bottom electrode wafers</b>
3.1	Spin coating	Gamma UV AZ 5214E positive resist 2.2 μm with HMDS <b>Recipe:</b> 3421- DCH 100mm 5214E 2.2 um HMDS 1 dummy wafer: 3421- DCH 100mm 5214E 2.2um Cleaning wafer: 0400 100mm Coater Clean	Clean spinner nozzle and run the dummy wafers
3.2	Exposure	MA6-2 aligner Mask: Cavity <b>Exposure dose:</b> 110 mJ/cm <sup>2</sup> <b>Exposure time:</b> 10 s <b>Intensity:</b> 11 mW/cm <sup>2</sup>	
3.3	Develop	TMAH UV developer Recipe: 1004	
3.4	Inspection	Optical microscope Check pattern	
3.5	Inspection	Dektak XT Check height, write it down	
<b>4</b>	<b>Cr mask etch</b>		<b>All Bottom electrode wafers</b>
4.1	Cr etch	Cr etch 18 in beaker Cr etch 18 Time: 1:30-2:00 min	Easy to see when etch is finished as glass will be clear
4.2	Inspection	Dektak XT Check height, write it down	
<b>5</b>	<b>Cavity etching</b>		<b>All Bottom electrode wafers</b>
5.1	Cavity etch	BHF plastic beaker Etch rate: ≈24nm/min Etch time: 24 min Target depth: 570 nm	
5.2	Inspection	Optical microscope Check for defects	
5.3	Inspection	Dektak XT Measure depth of the cavities	This measurement is not precise due to variation in thickness of resist. It does provide an indication.
<b>6</b>	<b>Removal of masking layers</b>		<b>All Bottom electrode wafers</b>
6.1	Resist strip	Resist strip wet bench Time: 10 min with ultrasonic agitation	

Process flow title <b>Anodic bonded CMUT</b>	Rev. <b>V1</b>	Date of revision 13-Sep-19	Contact email nicolai.michaelsen@gmail.com
---	-------------------	-------------------------------	---

6.2	Inspection	Dektak XT	Measure depth of cavities	
6.3	Cr removal	Cr etch 18 in beaker	Time: 5 minutes	Wafers need to be completely transparent when done
6.4	Inspection	Optical microscope		See if pattern is good, and see whether all Cr is gone
6.5	Inspection	Dektak XT		Final measurement of depth
<b>7 Lithography process 2 – Bottom electrode</b>				
7.1	Dehydration	250C Oven	Time: 5 hours	
7.2	Spin coating	Gamma-UV	Thickness: 2µm Resist: AZ nLOF 2020	
7.3	Exposure	MA6-2 aligner	Mask: Bottom electrode Time: 11 seconds Intensity: 11 mJ/cm <sup>2</sup>	Contrast in this step is not very good. Good alignment is critical
7.4	Development	TMAH-developer	Recipe: 60s PEB @110 + 60 s SP development	
7.5	Inspection	Optical microscope		Check that pattern is well defined inside cavities. Use dark field to make edges more visible
<b>8 Bottom electrode metal</b>				
8.1	Deposit Cr/Au	Temescal	Recipe: CrAu Final thickness Cr: 20 nm Cr deposition rate: 5 Å/s Final thickness Au: 150 nm. Au deposition rate: 10 Å/s	In this step, the Au thickness can be adjusted to fit a specific gap height.
8.2	Lift-off	Lift-off wet bench	Time: 1 hour 15 min	Time for this step can vary a lot. It is important that all metal outside of the cavities gets removed
8.3	Inspection	Optical microscope		See whether alignment is ok, or if metal have been deposited outside of cavities – this will result in short circuits
8.4	Inspection of cavities	Dektak XT	Measure depth of cavities with gold	

## Fabrication process for anodic bonding of top and bottom plate:

Step Heading	Equipment	Procedure	Comments	
<b>9</b>	<b>Cleaning before wafer bonding</b>		<b>All wafers</b>	
9.1	Cleaning-RCA	RCA bench	All top plates	
9.2	Cleaning-Piranha	Piranha in a beaker	Sulfuric acid H2SO4 (98%) and peroxide H2O2 (30%) in the ratio 4:1. Temp: 70-80C Time: 2 min	All bottom plates First add H2SO4 into a glass beaker then add H2O2.
<b>10</b>	<b>Wafer bonding</b>		<b>All wafers</b>	

Process flow title	Rev.	Date of revision	Contact email
<b>Anodic bonded CMUT</b>	<b>V1</b>	13-Sep-19	nicolai.michaelsen@gmail.com

10.1 Anodic bonding	Wafer bonder 2	Recipe: Anodic bonding CMUT 800 V no center pin  Voltage steps: -300V, -600V, -800V	Bottom and top plate directly from the cleaning process. Have Rune change the top electrode to a clean one before this step
10.2 Bond inspection	PL mapper	Use reflectance mapping for mapping voids after bonding.	<b>(optional step if necessary)</b> All bonded wafer – normally voids can be seen with the naked eye
10.3 Inspection	Optical microscope		Look for defects, also near edges
<b>11 Handle and box layer etching</b>			<b>All bonded wafers</b>
11.1 Poly-Si layer	Si KOH etch 3	Etch top not useable device layer away. Process 4: 90C Time: 5-10 min for a thickness of 3 µm	Time depends on the thickness of the poly-Si on the IHMSOI wafer.
11.2 Oxide etch	BHF	Etch of not useable box layer. Etch rate: 75 nm/min. Etch time: 6 minutes for a thickness of 400 nm	Time depends on the thickness of the oxide on the IHMSOI wafer. Surface is hydrophobic when etch is done
11.3 Si etch	Si KOH etch 3	Etch handle layer away Etch rate: 1.7µm/min Etch time: 3 hours 24 minutes for a thickness of 350 µm	This is a critical step of the process flow. It is recommended to check how the wafers look regularly during the step
11.4 Oxide etch	BHF	Etch of not useable box layer. Etch rate: 75 nm/min. Etch time: 6 minutes for a thickness of 400 nm	Time depends on the thickness of the oxide on the IHMSOI wafer. Surface is hydrophobic when etch is done
11.5 Cleaning-Piranha	Piranha in a beaker	Sulfuric acid H2SO4 (98%) and peroxide H2O2 (30%) in the ratio 4:1. Temp: 70-80C	First add H2SO4 into a glass beaker then add H2O2.
<b>12 Top electro deposition</b>			<b>All bonded wafers</b>
12.1 Deposition Al	Temescal	Recipe: Al Final thickness Al: 400 nm Deposition rate Al: 10 Å/s	The deposition rate looks to be fluctuating during deposition, however, the metal layer looks fine-.
<b>13 Lithography – top electrode</b>			<b>All bonded wafers</b>
13.1 Coat wafer	Gamma UV	Resist: AZ MiR 701 positive resist <b>Recipe:</b> 1411- DCH 100mm MiR 701 1.5 µm HMDS	HMDS doesn't work on Al Clean spinner nozzle and run the dummy wafers. Spin coat as soon as possible after metal deposition
13.2 Exposure	MA6-2 aligner	Exposure mode: Hard contact. <b>Exposure dose:</b> 189.2mJ/cm <sup>2</sup> . <b>Exposure time:</b> 17.2s <b>Intensity:</b> 11 mW/cm <sup>2</sup> Mask: Top electrode.	Align from backside.

Process flow title	Rev.	Date of revision	Contact email
<b>Anodic bonded CMUT</b>	<b>V1</b>	13-Sep-19	nicolai.michaelsen@gmail.com

13.3Develop	TMAH UV developer	<b>Recipe:</b> 3001 DCH 100mm PEB60s@110C+SP60s	
13.4Inspection	Optical microscope	Check pattern and alignment marks.	
<b>14 Etch – Top electrode</b>			<b>All bonded wafers</b>
14.1Al etch	Aluminum etch	Etch of pure aluminum. Etch rate: ≈100nm/min. Etch time: 4min.	
14.2Inspection	Optical microscope	Inspection of aluminum etch.	Control in microscope if all metal is gone.
<b>15 Etch - Bottom electrode access</b>			<b>All bonded wafers</b>
15.1Device layer etch	ASE	Dry etching of access to bottom electrode. 2+2 cycles, recipe: shallorc Use Al carrier – no backside cooling	
15.2Resist strip	Plasma asher 1	Photoresist stripping Pressure: 0.8-1.0mbar. Gas: Mixture of O2 and N2. Power: 1000watts. Time: 30-45 min	

## **F.4 LOCOS + Anodic bond**

Process flow title <b>RC CMUTs 2xLOCOS</b>			Revision <b>1.0</b>
<b>DTU Danchip</b> National Center for Micro- and Nanofabrication	Contact email <a href="mailto:ahav@nanotech.dtu.dk">ahav@nanotech.dtu.dk</a> <a href="mailto:rungra@dtu.dk">rungra@dtu.dk</a>		Contact person Andreas Havreland Rune Sixten Grass
	Labmanager group MEMS(3313)	Batch name 2D CMUT LOCOS	Date of creation 13-Sep-19
		Contact phone 81711536 42280068	Date of revision 13-Sep-19

## Objective

Batch name: **Error! Reference source not found.**

This is an example process flow to be used as a template. It should contain

- The objective of the process.
- Substrates/samples used in the flow. Both actual samples to be processed (device wafers) and monitor samples for the different process steps
- The Process flow main processes and steps
- Recommended: Figures illustrating the sample before and after each main process step.

How to use this template (works only with the .dotx template file):

- Fill out the fields in the heading!
- Add process steps in the following way:
  1. Select a process step header and one or more detail steps. Make sure to select the whole line so that the marking extends beyond the table to the right.

<b>1 Preparation</b>			
1.1 Wafer selection	Wafer box	Take the wafers from the storage and put them in a wafer box.	Note the wafer IDs in the batch traveler
<b>2 SiO<sub>2</sub> deposition</b>			
2.1 SiO <sub>2</sub> dry oxidation	Phosphor Drive-in (A3)	Place a test wafer in the center of the boat and place device wafers and eg. test wafers equally distributed on each side of the test wafer. No spacing between wafers. Recipe: Dry1050, time:100min Target thickness:100±10nm	Measure oxide thickness on the <u>filmtech</u> and note the result in the furnace log
<b>3 Lithography – 1.5µm standard</b>			
3.1 Surface treatment	HMDS oven	Load all wafers in oven for ~30 mins Recipe: program 4	Note time in logbook

2. Press <ctrl> C to copy the part.
3. Select the step header where you want to insert the new step. Again make sure to select the whole line.
4. Press <ctrl> V to insert to new step.

- The Content (TOC) on the last page is an option, but can give a nice overview for very long process flows.

## Substrates

Substrate	Orient.	Size	Doping/type	Polish	Thickness	Box	Device layer thickness	Purpose	# Sample I
Si	<100>	4"	n (Phos.) <0.025 Ω cm	DSP	525±25µm		20 µm	Bottom electrode	
SOI	<100>	4"	n (Phos.)	SSP	525±25µm		3 µm	Top electrode 400 nm box	

Comments: Number of wafers is for illustration only

Process flow title <b>RC CMUTs 2xLOCOS</b>	Rev. <b>1.0</b>	Date of revision 13-Sep-19	Contact email ahav@nanotech.dtu.dk ahav@nanotech.dtu.dk
---	--------------------	-------------------------------	---

Step Heading	Equipment	Procedure	Comments
<b>1 Preparation</b>			<b>Bottom electrode wafer</b>
1.1 Wafer selection	Wafer box		20 µm device layer
<b>2 Oxidation – Insulation oxide</b>			<b>Bottom electrode wafer</b>
2.1 RCA	RCA bench		All wafers
<b>3 Oxidation – 2nd Insulation oxide</b>			<b>Bottom electrode wafer</b>
3.1 RCA	RCA bench		All wafers
3.2 SiO <sub>2</sub> wet oxidation	Phosphorus Drive-in (A3)	Place a test wafer in the center of the boat and place device wafers and test wafers for equally distributed on each side of the test wafer. No spacing between wafers. Remember test wafers for later in the process LOCOS process  4.5 MHz <b>Recipe:</b> Dry1100, time:8h30min <b>Target thickness:</b> 400±10nm <b>Annealing time:</b> 20min	1-3 dummies Note time in logbook
3.3 Thickness measure	Filmtek/Ellipsometer	Measure oxide thickness on dummy wafer	Dummy wafer
3.4 Break down voltage		Out of clean room	Dummy
<b>4 Nitride deposition – 2nd LOCOS nitride</b>			<b>Bottom electrode wafer</b>
4.1 Si <sub>3</sub> N <sub>4</sub> deposition	Nitride furnace (4'')	Deposit nitride <b>Recipe:</b> Nitride4 <b>Time:</b> 14 min (@ 3.4 nm/min) <b>Target thickness:</b> 55 nm ±5nm	
<b>5 Polysilicon deposition – Nitride etch mask</b>			<b>Bottom electrode wafer</b>
5.1 Polysilicon deposition	Polysilicon furnace (4'')	<b>Recipe:</b> Poly620 <b>Time:</b> 11 min (@8.7 nm/min) <b>Target thickness:</b> 100nm	
<b>6 Lithography 1.5 µm – polysilicon etch/nitrid etch</b>			<b>Bottom electrode wafer</b>
6.1 Coat wafer	Spin coater: Gamma UV	<b>Resist:</b> nLOF (negative resist) <b>Recipe:</b> 2411 DCH 100mm nLOF 2020 1.5um HMDS <b>Thickness:</b> 1.5 µm	
6.2 Exposure	Aligner: MA6	Align to flat. Hard contact <b>Exposure time:</b> 10 sec <b>Intensity:</b> 11 mW/cm <sup>2</sup> <b>Mask:</b> Cavity (Darkfield)	
6.3 Develop	TMAH UV developer	<b>Recipe:</b> 3001 DCH 100mm PEB60s@110C SP60s PEB 110C	
6.4 Inspection	Optical microscope	Check pattern and alignment marks	
<b>7 Polysilicon etch</b>			<b>Bottom electrode wafer</b>
7.1 Polysilicon etch	Wet Poly Etch	Strip Poly-Si for 5 min	Might require 1 silicon wafer in the bath for conditioning



Process flow title <b>RC CMUTs 2xLOCOS</b>	Rev. <b>1.0</b>	Date of revision 13-Sep-19	Contact email ahav@nanotech.dtu.dk ahav@nanotech.dtu.dk
---	--------------------	-------------------------------	---

7.2 Strip resist	Plasma Asher 2	<b>Process time:</b> 10-15 min O <sub>2</sub> : 400 ml/min N: 70 ml/min Power: 1000W	
7.3 Inspection	Optical microscope	Check pattern and alignment marks	
<b>8 Nitride wet etch – 2nd LOCOS nitride</b>			<b>Bottom electrode wafer</b>
8.1 Nitride etch	Wet bench	Wet silicon nitride etch H <sub>3</sub> PO <sub>4</sub> @ 160 C (2.3 nm/min) <b>Time:</b> ~20 min	
8.2 7up	7up	Clean wafers after wet nitride etch due to possible contamination by potassium ions from people stripping nitride after KOH	
8.3 Inspection	Optical microscope	Check pattern and alignment marks	
8.4 Strip polysilicon mask	DRIE Pegasus	<b>Recipe:</b> 100nmPoly_SOI <b>Process time:</b> 12s (2 cycles)	
<b>9 Lithography 1.5 μm – oxide/Si etch</b>			<b>Bottom electrode wafer</b>
9.1 Coat wafer	Spin coater: Gamma UV	<b>Resist:</b> MiR 701 (positive resist) <b>Recipe:</b> 1411 DCH 100mm MiR 701 1.5um HMDS	
9.2 Exposure	Aligner: MA6	Align to flat. Hard contact <b>Exposure time:</b> 18 sec <b>Intensity:</b> 11 mW/cm <sup>2</sup> <b>Mask:</b> Bottom electrode	
9.3 Develop	TMAH UV developer	<b>Recipe:</b> 3001 DCH 100mm PEB60s@110C SP60s PEB 110C	
9.4 Inspection	Optical microscope	Check pattern and alignment marks	
<b>10 Oxide etch – insulation layer</b>			<b>Bottom electrode wafer</b>
10.1 Oxide etch	AOE	<b>Recipe:</b> SiO <sub>2</sub> _res <b>Time:</b> 2 min (@400nm oxide) <b>Temp:</b> 0C (or -5C to -10C)	Wait 30 min for temp to stabilize
10.2 Inspection	Optical microscope	Visual Inspection	Can you see silicon in the alignment marks?
<b>11 Silicon etch –</b>			<b>Bottom electrode wafer</b>
11.1 Etching Si	Pegasus	Etch 100 μm silicon from the top <b>Recipe:</b> Prototype/mae/DREM <b>Time:</b> approx. 36 min <b>Temp:</b> -19C	Check etch is all the way through the Si and you can see Oxide in the alignment marks
11.2 Strip resist	Plasma Asher 2	<b>Process time:</b> 45 min O <sub>2</sub> : 400 ml/min N: 70 ml/min Power: 1000W	
<b>12 Oxidation – 2nd LOCOS</b>			<b>Bottom electrode wafer</b>
12.1 RCA	RCA bench	Only first HF for half the time (10 sec)	
12.2 SiO <sub>2</sub> wet oxidation	Phosphorus Drive-in (A3)	Place a test wafer in the center of the boat and place device wafers and eg. test wafers equally	1-3 dummies Note time in logbook

Process flow title <b>RC CMUTs 2xLOCOS</b>	Rev. <b>1.0</b>	Date of revision 13-Sep-19	Contact email ahav@nanotech.dtu.dk ahav@nanotech.dtu.dk
---	--------------------	-------------------------------	---

distributed on each side of the test wafer. No spacing between wafers.		
4.5 MHz Recipe: Wet1100, time: 1 Hour 35 Min Target thickness: 840 nm Total on dummy: 750 nm		
12.3 Break down voltage	Out of clean room	Dummy
<b>13 Wafer bonding – PSOI Top electrode</b>		<b>All wafers</b>
13.1 RCA	RCA bench	RCA of wafers including new 3um (P)SOI wafers
13.2 Fusion bonding	Wafer bonder 02	<b>Recipe:</b> CMUT Transport wafers in dedicated box from RCA, after hand bonding. Minimize ambient exposure and handling time. Use RCA cleaned tweezers
13.3 Annealing	Anneal-bond furnace	<b>Recipe:</b> Ann1100 <b>Time:</b> 1h 10min
13.4 Inspection	PI mapper	Inspect post anneal voids <b>Detector:</b> Si + InGaAs <b>Gain:</b> x10 (corr.) <b>Filter:</b> 1100nm HP
13.5 Oxide etch 2: BHF Clean	BHF	Etch through to silicon on both sides. <b>Time:</b> 6 min
<b>14 Device layer etch from backside</b>		<b>Bonded</b>
14.1 Si etch	ASE/Grinding	Etch device layer until grooves/patterns are visible <b>Recipe:</b> etchaway (etchacar, use carrier if no clamping), ~1 hour to etch ~400µm (~6µm/min) 2 x 30 min + 1-5 x 5 min
14.2 Polish	Polisher/CM P	Polish backside of wafer prior to bonding Roughness 40 nm -> 0,5 nm 5 min CMUT Trench
<b>15 Wafer bonding – Borofloat/Pyrex Insulation wafer</b>		<b>Bonded wafers and borofloat wafer</b>
15.1 RCA	RCA bench	RCA of wafers including cleaning borofloat wafers in Piranha solution for 10 min in separate beaker
15.2 Anodic bonding	Wafer bonder 02	<b>Recipe:</b> CMUT (800V) Transport wafers in dedicated box from RCA, after hand bonding. Minimize ambient exposure and handling time. Use RCA cleaned tweezers
15.3 Annealing	Anneal-bond furnace	<b>Recipe:</b> Ann1100 <b>Time:</b> 1h 10min
15.4 Inspection	PI mapper	Inspect post anneal voids <b>Detector:</b> Si + InGaAs <b>Gain:</b> x10 (corr.) <b>Filter:</b> 1100nm HP
<b>16 Handle layer and box oxide etch</b>		<b>Bonded wafers</b>
16.1 Polysilicon or amorphous deposition	PECVD 3 or IBE/IBSD Ionfab 300	Deposits clampable a-Si or Poly-Si layer on glass side <b>Time:</b> approx. 35 min for 220 nm (PECVD3), or approx. 50 min for 200 nm (IBSD)

Process flow title <b>RC CMUTs 2xLOCOS</b>	Rev. <b>1.0</b>	Date of revision 13-Sep-19	Contact email ahav@nanotech.dtu.dk ahav@nanotech.dtu.dk
---	--------------------	-------------------------------	---

16.2 Si etch	ASE	Etch handle layer away, <b>Recipe:</b> etchaway, ~1 hour to etch 360 μm (~6μm/min)	Etch until the oxide become visible at the circumference of the wafer. Then abort the process.
16.3 KOH	Si Etch 3: KOH	Etch the remaining of the device layer. <b>Process time:</b> (~10-15min)	If voids have been detected in the PL mapper, then make sure to puncture them with a tweezer. Then dip the wafers in the KOH again peel of the membrane.
16.4Oxide etch	BHF	Etch box oxide away, Time: 7 min, check oxide is gone.	
16.5 Piranha	Fumehood	Clean wafers after wet nitride etch due to possible contamination by potassium ions from people stripping nitride after KOH	Don't use dirty single spin drier to dry
<b>17 Lithography - Access to bottom electrodes</b>			<b>Bonded wafers</b>
17.1Deposit Al	Wordentec or Temescal	Target Al thickness: 100nm	
17.2Coat wafer	Spin coater: Gamma UV	Mir 701 positive resist <b>Recipe:</b> 1411 DCH 100mm MiR 701 1.5um HMDS	
17.3Exposure	Aligner: MA6	Align to flat. Hard contact <b>Exposure time:</b> 13 sec <b>Mask:</b> Access to bottom electrode (Darkfield Mask)	
17.4Develop	TMAH UV developer	<b>Recipe:</b> PEB 110C 60s puddle develop	
17.5Inspection	Optical microscope	Check pattern and alignment marks	
<b>18 Etch - Access to bottom electrodes</b>			<b>Bonded wafers</b>
18.1Al etch	Wet bench 05: Al etch	<b>Etch rate:</b> ~60-100nm/min <b>Time:</b> 1.5 min	
18.2 Si etch	ASE	Etch through top plate layer, <b>Recipe:</b> prototype/shalolrc, 5 cycles, <b>Time:</b> 57 sec <b>Temp:</b> 20C	
18.3Oxide etch	ASE	Etch through post oxide layer <b>Recipe:</b> SIO2IPCc <b>Time:</b> 3 x 4 min (@1356nm oxide) <b>Temp:</b> 20C	Wait 30 min for temp to stabilize
18.4Strip resist	Plasma Asher 2	<b>Process time:</b> 45 min <b>O<sub>2</sub>:</b> 400 ml/min <b>N:</b> 70 ml/min <b>Power:</b> 1000W	
18.5 Al etch	Wet bench 05: Al etch	<b>Etch rate:</b> ~60-100nm/min <b>Time:</b> 1.5 min	
<b>19 Metallization</b>			<b>Bonded wafers</b>
19.1Deposit Ti+Al	Wordentec or Temescal	Target Ti thickness: 20nm Target Al thickness: 400nm	
<b>20 Lithography – Top electrode</b>			<b>Bonded wafers</b>
20.1Coat wafer	Spin coater: Gamma UV	Mir 701 positive resist <b>Recipe:</b> 1411 DCH 100mm MiR 701 1.5um HMDS	

Process flow title	Rev.	Date of revision	Contact email
<b>RC CMUTs 2xLOCOS</b>	<b>1.0</b>	13-Sep-19	ahav@nanotech.dtu.dk ahav@nanotech.dtu.dk

20.2Exposure	Aligner: MA6	Align to flat. Hard contact <b>Exposure time:</b> 5.5 sec <b>Mask:</b> Top electrode	
20.3Develop	TMAH UV developer	<b>Recipe:</b> DCH 100nm SP 60s	
20.4Inspection	Optical microscope	Check pattern and alignment marks	
<b>21 Etch top electrode</b>			<b>Bonded wafers</b>
21.1 Al etch	Wet bench 05: Al etch	<b>Etch rate:</b> ~60-100nm/min <b>Time:</b> 1.5 min	
21.2 Si etch	ASE	Etch top plate (3 μm) to separate elements <b>Recipe:</b> prototype/shalolrc, 5 cycles, <b>Time:</b> 57 sec <b>Temp:</b> 20C	
21.3Strip resist	Plasma Asher 1	<b>Process time:</b> 45 min <b>O<sub>2</sub>:</b> 400 ml/min <b>N:</b> 70 ml/min <b>Power:</b> 1000W	If cannot clamp do Si etch
<b>22 Dicing</b>			<b>Bonded wafers</b>
22.1Coat wafers	Spin coater: Gamma UV	Recipe: 3441 DCH100 5214E 4.2 μm	Protecting resist for the dicing process. Potentially use a mask to expose contacts.
22.2Dicing out chips	Disco Saw	Dicing out chips	Disco Saw

**Contents**

<b>1</b>	<b>Preparation .....</b>	<b>2</b>
1.1	Wafer selection .....	2
<b>2</b>	<b>Oxidation – Insulation oxide .....</b>	<b>2</b>
2.1	RCA .....	2
<b>3</b>	<b>Oxidation – 2nd Insulation oxide .....</b>	<b>2</b>
3.1	RCA .....	2
3.2	SiO <sub>2</sub> wet oxidation .....	2
3.3	Thickness measure .....	2
3.4	Break down voltage.....	2
<b>4</b>	<b>Nitride deposition – 2nd LOCOS nitride.....</b>	<b>2</b>
4.1	Si <sub>3</sub> N <sub>4</sub> deposition .....	2
<b>5</b>	<b>Polysilicon deposition – Nitride etch mask.....</b>	<b>2</b>
5.1	Polysilicon deposition.....	2
<b>6</b>	<b>Lithography 1.5 µm – polysilicon etch/nitrid etch .....</b>	<b>2</b>
6.1	Coat wafer .....	2
6.2	Exposure .....	2
6.3	Develop .....	2
6.4	Inspection .....	2
<b>7</b>	<b>Polysilicon etch .....</b>	<b>2</b>
7.1	Polysilicon etch.....	2
7.2	Strip resist.....	3
7.3	Inspection .....	3
<b>8</b>	<b>Nitride wet etch – 2nd LOCOS nitride.....</b>	<b>3</b>
8.1	Nitride etch.....	3
8.2	7up.....	3
8.3	Inspection .....	3
8.4	Strip polysilicon mask .....	3
<b>9</b>	<b>Lithography 1.5 µm – oxide/Si etch.....</b>	<b>3</b>
9.1	Coat wafer .....	3
9.2	Exposure .....	3
9.3	Develop .....	3
9.4	Inspection .....	3
<b>10</b>	<b>Oxide etch – insulation layer.....</b>	<b>3</b>
10.1	Oxide etch .....	3
10.2	Inspection .....	3
<b>11</b>	<b>Silicon etch –.....</b>	<b>3</b>
11.1	Etching Si .....	3
11.2	Strip resist.....	3
<b>12</b>	<b>Oxidation – 2nd LOCOS .....</b>	<b>3</b>
12.1	RCA .....	3
12.2	SiO <sub>2</sub> wet oxidation .....	3
12.3	Break down voltage .....	4
<b>13</b>	<b>Wafer bonding – PSOI Top electrode .....</b>	<b>4</b>
13.1	RCA .....	4
13.2	Fusion bonding .....	4

- 13.3 Annealing..... 4
- 13.4 Inspection..... 4
- 13.5 Oxide etch 2: BHF Clean ..... 4
- 14 Device layer etch from backside..... 4**
- 14.1 Si etch ..... 4
- 14.2 Polish ..... 4
- 15 Wafer bonding – Borofloat/Pyrex Insulation wafer..... 4**
- 15.1 RCA ..... 4
- 15.2 Anodic bonding..... 4
- 15.3 Annealing..... 4
- 15.4 Inspection ..... 4
- 16 Handle layer and box oxide etch ..... 4**
- 16.1 Polysilicon or amorphous deposition ..... 4
- 16.2 Si etch ..... 5
- 16.3 KOH..... 5
- 16.4 Oxide etch ..... 5
- 16.5 Piranha ..... 5
- 17 Lithography - Access to bottom electrodes ..... 5**
- 17.1 Deposit Al ..... 5
- 17.2 Coat wafer ..... 5
- 17.3 Exposure ..... 5
- 17.4 Develop ..... 5
- 17.5 Inspection ..... 5
- 18 Etch - Access to bottom electrodes ..... 5**
- 18.1 Al etch..... 5
- 18.2 Si etch ..... 5
- 18.3 Oxide etch ..... 5
- 18.4 Strip resist..... 5
- 18.5 Al etch..... 5
- 19 Metallization..... 5**
- 19.1 Deposit Ti+Al ..... 5
- 20 Lithography – Top electrode ..... 5**
- 20.1 Coat wafer ..... 5
- 20.2 Exposure ..... 6
- 20.3 Develop ..... 6
- 20.4 Inspection ..... 6
- 21 Etch top electrode..... 6**
- 21.1 Al etch..... 6
- 21.2 Si etch ..... 6
- 21.3 Strip resist..... 6
- 22 Dicing..... 6**
- 22.1 Coat wafers..... 6
- 22.2 Dicing out chips ..... 6